UNIVERSITY OF CALIFORNIA

Santa Barbara

Accelerated Design and Characterization of Oxidation Resistant Co-Based Gamma / Gamma-Prime Superalloys

A dissertation submitted in partial satisfaction of the

requirements for the degree Doctor of Philosophy

in Materials

by

Colin Alistair Stewart

Committee in charge:

Professor Carlos G. Levi, Co-Chair

Professor Tresa M. Pollock, Co-Chair

Professor Anton Van der Ven

Professor Daniel R. Mumm (UC Irvine)

March 2019

The dissertation of Colin Alistair Stewart is approved.

_____
Anton Van der Ven

_____
Daniel R. Mumm

_____
Tresa M. Pollock, Committee Co-Chair

_____
Carlos G. Levi, Committee Co-Chair

February 2019

Accelerated Design and Characterization of

Oxidation Resistant Co-Based Gamma / Gamma-Prime Superalloys

by

Colin Alistair Stewart

Acknowledgements

The work presented herein, as well as the rest of my graduate career at UC Santa Barbara, is the product of many people beyond myself. I would first like to thank my advisors Profs. Tresa Pollock and Carlos Levi for their advice and mentorship. Over the past 5 years I have been able to grow significantly as a researcher and scientist, and it has only been possible through their guidance and leadership. My committee members Profs. Anton Van der Ven and Dan Mumm have been invaluable role models, and I greatly appreciate their involvement over the years, especially Dr. Mumm who took the time to visit from UC Irvine. Our industry collaborators at GE Global Research have been invaluable, and I would like to thank Drs. Akane Suzuki and Don Lipkin for their time, support, and advice over the years. I also owe Dr. Jun Zhu of Computherm LLC my most sincere thanks for his assistance in thermodynamic modeling, and his original efforts in establishing the 2011 version of the cobalt database used throughout my thesis. Tresa and Carlos have also been kind enough to allow me to spend a summer expanding my knowledge as an intern in industry with Dr. Sesh Tamirisakandala at Arconic, and I would like to thank Sesh and all the other Arconic interns for such an incredible opportunity.

Throughout my time at UCSB, I have been lucky enough to meet some of the most kind, helpful, excited, and intelligent people I have ever met. All of the development engineers and technical staff past and present: Deryck Stave, Chris Torbet, Pete Maxwell, Mark Cornish, Aidan Taylor, Stephen Krämer, Amanda Strom, Alexander Mikhailovsky, Lee Sawyer, without all of whom I would never have been able to accomplish this body of research. To all of my group mates in both Levi and Pollock research groups, I owe a most

profound debt for their friendship, intellectual contributions, support, and advice. In particular I would like to thank Wes Jackson for the many, many hours he kindly spent with me when I was a 1st year, discussing oxidation phenomena; Mike Titus and Rob Rhein for originally mentoring me and teaching me about cobalt alloys; Betsy Clarke for showing me the ropes of oxidation experiments; Will Lenthe for programming and image analysis expertise, as well as a great deal of board games and lovely dinners; Tori Miller and Jackie Avallone for taking me under their wings on my very first visit to UCSB during prospective student weekend, and the subsequent 5 years of dinners, technical discussions, ice cream, conferences, and friendship. With endearing gratitude to my cohort-mates: Marissa Lafata for discussions on PSLS and superalloys, pot lucks, sushi, and game nights; Rebecca Reitz for support with classes and presentations, tea parties, and beautiful hikes. To my office mates Collin Holgate, Maylea Aldaz, Tom Drtina, and Stefan Heinze for discussions on everything from sample preparation to IV lunches (and invaluable emotional support). To my interns Alejandro Hinojos and Maita Roberts for their incredible perseverance and creativity. To my group mate Sean Murray, who has been an absolutely marvelous partner both scientifically and personally, and who I cannot thank enough for his enthusiasm, insight, and tenacity. To my roommates Leanne Friedrich, Brian Cabinian, Kelly Peterson, and Amanda Ruschel, as well as my gym buddies Brent Goodlet and Paul Christodoulou for both technical discussions and keeping me sane. To my friends Erin Perry, Billy Wonderly, Emily Wonder, Will Elliott, and a great many others.

I would also like to make a point of thanking all the people who have prepared and supported me to become a graduate student in the first place. Deepest gratitude to my undergraduate mentors, advisers, and role models, Drs. Paul Braun, John Busbee, Jennifer

Lewis, Trudy Kriven, Charles Marsh, and Angus Rockett. My high school teachers Messrs. Casper, Will, and Welter. My friends Matt, Scott, Marietta, Jason, Anthony, and many, many others. And most importantly, my parents and family, Gretchen & Charles Stewart, Graham & Quinn Stewart, and Holly, Doug, Kyra, and Ryan Oliver. There are no words that can do justice to how much you have helped and supported me.

Vitae of Colin Alistair Stewart

March 2019

Education:

UNIVERSITY OF CALIFORNIA SANTA BARBARA March 2019
- **Prof. Tresa M. Pollock, Prof. Carlos G. Levi**
- **Doctor of Philosophy in Materials**

UNIVERSITY OF ILLINOIS AT URBANA-CHAMPAIGN May 2012
- **Bachelor of Science in Materials Science and Engineering**
- Minor in International Engineering (Spanish)
- Engineer in Training Certification (EIT/FE Illinois, License 061036841)

Publications:

- **C. A. Stewart**, R. K. Rhein, A. Suzuki, T. M. Pollock, C. G. Levi, "Oxide Scale Formation in Novel γγ' Cobalt-Based Alloys", Superalloys 2016: Proceedings of the 13th International Symposium on Superalloys, 2016, pp. 991-999. [https://doi.org/10.1002/9781119075646.ch105]
- **C. A. Stewart**, A. Suzuki, T. M. Pollock, C. G. Levi, "Rapid Assessment of Oxidation Behavior in Co-Based γ/γ' Alloys", Oxidation of Metals, 2018, pp. 1-14. [https://doi.org/10.1007/s11085-018-9849-2]
- **C. A. Stewart**, R. K. Rhein, A. Suzuki, T. M. Pollock, C. G. Levi, "Oxidation Behavior Across Composition Space Relevant to Co-Based γ/γ' Alloys", Corrosion Science (in preparation)
- **C. A. Stewart**, S. P. Murray, A. Suzuki, T. M. Pollock, C. G. Levi, "Accelerated Discovery Of Oxidation Resistant Co-γ/γ' Alloys With High $L1_2$ Solvus And Low Density", Acta Materialia (in preparation).

Oral Presentations:

- **C. A. Stewart**, A. Suzuki, T. M. Pollock, C. G. Levi, "Evolution of Thermally Grown Oxides in Novel Co-based γ-γ' Superalloys". The Minerals, Metals & Materials Society, 2018 TMS Annual Meeting & Exhibition, March 2018, Phoenix, AZ, USA.
- **C. A. Stewart,** A. Suzuki, C. G. Levi, T. M. Pollock, "Combinatorial Exploration of Oxidation Behavior in Novel Co-Base γ/γ' Alloys". Air Force Research Lab (AFRL), July 2017, Dayton, OH, USA. (Invited)

- **C. A. Stewart**, A. Suzuki, T. M. Pollock, C. G. Levi, "Influence of Alloy Composition on Oxide Scale Formation in Novel Co-Based γ-γ' Superalloys". The Minerals, Metals & Materials Society, 2017 TMS Annual Meeting & Exhibition, March 2017, San Diego, CA, USA.
- **C. A. Stewart**, R. K. Rhein, A. Suzuki, T. M. Pollock, C. G. Levi, "Effects of Composition on the Oxidation Behavior of Co-Based γ-γ' Alloys". Academy for Co-creative Education of Environment and Energy Science, Tokyo Institute of Technology, December 2016, San Diego, CA, USA.
- **C. A. Stewart**, A. Suzuki, T. M. Pollock, C. G. Levi, "Oxide Scale Formation in Novel γ-γ' Co-Based Alloys". The Minerals, Metals & Materials Society, 13th International Symposium on Superalloys, September 2016, Seven Springs, PA, USA.

Poster Presentations:

- **C. A. Stewart**, S. P. Murray, A. Suzuki, T. M. Pollock, C. G. Levi, "Accelerated Discovery of Novel Co-Based γ/γ' Alloys Using High-Throughput Techniques". 2018 Winter Study Group on High Performance Materials, January 2018, Santa Barbara, CA, USA.
- **C. A. Stewart**, A. Suzuki, T. M. Pollock, C. G. Levi, "Combinatorial Exploration of Oxidation Behavior in Co-Based Alloys for Novel γ/γ' Superalloy Development". 2016 Winter Study Group on High Performance Materials, January 2016, Santa Barbara, CA, USA.
- **C. A. Stewart**, A. Suzuki, T. M. Pollock, C. G. Levi, "Combinatorial Exploration of Oxidation Behavior in Co-Based Alloys for Novel γ/γ' Superalloy Development". Gordon Research Conference on High Temperature Corrosion, July 2015, New London, NH, USA.

Honors

- NRC Research Associateship Award, Naval Research Laboratory, 2018
- Best Speaker Award, Tokyo Tech ACEEES Conference 2016
- Honorable Mention, NSF Graduate Research Fellowship Program
- Arthur L. Friedberg Scholarship, University of Illinois
- Cullen Parmelee International Research Scholarship, University of Illinois

---

Mentoring:

Research Mentor, University of California Santa Barbara

- Maita Roberts (Masters Student, Saarland University, Germany) 6/15 – 8/15
- Alejandro Hinojos (Undergraduate, University of Texas El Paso) 6/14 – 8/14

Research & Work Experience:

Arconic (ATEP Division) Niles, OH
Research & Development Graduate Intern Summer 2017

- Developed a heat treatment to maximize the mechanical properties of high temperature titanium alloy RTI-THOR™ originally designed for oxidation resistance
- Applied a data-driven modeling approach to predict fatigue behavior in titanium alloy Ti-64
- Conducted fracture analysis of additively manufactured Ni alloy tensile specimens to evaluate process viability

Xerion Advanced Battery Corp. Champaign, IL
Ceramist Intern Fall 2012 - Spring 2013

- Optimized aqueous ceramic colloidal slurries to resist cracking when tape cast on metal substrates
- Analyzed and prevented occurrence of micro-domains within cast colloidal tapes via SEM and slurry additives
- Assessed the effects of ceramic precursor polydispersity on Li ion battery performance

US Army Corps of Engineers,
Construction Engineering Research Laboratory Urbana, IL
Undergraduate Researcher Summer 2012

- Prepared TEM samples from spark-plasma sintered SiC-Carbon Nanotube composites
- Performed preliminary TEM on samples to verify SiC crystallinity had been maintained during preparation
- Conducted microindentation, flexural testing, and Archimedes method to calculate sample attributes

MSE Senior Design: The Boeing Company Urbana, IL
Senior Undergraduate Spring 2012

- Collaborated with representative from the Boeing Company to devise realistic environmental simulation conditions for samples of commercial aerospace polymer films
- Designed and built equipment to simulate long-term chemical, humidity, and thermal exposure of polymers
- Evaluated the cost, flame resistance, and degradation of polymer films after simulated long-term exposure, and made recommendation of which film was ideal for commercial aerospace applications

Vesuvius Research Pittsburgh, PA
Research Intern Summer 2011

- Optimized the material composition and processing of ceramic refractory composites
- Analyzed effect of binder content on composites' porosity, microstructure, and other green and fired properties
- Performed mechanical testing and SEM analysis on variations of refractory composites.

Department of Materials, Imperial College London London, UK
Research Assistant Summer 2010

- Ground, polished, and imaged metal samples of varying tin, copper, nickel, and zinc compositions
- Cast and recorded temperature during solidification of zinc, zinc oxide, and tin sample ingots
- Calculated grain size and area ratio of intermetallic compounds using the program ImageJ

Department of Materials Science & Engineering Urbana, IL
Research Assistant Summer 2009

- Researched possible methods of reinforcement and composite improvement for high-temperature applications
- Prepared geopolymer composite samples with combinations of different additives
- Tested geopolymer composite samples for crack prevention upon dehydration and heating

---

Abstract

Accelerated Design and Characterization of Oxidation Resistant Co-Based Gamma / Gamma-Prime Superalloys

by

Colin Alistair Stewart

Superalloys are metallic materials comprising predominantly an FCC matrix (γ) with an $L1_2$ intermetallic reinforcing precipitate (γ'), capable of load-bearing applications at high temperatures such as the hot section components of gas turbine engines. Recently discovered Co-based γ/γ' alloys offer a potential avenue for improving engine performance beyond the current limit of commercial Ni-base alloys. To exploit their potential, Co-base alloys must be able to grow a protective, continuous α-Al_2O_3 scale after brief (minutes) exposure to an oxidizing environment at temperatures on the order of 1100°C. Simultaneously, an alloy must also maintain high thermal stability of the strengthening γ' phase. The composition space available to achieve such behavior is vast, with commercial Ni-base superalloys typically containing 11+ elements. Instead of a more traditional alloy design process by incremental trial and error, this dissertation employs modern

computational modeling in combination with high-throughput experimental techniques, pursuant to the mission statement of the NSF DMREF program.

Combinatorial ion plasma deposition was used to systematically synthesize 234 distinct alloy samples in Co-Ni-W-Al-Cr-Ta space. The alloy phase constitution and oxidation behavior after 1 h in air at 1100°C were investigated. Photostimulated luminescence spectroscopy (PSLS) was employed to rapidly screen for the presence of α-Al_2O_3 in the oxide scales. While PSLS can adequately detect the formation of α-Al_2O_3, its ability to do so is moderated by the presence of extraneous, non-desirable oxides with varying thickness and composition. Notably, it was concluded that overlaying CoO was more opaque to the PSLS signal than NiO. Nevertheless, it was shown that a large number of positive PSLS spectra was often related to the overall thickness of the scale, with thinner scales usually characterized by an underlying continuous α-Al_2O_3 scale. The merging of these synthesis and characterization techniques identified the compositional space of promising oxidation behavior, and the effects of Al, Cr, and to a lesser extent W and Ni, on this behavior.

The experimental results were combined with calculations of the senary phase equilibria using available thermodynamic databases. In this manner, the design space for Co-base γ/γ' alloys with suitable stability of the reinforcing phase and desirable oxidation resistant were identified. New compositions designated as "DMREF" alloys were synthesized, and were found to achieve a superior combination of properties relative to other Co-base alloys reported to date. Thus, this dissertation has established the oxidation behavior and phase-constitution in composition space relevant to Co γ/γ' superalloys, designed and generated a novel alloy with markedly improved properties, and demonstrated proof of concept for the strategy of accelerated exploration, design and characterization of new alloy systems.

Glossary of Abbreviations

APB	Anti-Phase Boundary
BC	Bond Coating
BCC	Body Centered Cubic crystal structure
BF	Bright Field mode/image
BSE	Backscattered Electron mode/image
CALPHAD	Calculation of Phase Diagrams method
CASM	Cluster expansion Approach Statistical Mechanics
CLEX	Cluster Expansion
CN	Coordination Number of atomic neighbors
CTE	Coefficient of Thermal Expansion
DF	Dark Field mode/image
DFT	Density Functional Theory
DP	Diffraction Pattern
DSC	Differential Scanning Calorimetry
DTA	Differential Thermal Analysis
EDM	Electric Discharge Machining
EDS	Energy Dispersive [X-ray] Spectroscopy
EIA	Energy Information Administration (USA)
EPMA	Electron Probe Micro-Analysis
ERR	Energy Release Rate of fracture
FAA	Federal Aviation Administration (USA)
FCC	Face Centered Cubic crystal structure
FIB	Focused Ion Beam
HAADF	High Angle Annular Dark Field mode/image
HCF	High Cycle Fatigue loading
HCP	Hexagonal Close Packed crystal structure
HOMO	Highest Occupied Molecular [electron] Orbital
IGT	Industrial Gas Turbine engine
IOF	Internal Oxidation Front
IOZ	Internal Oxidation Zone
IPD	Ion Plasma Deposition
ITIC	Iso-Thermal Iso-Concentrate section
LCF	Low Cycle Fatigue loading
LMC	Liquid Metal Cooled casting furnace
LUMO	Lowest Unoccupied Molecular [electron] Orbital
MMT	Million Metric Tons
MPEA	Multiple Principle Element Alloy
OEM	Original Equipment Manufacturer
PBR	Pilling-Bedworth Ratio of oxide:metal at. volume
PBE	Perdew, Burke, Ernzerhof approximation
PDAS	Primary Dendrite Arm Spacing
PSLS	Photostimulated Luminescence Spectroscopy
PSZ	Partially Stabilized Zirconia [TBC]
PVD	Physical Vapor Deposition

QCM ..... Quartz Crystal Microbalance sensor
SE..... Secondary Electron mode/image
SEM ..... Scanning Electron Microscopy
SESF ..... Superlattice Extrinsic Stacking Fault
SISF ..... Superlattice Intrinsic Stacking Fault
SPLCF..... Sustained Peak Low Cycle Fatigue loading
TBC ..... Thermal Barrier Coating
TCP..... Topologically Close Packed phases
TEE..... Third Element Effect
TEM..... Transmission Electron Microscopy
TGO ..... Thermally Grown Oxide
VASP ..... Vienne *Ab initio* Simulation Package
YSZ..... Yttrium Stabilized Zirconia (TBC)
ZMG ..... Zero Mass Gain point during oxidation

Table of Contents

1 Introduction

Combustion turbine engines power the aviation industry, as well as electricity generation from natural gas, both of which have an enormous impact on the US economy and environment. In 2017, the United States generated 31.7% of its electricity from about $2.5*10^{11}$ m^3 of natural gas [1], which cost ~$35B [2]. Furthermore, in 2017 US aviation carriers burned over 20B gallons of jet fuel, at a cost of ~$77B[‡] [3]. According to 2015 data, burning of natural gas for electricity generation released 526 MMT[§] CO_2 equivalent, while burning jet fuel for aviation released 161 MMT CO_2 equivalent, together accounting for about 10% of the US annual gross emissions of CO_2 equivalent greenhouse gases [4]. Owing to the size of these industries, even small improvements in jet turbine efficiency have the capacity to yield great economic and environmental benefits. One way to increase turbine efficiency is through novel materials with higher temperature capabilities, which allow greater combustion temperatures. Every 30°C increase in combustion temperature is equivalent to an approximately 1% efficiency increase [5]. Many of the hot-stage components of jet engines are currently made from nickel-base superalloys such as René N5 (Figure 1.1b). However, these alloys are considered to be reaching maturity as the solvus temperature of the strengthening γ' phase approaches the solidus temperature [6]. Fortunately, a potential path forward was enabled by a discovery in 2006 by Sato et al. [7]. A new class of Co-base alloys were observed to exhibit the same strengthening γ' phase as Ni-base alloys, yet with a melting temperature 100-150°C higher than that of nickel. If such temperature increases were achieved, the benefits would equate to a 3-5% increase in

‡ FAA Forecast lists jet fuel cost in dollars per barrel, with one barrel equivalent to 42 US gallons.

§ Million-metric-tons, equivalent to a teragram (Tg) in SI units.

turbine efficiency, leading to over $3B-5B annual fuel savings and 20-34 MMT CO_2 equivalent reduction in annual emissions.

The single-crystal Ni-base superalloys currently used in many hot-stage turbine components are the product of over seven decades of research and development both of the alloy composition and the casting method (Figure 1.2) [6]. Further increases in temperature capabilities have been achieved by the addition of internal cooling passages and protective coating systems overlying the structural alloys (Figure 1.3). These coating systems, which include a thermal barrier coating (TBC) and a bond coat (BC), provide not only thermal resistance, but also oxidative resistance via the formation of a passivating thermally grown oxide (TGO). While the performance of the structural alloys is thus dependent on other material systems, it is critical for the underlying alloy to have some measure of thermal and oxidative resistance in the event of coating spallation. To achieve these properties at the temperatures of interest, nominally 1100°C, a Co-base superalloy must have both a high γ' solvus temperature, a large γ' phase fraction (e.g. 60 vol.%) at the operating temperature, and form and maintain a passivating oxide layer when exposed to the harsh combustion environment in the engine.

This dissertation will address primarily the oxidation behavior of Co-base γ/γ' while exploring the relationships with composition, oxidation, and phase constitution. Chapter 2 will present a review of the relevant theory and literature regarding both Co-base γ/γ' alloys, as well as the established Ni-base superalloys as needed. This will include a review of the desired properties for superalloys in structural applications, as well as the known material properties of current superalloys and relevant constituent systems. The general alloy oxidation process will also be covered, with a focus on those aspects relevant for Co- and

Ni-base superalloys. Chapter 3 will discuss the experimental procedures used in the present work, including sample synthesis and preparation, oxidative exposure, characterization by a variety of methods, and phase equilibria calculations using available thermodynamic databases.

These procedures are then used to investigate an initial set of higher-order (multicomponent) Co-base superalloys in Chapter 4. Discussion will address not only the properties of these alloys, but also the traditional evolutionary approach in which they were designed. Chapter 5 will then describe a non-destructive rapid-screening technique for oxidation behavior, along with validations of its use and assessment of its principles of operation. This technique will then be used in combination with a high-throughput combinatorial synthesis technique discussed in Chapter 6. Together, these synthesis and characterization techniques may be coupled with thermodynamic calculations to form a new rapid approach towards alloy development, in contrast to that first discussed in Chapter 4. Such a novel approach allows for the discovery of new superalloy compositions more quickly and systematically than the historical development of the Ni-base systems. This is exemplified in Chapter 7, whereby the insights learned from the previous chapters are used to design a series of novel Co-base γ/γ' alloys which surpass the capabilities of those reported in the literature to date. Lastly, the emerging conclusions and implications of this body of work, as well as recommendations for future work, will be given in Chapter 8.

1.1 Figures

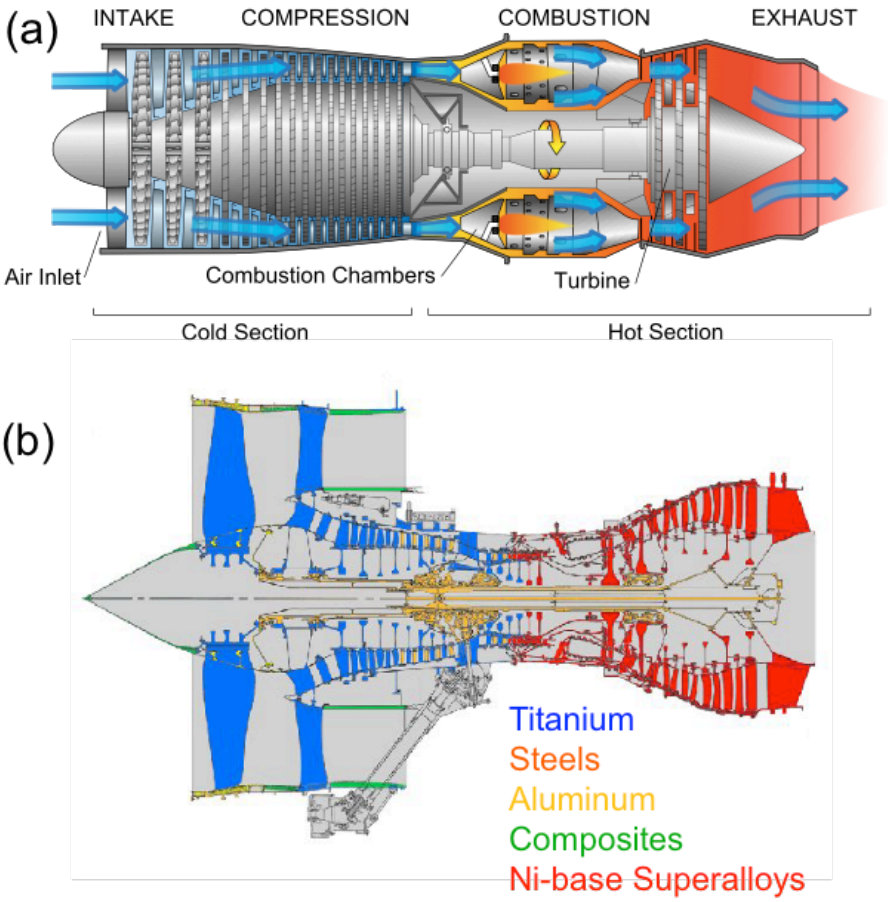

Figure 1.1: Schematic of (a) the operating process of a turbine engine [8], and (b) the materials used for the different components in a Rolls-Royce Trent 800 aero-engine [9]. Colors in parts denote constituent material: blue for titanium alloys, orange for steels, yellow for aluminum alloys, green for composites, and red for nickel-base superalloys.

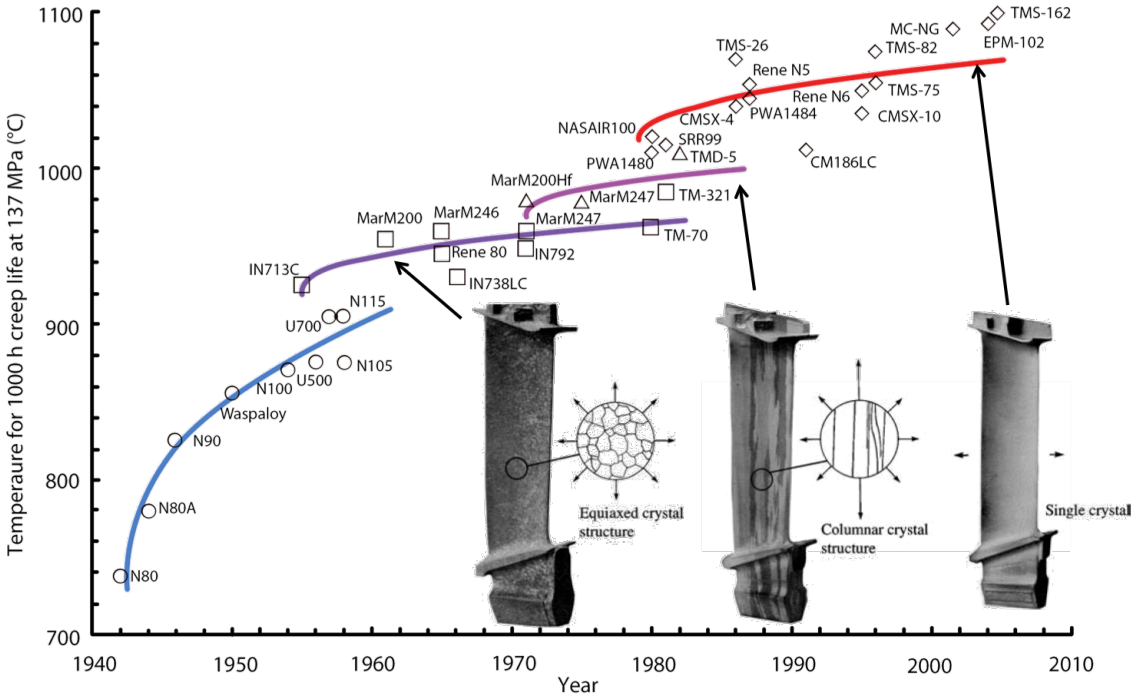

Figure 1.2: Timeline of evolution for gas turbine airfoil material temperature capabilities, showing the effects of changing alloy composition and casting method. Adapted from [6].

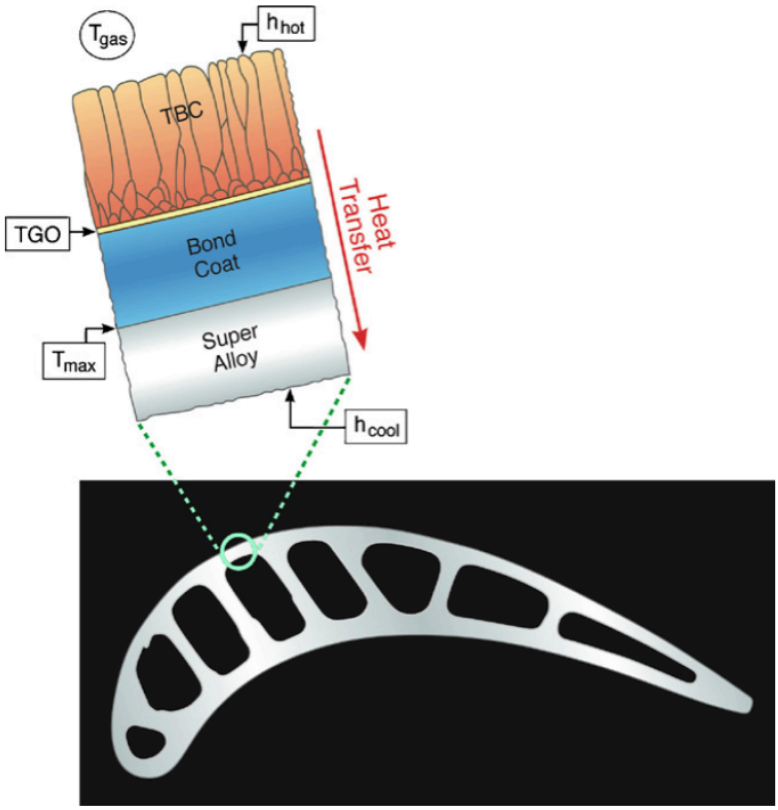

Figure 1.3: An image of a turbine blade in cross-section, showing the internal cooling channels, and a schematic of the protective coating system on the exterior of the blade, from reference [10].

2 Background

Superalloys are so named based on their ability to resist mechanical and chemical degradation at high homologous temperatures, i.e. T/T_M, where T_M is the melting (solidus) temperature. This makes them unique candidates for turbine engine components, where oxidation resistance must be combined with high temperature load-bearing ability. It should be noted that the cobalt-based superalloys discussed herein will not refer to Co-Cr base alloys used for many turbine applications in the 1900s [11]. Such alloys do not possess ordered intermetallic precipitates, and eventually became overshadowed by the Ni-base alloys due to the presence of a strengthening γ' phase. It was in 2006 Sato et al. [7] discovered the presence of γ' precipitates in ternary Co-W-Al, re-opening the door for Co as a base element in superalloy components. Thus, the following sections will be discussing Co-base γ/γ' superalloys and Ni-base alloys as needed for comparison, excluding the earlier Co-Cr (Haynes-type) alloys devoid of γ', historically referred to as "cobalt superalloys".

2.1 Composition and Structure of γ/γ' Superalloys

Cobalt and nickel are the base (solvent) metals of interest in the following review. While nickel exists as the γ-FCC phase up to its melting point of 1455°C, cobalt instead exists as the ε-HCP phase at lower temperatures until it transitions to γ at 422°C and melts at 1495°C [12]. At the elevated temperatures of interest for superalloys, a complete solid solution will exist between the γ phase of the two metals (Figure 2.1). In nickel, the γ' ($L1_2$) ordered phase is found in the binary Ni-Al system, and is stable up to 1370°C (Figure 2.2) [13,14]. However, the Co-Al binary contains no γ' phase, and instead the γ phase is simply in equilibrium with the ordered β (B2) phase at greater Al contents (Figure 2.3) [15]. Examining the ternary Co-Ni-Al space reveals that the β phase exists as a complete solid

solution between the Co-Al and Ni-Al binaries; however, the γ' phase only extends out to ~10-20 at.% Co in this space (Figure 2.4) [16]. Neither is the γ' phase present in the Co-W binary system (Figure 2.5,) or the partial Co-Ni-W ternary (Figure 2.6) [17]. It is only by combining W and Al additions that one can stabilize the γ' phase in the ternary Co-W-Al system, as shown in Figure 2.7 [7]. The γ/γ' field is rather small in the Co-W-Al system, and the γ' solvus temperature of 990°C [7] is much lower than the binary Ni-Al γ'. However, the cobalt-base space offers promise for superalloy development due to high solidus temperatures, ~1460°C for Co - 9.2 Al – 9 W (in at.%) [18]. This suggests that the drop in solidus with Al addition in Figure 2.3 is compensated by the relatively shallow variation in solidus with W shown in Figure 2.5. Trading Co for Ni content in the quaternary Co-Ni-W-Al space expands the size of the γ/γ' field (Figure 2.8) and increases the γ' solvus temperature [19], at the cost of slightly depressing the solidus [18]. The phase equilibria changes with Cr additions deserve particular attention, as this metal plays an important role in oxidation resistance [20,21] but it is reported to reduce the γ' solvus [22,23]. Co and Ni both have significant solubility for Cr, limited in Co by the formation of a σ-Co_7Cr_8 phase at ~40 at.% Cr (Figure 2.9), which is destabilized by increasing Ni contents and higher temperatures, (Figure 2.10) [24,25]. Conversely, W additions stabilize the σ phase at high temperatures ~1300-1350°C as shown in Figure 2.11 [26].

2.1.1 Elemental Partitioning Between γ and γ'

Partitioning of different elements between the γ and γ' phases plays an important role in several relevant material properties. Whether an element partitions to the ordered or the solid solution phase, and to what extent, can essentially be estimated from the phase diagrams in the previous section and the relevant tie lines. For example, Al partitions to the

γ' phase while Ni partitions to γ in the binary Ni-Al system (Figure 2.2). Less obvious is the behavior of ternary systems, such as Co-W-Al, where W is seen to partition to the γ' phase as in Figure 2.7(a). However, as Ni content is added in substitution for Co, the tie lines at higher W rotate, leading to alloys that can achieve opposite behavior in the Ni-rich system, wherein W partitions to the γ phase—e.g. Figure 2.8(d). The visualization of partitioning behavior on phase diagrams becomes more difficult when moving to higher-component systems, but it can still be calculated from a reliable thermodynamic database. Several authors have explored the partitioning behavior of different elements experimentally, as summarized in Table 2.1. The phase preference of elements will change both based on the solvent metal, as well as the concentrations of the different alloying additions. In general, phase preference will not change dramatically with moderate shifts in composition space. However, the present discussion looks at large compositional changes between primarily Ni-rich vs. primarily Co-rich alloys. Large compositional alterations can indeed have a pronounced effect on the partitioning behavior among solvent metals, as illustrated in Table 2.1.

2.1.2 Contiguous Alloy Phases

While the γ and γ' phases of interest are both based on FCC orderings, a variety of other structures exist in surrounding phase fields. These other phases will be of importance for mechanical properties of the alloy, as well as stability, diffusion, and oxidation behavior based on the effects on the chemical potentials of the components. Both the Co-Al and Ni-Al binary systems exhibit the intermetallic β-(Co,Ni)Al phase, which neighbors the γ' field in Ni-Al. As an ordered BCC phase (B2), β is known to be more brittle than the γ matrix at low temperatures. The β phase will also incorporate preferentially Al from the matrix,

bonding it strongly and lowering the chemical potential of aluminum, μ_{Al} [27,28]. Other phases typically found in some superalloys are topologically close packed phases (TCP), which include the σ, μ, and R phases identified in the materials systems of interest in section 2.2. TCP phases are intermetallics of complex crystal structures with high packing density and a limited number of coordination environments [29,30]. A subset of these alloys with stoichiometry AB_2 are referred to as Laves phases. The formation of TCP phases involves elements such as Ni, Co, W, Ta, and Cr, and are typically considered to undesirably affect mechanical properties [6]. It is noted that if the γ' phase becomes suppressed in the Co-W-Al ternary, the TCP μ phase will be in equilibrium with the γ phase at 1000°C (Figure 2.7). This brittle phase often forms in a lathe-like morphology [31], and will thus act as a stress concentrator in the alloy, making its formation undesirable for its effects on toughness.

2.2 Phase Stability at Elevated Temperatures

Microstructural stability and phase equilibria at elevated temperatures are important for mechanical properties and, in principle, oxidation behavior. Moreover, the high temperature phase equilibria are relevant to assess challenges to fabrication, such as during directional solidification and subsequent homogenization treatment.

2.2.1 γ' Solvus and Solidus Temperatures

The γ' phase is stable in the binary Ni-Al up to the peritectic temperature of 1370°C, with the ratio of γ to γ' depending on the composition. On the other hand, γ' is present in the ternary Co-W-Al system up to a maximum solvus temperature of 1033°C, albeit with a higher solidus temperature of 1451°C. The inference is that an alloy optimization strategy should be focused on increasing the γ' solvus without compromising the nominal temperature capability dictated by the solidus. It should also be noted that despite the

experimentally measured γ' solvus temperature in the ternary Co-W-Al system, recent investigations have suggested that the $L1_2$ phase is actually metastable in those alloys. This is reflected in a decreasing γ' phase fraction with temperature, as well as experimentally observed coexistence of the γ (A1), χ-Co_3W ($D0_{19}$), and β-CoAl (B2) phases at 900°C [32,33]. First principles calculations have shown that the γ' formation energy is only marginally different that the competing γ-β-χ three-phase field. The stabilization of γ' at finite temperatures is apparently the result of Co antisite defects on Al/W sublattice sites and vibrational contributions to the free energy [27]. Nevertheless, the presence of appreciable phase fractions of γ' after 8000+ hours at 900°C suggest that its dissolution kinetics are very slow [33].

In understanding the role of alloying additions on γ' stability it is important to assess not only changes in the phase fraction with composition, but also on the solvus temperature because the γ' phase fraction may not be a true indicator of its temperature stability. One example is the behavior of Cr when added to Co-W-Al. While Cr partitions to the γ phase, a non-negligible amount is also present in the γ' and is observed to increase the phase fraction of the γ' precipitates [34]. However, Cr still destabilizes the γ' phase as seen in the reduced solvus temperature shown in Figure 2.12(a) [35]. Of the other transition metals, Ta was found to have the greatest beneficial effect on the Co-base γ' solvus, followed by Ti, and Nb [35]. Conversely, Re was not effective in stabilizing the γ' phase in Co-base systems [36]. Finally, greater Ni additions will increase the γ' solvus, transitioning between the Co-base and Ni-base systems by substitution of the solvent element [19]. In the same context, it is desired for superalloys to have a reasonable temperature difference between the γ' solvus

and the solidus, allowing for solutionizing heat treatments without risking incipient melting of the component.

2.2.2 Liquidus and Solute Segregation

Elemental partitioning between the liquid and solid phases is critically important during solidification, not just in terms of the extent of segregation that must be subsequently homogenized, but also to minimize casting defects such as freckles or cracking. Segregation is the result of the difference between solid and liquid phase compositions in equilibrium, coupled with the limited diffusion in the solid that precludes its composition to be adjusted as it evolves, and thus the attainment of global equilibrium (see Figure 2.13). If diffusion in the liquid is considered sufficient to homogenize its composition and local equilibrium is assumed at the liquid-solid interface, the segregation behavior in binary systems would be described by the Scheil-Gulliver equation [37]:

$$X_S = k * X_o(1 - f_s)^{k-1} \tag{2.1}$$

where X_S is the composition of the solid at the interface, X_o the composition of the alloy, f_s the fraction solidified, and k the partition coefficient defined as the ratio X_S/X_L (shown graphically in Figure 2.13). As such, components of an alloy system with a k value further diverging from 1 segregate more strongly. In principle, partition coefficients depend on temperature, but the Scheil-Gulliver model approximates the liquidus and solidus as linear functions of composition, so k is constant through the solidification range in a binary system. Furthermore, partition coefficients for given components would normally be different between Ni-base and Co-base alloys, yielding important differences in solidification behavior (Table 2.2).

The most impactful differences between Co- and Ni-base alloys from the above table will be the changes in W and Al segregation behavior. In Ni alloys, heavier W segregates toward the solid during solidification, whereas less dense aluminum segregates towards the melt, leading to a phenomenon called "density inversion". Under such conditions composition gradients within the melt at different locations within the semi-solid "mushy" zone lead to less-dense liquid lower towards regions of greater solid fraction, driving convection toward the bulk melt. The ensuing flow can break off and reorient dendrite fragments, leading to freckle defects in directionally solidified alloys, e.g. those illustrated in Figure 2.14. Such defects are frequently a reason for rejection of directionally solidified aircraft engine parts [6]. A promising aspect of Co-base alloys is that the segregation of W and Al is much less significant than in Ni alloys, and so is the likelihood of density inversion. Furthermore, Ta tends to segregate to the melt more strongly in Co than Ni alloys, which leads to denser liquid at higher solid fraction, further counteracting density inversion [38–40]. This is advantageous for casting large parts, as well as for additive manufacturing, where the feedstock material is melted once upon deposition and again partially melted with consecutive build layers.

2.3 Oxidation Behavior

For a superalloy to be deployed in a high temperature turbine environment it is required to have some measure of intrinsic oxidation resistance, i.e. to undergo some form of surface passivation in the event of loss of the protective overlay coatings (BC/TBC). The rationale is that the latter cannot be prime reliant, which implies that coating spallation cannot be precluded completely [10], exposing the structural superalloy to the harsh combustion environment. The alloy must successfully endure in such environment until the next engine

inspection cycle. Furthermore, not all component surfaces are (or can be) endowed with protective coatings, further motivating the need for intrinsic oxidation resistance.

2.3.1 Isothermal Exposure

Among the multiple aspects of environmental resistance a superalloy must possess, the most foundational is arguably the ability to form a thin, slow growing thermally grown protective oxide (TGO) in a suitable short exposure to engine-relevant conditions. It is desirable to form this TGO as quickly as possible to minimize the degradation of the substrate and prevent excessive oxidation of the base metal and key alloying elements. Once the TGO has been established it is important that its subsequent growth is slow, both to minimize depletion of the key oxide-forming element as well as to enable durability under thermal cycling and the associated thermal mismatch stresses [41]. The oxides of primary interest in gas turbines are Al_2O_3, Cr_2O_3 and SiO_2. Of these, α-Al_2O_3 typically has the lowest growth rate (Figure 2.15 [42]), the highest oxygen affinity (Figure 2.16 [43]), and is the least susceptible to volatilization by hydroxylation in water vapor [42,44]. Earlier Co-base alloys were typically designed to form a chromia TGO [11], but replacing γ/γ' Ni base superalloys with Co-γ/γ' involves temperatures at which alumina is more desirable. Yet, alumina tends to form transient metastable structures, notably spinel derivatives like θ and γ, which grow significantly faster than the stable α polymorph (Figure 2.17 [45]). Therefore, the design goal for oxidation resistance in Co-γ/γ' is to develop a composition that forms a thin, continuous α-Al_2O_3 scale at time scales on the order of minutes, and with little other oxidation products if any.

2.3.2 Cyclic Exposure

Component durability depends not only on the establishment of a protective scale, but also on the ability of that scale to tolerate the thermal cycles inherent to engine service. Stresses are generated by the thermal expansion mismatch between the alloy and the scale, which generally causes a compressive stress in the scale on cooling, assuming the high temperature hold produces a stress-free condition by creep. However, it has been shown that cracking under tension may also occur upon rapid heating, especially if some relaxation occurs on cooling [46]. Whether the scale remains attached or not depends on the interplay between the energy release rate (ERR) generated during the thermal cycle and the toughness of the TGO and/or the interface with the metal [41,47]. When the scale involves additional oxides that are non-protective, these can contribute to the ERR but not necessarily to the oxidation resistance.

2.3.2.1 Sources of Oxide Stress

The main source of stress evolution during cyclic oxidation is the CTE mismatch between the oxide and the alloy substrate, as noted earlier. Because the CTE of the oxide cannot be substantially modified chemically for α-Al_2O_3, one desired property of a superalloy is a reduced CTE. Growth stresses may also contribute to the ERR [48], but they are even less understood than those arising from CTE mismatch [49,50]. The volumetric change between a component in metallic form vs. that within an oxide is termed the Pilling-Bedworth ratio (PBR) [51], defined as:

$$PBR = \frac{Volume\ of\ a\ mole\ of\ oxide\ B_xO_y}{Volume\ of\ x\ moles\ of\ B\ within\ reactant\ phase} \tag{2.2}$$

which can logically be expanded in a similar manner for polycationic oxides [51]. Typically in the systems of interest, the incorporation of oxygen into the metal system results in a

volume expansion, PBR > 1. Volume changes from any phase transformations and compositional changes within the system will also influence the stress state, such as the transition of θ-Al_2O_3 to α-Al_2O_3, which involves a ~5% shrinkage and can generate local tensile stresses [52,53]. Lastly, the geometry of a system can play an important role in concentrating stresses at samples corners and edges and enhanced out of plane stresses at curved surfaces, especially at larger scale thicknesses [42]. Typically, measured stresses in alumina scales on Ni-base alloys have been estimated as comprised of 3-5 GPa from CTE mismatch, and 0-1 GPa from growth [54].

2.3.2.2 Relaxation of Oxide Stress

There are also mechanisms by which the stresses in the scale can be relaxed, including creep of the scale and creep or plasticity in the metal substrate. Due to the thermally activated nature of creep, it is typically approximated that both the oxide and metal will be sufficiently plastic at the high exposure temperatures to rapidly reduce the stresses generated upon heating. During cooling, however, creep will slow until it cannot counteract the generated stresses, leaving behind residual stresses in the room temperature TGO. The implication is that a slower cooling rate will provide greater time at high temperatures where creep is more rapid, allowing greater relaxation of generated stresses [55].

2.3.2.3 Decohesion of Oxide Scale

After considering both stress generation and relaxation processes, the residual stress should be compared to the interface toughness in order to determine if failure will result. There are multiple modes of scale failure, and several detailed analyses have been conducted [47,55–58] as they are especially relevant for not only for alloy/TGO systems, but also for the superalloy/BC/TGO/TBC protection system at large. In the context of the problems

considered in this dissertation, however, only the interface separation between an oxide scale under biaxial compression and the underlying metal substrate will be considered. For the simplified case of a thin film thickness *h* and modulus *E* on an infinitely thick substrate under uniform stress σ, the energy release rate may be described by [59]:

$$\Gamma_{ERR} = \frac{\sigma^2 h}{2E_{oxide}} \tag{2.3}$$

This equation may also be used to calculate a maximum scale thickness allowable before spallation, given known values of interfacial energy, TGO stress, and oxide modulus. It should be noted that testing of a bulk oxide to determine the modulus *E* is not necessarily representative of the oxide in TGO form. In addition to the difficulties in measuring the TGO properties, ascertaining the interfacial toughness between TGO and metal substrate is particularly challenging. Care must be taken in the testing setup to account for the confounding factors of crack mode mixity, residual stresses (in addition to the stresses applied during testing), and pre-cracks [60]. The potential mode of failure, whether ductile, manner, or by interfacial decohesion will also affect the measurement of Γ_i. While a system of Al_2O_3 TGO on Al metal substrate tends to have ductile interfacial cracks [60] (with some metal attached to the ceramic side of the fracture), Al_2O_3 on Ni alloys instead will delaminate in a brittle manner and is reported to have an interfacial energy Γ_i >100 J/m^2 [61]. Yet an important consideration is that contaminants within the system such as sulfur can segregate to the TGO-alloy interface, lowering Γ_i by an order of magnitude, i.e. 5-20 J/m^2.

2.4 Internal Oxidation

Internal oxidation is a phenomenon common in multicomponent alloy systems where particles of oxide form under the surface, within a surrounding metal matrix. This occurs when the alloy system contains a low concentration solute of greater oxygen affinity than the solvent, leading to selective oxidation of the solute within the bulk alloy. Due to the low concentration of the solute, a continuous oxide scale is not established across the entire sample surface, allowing continued oxygen diffusion into the alloy and precipitation of solvent-oxides as discrete particles. This behavior is evidently important for superalloy oxidation, as Al has a much higher oxygen affinity than the solvent Ni or Co, and the formation of an internal oxidation zone (IOZ) will be non-protective and undesirable.

A basic quantitative description of internal oxidation in binary alloys has been achieved by Wagner [62,63]. Essentially, the inward flux of oxygen through the solvent metal will react with the outward flux of solute through an alloy depletion region to form a stoichiometric amount of oxide product as internal particles, thus forming an IOZ. Because these particles locally block inward oxygen flux, if the volume fraction of IOZ, $f(Al_3O_3)$ were to achieve some critical value f*, the solute metal would instead be able to form enough oxide product to produce a continuous scale [42]. Based on this model, the effects of alloy composition changes on internal oxidation can be estimated on a kinetic basis. Those that decrease oxygen solubility or diffusivity in the IOZ, and those that increase the concentration or diffusivity of the solute metal in the alloy will benefit continuous scale-forming behavior. From a practical standpoint, the critical concentration of solute metal (typically Al or Cr) necessary to form a corresponding continuous scale will be of greater importance, and is easier to measure experimentally.

Accurate quantitative predictions of oxidation behavior a priori are fraught, however, because N_B*, the critical solute concentration to generate a continuous oxide scale, will scale directly with the value of f*; therefore, any error in this value will yield appreciable differences in the prediction of critical solute fraction. Unlike the kinetic parameters involved in oxygen and solute fluxes previously mentioned, the factors which determine critical volume fraction f* are less clear. Research by Rapp [64] on Ag-In alloys at 550°C is often cited, wherein an f* value was found for this system of approximately 0.3. Many authors have since used this value for a variety of material systems and oxidation conditions, though the validity of such assumptions is questionable. Zhao et al. have recently attempted to describe a more theoretical approach for determining f* values [65], although the predicted f* value for Rapp's Ag-In system was 0.53 compared with the experimentally measured 0.3, a 77% error. In light of the large error in f* and consequently N_B* when attempting to quantitatively predict internal oxidation in a binary alloy, empirically determined critical solute concentrations N_B* will be given for various applicable alloys in the following section.

2.5 Oxidation Behavior of Constituent Systems

2.5.1 Unary Co, Ni, Cr, Al

Considering the oxidation of pure metals, Ni is fairly simple in that it only forms one stable oxide, NiO, with the rock salt structure (B1). This phase grows by outward cation diffusion (p-type oxide), has a parabolic rate constant k_p of ~$4*10^{-10}$ g^2/cm^4s at 1100°C (Figure 2.15), and a dissociation pressure of ~$1*10^{-9}$ atm at 1100°C (Figure 2.16) [42,66], such that:

$$\left(\frac{m}{A}\right)^2 = k_p * t \tag{2.4}$$

where *m* is sample mass, *A* is surface area, and *t* is time. Comparatively, Co is slightly more complicated in that it has three oxide products, Co_2O_3, Co_3O_4, and CoO. The dissociation temperatures of Co_2O_3 and Co_3O_4 at 1 atm O_2 are relatively low, approximately 300°C and 900°C respectively [67], so focus will primarily on the monoxide CoO. CoO is isostructural with NiO, and both are completely miscible at 1100°C [68]. CoO also grows via outward cation migration (p-type oxide), but it has a substantially faster parabolic rare constant k_p = ~7*10^{-8} g^2/cm^{4}s at 1100°C, and is slightly more stable with a dissociation pressure of ~3*10^{-11} atm at 1100°C. Both the NiO and CoO oxidation rates are too rapid to be desirable for structural alloy components, and neither is considered protective.

On the other hand, pure Cr and Al produce sesquioxides Cr_2O_3 and α-Al_2O_3 which are more effective passivating layers, with k_p of ~1*10^{-10} and ~8*10^{-13} g^2/cm^{4}s respectively at 1100°C [42]. While both oxides share the corundum structure, they are not completely miscible until 1200-1250°C. Al_2O_3 has a limited Cr solubility of ~10 at% at 1100°C [69,70], though in practice Cr is not observed in the TGO on alloys due to the much higher oxygen affinity for Al. In the case of alumina, the generally low solubility for defects yields its low growth rate, which is principally controlled by oxygen diffusion along grain boundaries [71]. In contrast, chromia is less stable than alumina, with dissociation pressures of ~3*10^{-20} atm and ~5*10^{-32} atm at 1100°C, respectively [66]. The chromium system also includes a variety of volatile products (those with a high partial pressure), notably CrO_3 [44]. Volatilization is also enhanced in water vapor environments [72,73]. In essence, alumina is the preferred oxide scale to protect superalloy components in gas turbines at typical gas temperatures. Conversely, for applications other than turbine engines, chromia is

often more resistant than alumina to attack by aqueous environments (marine corrosion) [42,74].

2.5.2 Binary Ni-Al, Ni-Cr, Co-Al, Co-Cr

The binary systems Ni-Al, Ni-Cr, Co-Al, and Co-Cr can achieve both the mechanical properties of Ni and Co, and the oxidation protection provided by alumina or chromia. The Ni-Al system has the added benefit of forming the strengthening γ'-Ni_3Al phase, not present in any of the other binaries. The level of Cr or Al additions necessary to achieve oxidation resistance is based on that needed to prevent the formation of an IOZ. A conservative alloy design, however, will possess a solute content above this critical value (N_B*), which will differ between the four binary systems. Reported critical values for continuous scale growth in these binary systems are summarized in Table 2.3.

Commercial alloys based on these binary systems such as many Haynes alloys (Table 2.4) include greater solvent Cr content above ~30 at% [75]. This is to allow maintenance of a stable scale at long exposure times, as well as immediate reformation in the event of scale spallation. Additionally, moving from the unary to binary alloy systems introduces the possibility of polycationic oxides, namely spinels, $(Co,Ni)(Al,Cr)_2O_4$ ($H1_1$). Unlike Co_3O_4, which is also a spinel, these polycationic spinels with Al and/or Cr are stable above 1100°C.

2.5.3 Ternary Ni-Cr-Al, Co-Cr-Al

Increasing in complexity, ternary additions of Cr to (Co/Ni)-Al alloys have synergistic effects between Cr and Al in promoting corundum formation. This is known as the "third element effect" (TEE). The proposals for TEE mechanisms include secondary gettering, templating, and a so-called "cross-turn" or "booster" effect. The secondary gettering hypothesis proposed by Wagner [76] is simply that additions of a second solute with

intermediate oxygen affinity to the solvent and primary solute will absorb additional oxygen. This reduces the inward flux approaching the oxidation front, thereby allowing continuous scale formation of the primary solute at lower concentrations. One classic counter-example to the secondary gettering hypothesis is the addition of Mn to Fe-Al, which does not facilitate the establishment of alumina scale despite being of intermediate oxygen affinity [62,77–79].

With respect to Cr and Al specifically, a templating effect has been proposed due to the isostructural nature of α-Al_2O_3 and Cr_2O_3 [80], whereby pre-formed chromia with the corundum structure can provide heterogeneous nucleation sites for α-Al_2O_3. It is less clear, however, that a templating effect is contributing to α-Al_2O_3 formation in cases where a chromium oxide is not observed after oxidation. Yet it is certainly clear that Cr additions promote the transformation of metastable alumina phases to α [81–83].

Lastly, the "booster" effect hypothesis essentially states that not only is the direct diffusivity of aluminum down its own chemical potential gradient (D_{AlAl}) driving outward solute flux, but also the cross diffusivity D_{AlCr}, whereby Al also diffuses down the Cr depletion zone underneath the surface oxide [84,85]. Regardless of the exact mechanism(s) behind its operation, the beneficial Cr TEE on protective scale formation is well established experimentally. This has lead to the widespread use of MCrAl (M = Ni, Co, Fe) as oxidation protection coatings and bond coats for thermal barrier coatings on superalloys. These ternary systems also form the basis of structural superalloys; however this involves further alloying to improve mechanical properties.

2.5.4 Effects of Tungsten (W) Addition

The binary W-O system includes monoclinic WO_2, monoclinic WO_3, and a large range of compounds with intermediate stoichiometry WO_x [86]. The dioxide form is slightly more stable than the trioxide, with dissociation pressures of ~$7*10^{-14}$ atm and ~$3*10^{-12}$ atm respectively at 1100°C, placing them between (Co/Ni)O and $(Cr/Al)_2O_3$ (Figure 2.16) [43,66]. Diffusion through thermally grown tungsten oxide is observed to occur via inward migration of oxygen anions in the range 600-900°C [87]. While practically nonvolatile in dry air or vacuum, small amounts of water vapor lead to high volatility [88,89]. However, in the present alloy systems of interest, tungsten typically forms tungstate oxides $(Co,Ni)WO_4$ which are much less volatile [90]. Although minimal work has been done on the oxidation behavior of lower-order (Co,Ni)-W-(Al,Cr) systems, there is some evidence that W additions increase the oxidation rate of Ni-Cr alloys, while decreasing the oxidation rate of Co-Cr alloys [90–92]. It was observed that a Ni-W-rich depletion layer forms below the chromia scale in Ni-Cr-W alloys, which led to the hypothesis that W additions increase the oxygen activity in this layer and promote inward oxygen flux. The marked difference in effects of W additions between Co- and Ni-base systems has been attributed to the formation of substantial volume fractions of Cr-rich σ phase in the Co alloy, not present in the Ni-system [91,92], though further investigation is warranted. In higher-order alloys, Yeh et al. [93] observed a marked increase in oxidation rate with increasing W content in Co-Ni-Si-Al-W alloys (Figure 2.18). An expansive design of experiments study by Yun et al. [94] in Ni-Co-Cr-Mo-W-Al-Ta-Re-Ru alloy systems observed variable oxidation effects at 1100°C from W additions, depending on the compositions investigated. Generally W additions are considered deleterious to oxidation resistance, though at increasing Al and Cr concentrations, W additions can be slightly beneficial, or at least neutral. Clearly these alloy

systems are quite complex, and the nature of W effects on oxidation behavior could benefit from a more systematic study.

2.5.5 Effects of Tantalum (Ta) Addition

Ta additions up to roughly ~4 at.% Ta may be used to modify the γ' phase stability in superalloys, and open up the possibility for the formation of tantalate compounds, including Ta_2O_5, $(Co,Ni)Ta_2O_6$, and $(Cr,Al)TaO_4$ [95–97]. The effects of Ta additions on Ni- and Co-base alloy oxidation resistance are not generally consistent. Yan et al. [20] showed that 2 at.% Ta additions to a Co-W-Al alloy slightly decrease the isothermal oxidation rate constant at 800°C, and decrease the cyclic oxidation mass change and scale thickness after 196 h at 800°C. These results are at variance with research by Klein et al. [98], who found that 2 at.% Ta additions to a Co-W-Al alloy increased the oxide layer thickness by over 30% after 400 h at 900°C. A complex 16 component Ni-base superalloy "René N'5 Y+" was studied by Baik et al. [99] at 1100°C for 100 h. The 3 at.% Ta present in the alloy was sufficient to cause the formation of oxides Ta_2O_5, $CrTaO_4$, and $NiTa_2O_6$ among others. Further investigations on Ni alloys with a variety of refractory elements by Kawagishi et al. and Yun et al. [94,100] suggest that Ta may have a beneficial effect in conjunction with W, Mo, and Ru in stabilizing the oxides of these elements and preventing undesirable volatility. It is thus apparent that the effects of Ta in alloy oxidation have not been characterized in a systematic way, and there are likely a variety of operative mechanisms in play when present in higher-order alloys.

2.5.6 Effects of Reactive Elements / Rare Earths (RE)

The beneficial effects of certain reactive elements (RE) on oxidation resistance in M-Cr-Al alloys has been known for many decades, first patented by Pfeil in 1945 [101,102]. Yet

the mechanism or mechanisms by which REs have such an effect is still under debate today. While a wide variety of elements may be considered "reactive", the general criteria are that they have a large affinity for O and S, and that they have a relatively large ionic radius relative to Al or Cr [103]. Such elements have the primary effects in Al_2O_3 and Cr_2O_3 scales of improving TGO adhesion, and decreasing the growth rate of the scale once established [104]. While RE may be added in the form of either a metallic or oxide dispersion (ODS), the metallic form has generally been observed to be more beneficial [103]. When adding REs as a metallic alloy component, it is also important to avoid a phenomenon known as 'over-doping', whereby there is sufficient concentration to form reactive element oxides that generate particles often embedded in the alumina scale [105]. Because the REs tend to have a high oxygen affinity, they may also form internal oxides underneath any potential Al_2O_3 or Cr_2O_3 layers, leading to increased weight gain.

The reactive element oxides are also not particularly protective, generally displaying a high oxygen conductivity [106]. With respect to their two primary beneficial attributes, improving TGO adhesion and slowing growth, a variety of potential mechanisms have been suggested. Sulfur has long been known to segregate to the oxide-metal interface and reduce TGO adhesion [107,108], and RE additions have been proposed to getter any native S to prevent such undesirable segregation [109]. However, S gettering is not the only beneficial effect of REs on improving interfacial adhesion, as de-sulfurized alloys also show an improvement from RE additions. A phenomenon called "oxide pegging" or "mechanical keying" has been proposed by which alloys with sufficient RE concentrations to oxidize into particles (coarser than ODS particles) employ such particles to help anchor the TGO to the underlying metal substrate [103]. The validity of these mechanisms has not yet been

demonstrated, as there have been observed benefits to oxidation resistance in alloys with sufficient metallic RE additions to form oxide pegs over the much smaller oxide particles in ODS alloys. Yet contradictory evidence exists showing a reduced concentration of metallic RE additions, leading to lower concentrations of oxide pegs, also benefits oxidation resistance. With respect to reducing the sesquioxide scale growth rate, TEM EDS investigations have shown that while the solubility of REs in the bulk sesquioxide crystals is remarkably low [102,103], REs do segregate to oxide grain boundaries. They are reported to alter the diffusion mechanisms in Al_2O_3 from the non-trivial contributions of both outward cationic diffusion and inward anionic diffusion to primarily inward O diffusion. This leads to finer, more columnar alumina grains over those TGO without RE additions [49].

Though the exact mechanisms of the RE effect are still being investigated, further studies on the optimal species and concentration of RE to add have yielded empirical results. Hf and Zr additions in alumina formers typically benefit most from ~0.05 at.% RE additions. Furthermore, recent work suggests added benefit from co-doping, such as by both Y and Hf to prevent the formation of RE oxides [103].

2.5.7 Prediction of Oxidation Behavior and Oxidation Maps

Phase diagrams are an invaluable tool in alloy design, allowing for the prediction of phases present at a given composition and temperature. Similarly, it would be helpful for alloy design to generate a predictive tool for oxidation behavior in a given alloy system. However, unlike alloy phases in equilibrium, oxidation is an inherently dynamic process and thus prediction of its behavior cannot simply be ascertained from a thermodynamic database. Similar application of the calculation of phase diagrams (CALPHAD) method [110] has

been applied to kinetic diffusion constants for the development of a relevant DICTRA [111] database. This database has been used somewhat successfully in the prediction of alloy-bond coating interdiffusion rates [112], and while this is an important development in modeling capabilities, it alone is insufficient to allow the prediction of oxidation behavior. Pragmatically, it would be desirable to predict the formation of internal vs. external oxidation of alumina (or other high-oxygen affinity oxides), the presence of various other oxides and their respective thicknesses, as well as any loses by volatilization. As discussed previously in Section 2.4, there are several remaining gaps in the current models for internal oxidation, with a few key challenges including the quantitative prediction of solid-solid nucleation of IOZ particles within a metal matrix, as well as resultant changes in diffusivity along the formed oxide-metal interfaces.

Due to the current inability to reasonably calculate oxidation behavior a priori, an empirical, pragmatic approach is taken with the creation of oxidation maps. Such maps consist of an alloy phase diagram at a given temperature, superimposed with the qualitatively observed oxidation behavior of the alloys at that temperature, for a given atmosphere. The alloy grain size and surface roughness prior to oxidation are not usually taken into account. These figures allow for a broader understanding of which compositions give rise to IOZ formation vs. continuous scale, though even in simpler binary alloy cases, the complexity of the oxidation process leads to broad 'intermediate' or transitionary regions [13] (Figure 2.19). As the theoretical understanding of oxidation is developed further, and computational capabilities continue to advance, oxidation maps will have an importance not only as a tool for alloy development (Figure 2.20), but also to validate future calculations of oxidation behavior. It should be noted, however, that general, often vague and subjective

labels are frequently given to different regions of oxidation behavior seen in some oxidation maps (Figure 2.21). Thus, such maps should ideally be coupled with oxide micrographs for true validation purposes of identifying all the different oxide phases and morphologies present.

2.6 Oxide Characterization by Photostimulated Luminescence

Photo-stimulated Luminescence Spectroscopy (PSLS) uses incident light to excite emission from a target material in the form of scattered light of a different wavelength. Figure 2.22 shows the potential outcomes of incident light striking a material sample. Of the original incident intensity, only a small portion will be scattered at a changed frequency. Such changes in frequency are due to the properties of the material, including the vibrational modes and the electronic band structure. These two types of interaction, vibrational vs. electronic, produce fundamentally different results in terms of the subsequently emitted light. In the case of light interacting with the vibrational or rotational modes of the material, the resultant scattering will have a frequency shift:

$$\Delta E = h\,|\nu_o - \nu_i| \tag{2.5}$$

where ΔE is the change in energy from the incident light, which is absorbed by the vibration of the material at a characteristic value, based on the mode [113]. These vibrational modes do not require a specific excitation frequency, and thus are characterized by the frequency shift of the light relative to the incident wavelength. Such measurements are typically referred to as Raman spectroscopy [114]. In contrast, light can also interact with the electronic structure of the material. In this case, electrons in the material can be excited over a present band gap, but only if the incident light is of energy equal to or greater than the band gap energy (Figure 2.23). These excited electrons can subsequently relax across the

band gap to emit a fluorescence signal of energy equal to the band gap energy. The technique of fluorescence spectroscopy refers to the process of scanning through incident light wavelengths to determine the lowest energy that excites electrons across this band gap. Photostimulated luminescence spectroscopy is thus the process of using incident light to excite different scattered frequencies, regardless of whether these frequencies are the result of vibrational or electronic interactions.

In the material systems of interest there are relevant characteristic PSLS signals. The first is from the α-Al_2O_3 phase. Small amounts of substitutional Cr are ubiquitous in Al_2O_3, and they sit on the octahedrally coordinated Al sites in corundum. On these sites, corundum has the Cr^{3+} oxidation state with the $3d^3$ valence undergoing crystal field splitting into t_{2g} – e_g orbitals [115,116]. As such, distortions in the octahedral sites produce two distinct emission lines, termed R_1 and R_2 at approximately 693.5 nm and 692.3 nm, respectively (approximately 1.442 μm^{-1} and 1.445 μm^{-1} respectively) in an unstressed state at cryogenic temperatures [115–117]. Because this characteristic α-Al_2O_3 doublet is the product of Cr substitutions, the intensity of the doublet will also scale with additional Cr doping [117]. Doublet intensity has been observed to increase by several orders of magnitude up to ~0.8 wt.% Cr, after which the intensity begins to decrease at greater Cr contents (Figure 2.24). The Cr content also influences the presence of characteristic PSLS signal termed N-lines, which come from Cr^{3+} - Cr^{3+} interactions, present at approximately 1.42 μm^{-1} and 1.427 μm^{-1} at cryogenic temperatures (Figure 2.25) [117]. As such, the ratio between the N-line and R-line intensities can be used to judge the level of Cr present in the corundum. Cr doping will also have a slight impact on the R-line frequency:

$$\nu_{doped} = \nu_{R2} + 0.827*X_{Cr} \quad (2.6)$$

where ν is frequency in wavenumber at room temperature, and X_{Cr} is the chromium content in wt.% [117]. The R-line frequencies were also found by He and Clarke to be slightly temperature sensitive:

$$\nu(T) = \nu(T_o) + (-0.144, -0.134\ cm^{-1}/°C)*(T-T_o) \quad (2.7)$$

where the coefficients given are for the R_1 and R_2 lines respectively [118]. However, the largest and most useful factor influencing the R-line frequencies is the stress state. This stress-dependence is logical as the fluorescence signal arises from the electronic state of the Cr-doped alumina, and the electronic bonds will certainly change under stress. In a biaxial loading condition, such as that approximately found on flat TGO due to CTE mismatch and growth stresses, the peak shift may be described:

$$\Delta\nu = (2.533\ cm^{-1}/GPa)*\sigma_{total} \quad (2.8)$$

where σ_{total} is the biaxial in-plane stress from all sources [119]. Using PSLS in this manner to evaluate the stress state of α-Al_2O_3 is known as piezospectroscopy [119]. Any gradients in stress-state through a TGO film can thus lead to peak-broadening, and a bimodal stress state may arise due to local relaxation from scale fracture or spallation.

2.7 Tables and Figures

Table 2.1: General partitioning behavior of different elements between γ and γ' phases in Ni-rich and Co-rich systems

Ni-base Alloys		
γ' (Ordered)	**Weak Partitioning**	**γ (Solid Solution)**
(Al, Ti, Ta)[120] (Al) [19] (Ti,Ta,V,Nb,W,Si,Mo) [121] (Al,Ti) [122] (Al) [123]	(Ni, W, Ir) [120] (Ni) [19] (Mo) [121] (Ni) [123]	(Co, Mo, Cr, Re, Ru) [120] (Co, W) [19] (Co,Mo,Cr,Mn,Fe,) [121] (Cr, Mo,W)[122] (Co, Cr, Ru)[123]
Co-base Alloys		
γ' (Ordered)	**Weak Partitioning**	**γ (Solid Solution)**
(Al, W)[19] (Ti,V,Nb,Ta,Mo,)[31] (Ni,Al,W,Ti,Ta)[124]	(Ni, Co)[19] (Ni,Al)[31]	(Cr,Mn,Fe)[31] (Co,Re) [124]

Table 2.2: Solute partitioning of alloying elements in Ni- and Co-base superalloys [38–40]

Ni-base Alloys		
Solid (k > 1)	**Weak Segregation**	**Liquid (k < 1)**
Cr, W, Re, Mo	Co, Ni	Al, Ta
Co-base Alloys		
Solid (k > 1)	**Weak Segregation**	**Liquid (k < 1)**
Cr	Co, Al, W	Ta, Ti

Table 2.3: Experimentally determined critical solute concentrations ($N_{Al,Cr}$*) for continuous oxide scale growth

System	800°C	900°C	1000°C	1100°C	1200°C
Ni-Al		14-23 at.% [13]			6-14 at.% [13]
Co-Al	14-25 at.% [125]	20-25 at.% [125]	25 at.% [125]		
Co-Cr			30 at.% [126] 32 at.% [127]	30 at.% [126]	30 at.% [126]

Table 2.4: Compositions in atomic% of select commercial Co- and Ni-base alloys.

Alloy	Haynes 6B	René N5+	CMSX-4	Alloy	Haynes 6B	René N5+	CMSX-4
Ni:Co	0.04	8.43	6.95	Mo	0.87	0.94	-
Co	52.91	7.64	9.24	Fe	3.00	-	-
Ni	2.38	64.41	64.22	Si	1.39	-	-
Al	-	13.79	12.56	Mn	1.42	-	-
W	1.21	1.63	1.98	C	4.64	0.25	-
Ta	-	2.16	2.17	B	-	0.022	-
Cr	32.18	8.08	7.56	Y	-	0.007	-
Ti	-	-	1.26	Hf	-	0.050	0.034
Re	-	0.97	0.98	Ref.	[11]	[128]	[128]

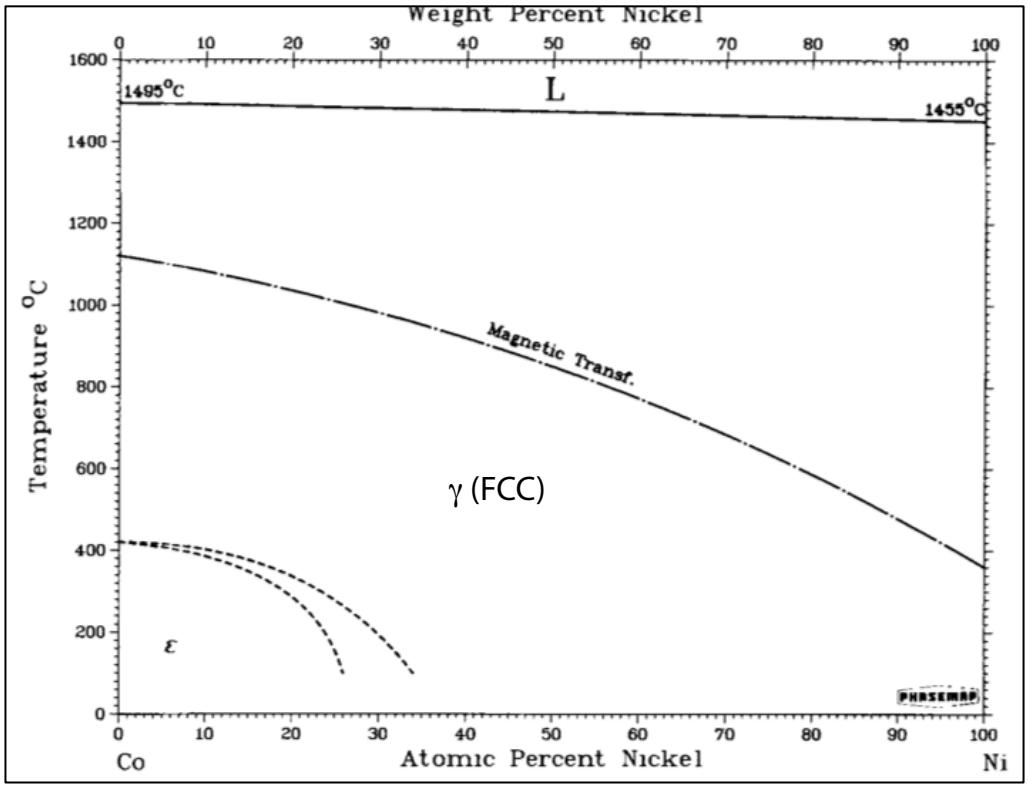

Figure 2.1: The Co-Ni binary phase diagram showing the low-temperature ε (HCP) phase, γ (FCC) phase, magnetic transition (Curie temperature) above which the metals transition from ferromagnetic to paramagnetic, and lastly the liquidus (L), modified from [12].

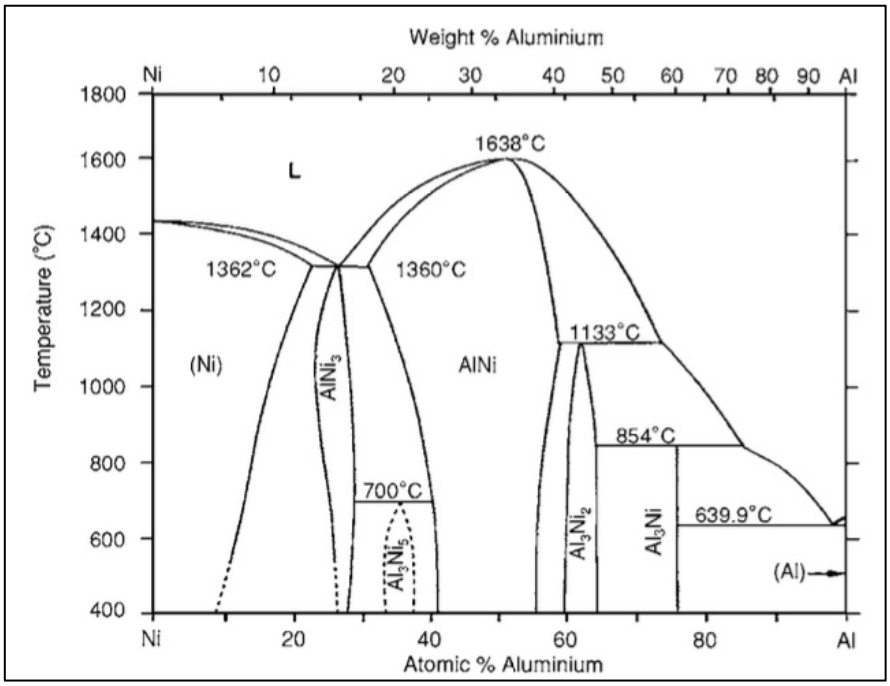

Figure 2.2: Ni-Al binary phase diagram, showing the Ni FCC solid solution (γ), $L1_2$ ordered Ni_3Al (γ'), B2 intermetallic NiAl (β), and liquid (L) [13,129].

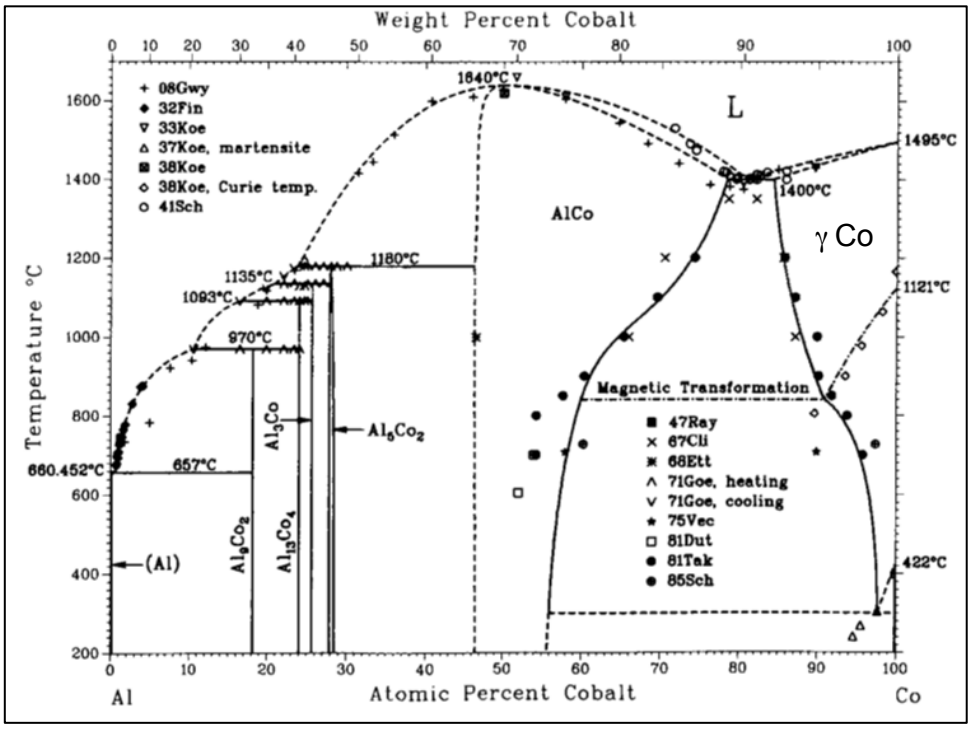

Figure 2.3: The Co-Al binary phase diagram. Of note are the γ-FCC phase and β-AlCo ordered intermetallic at high Co-contents, modified from [15].

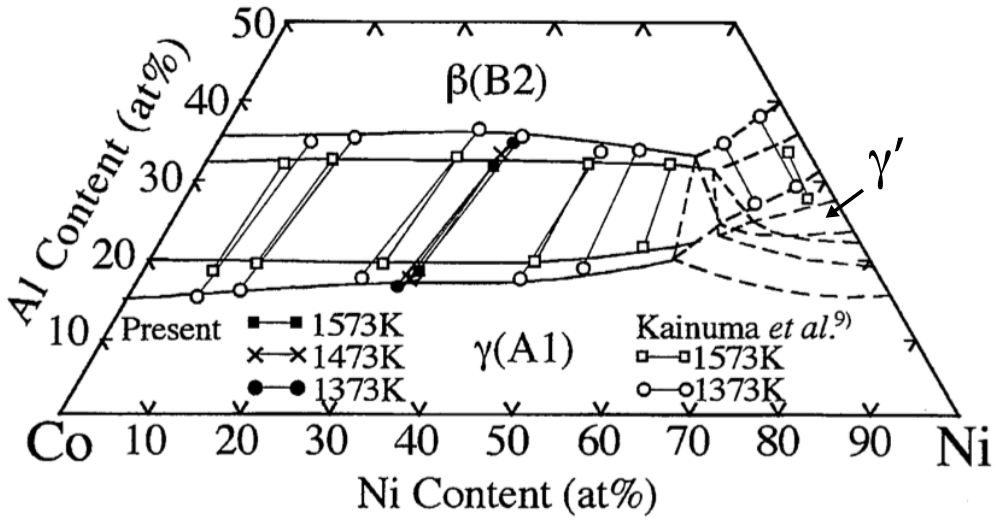

Figure 2.4: The Co-Ni-Al ternary phase diagram at 1100-1300°C, showing the stability of the ordered γ' phase in the Ni-Al binary, but with limited Co solubility. In contrast, the ordered β (B2) phase has complete Co-Ni solubility at these temperatures [16].

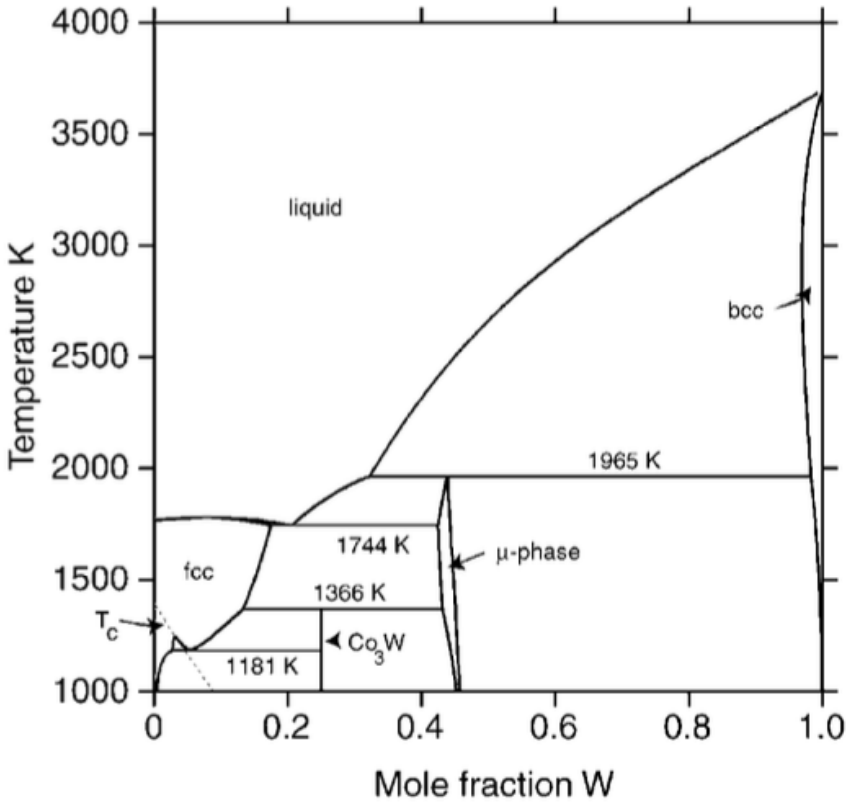

Figure 2.5: The Co-W binary phase diagram showing the intermetallic μ phase (rhombohedral $D8_5$, R-3m, Co_7W_6), and Co_3W (ordered hexagonal $D0_{19}$) phases, as well as the unusual feature of a small magnetic miscibility gap following the Curie temperature (T_C) [17].

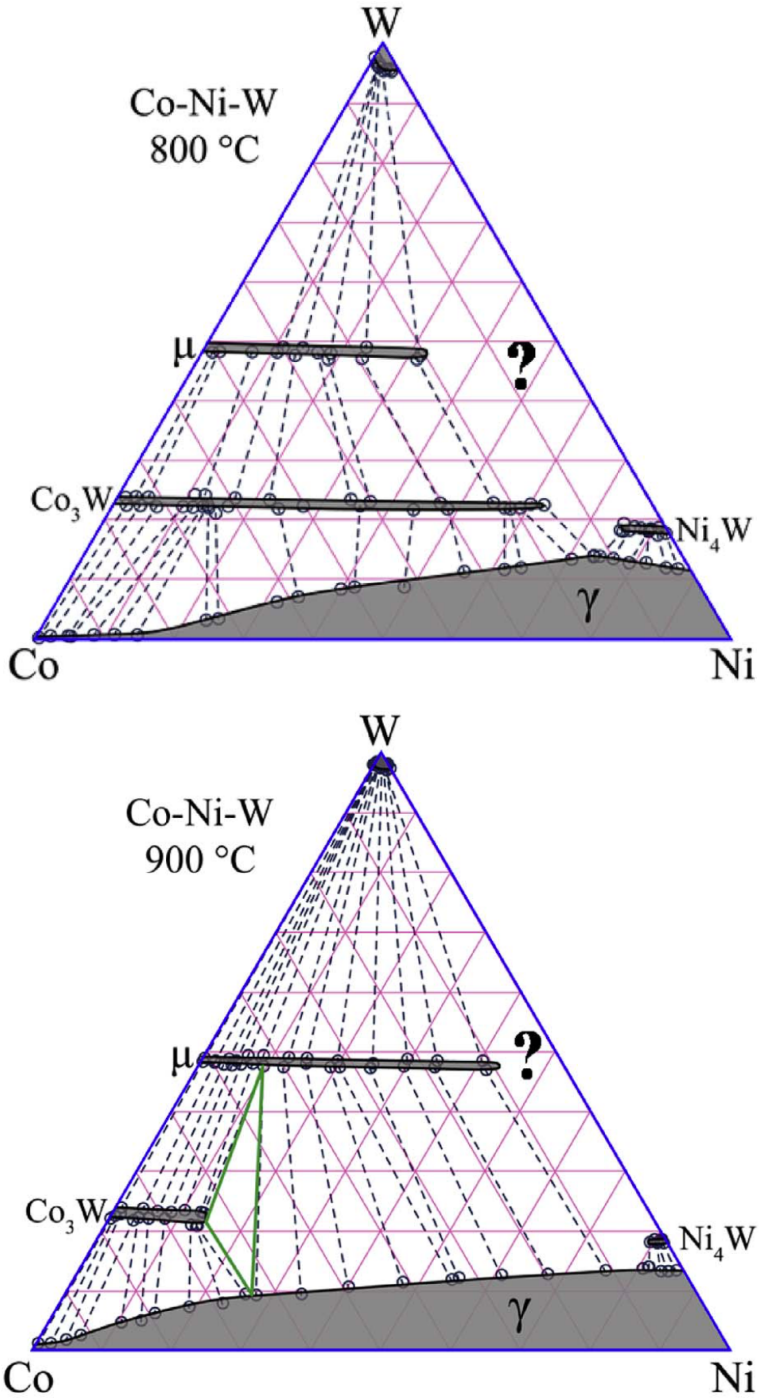

Figure 2.6: Co-Ni-W ternary phase diagrams at 800°C and 900°C, showing the solid solution γ-FCC phase, and the ordered Co_3W and μ-Co_7W_6 with significant (but not complete) Ni solubility. Also visible is the Ni_4W phase with limited Co solubility [130].

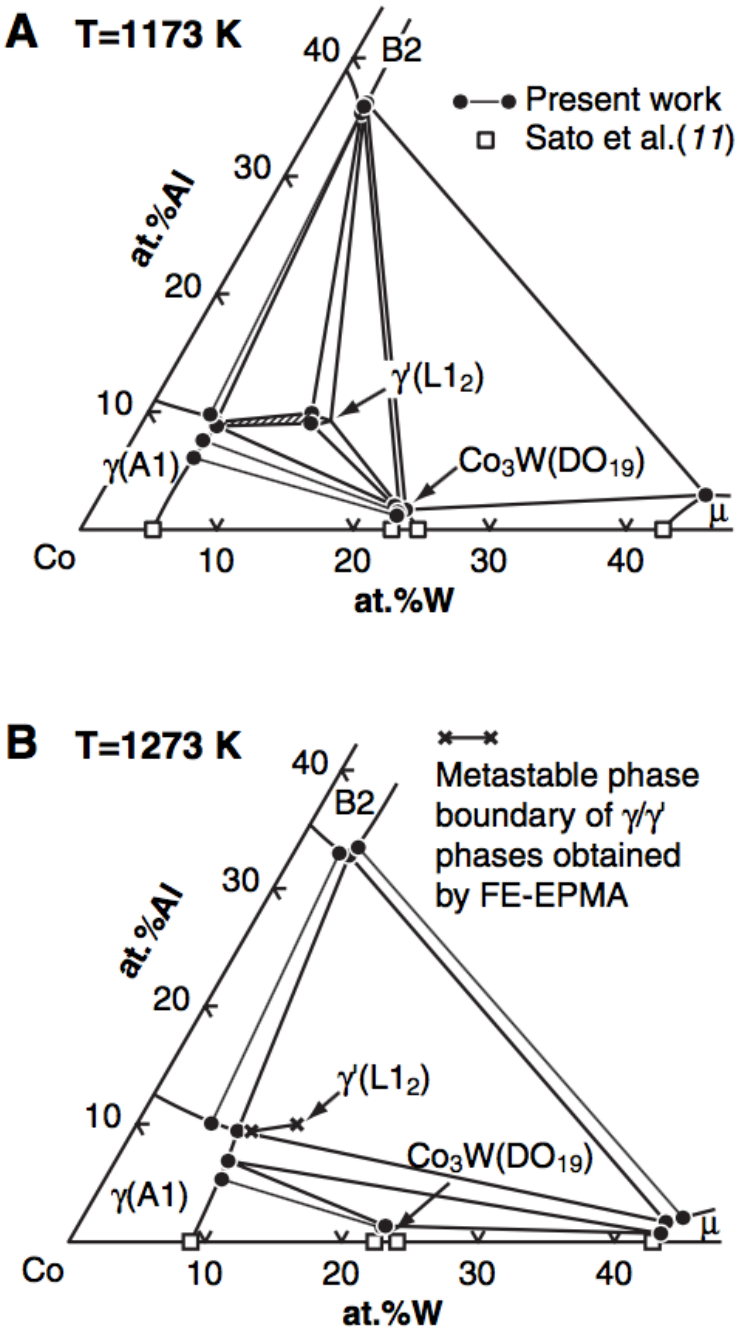

Figure 2.7: The Co-W-Al ternary phase diagrams at 900°C (A) and 1000°C (B), showing a small γ/γ' two-phase field to be present at the lower temperature (shaded) [7].

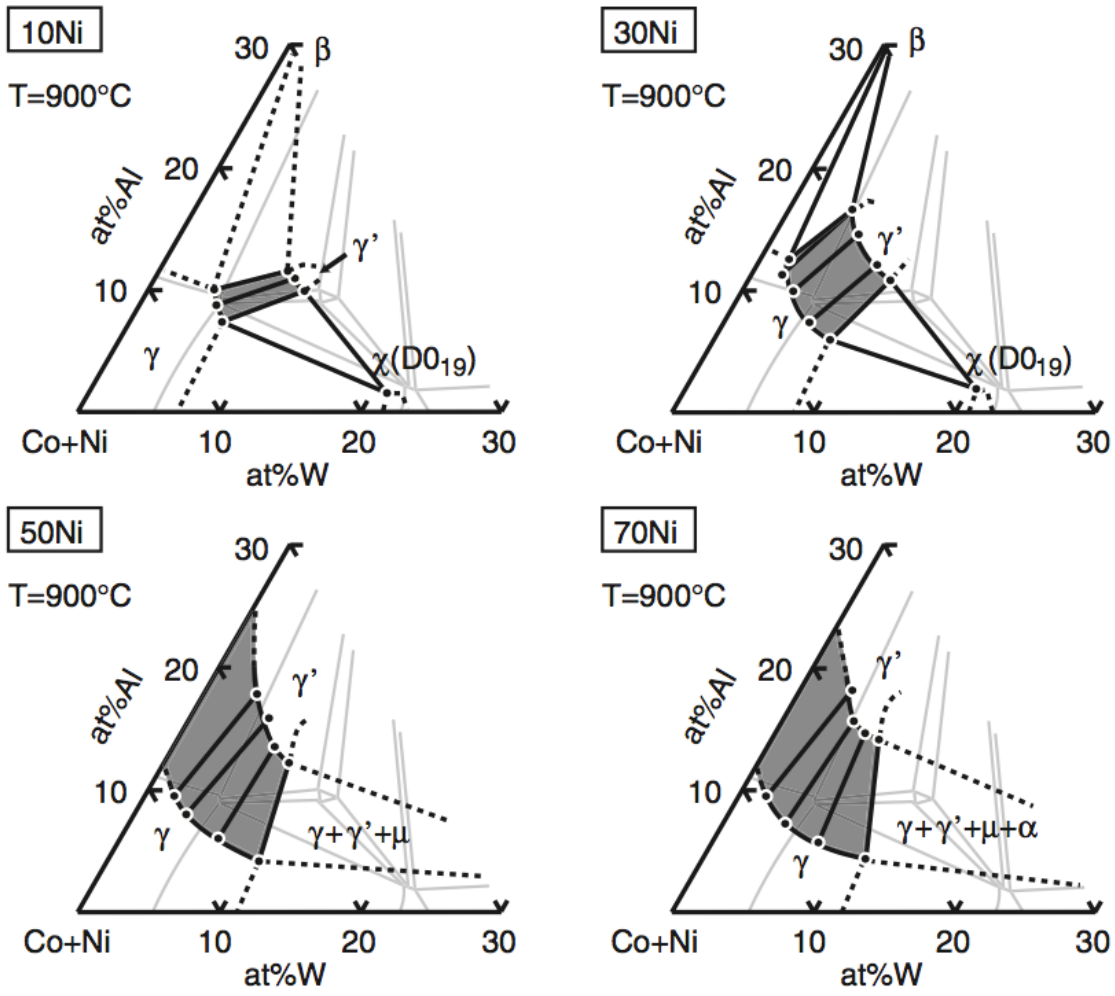

Figure 2.8: Isothermal isoconcentrate (ITIC) sections of the Co+Ni-W-Al phase diagrams at 900°C. The γ/γ' two-phase field is shown (shaded) to increase in size with greater Ni additions [19].

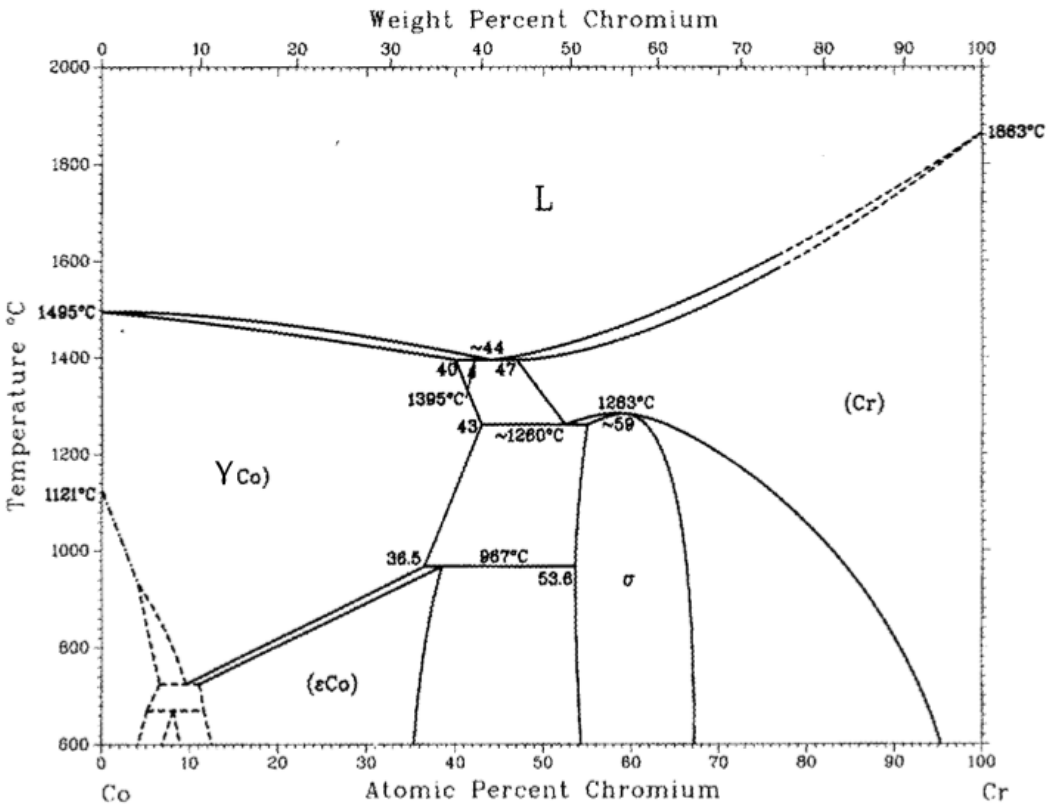

Figure 2.9: The Co-Cr binary phase diagram, showing significant Cr solubility in the γ (FCC) and ε (HCP) Co phases, as well as the σ-Co_7Cr_8 intermetallic (tetragonal P42/mnm) phase [24,26].

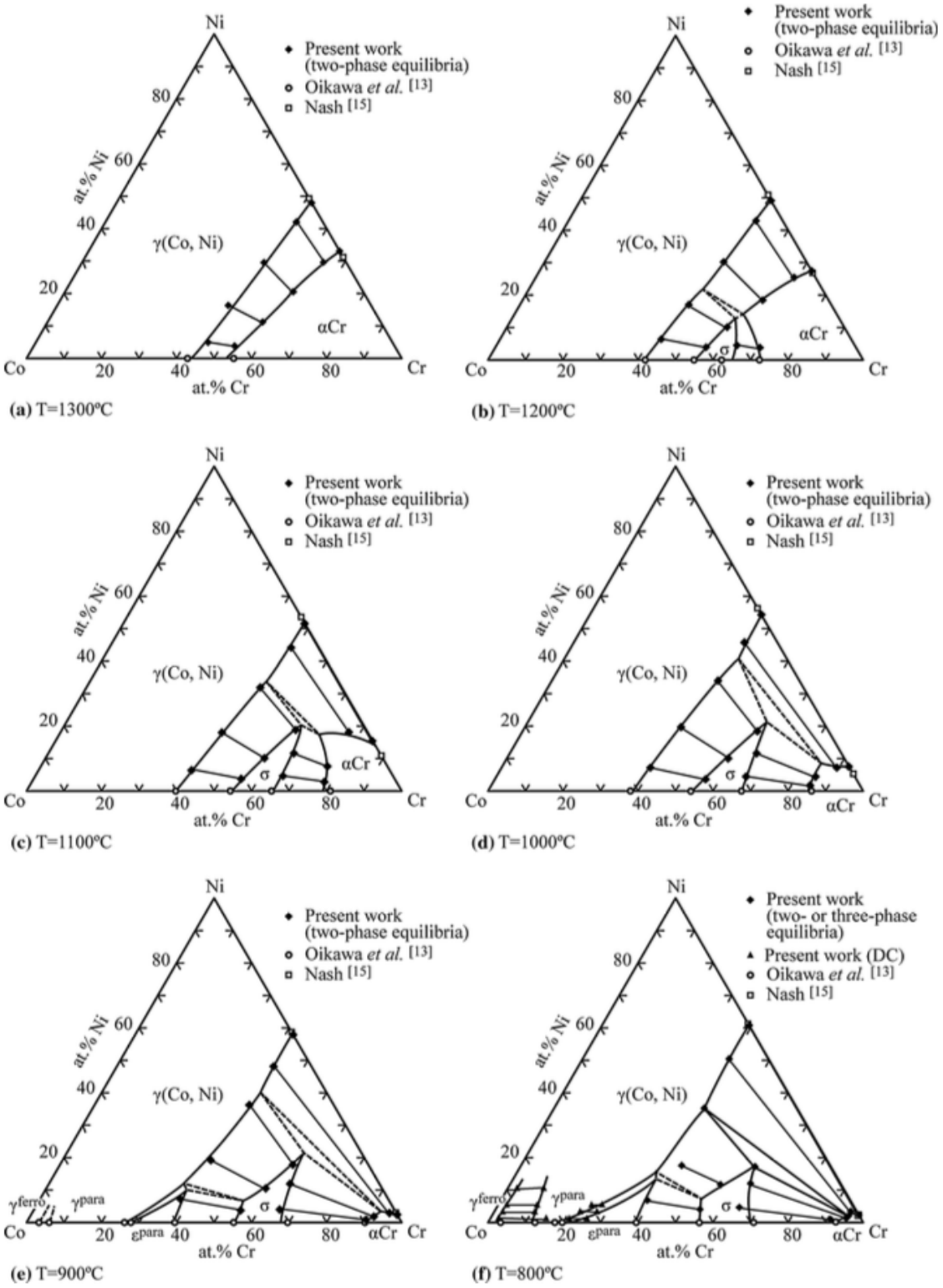

Figure 2.10: Co-Ni-Cr ternary phase diagrams at temperatures from 800-1300°C. There is complete solid solubility between the γ-FCC Co and Ni phases, and increasing solubility of Co and Ni in α-BCC Cr at increasing temperatures. The σ present in the Co-Cr binary has some Ni solubility, but becomes unstable by 1300°C [25].

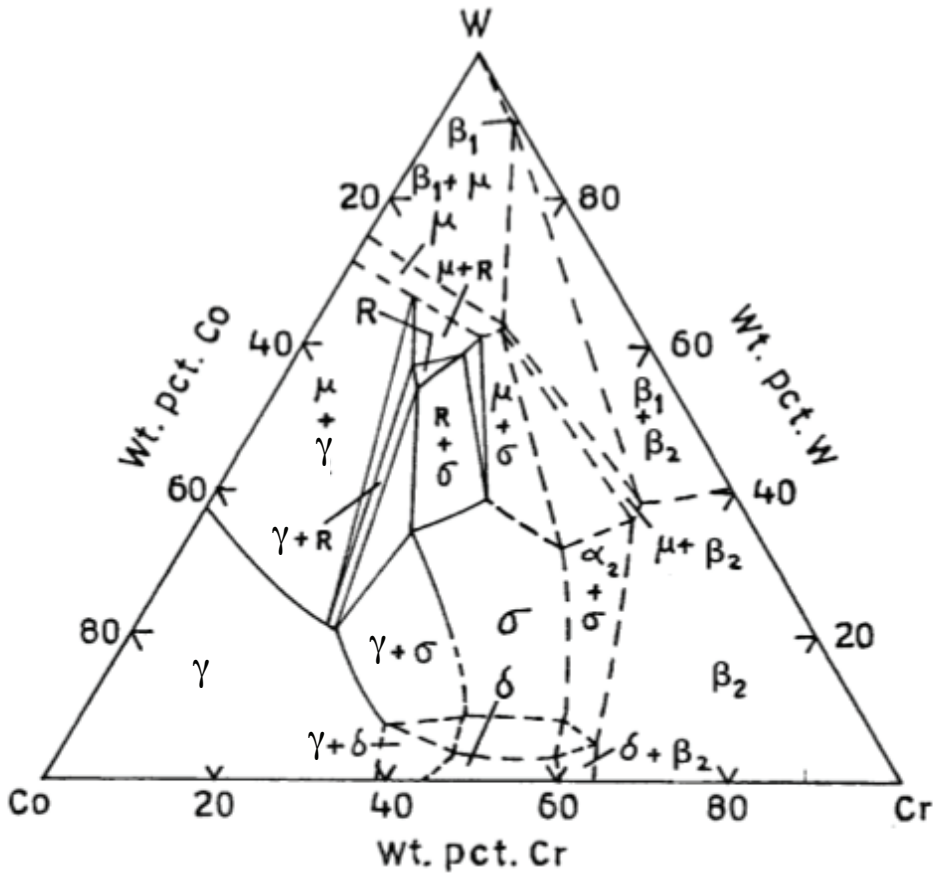

Figure 2.11: The Co-Cr-W ternary phase diagram at 1350°C (modified from [26]). In comparison with the Co-Ni-Cr ternary diagrams in Figure 2.10, it is seen that the σ phase is not present at 1300°C in the Co-Cr binary, but becomes stabilized with ternary W additions [26]. There is also significant solubility of Cr in the μ phase, which extends out from the Co-W binary. Also present is the ternary compound labeled R (rhombohedral, R-3, $Co_{23}Cr_{15}W_{15}$).

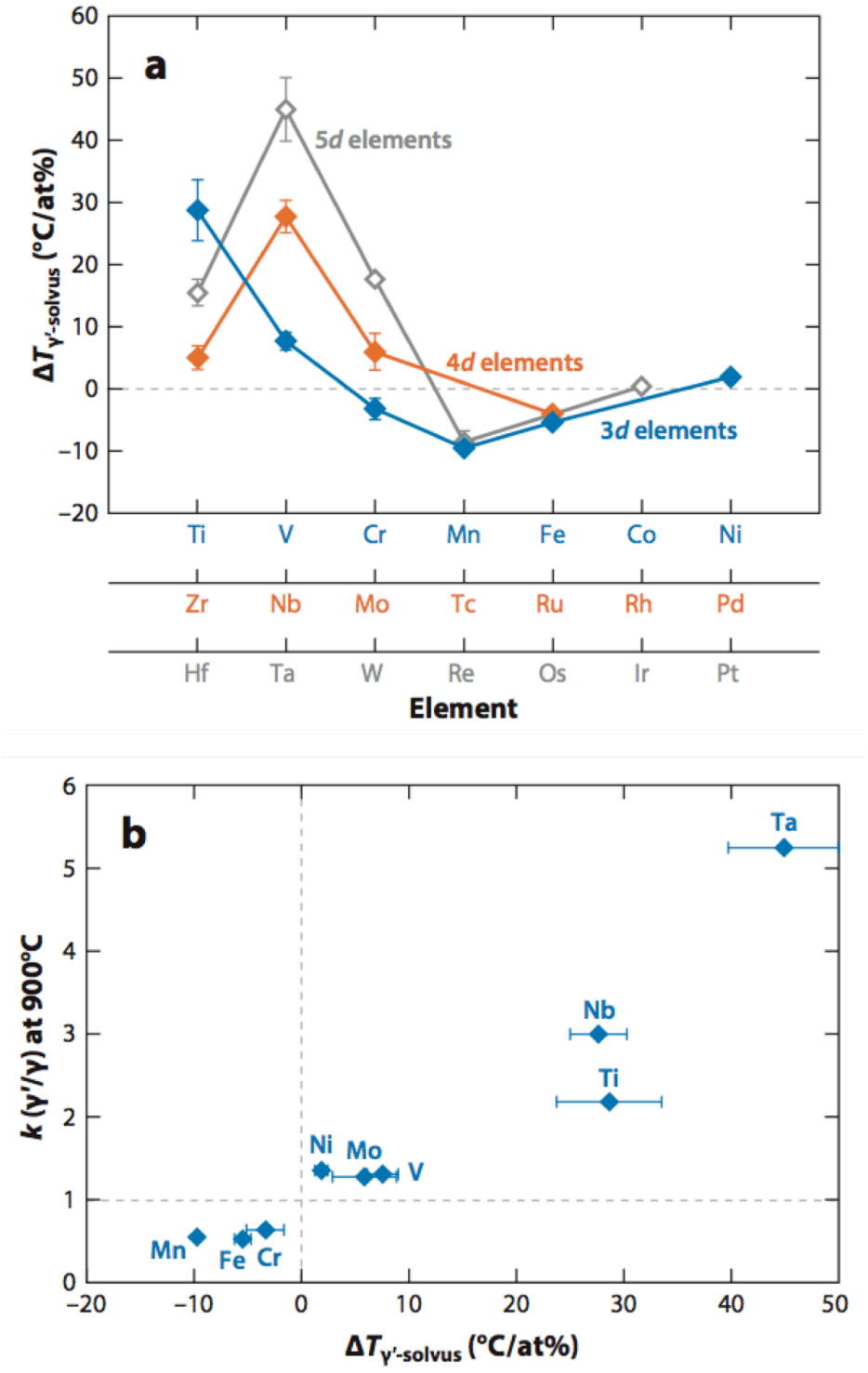

Figure 2.12: Effects of various alloying additions on the γ' solvus temperature in Co-base superalloys (a), as well as partitioning behavior of said elements (b). Overall, γ' stabilizing elements partition to the γ' phase, and vice versa for γ' destabilizing elements [35].

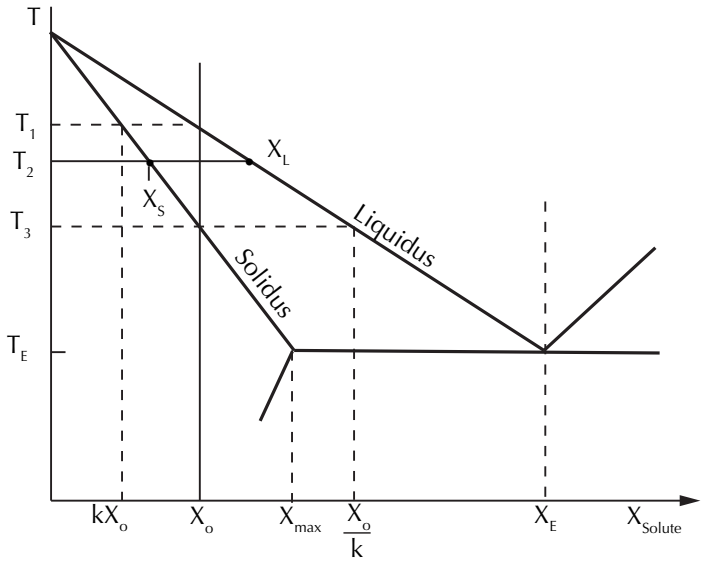

Figure 2.13: Schematics of a eutectic binary materials system during solidification. Points are labeled: net alloy composition (X_o), solid composition (X_s), liquid composition (X_L), eutectic composition (X_E), eutectic temperature (T_E), and partition coefficient (k), modified from [37].

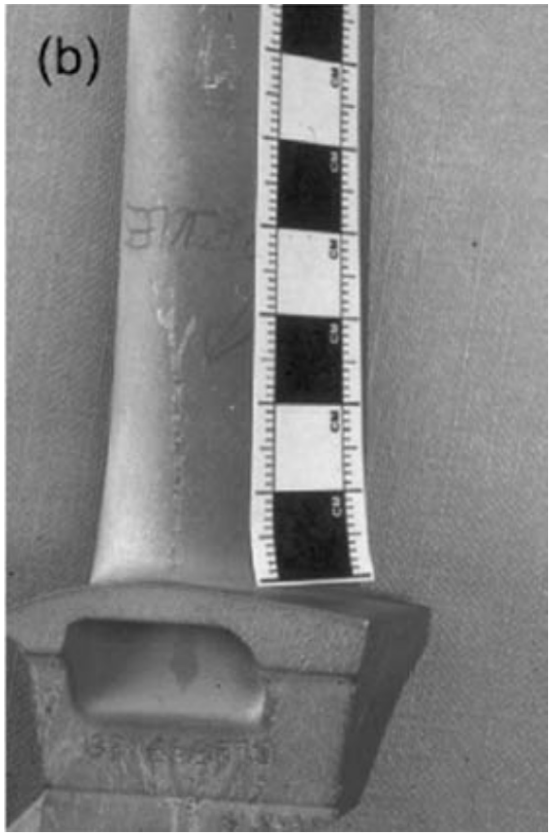

Figure 2.14: Freckle chain defects in directionally solidified superalloys [6].

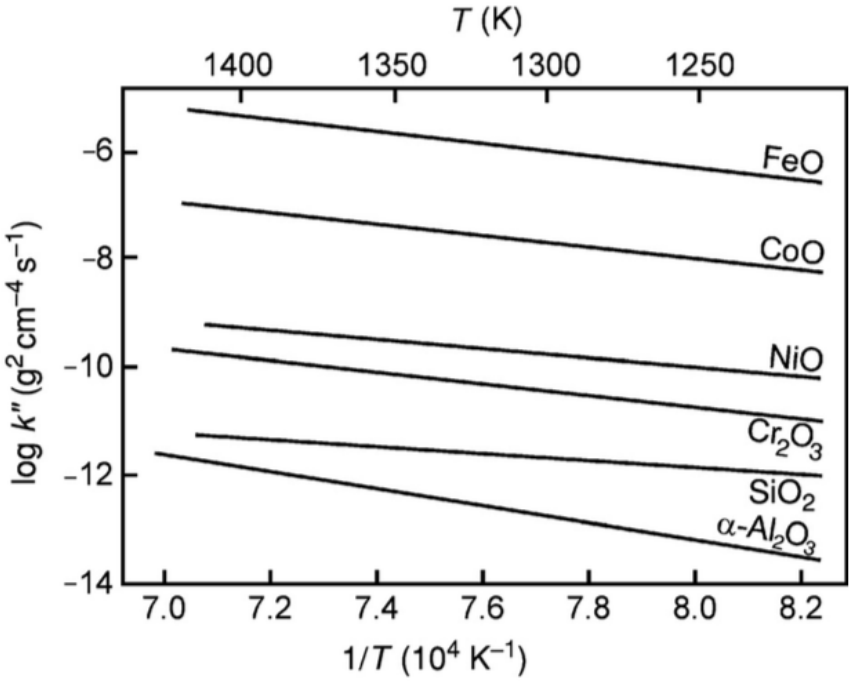

Figure 2.15: Parabolic growth rate constants for common oxides as a function of temperature at 1 atm [42].

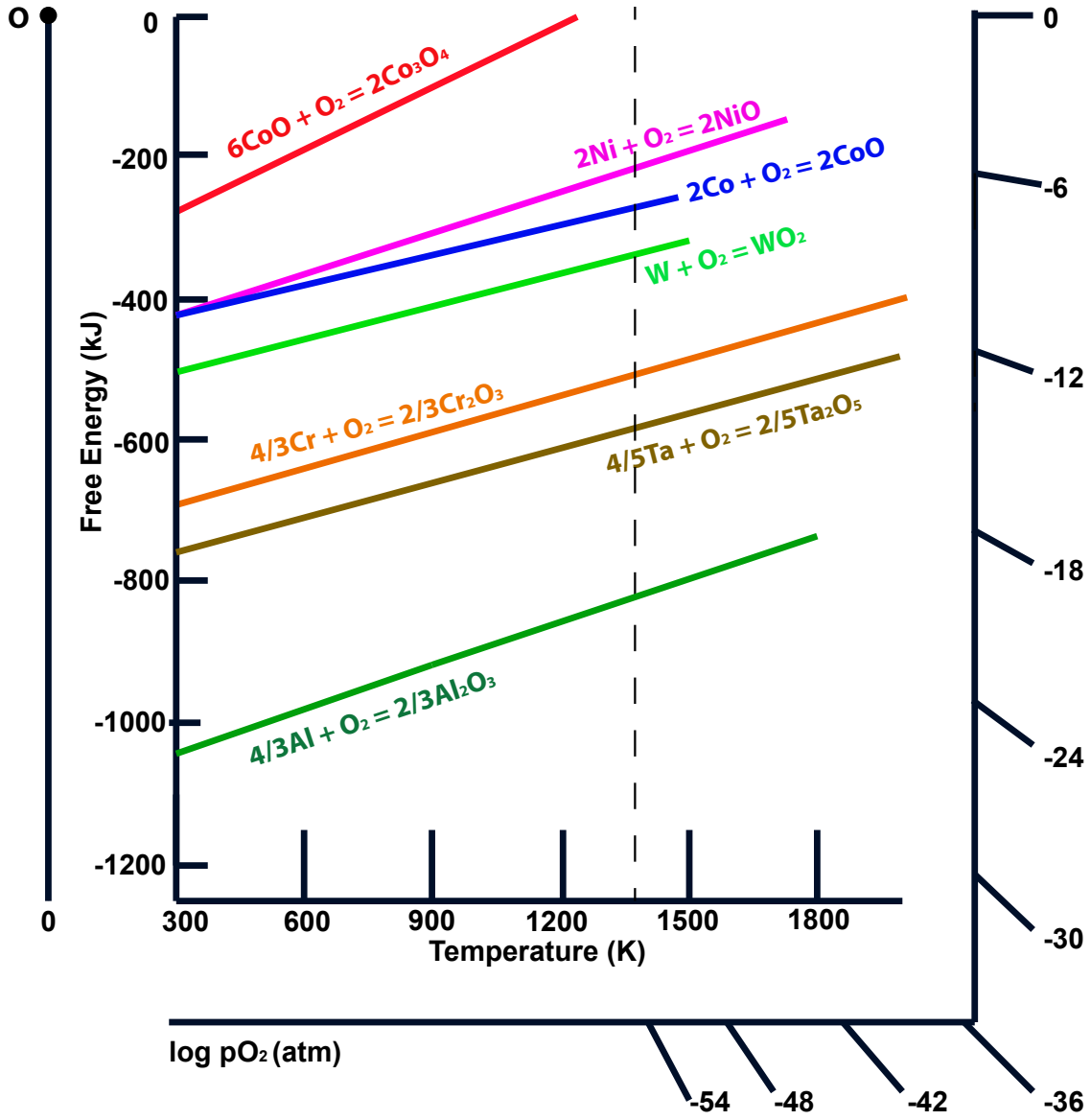

Figure 2.16: Ellingham diagram of various oxidation reactions, with 1100°C marked as the vertical dashed line. Adapted from [43,66].

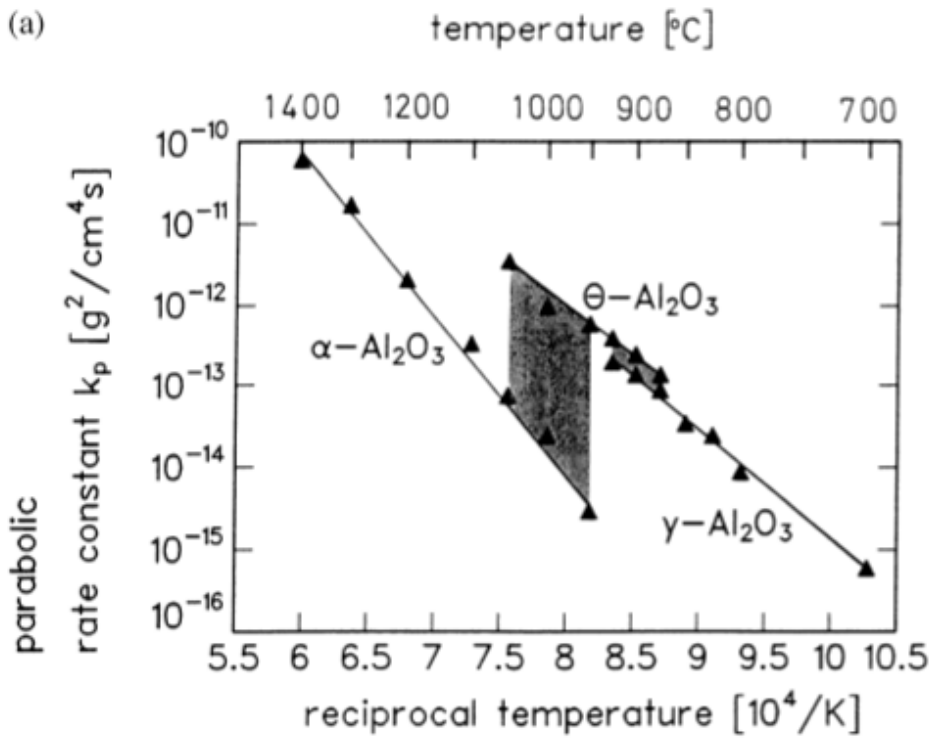

Figure 2.17: Relative growth rates of alumina polymorphs on pure NiAl [45].

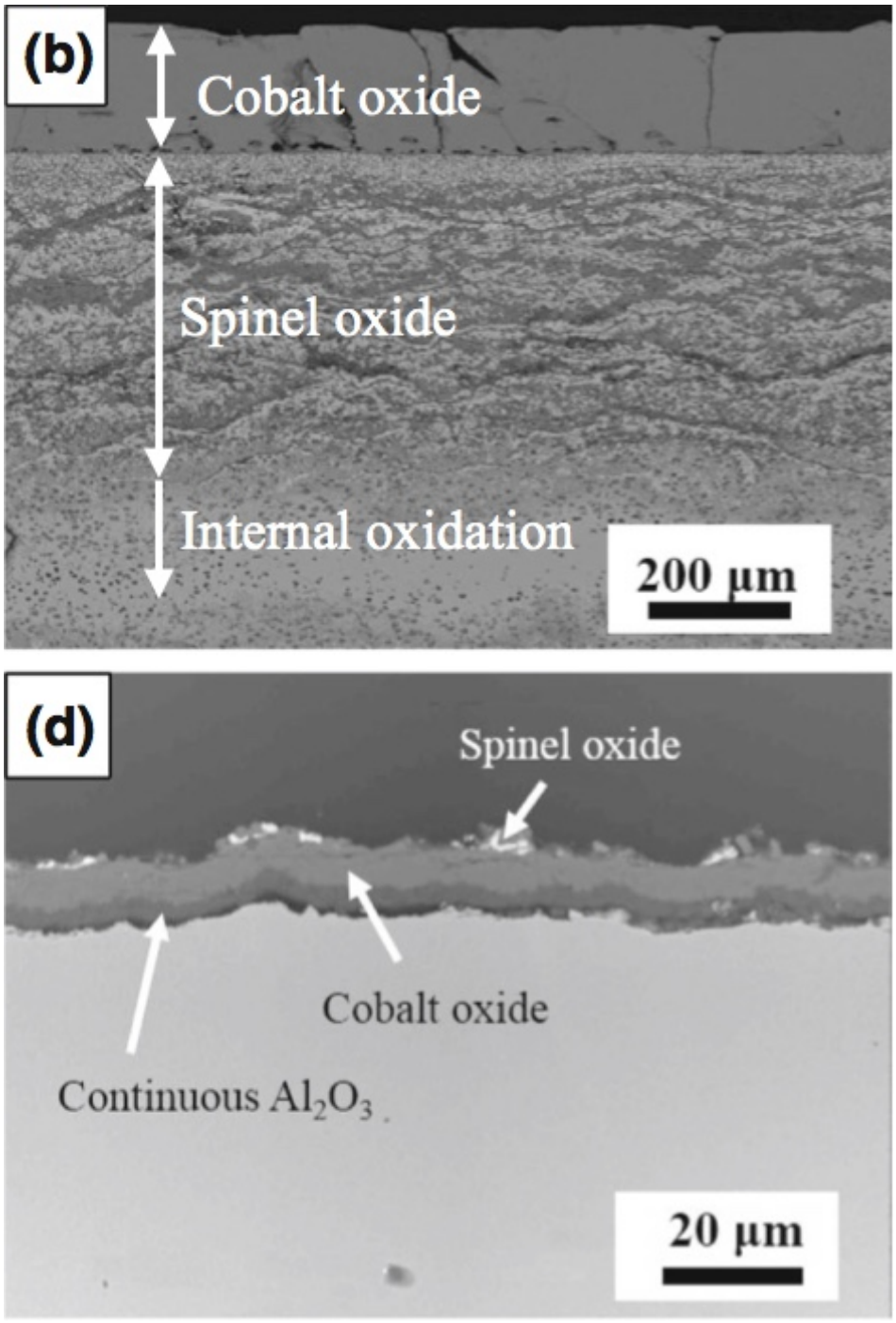

Figure 2.18: TGO in cross-section after a 146 h exposure at 1150°C. Alloy (b) is Co-30Ni-2Si-10Al-10W at.%, while (d) is Co-30Ni-2Si-10Al-5W [93].

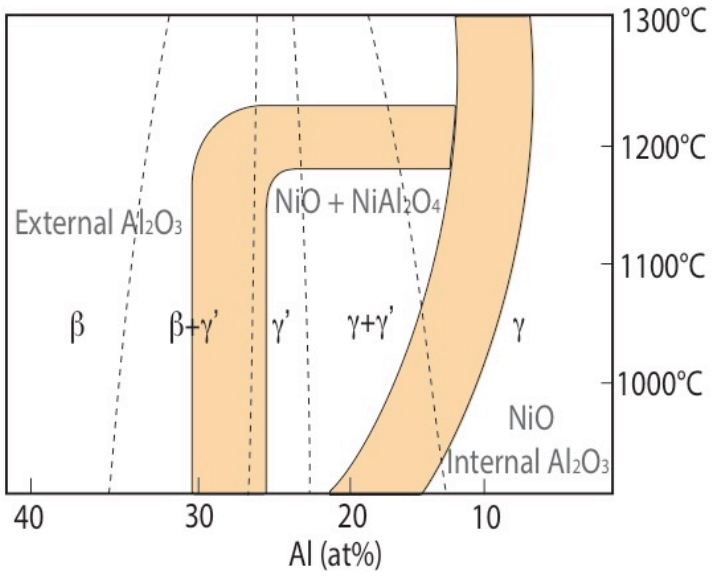

Figure 2.19: Oxidation map of Ni-Al alloys in air at various temperatures, modified from [13].

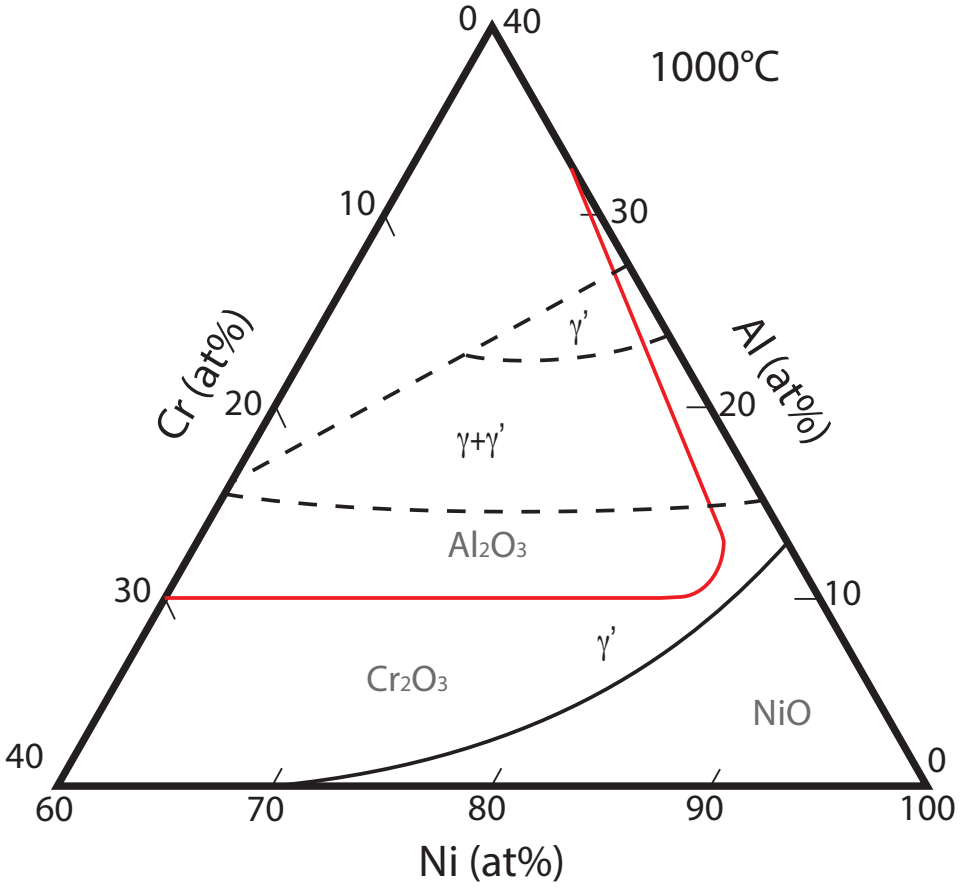

Figure 2.20: Oxidation map of Ni-Cr-Al alloys in air at 1000°C, compiled from [42,131]

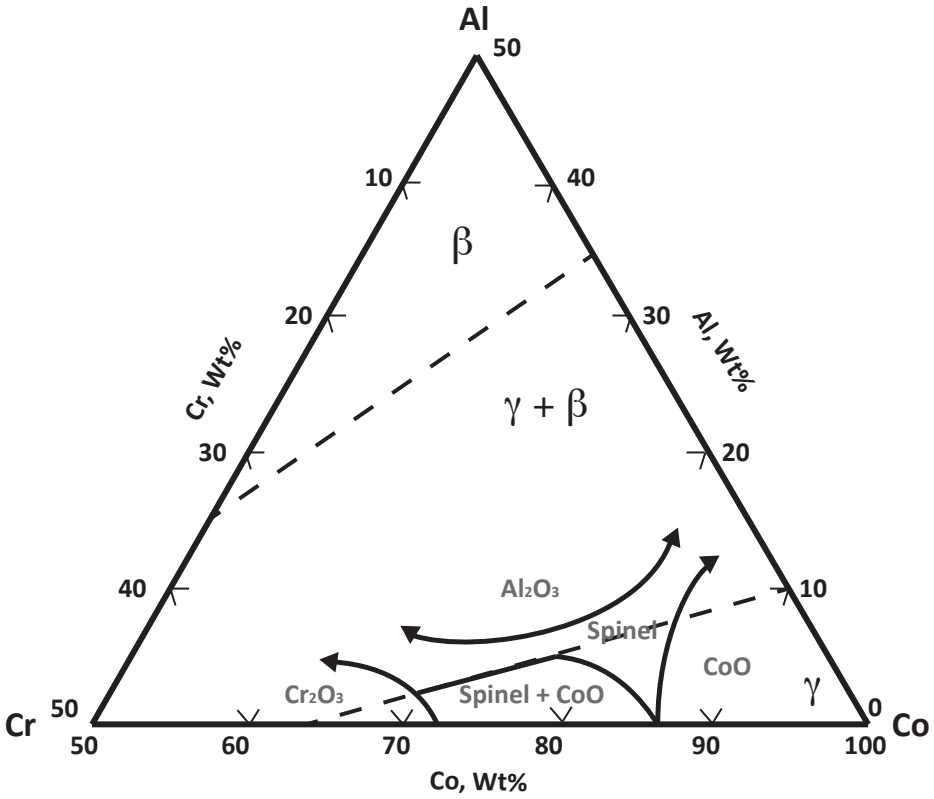

Figure 2.21: Oxidation map of Co-Cr-Al alloys in air at 1100°C, modified from [21]

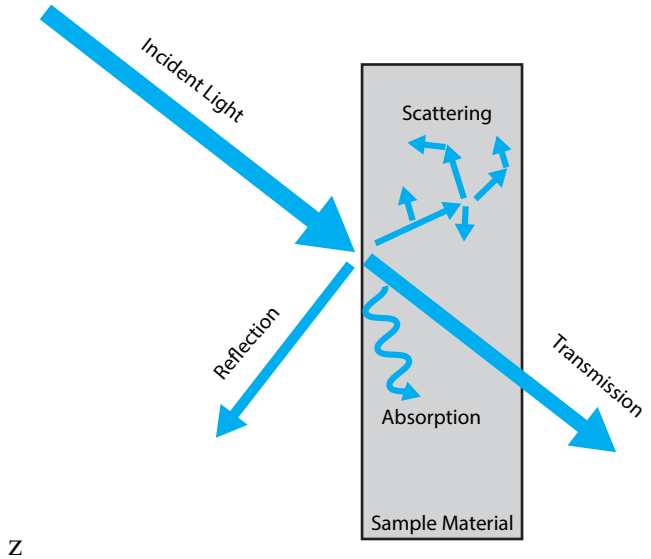

Figure 2.22: Diagram of the potential interactions of incident light with a sample material, including transmission, reflection, absorption, and scattering [132]. Of the scattered light, some experiences a change in frequency due to vibrational or electronic interactions with the material.

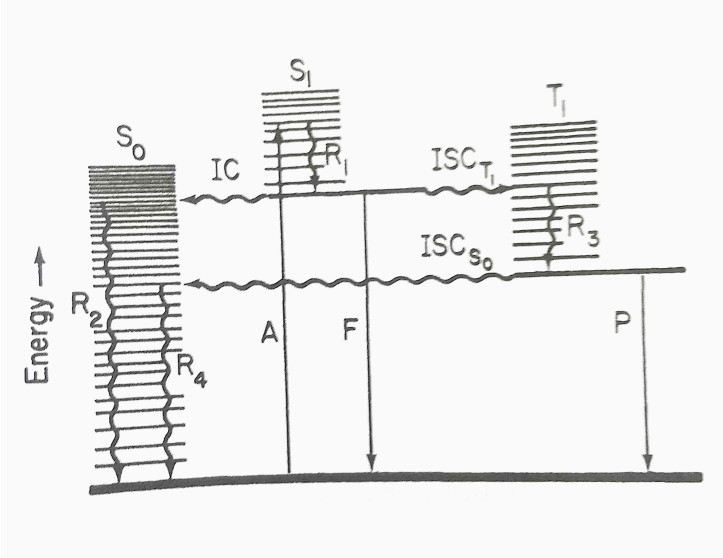

Figure 2.23: Electronic responses of a target material to absorbed light. The bold horizontal line at the bottom represents the HOMO from which electrons may be excited upon the (A) absorption of incident light. The smaller horizontal dashed lines are the available higher energy states to which electrons may be excited, labeled S_o, S_1 and T_1 for the singlet ground states, and lowest excited singlet and triplet states respectively [113]. Excited electrons may then (R) relax to lower available states, undergo (IC) internal conversion, or (ISC) intersystem crossing. Upon relaxing to the LUMO, electrons can then relax across the band gap to emit light as (F) fluorescence, or (P) phosphorescence photons.

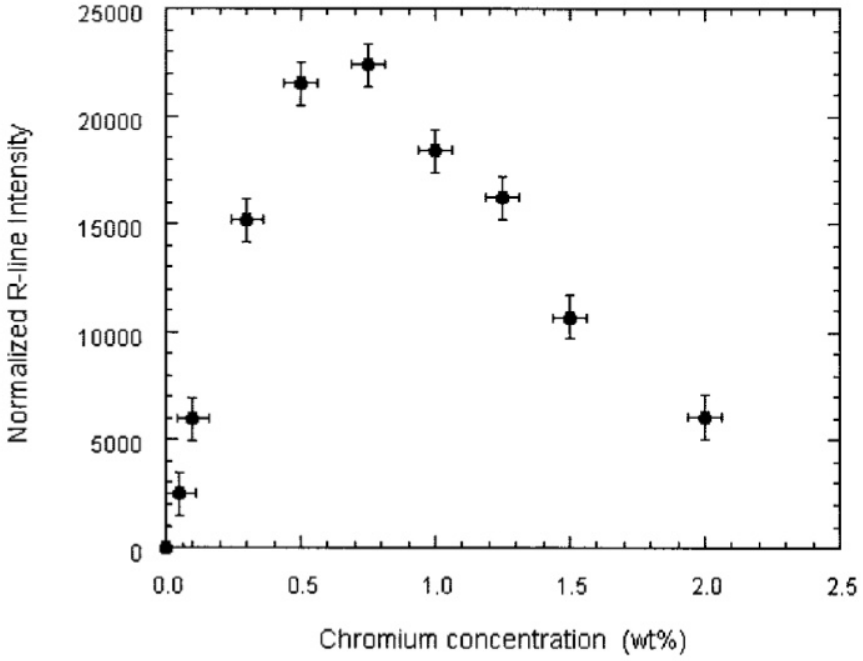

Figure 2.24: α-Al_2O_3 PSLS doublet intensity with increased Cr doping normalized to undoped material. [117]

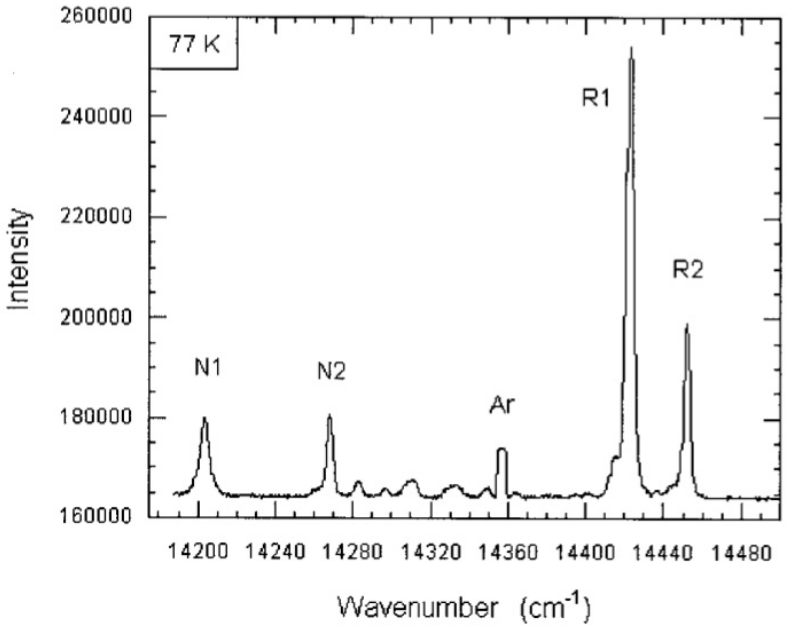

Figure 2.25: PSLS spectrum of 0.86 wt.% Cr single crystal α-Al2O3 at cryogenic temperature, demonstrating the characteristic R-peaks from Cr^{3+} substitutions on Al sites, and N-peaks from Cr^{3+}-Cr^{3+} pairs, as well as an Ar calibration line. [117]

3 Experimental Procedures

Understanding the alloy phases and oxidation behavior across composition space is necessary to develop novel Co-based γ/γ' alloys with superior properties. To approach this challenge systematically, a combinatorial synthesis approach was undertaken to generate three libraries covering a wide range of alloy compositions. The resulting specimens were prepared metallographically to achieve a consistent surface finish, oxidized, and then their thermally grown oxide (TGO) was characterized to ascertain the presence of α-Al_2O_3. Bulk alloy samples were then created iteratively based on the developed knowledge from the combinatorial samples. The various procedures used in this research are discussed in the current chapter; further details or deviations from the standard procedures described here will be given in subsequent chapters, as appropriate.

3.1 Alloy Synthesis

Three different alloy synthesis techniques were used in this study. First, an ion plasma deposition technique was employed to create a large number of alloys in a combinatorial approach, each alloy in a small volume. Arc melting, conversely, was used to create selected samples in small numbers but with larger volumes. Physical vapor deposition was also used sparingly to create thin model systems for investigating the properties of specific oxides. Once an alloy composition had been identified with promising characteristics, a bulk ingot was ordered from a commercial supplier (Sophisticated Alloys, Butler, PA), created via vacuum arc melting.

3.1.1 Combinatorial Synthesis by Ion Plasma Deposition

To create a wide variety of alloys across composition space, a synthesis technique was sought to generate a large number of samples of systematically varying compositions. Furthermore, because these exploratory alloys would be consumed to some extent by high-temperature oxidation and interdiffusion with the substrate, the thickness of the sample had to be sufficient to retain the original composition in a significant fraction of the volume after the oxidation tests. Although combinatorial synthesis of alloys is not uncommon, the latter goal is not readily achieved. For example, co-deposition from multiple sources using techniques such as magnetron sputtering can yield only thin films ≤ 1 μm [133–136]. As a result, oxidation testing must be conducted at fairly low temperatures (e.g. < 500°C), and care must be taken to deposit onto a substrate that limits interdiffusion with the deposited test alloy, thereby consuming the bulk of the alloy. Alternatively, vacuum arc melting can be used to create a variety of alloy ingots that can retain the bulk composition away from the surface after oxidation. However, the number of different combinations that can be generated by this approach in a reasonable time is rather limited [94]. Ion plasma deposition (IPD) [137] offers an attractive compromise between these techniques, as it creates many compositions in parallel by co-deposition from multiple sources, but is able to achieve thick films, in the range of 50 μm to over 100 μm, that could retain the bulk composition after oxidation.

In the IPD approach used in this investigation, three metal cathodes were arranged over the corners of a triangular array of substrate buttons, as illustrated in Figure 3.1. The cathodes are then subject to an electric arc under vacuum to generate a plasma that produces plasma as well as droplets which are deposited concurrently onto the substrates.

In consequence, the generated IPD coatings have variable compositions depending on their relative location in relation to the three source cathodes, forming a 'library' of test buttons. Three libraries of buttons were created by using two common cathodes and changing the third one, each cathode being multi-component as shown in Table 3.1. Cathodes 1 and 2 were common to all three libraries, representing a change in the Ni:Co ratio across one axis. Individually, the third cathode for each library was 3, 4, or 5 corresponding to changes in the Al, W, or Cr content. The substrate material was based on the composition of Cathode 1 to minimize interdiffusion and CTE mismatch with the IPD coatings.

All cathodes were cast and machined by Sophisticated Alloys. Measurement of the bulk compositions was performed by inductively coupled plasma emission spectroscopy (ICP) at Northern Analytical Laboratory Inc. (Londonderry, NH) and Sherry Laboratories (Daleville, IN). The IPD was conducted at General Electric Global Research (Niskayuna, NY). A heat treated, polycrystalline ingot of the substrate alloy was cut by EDM into 234 buttons of approximately 12.7 mm diameter and 2.5 mm in thickness. The EDM surfaces were then removed from the flat faces using a surface grinder and 400 grit cubic boron-nitride grinding wheel fed at 2 μm per pass. Sets of 80 buttons were adhered to a magnetic plate with Crystalbond 509 (Thermo Fisher Scientific) to grind a large batch at once, and to keep both sides of the buttons approximately parallel. Once the faces were polished, the buttons were adhered to metal rods & mounted in a drill press, whereby the EDM surface on the curved edges was removed with SiC paper down to 800 grit by hand. Following removal of all EDM surfaces, buttons were ultrasonically cleaned in acetone for 20 minutes and then in isopropanol for 15 minutes. These cleaned buttons were then supplied to GE Global Research for IPD deposition. The arrangement of substrate buttons and source

cathodes is shown in Figure 3.1. There was an approximately 7.6 mm separation between the substrate buttons (edge to edge) and an approximate 16.2 cm separation between the source cathodes (center to center).

3.1.2 Arc Melting

Once regions of more promising oxidation behavior were identified by analysis of the combinatorial libraries, larger amounts of select compositions were generated by arc melting individual buttons in the shape of spheroidal caps, approximately 11 mm tall by 28 mm in diameter, weighing ~40 g. Shot, pellets, and granules of chemically pure elements (>99.9%) and cut pieces of pre-alloyed buttons were combined in the appropriate amounts to achieve the compositions of interest. A Centorr (Nashua, NH) #5 arc-melter was used to melt the constituent metals into a combined button on a copper chill-plate in a gettered argon atmosphere ($X_O < 10^{-11}$ or < 0.1 ppb). A titanium button was also melted within the chamber in a pocket next to the sample to getter any oxygen evolving by degassing from the furnace surfaces. After the initial arc-melting step, the sample was flipped over and re-melted twice to ensure homogenously throughout the button.

3.1.3 Single Crystal Growth

A select alloy composition, discussed in a Chapter 7, was ordered in bulk (~8 kg) from commercial supplier Sophisticated Alloys, created using vacuum arc melting. This alloy was used in both the as-cast polycrystalline (PX) state, as well as cast into single crystals (SX). Single crystal growth was performed in a vacuum casting furnace in Bridgman mode (ALD Vacuum Systems Inc., Wixom, MI) [138]. The 2.4 kg of ingot material was loaded into an induction heated ceramic crucible inside the furnace. A 5-bar ceramic investment casting mold with spiral grain selectors was mounted on a water cooled chilled plate inside

the furnace. The mold was preheated to 1575°C under vacuum below 10^{-4} mbar, and held at this temperature until pouring. The alloy was melted to fill the pre-heated mold with liquid metal, and then the mold was withdrawn from the bottom of the heater at a rate of 3.4 mm/min. After cooling and removal from the mold, SX bars were macroetched in a solution of 800 ml HCl, 20 ml HNO_3, 110 ml H_2O, and 160 g $FeCl_3$ for 5 h. Etching was conducted to observe any grain defects on the nominally single-crystalline bar.

3.1.4 Physical Vapor Deposition

It was desired to create model systems of some thin oxide layers on top of a specific substrate. For this purpose, an electron-beam physical vapor deposition (PVD) system was used to deposit a metal film in the range 10-40 μm thick onto a wafer of polycrystalline α-Al_2O_3 (CoorsTek, Golden, CO) with an area of ~1 cm^2. The alumina wafer surface was prepared by ultrasonic cleaning in isopropanol followed by sputtering Au-Pd onto the surface using a Hummer 6.2 Sputtering System (Anatech USA, Union City, CA) under ~90 mTorr of Ar at 10 mA for 120 seconds. This sputtered material was to promote adhesion of the metal film during deposition, which was then oxidized into a single oxide phase adherent to the substrate. A custom deposition system was used to conduct the PVD, made from three SFIH-270 e-beam sources allowing co-deposition, as well as a Simba 2 power supply (both FerroTec, Santa Clara, CA, formerly Airco-Temescal). An SQS-242 deposition control system was incorporated (Inficon, Bad Ragaz, Switzerland, formerly Sigma Instruments). Metallic cobalt and/or nickel targets were used for the deposition process (> 99.9% purity), with the plating thickness monitored by a quartz crystal microbalance (QCM) sensor.

3.2 Alloy Heat Treatment

Both cast ingots and IPD combinatorial samples were heat treated to homogenize the alloys prior to testing. Unless otherwise noted, heat treatments were conducted in a vacuum resistance furnace with tungsten heating elements (Vacuum Industries, model 1822, Somerville, MA) at ~10^{-6} Torr. Samples were placed on an alumina plate and covered (not in contact) by a solid titanium cage to getter any residual oxygen in the system. This and other furnaces used in this study (e.g. for oxidation) were controlled with a Eurotherm 2404 PID controller (Ashburn, VA). Typically, bulk alloy samples were subjected to a two-step heat treatment consisting of solutioning and aging. Combinatorial samples produced by IPD only received a solutioning treatment, and were considered to age in situ during oxidation. Solutioning achieved both homogenization of the segregation produced during solidification as well as dissolution of all the γ' into the γ matrix. This is ideally conducted above the γ' solvus, but since the solvus changes with composition, the appropriate treatment temperature will be noted in each section, typically 1200°C. After a prescribed dwell time the alloys were rapidly cooled to promote size uniformity of any precipitated γ' particles. Secondly, an ageing treatment was applied to fully precipitate the γ' phase uniformly throughout the material. The exact conditions of heat treatment will be discussed in the individual sections, based on the alloys under investigation. The heterogeneous microstructure of the as-deposited IPD alloys compared with the homogenized coatings post-solutioning are shown in Figure 3.2.

3.3 Oxidation

The thermally grown oxides produced on alloys could be influenced by various environmental effects, including the presence of water vapor and dust or salt in the air. For this reason, samples were usually oxidized in a controlled-atmosphere furnace.

3.3.1 Controlled Atmosphere Isothermal Exposure

Isothermal oxidation was conducted in a tube furnace (CM Furnaces, Bloomfield, NJ) using a 76 mm diameter fused silica enclosure. The furnace was pre-heated to the prescribed temperature and samples loaded onto a refractory boat inside the enclosed chamber. The chamber atmosphere was flushed; this was conducted by pulling vacuum on the enclosed tube to ~0.1 Pa, filling the tube back up with filtered air, and repeated once more. After flushing, a slow gas inlet of 0.1 l/min was established to ensure laminar flow across the samples. The inlet air was filtered using three Parker Balston filters (Lancaster, NY) in series: models A914-DX and A914-BX to remove 99.99% of particles down to 0.01 μm, oil down to a maximum of 0.012 ppm, and water vapor down to a maximum of ~2700 ppm prior to secondary removal of any remaining water vapor using a model CI100-12-000 filter. Once the furnace temperature and environment were established, samples were injected into the hot zone under the controlled atmosphere. The injection was conducted using a push-rod that entered the chamber through a sealed-interface. As such, injection did not alter the controlled atmosphere inside the furnace. After dwelling in the hot zone for the desired oxidation time, samples were then withdrawn over the course of 5 min to avoid spallation of the scale that may occur under a faster cooling rate.

3.3.2 Thermal Cycling

Thermal cycling was conducted using an alumina boat resting on a robo-loader, and as such a controlled atmosphere could not be established. Instead, a Lindberg/Blue M General-Purpose furnace (Thermo Fisher Scientific, Hampton, NH) was heated to the prescribed temperature open to laboratory air. Samples were then inserted into the hot zone, held at temperature for 1 h, and then withdrawn following a thermal cycle depicted in Figure 3.3. At select cycle numbers, the treatment was interrupted and the samples were weighed to measure the progress in oxide growth.

3.4 Thermophysical Characterization

3.4.1 Differential Thermal Analysis

DTA was performed on pieces of alloy post-heat treatment, primarily to identify the γ' solvus, solidus, and liquidus temperatures. Samples were cut via electric discharge machining (EDM) into cylinders approximately 6 mm tall, 3 mm in diameter, and 400 mg in weight. The surfaces were then polished and the sample was cleaned ultrasonically in isopropanol. A given sample was then placed in an alumina crucible, and loaded into a Setaram Setsys 1750-ATD (Setaram, Caluire, France) DTA, along with a 341.2 mg platinum reference sample in a similar alumina crucible. Within an argon environment, the DTA is then heated through 1300°C and cooled to room temperature both at a rate of ~ 5 °C/min, and the heat flux relative to the reference is measured vs. time to observe any endothermic or exothermic reactions.

3.4.2 Dilatometry

Dilatometry was conducted using a Orton 2016 HU (Orton, Westerville, OH) under Ar. Sample bars approximately 25 mm long and 9.5 mm in diameter were cut using EDM, and

the long ends gently polished to remove any machining debris. Sample alloys were cut post-heat treatment, and measured with respect to a polycrystalline standard alumina cylinder. Change in sample length was measured with the dilatometer's extensometer as the material is heated at a rate of 3°C/min. Because the setup is contained in a fused silica tube, the temperature was limited to a maximum temperature of 1200°C to avoid softening of the glass. In this manner, the CTE of the alloys is measured, as well as the γ' solvus temperature based on changes in the net CTE as the ordered phase dissolves. Provided the solvus is below 1200°C, this measurement can be compared with DTA measurements.

3.4.3 Archimedes' Method of Density Calculation

While density is important for aerospace components, the present investigations were primarily focused in altering the oxidation behavior and alloy phase stability. Once a promising alloy composition was achieved, its density was measured by the traditional Archimedes method. A bulk alloy sample was measured in air on a microbalance, as well as submerged in deionized water. The difference between these measurements combined with the known density of water is used to calculate the alloy density based on buoyant forces.

3.5 Metallographic Preparation

Standard metallographic preparation techniques were used both to prepare sample surfaces prior to oxidation, as well as to prepare samples for characterization, typically by scanning electron microscopy (SEM).

3.5.1 Surface Finish Pre-Oxidation

A consistent surface finish was desired prior to oxidation not only to remove any contaminants from the material, but also to achieve a uniform surface condition, including a

suitably low roughness and minimizing the dislocation density that may have resulted from cutting and grinding. Preparation of samples prior to oxidation can generally be divided into three categories based on the type of sample: combinatorial buttons, bulk alloys for isothermal oxidation, and bulk alloys for cyclic oxidation.

3.5.1.1 Polishing of Combinatorial Samples Prior to Oxidation

Combinatorial buttons presented the unique challenge that the material volume of interest was fairly small, approximately ~110 μm of heat-treated IPD coating on top of the substrate alloy. Therefore, care must be taken to minimize the amount of IPD layer removed during preparation. With this in mind, the combinatorial buttons were taken from heat treatment immediately into polishing using a vibromet polisher with a 30 cm MicroCloth pad (Buehler, Lake Bluff, IL) and a solution of 50 nm colloidal alumina grit (MasterPrep, from Buehler). To mount the buttons in the weighted vibromet sample holders, the IPD-coated face of the combinatorial buttons was placed face-down on a surface-ground metal slab. A small amount of Crystalbond 509 was melted to the exposed back of the buttons, and a 25 mm diameter aluminum puck was adhered onto the button via a tight-fitting die set, to assure that the button face of interest was parallel to the back of the adhered face. The pucks with attached combinatorial buttons were then loaded into the Vibromet sample holders, and six at a time were polished for approximately 18-36 hours. Periodically during this time, the surfaces of the buttons were inspected by optical microscopy to verify that the rough surface layer had been polished through. It should be noted that a small amount of porosity remained in the combinatorial coatings even after solution heat treatment, but this was clearly distinct from any remaining surface roughness. Polished combinatorial buttons were then removed from the Vibromet, rinsed in water, and the surface scrubbed gently with

soap and a cotton swab to remove residual media from the polished face. Then, combinatorial buttons were ultrasonically cleaned in acetone for 20 minutes to dissolve the Crystalbond and separate them from the aluminum pucks. The polished faces of the buttons were then gently scrubbed with isopropanol and a cotton swab to help remove any residual polishing media that might have been incorporated from the acetone bath. Buttons were then ultrasonically cleaned in isopropanol for 20 minutes, blown dry with filtered air, and placed into membrane boxes (Ted Pella Inc., Redding, CA). Before oxidation, polished and cleaned buttons were inspected in SEM to measure the alloy composition via EDS, as well as to verify that there were no surface abnormalities. If any regions of remaining surface roughness were identified, the buttons were re-polished on the vibromet following the same procedure.

3.5.1.2 Polishing Bulk Alloy Buttons Prior to Isothermal Oxidation

Bulk alloy samples, such as those created by arc melting, single crystal growth, or commercially procured were cut into a manageable size, typically similar to those of the combinatorial buttons. Because there was significantly more material present than the IPD alloys, cuttings from bulk alloy samples were polished more rapidly by hand using SiC grit papers (Allied High Tech Products, Rancho Dominguez, CA). Grinding papers were used in succession from 300 to 400, 600, 800, and 1200 grit respectively. Samples were then ultrasonically cleaned in isopropanol for 10 minutes. Next, polishing was conducted using diamond suspensions applied to a napped cloth (Buehler). Diamond suspensions were again used in succession from coarse to fine, with 9 μm, 3 μm, and 1 μm respectively. Samples were then ultrasonically cleaned in isopropanol for 5 minutes, and adhered to aluminum pucks using the same procedure as the combinatorial buttons. As a final polishing step, the

cuttings from bulk alloys were polished on the Vibromet with 50 nm colloidal alumina suspension, and then ultrasonically cleaned in acetone for 20 minutes and isopropanol for 20 minutes, and placed into membrane boxes.

3.5.1.3 Polishing Bulk Alloy Buttons Prior to Cyclic Oxidation

Cut pieces of bulk alloys prepared for cyclic oxidation were different than those used for isothermal oxidation in that all exposed faces of the sample must be polished to the same finish. This is because samples used in cyclic oxidation were weighed after set amounts of cycles, with this change in weight coming from the oxidation of all exposed parts of the alloy. Because of these requirements, such samples were cut into rectangular prisms, with a platelet-like aspect ratio. All faces were then polished by hand using SiC grinding papers down to 1200 grit.

3.5.2 Cross-Section Preparation Post-Oxidation

After oxidation, it was often desirable to examine the TGO on top of the alloys in cross-section. This presented a polishing challenge as the formed oxides were often much harder, as well as more friable than the underlying metal. As such, any dislodged oxide particles during polishing could scrape against the rest of the sample and reduce the surface finish. The following procedure was adopted to address this problem. First, after oxidation, the TGO surface of interest was painted with a layer of low-viscosity M-bond 610 (Ted Pella) such that any rough oxide facets and exposed cracks were infiltrated. The sample was then left to dry overnight, and the M-bonded sample was subsequently cured at 175°C for 1 h. This sealed the oxide surface in a hard resin layer. The sealed samples were then embedded into cold-mount EpoxySet Resin (Allied) at room temperature under vacuum, and left to cure for at least 8 h. After the epoxy had cured, the embedded samples were sectioned

normal to the oxidized face using a slow saw with a 5 in x 0.015 in x 0.5 in diamond wafering blade (Allied). The sample was aligned with a shallow angle between the wafering blade and the TGO surface, and a light load was used on the blade to help prevent fragmentation of the oxide during cutting. After the sample was sectioned, one of the pieces was re-embedded in cold-mount epoxy to infiltrate any exposed pores or cracks during sectioning.

After the oxidized samples had been sealed, sectioned, and embedded, the resulting pieces were ready for polishing. SiC grinding papers, diamond suspensions, and Vibromet polishing were used sequentially in a process similar to that of preparing metal samples for isothermal oxidation. However, in the case of cross-sectioned oxidized samples, a 50 nm diamond suspension was applied to the vibromet, such that any polishing media which became embedded or remained in the exposed TGO/metal cross section would not confuse the SEM EDS analysis.

3.5.3 Surface Preparation for Microstructure Observation

Select alloy samples were polished without oxidation to analyze the alloy microstructural features themselves, such as the γ/γ' structure. Alloy pieces were hot-mounted in EpoMet F compound (Buehler) pressed to 28 kPa at 120°C and held for 5 minutes. The face of interest was then ground in a similar manner as bulk Alloy pieces prior to isothermal oxidation, however a 50 nm colloidal silica solution (MasterMet, Buehler) was used on the vibromet as a final polishing step. The polishing mechanism of this solution is a combination of both mechanical abrasion as well as chemical etching. Thus, the compositional difference between the matrix and precipitates will cause different amounts of removal, and reveal the γ/γ' morphology.

3.6 Electron Microscopy Characterization

The great majority of analysis on both the alloys and formed oxides was done using scanning electron microscopy. Select samples of interest were subsequently chosen for liftout by focused ion beam (FIB) and TEM analysis.

3.6.1 Scanning Electron Microscopy

Scanning electron microscopy was conducted using an FEI XL30 Sirion FEG Digital Electron Scanning Microscope (Thermo Fisher Scientific, Hillsboro, OR), an FEI Nova Nano 650 FEG SEM, and a ThermoFisher Apreo C LoVac FEG SEM. Microchemical analysis was conducted using an attached Apollo X SDD EDS detector (EDAX Inc., Mahwah, NJ). Imaging of the oxides in cross-section was typically conducted at 10 kV to help prevent drift of the sample. Imaging of alloys and EDS analysis was typically conducted at 15 kV.

3.6.2 Transmission Electron Microscopy

Transmission electron microscopy was conducted using an FEI Tecnai G2 Sphera Microscope with EDS, and an FEI Titan 300 kV FEG TEM/STEM with EDS (Thermo Fischer Scientific). Lamellae were analyzed at 200 kV on the G2 Sphera and 300 kV on the Titan. Lamellae were extracted using an FEI Helios Dualbeam FIB Nanolab 650 and thinned down to approximately 100 nm, using progressively smaller accelerating voltages down to a final thinning step with 5 kV.

3.7 Luminescence Spectroscopy Characterization

The presence of alpha alumina was investigated using photostimulated luminescence spectroscopy (PSLS), performed on a LabRam Aramis spectrometer (Horiba Ltd., Kyoto,

Japan) with a 50x long range objective lens and a 3.3 mW 633 nm laser. An average of 3 measurements was taken per location, each with a dwell time of 3 seconds. Typically, 24 locations across the oxidized surface of a given sample were measured to gain a representative understanding of the material. Occasionally, PSLS mapping was conducted on a T64000 Advanced Research Raman System (Horiba) with a 488 nm laser.

3.8 Chemical Analysis

3.8.1 Energy Dispersive X-ray Spectroscopy

The SEM EDS measurements taken were quantified using ZAF correction on the EDAX Genesis software. The energies of the commonly observed elements are given below in Table 3.2. Due to the very close energies of the Cr-Lα and O-Kα, only the Cr-K peaks were used for quantification. The accelerating voltages used for SEM EDS analysis were less than ideal to excite the Ta- and W- L peaks, such that the measurements of these elements via SEM were of a somewhat greater error than the other elements. Error in EDS measurements compared with other chemical analysis methods will be discussed at greater length in Chapter 6.

3.8.2 Electron Probe Micro Analysis

Electron probe micro-analysis (EPMA) was conducted at 20 kV using a Cameca SX100 and wavelength-dispersive spectroscopy (WDS) detector. These composition measurements were quantified with respect to pure element standards, as well as a Co-W-Al-Cr-Ta alloy that had a composition verified by ICP analysis. Comparisons between quantification standards will be discussed in a subsequent section, however the differences between

quantified results were essentially the same regardless of whether pure element or ICP alloy standards were used.

3.9 Thermodynamic Calculations

Thermodynamic calculations were used periodically throughout this study to both estimate the γ' solvus temperature, as well as the potential presence of any minor tertiary alloy phases beyond the main γ/γ' constituents. Only alloy systems were calculated, no oxide databases were used, nor were kinetic databases (e.g. DICTRA) applied. As experimental results were compiled, observations were compared with calculations to evaluate the accuracy of the applied database, to be presented in a later section.

3.9.1 PANDAT Database

The PANDAT software [110] based on the CalPhaD method [139] was used with the 2011 version (unless otherwise noted) of the PanCobalt database [140], containing the six principal alloy elements of interest: Co-Ni-W-Al-Cr-Ta. Calculations were conducted for individual alloy compositions across varying temperature to determine the γ' solvus temperature. The accuracy of the database was validated by comparing γ' solvus and solidus calculations with experimentally measured values, and were typically within 50°C as shown in Figure 3.4. Additionally, phase equilibria were calculated and plotted as isothermal, isoconcentrate (ITIC) sections on Gibbs triangles.

3.9.2 First Principles Calculations

Relevant first principles calculations were conducted by another student involved in Co-alloy research (Robert Rhein). Calculations of formation energies were performed to assess the effects of alloying additions on the chemical potential of the different components.

These calculations were performed for several hundred distinct FCC structures in the Co-Al-W and Ni-Al-W ternary systems using the Vienna ab initio simulation package (VASP) [141,142] and the Perdew, Burke, and Ernzerhof (PBE) generalized gradient approximation [143]. The cluster expansion statistical mechanics (CASM) formalism [144–147] was used to fit the calculated energies to obtain an expression for formation energy as a function of composition and local ordering. Subsequent Monte Carlo simulations were performed on the cluster expansion in order to obtain elemental chemical potentials as a function of composition at elevated temperature.

In addition, the potential ordering of possible oxide scales was predicted for limited combinatorial alloys. To do so, the formation energies of α-Al_2O_3 and other oxides relevant to Co-base alloys were obtained from the Materials Project database [148]. The oxide formation energies, $\boldsymbol{g}$, were then modified to obtain a new characteristic potential, ϕ,

$$\phi = g - \mu_O N_O \tag{3.1}$$

where μ_O is the oxygen chemical potential and N_O is the number of oxygen atoms in the chemical formula. This new potential was minimized at increasing oxygen chemical potentials to assess the most thermodynamically stable sequence of oxide formation for several Co-Ni-W-Al-Cr-Ta compositions.

3.10 Figures and Tables

Table 3.1: Composition of the source cathodes used in IPD alloy synthesis measured by inductively coupled plasma spectroscopy (ICP).

	Co (at.%)	Ni (at.%)	W (at.%)	Al (at.%)	Cr (at.%)	Ta (at.%)	S (ppmw)	Ni:Co (at.)
Substrate	79.7	0.0	6.7	8.9	3.3	1.5	0.5	0:1
Cathode 1	77.1	0.0	5.9	12.2	3.4	1.4	3	0:1
Cathode 2	33.5	35.4	11.8	14.4	3.4	1.5	2	1:1
Cathode 3	30.0	29.3	6.0	11.8	21.5	1.4	4	1:1
Cathode 4	40.9	40.4	0.0	13.8	3.5	1.4	1	1:1
Cathode 5	33.4	34.6	6.5	20.7	3.4	1.4	1	1:1

Table 3.2: EDS Energies of the α peaks of the most commonly observed elements [149].

(keV)	C	N	O	Al	Cr	Co	Ni	Ta	W
K α	0.277	0.392	0.523	1.486	5.414	6.929	7.477	57.450	59.305
L α	-	-	-	-	0.573	0.776	0.851	8.145	8.396
M α	-	-	-	-	-	-	-	1.709	1.774

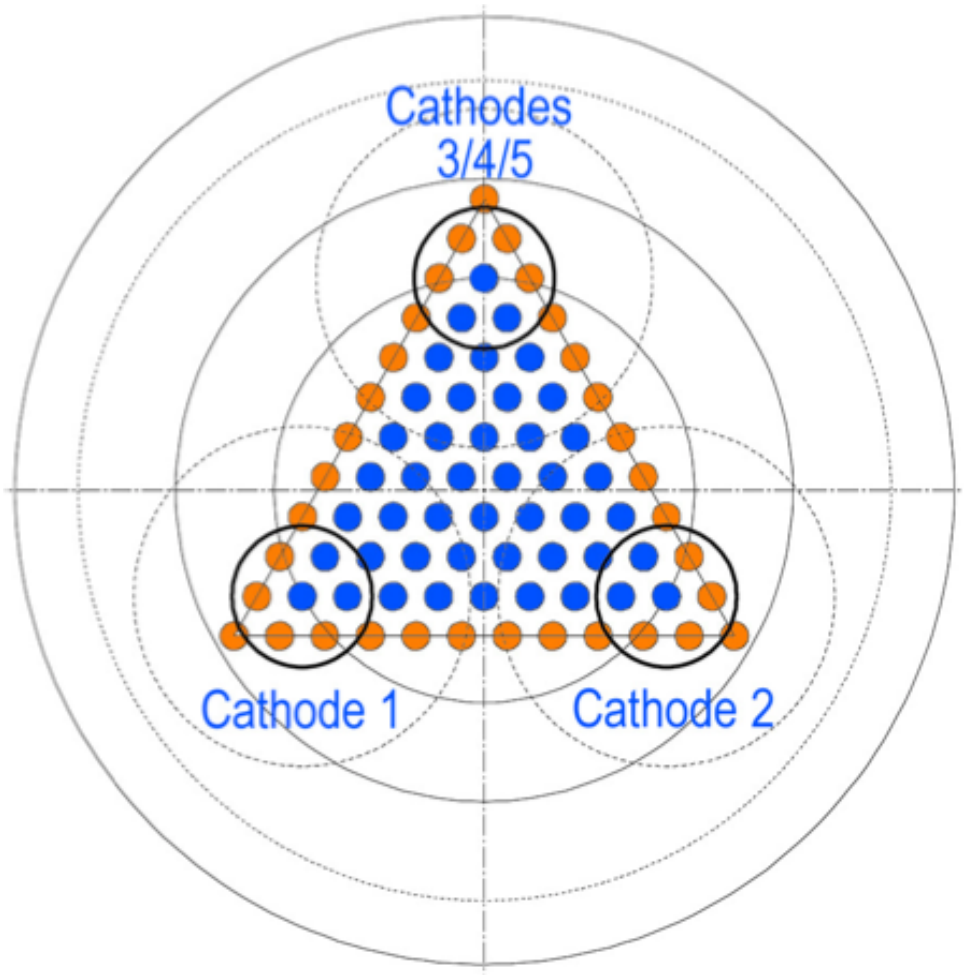

Figure 3.1: Arrangement of the substrate buttons during combinatorial deposition relative to the source cathodes.

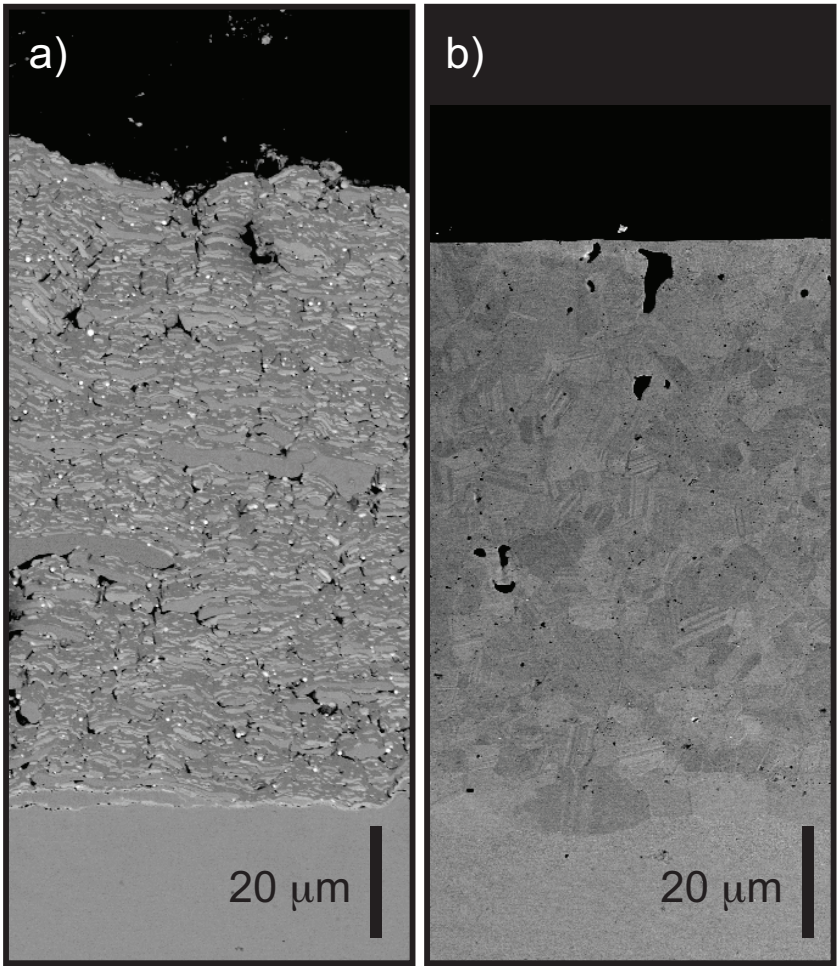

Figure 3.2: Backscattered electron micrographs of the IPD combinatorial coatings in the as-deposited state (a), and after solution heat treatment and surface polish (b). The coatings prior to oxidation (b) are thus homogenized, dense, and have a 0.05 μm surface finish, leaving ~100 μm of coating material for experimentation, which will contain the entire oxidation region [150].

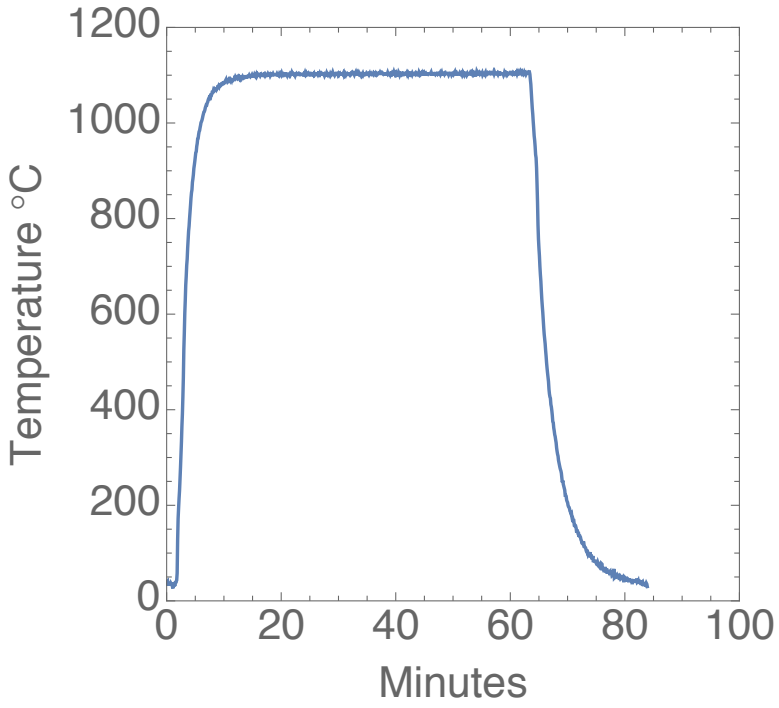

Figure 3.3: Example temperature profile of one cycle during cyclic thermal exposure.

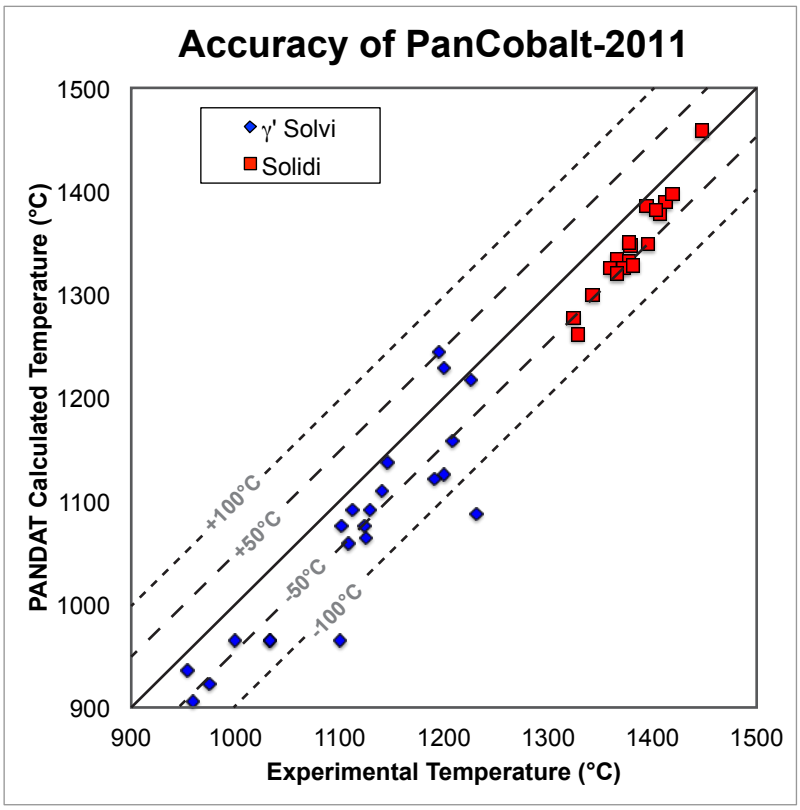

Figure 3.4: Solidi and γ' solvi in senary Co-Ni-W-Al-Cr-Ta alloys measured experimentally by DTA, compared with PanCo-2011 thermodynamic predictions. The database generally appears to under-predict both values by ~50°C.

4 Preliminary Studies of Co-γ/γ' Alloys

Prior to the extensive combinatorial study discussed in Chapter 6, three developmental Co-base γ/γ' superalloys were cast by collaborators at GE Global Research to explore the feasibility of achieving desirable mechanical properties with reasonably adequate oxidation resistance. These alloys were designed using the more 'traditional' route of outlining desirable composition regions based on prior experimental evidence, and generating a limited series of materials for testing. While such a strategy is often useful in industrial practice, it makes it difficult to develop a thorough scientific understanding of the phenomena underpinning the material behavior. It will be shown in this section that it is non-trivial to achieve protective alumina-forming behavior in novel Co-base γ/γ' alloys. As a consequence, the oxidation behavior of these alloys was not exhaustively characterized but used to motivate a more comprehensive investigation based on a combinatorial approach, to be discussed in chapters 5 and 6. Investigations of the developmental alloys also served to validate the use of the characterization and computational techniques proposed to analyze experimental Co-γ/γ' alloys, and to catalogue frequently observed oxide morphologies.

4.1 Experimental Details

Three developmental Co-base alloys with the compositions shown in Table 4.1 were cast using vacuum induction melting. These alloys will be referred to as B (for baseline), B+Y, and B+Y+Mo, where Y and Mo are alloying additions. It is of note, however, that there are substantial differences in the other alloying additions as well (e.g. Ni:Co ratio, Cr and Ta contents, etc.). Therefore, changes in behavior between alloys cannot be ascribed solely to the Y and/or Mo contents. The three alloys were received from GE Global Research in the

heat-treated condition, comprising solutioning at 1200°C for 4 h, followed by aging at 950°C for 50 h. Alloys were cut into buttons 15.5 mm diameter and 2.5 mm in height, ground to 800 grit finish and ultrasonically cleaned in acetone and isopropanol, each for 20 minutes. A button of Ni-base René N5 was similarly prepared for comparison with the Co alloys. All buttons were then oxidized in either filtered air or gettered Ar at 1100°C for a prescribed amount of time, as described in Chapter 3. Analysis was conducted using scanning electron microscopy (SEM), Photostimulated luminescence spectroscopy (PSLS), dilatometry, and optical imaging. Because the PanCo-2011 database used for the thermodynamic calculations included only six elements: Co, Ni, W, Al, Cr, and Ta, the compositions of the higher order alloys were modeled by normalizing them into the senary space keeping the atomic ratios constant.

4.2 Results

The microstructures of the developmental Co-base alloys were analyzed by backscatter SEM in the heat-treated state prior to oxidation, shown in Figure 4.1. The samples were found to be all polycrystalline, with γ grain sizes on the order of ~50-250 μm. The only minor phases detected beyond γ and γ' were carbides along the grain boundaries (Figure 4.1c). While all three developmental Co-base alloy exhibit a substantial fraction of the strengthening γ' phase, it is notable that the precipitates are somewhat rounded in all cases. It is also of interest that despite the stabilizing effects of Ni and Ta additions, all three Co-base alloys have fairly low γ' solvus temperatures (Table 4.2) also attributable to the significant amounts of destabilizing Cr added. For the purposes of verifying the accuracy of the PanCo-2011 database, the solvus temperatures of these alloys were calculated by normalizing alloy compositions into the Co-Ni-W-Al-Cr-Ta senary space covered by the

database. Comparing these calculations with experimental DTA values (Table 4.2), it is observed that the PanCo-2011 predictions lie within a reasonable margin of error, approximately ±50°C of the experimental values (Figure 3.4).

After oxidation for 1 h in air at 1100°C, the Co-base samples appeared to have formed a variety of different oxides, with clearly observed spallation in the case of the B and B+Y+Mo alloys (Figure 4.2). The oxide scales present are more easily compared in the cross-sectioned samples, shown in Figure 4.3. In this view, the layered oxide morphologies are clearly seen, with a stark difference between the Ni-base René N5 and the developmental Co-base alloys. While René N5 generates a thin, continuous layer of Al_2O_3 after 1 h in air at 1100°C, all three Co-base alloys instead form internal Al_2O_3 particles (feature 1), which are non-protective. The alumina IOZ is seen within a metal matrix in the Base and B+Y samples, while the B+Y+Mo had an IOZ within a metal matrix near the oxidation front, but a matrix consisting of W-rich oxide closer to the surface (feature 4). Spallation was often observed at the top of this layer in the B+Y+Mo sample. Above these IOZ regions were W/Ta-rich oxides and $(Co,Ni)(Cr,Al)_2O_4$ spinel. Alloy B forms these phases as distinct layers, while the B+Y and B+Y+Mo alloys form a mixed layer of W/Ta-rich oxide particles embedded within the spinel. Finally, the samples with the greater amounts of oxide, B+Y and B+Y+Mo contained an outer monoxide layer (Co,Ni)O. Viewed from the surface, this outer monoxide had a characteristic faceted morphology (Figure 4.4), which is easily identifiable in optical microscopy as well.

Oxidized buttons were then analyzed via PSLS to determine whether this technique is able to distinguish samples where α-Al_2O_3 forms a continuous layer vs. those that form an alumina IOZ. To establish a reference for comparison, a piece of polycrystalline α-Al_2O_3

was scanned in addition to the alumina scale-forming René N5 button (Figure 4.5). As expected, the α-Al_2O_3 exhibited only the characteristic corundum doublet at ~1.44 μm^{-1} [83]. René N5 exhibited both doublets from the stable α-Al_2O_3 and metastable θ-Al_2O_3 at ~1.44 and ~1.46 μm^{-1} respectively, as well as NiO peaks at ~1.43 and 1.47 μm^{-1} [151]. Conversely, the three Co-base alloys often exhibited the NiO peaks, but typically did not show the α-Al_2O_3 doublet (Figure 4.6a). The only case where the alumina doublet was visible on the Co-base alloys oxidized for 1 h in air was within the regions of the B+Y+Mo sample where the outer (Co,Ni)O had spalled off (darker regions in Figure 4.2). In an effort to identify the origin of oxide spallation, the CTE of the alloys was measured by dilatometry to assess the thermal-mismatch induced stresses between TGO alumina and the metal substrates (Figure 4.7). All three Co-base alloys were observed to have a significantly greater CTE than René N5, especially at the oxidation temperature 1100°C.

After it was evident that the Co-base alloys did not form a continuous alumina scale in air at 1100°C, samples were oxidized in gettered Ar (~10^{-10} ppm O_2) to minimize the tendency to form less stable oxides and promote the formation of α-Al_2O_3. After this low-P_{O2} oxidation, samples appeared grey upon optical inspection (Figure 4.2), with apparently more uniform scales. However, significant spallation was still observed on the Base alloy. Despite this, all compositions demonstrated primarily α-Al_2O_3 formation detectable on the surface of the sample (Figure 4.8) by strong doublets in the PSLS spectra (Figure 4.6b). The surface topology of all TGO alumina formed in the low-P_{O2} condition appeared web-like, similar to that observed by Tolpygo et al. due to preferential diffusion and growth along oxide grain boundaries [71].

Lastly, a series of short-time oxidation exposures were conducted on the Base alloy to provide insight into the sequence of oxide formation (Figure 4.9). In this series, small particles of internal Al_2O_3 nucleate rapidly within the metal matrix by 3 minutes, with a small amount of overlying spinel. As time progresses to 10 minutes, these particles coarsen, the overlying spinel layer grows, and in between the two a layer of W/Ta-rich oxide forms. As the system progresses to 1 h, the IOZ particles continue to grow and coarsen, while the overlying layers grow in thickness.

4.3 Discussion

Since one of the primary purposes of these developmental alloys was to assess the feasibility of oxidation resistance in Co-base γ/γ' alloys, it is of interest to understand the marked differences in spallation behavior among the different samples. Notably, extensive spallation is observed in the Base alloy leading to many areas of the metal substrate being exposed both after the 1 h exposure in air and the exposure to low P_{O2} (Figure 4.2). One may hypothesize that oxide scales may have formed and subsequently spalled off above those shown in Figure 4.3(b). The spallation is likely driven by the CTE mismatch between the substrate and the TGO layers and the ensuing thermal stress and energy release rate (ERR) in the scale, which increase with the oxide thickness. While the oxide scale in the Co-base alloys after exposure to air is a complex system of multiple phases, one of the primary constituents is spinel, which also has a significantly lower CTE than the base alloys, but not as low as alumina (Figure 4.7). Therefore, it is inferred that the reason for the more abundant spallation in the developmental Co-alloys than in René N5 is that the scale formed is much thicker in the former (Figure 4.3), even though the CTE mismatch is higher in the latter (Figure 4.7). Reactive element additions are known to increase TGO adhesion in Ni

and Fe alloys that form alumina scales, thus requiring a greater ERR to drive spallation. The same effect is present in these Co alloys, as the B alloy spalls much more readily than the related alloys with Y additions. While the B+Y+Mo appears to spall more readily than the B+Y sample notwithstanding the same Y content, the scale on the former is considerably thicker as shown in Figure 4.3, leading to a greater ERR. In the samples oxidized for 9 h in a low P_{O2} environment, the alumina scale formed should be much thinner, and as such none of the samples with Y spall (Figure 4.2). RE additions will later be applied to address spallation on Co-base alloys in Chapter 7.

The PSLS measurements suggest the viability of using this technique to ascertain the presence of α-Al_2O_3 in a scale, a strategy that will be explored more extensively in Chapter 5. The polycrystalline α-Al_2O_3 piece, René N5 oxidized for 1 h in air (Figure 4.5), and three developmental alloys oxidized for in low P_{O2} all exhibited a clear doublet at ~1.44 μm^{-1} indicative of α-Al_2O_3 (Figure 4.6). René N5 also exhibited a doublet for the metastable θ-Al_2O_3 and peaks for the NiO, though NiO was not readily observed on the sample surface. In contrast, α-Al_2O_3 was not detected in the Co-base alloys oxidized for 1 h in air, which is consistent with the observation that alumina is present only in the IOZ as isolated particles embedded in metal that is opaque to the probing laser (Figure 4.3). One exception is the B+Y+Mo sample, where the α-Al_2O_3 signal was occasionally detected. This is explained by the fact that the IOZ particles are partially embedded in oxide, above which spallation occurs (Figure 4.3). Such spallation can expose the embedded alumina particles to detection from the surface, and this is confirmed by the fact that the PSLS spectra where α-Al_2O_3 was detected were consistently arising from spalled areas of the button. One can hypothesize

that the detection of alumina by PSLS may depend on the translucency of the oxides surrounding or overlying it, as further elaborated in Chapter 5.

The oxidation studies on the developmental alloys reveal that the formed Al_2O_3 morphology is highly important; the discontinuous IOZ alumina is clearly non-protective, allowing the formation and continued growth of the undesirable overlying oxides. In contrast, the René N5 sample is able to form a thin, continuous Al_2O_3 scale that precludes the formations of similarly thick, undesirable oxides. In the context of Wagner's model of internal oxidation [42,62,152], it is of interest to measure the phase fraction of the alumina observed within the IOZ, as this should be below the critical f_v^* value required to induce the transition to a continuous scale (as described in Chapter 2). The approximate phase fractions of the IOZ at various depths were assessed using ImageJ [153] segmentation, shown in Figure 4.10. The following notable observations emerge from this assessment. First, the traditional approximation of $f_v^* \approx 0.3$ [154] is obviously inapplicable in the current materials, as many locations within the various IOZs exceed this amount without transitioning to continuous scales. This discrepancy is likely attributable to factors in the present alloys not explicitly included in the classical Wagner model, notably the well-documented enhanced diffusion of oxygen along alumina-metal interfaces [155,156].

It is useful in the context of the above discussion to calculate the approximate volume fraction of alumina expected if all of the Al present in the alloy were to oxidize into Al_2O_3. While the lattice parameters for the preliminary alloys were not measured, an approximate value was taken to be $a_{\gamma'} = 0.359$ nm based off the similar Co-30Ni-10Al-7.5W at.% alloy investigated by Shinagawa et al [19]. Using this value to calculate the Pilling-Bedworth Ratio (PBR) and subsequently the vol.% of alumina expected after oxidation ([157]):

$$(0.359\ nm)^3 * \frac{2}{4} * N_A = 13.93\ \frac{cm^3}{2mol\ Al} \quad (4.1)$$

$$\text{PBR}_{\gamma' \rightarrow \alpha-\text{alumina}} = 25.59\ \frac{cm^3}{1mol\ \alpha-Al_2O_3} \Big/ \ 13.93\ \frac{cm^3}{2mol\ Al} = 1.83 \quad (4.2)$$

$$1.83 * 8.6\ at.\%\ Al\ /\ (1.83 * 8.6\ at.\%\ Al + 91.4\ at.\%\ Metal) \approx 15\ vol.\% \quad (4.3)$$

The calculations are conducted as follows: the volume of one alloy unit cell is determined from equation (4.1). There are 4 atoms per unit cell, and 2 are desired (two Al atoms to form one Al_2O_3). The volume of 1 mole α-Al_2O_3 is divided by the volume of the constituent 2 moles of Al in the alloy, to arrive at the $PBR_{\gamma' \rightarrow \alpha\text{-alumina}}$ using equation (4.2). This PBR is then applied to the concentration of Al in the alloy to find the volume fraction of alumina after oxidation using equation (4.3). This 15 vol.% does not change by more than ~1 percentage point regardless of whether the lattice parameter for γ metal is used instead of that for γ', nor if the molar volumes of θ- or γ-Al_2O_3 [52] are used instead of α. The calculations using such different parameters are considered in Table 4.3 and Table 4.4, demonstrating that the phase fraction of Al_2O_3 expected does not appreciably change, yet is much lower than the experimentally observed values. Compared to these predicted values, it is seen that all of the regions within the IOZ of all Co samples exhibit an alumina phase fraction greater than 15 vol.%, implying that there is substantial outward diffusion of Al solute from the bulk to the IOF during oxidation. This is a reasonable conclusion since the content of Al in the bulk alloy is significant, likely leading to an Al depletion zone in the alloy. Appreciable solute diffusion from the alloy bulk leading to an increase in IOZ phase fraction has also been reported by other authors [155,158].

Overall, many of the oxide features observed will also be seen in later sections, and it will be important to understand the relevant processes of formation in order to achieve more

desirable oxidation behavior. However, the large number of components and variety of oxide features in the present samples make it difficult to definitively outline such mechanisms of formation without substantial and in-depth analysis. Indeed, as shown by the calculations in this chapter, the oxidation behavior is not adequately described in a quantitative manner by current models for internal oxidation. Therefore, a more systematic combinatorial study was pursued, presented in Chapter 6.

4.4 Synopsis

The studies presented in this chapter act as a prelude to the more in-depth analyses conducted in subsequent chapters. Investigating these three preliminary Co-base alloys in comparison with Ni-base René N5 suggests that achieving alumina-forming behavior simultaneously with a high γ' solvus temperature is non-trivial for this new Co system. As such, the primary focus going forwards will be to identify regions of compositions space allowing reasonable alumina scale formation, and subsequently look within that space to identify samples also achieving a high γ' solvus and desirable mechanical properties. To do so will require a more fundamental understanding of how Co alloy composition affects oxidation behavior. While the three preliminary Co alloys begin to show the extent to which alloy composition can change TGO formation, the oxides seen are too complicated and there are too many variables between test alloys to gain clear knowledge of the impacts of individual elements. As such, subsequent work should vary alloy composition much more systematically.

4.5 Tables and Figures

Table 4.1: Compositions of the preliminary alloys in atomic %.

Alloy	Co	Ni	Al	W	Cr	Ta	Mo	C	B	Y
Base	43.61	27.41	8.82	5.60	12.37	1.88	-	0.27	0.03	-
B+Y	42.84	30.08	8.64	5.44	8.97	3.68	-	0.28	0.03	0.04
B+Y+Mo	42.37	32.00	8.55	5.56	7.60	2.55	1.03	0.27	0.03	0.04

Table 4.2: Experimentally measured γ' solvi (DTA) vs. those calculated by the PanCo-2011 database for the three Co-base alloys.

	Base	B+Y	B+Y+Mo
DTA γ' Solvus (°C)	1035	1118	1090
PanCo-2011 (°C)	1069	1078	1069

Table 4.3: Pilling Bedworth Ratio calculations for the formation of various Al_2O_3 polymorphs from γ and γ' alloy phases [19,52]

PBR	α-Al_2O_3 (25.59 cm^3/mol)	θ-Al_2O_3 (28.21 cm^3/mol)	γ-Al_2O_3 (27.9 cm^3/mol)
γ (A1) (a = 0.3587 nm)	1.84	2.03	2.01
γ' ($L1_2$) (a = 0.3576 nm)	1.86	2.05	2.03

Table 4.4: Calculations of the expected Al_2O_3 phase fraction, assuming no Al flux, using PBR values from Table 4.3, in comparison with experimentally measured phase fractions (Figure 4.10)

Alloy	Phase	α-Al_2O_3	θ-Al_2O_3	γ-Al_2O_3	Ave. Al_2O_3 Observed
Base (Al = 8.82 at.%)	γ (A1)	15%	16%	16%	28%
	γ' ($L1_2$)	15%	17%	16%	
B + Y (Al = 8.64 at.%)	γ (A1)	15%	16%	16%	28%
	γ' ($L1_2$)	15%	16%	16%	
B + Y + Mo (Al = 8.55 at.%)	γ (A1)	15%	16%	16%	30%
	γ' ($L1_2$)	15%	16%	16%	

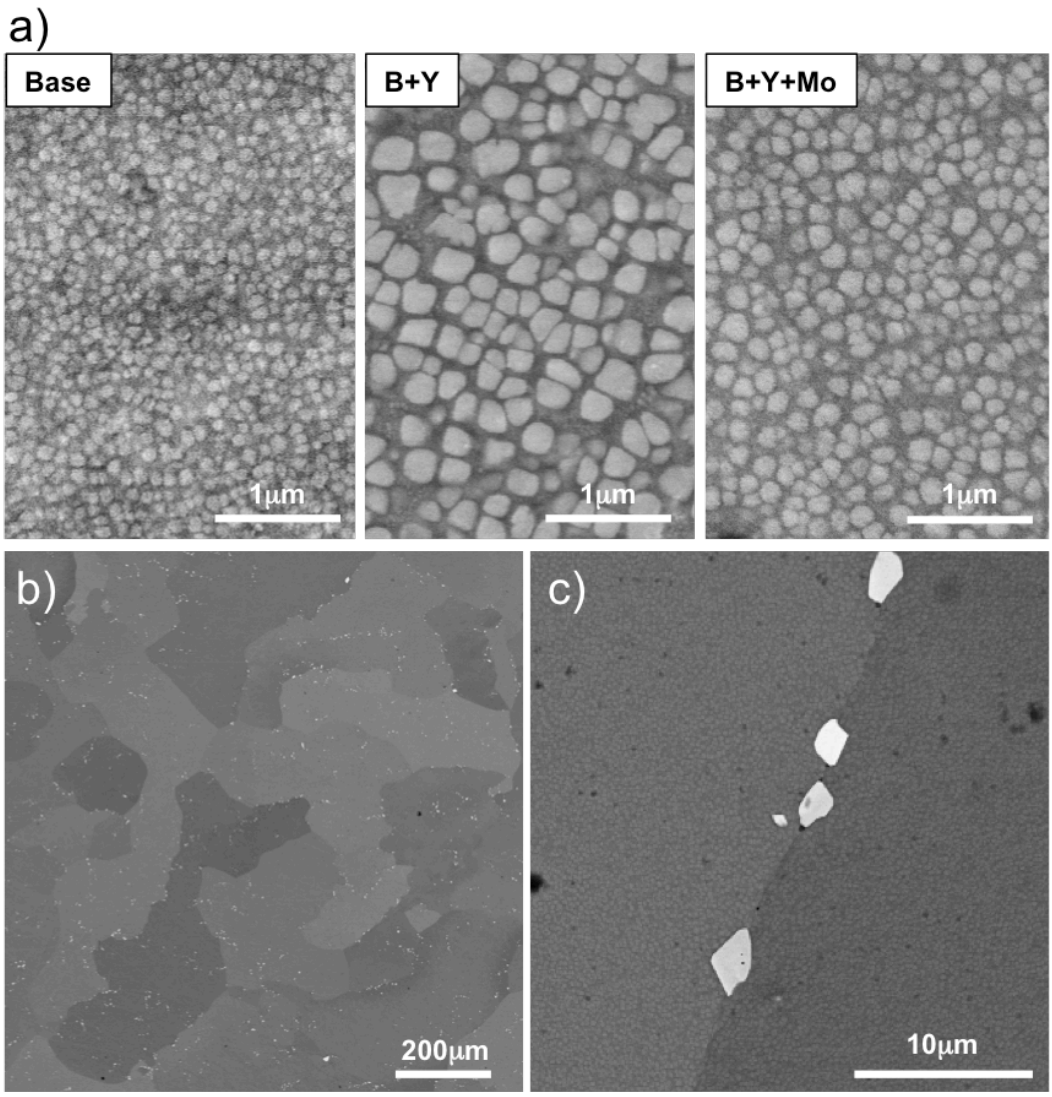

Figure 4.1: SEM BSE micrographs of the preliminary cast alloys after solution and ageing heat treatments [150]. (a) the γ/γ' microstructure is clearly seen in all alloys, albeit somewhat rounded (b) all cast alloys were polycrystalline with ~50-250 μm grains, and (c) small phase fraction of carbides primarily along grain boundaries.

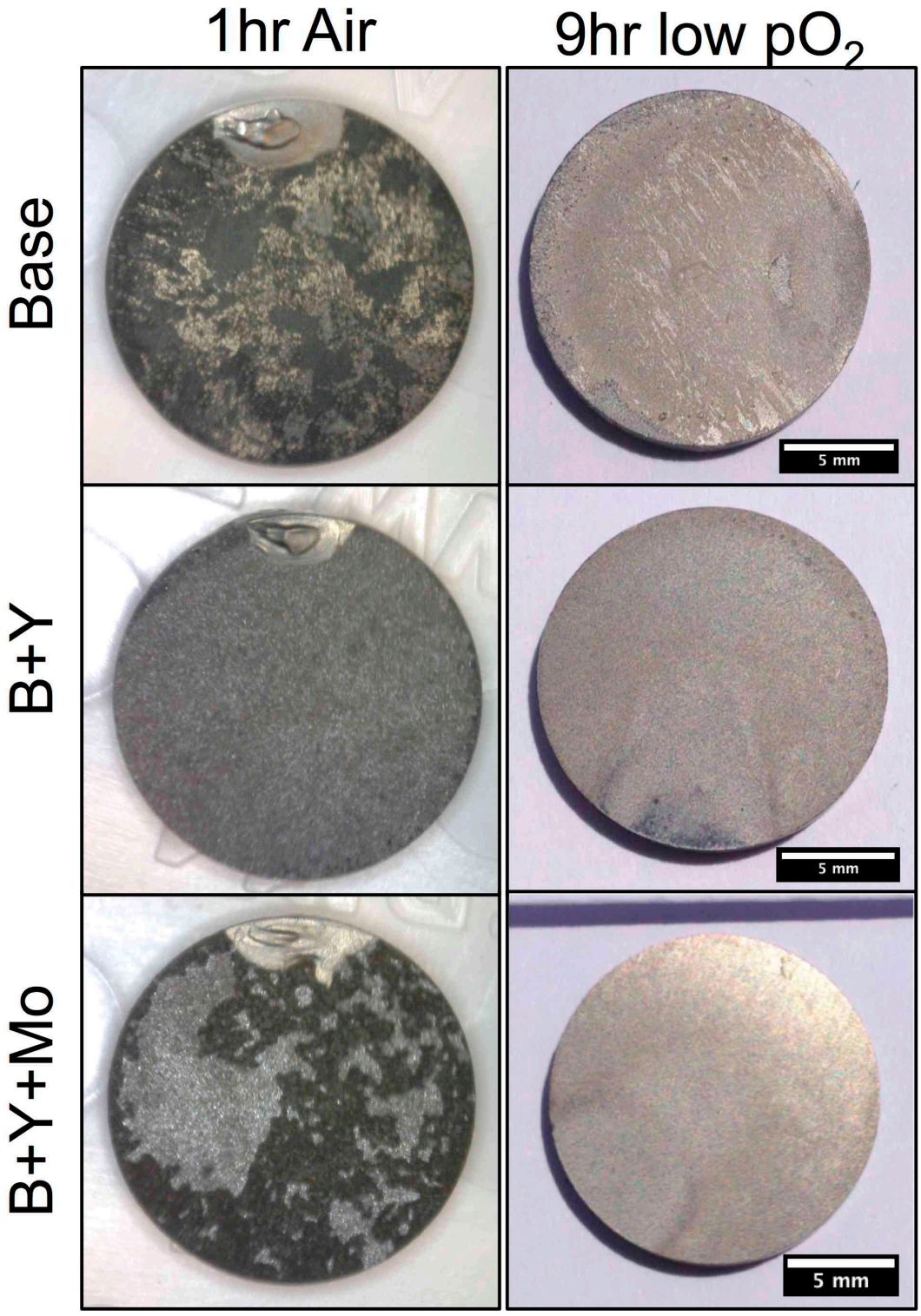

Figure 4.2: Optical macro images of the preliminary Co alloy buttons after oxidation under different conditions at 1100°C. Oxide spallation is most significant on the Base alloy, and least on the B+Y alloy.

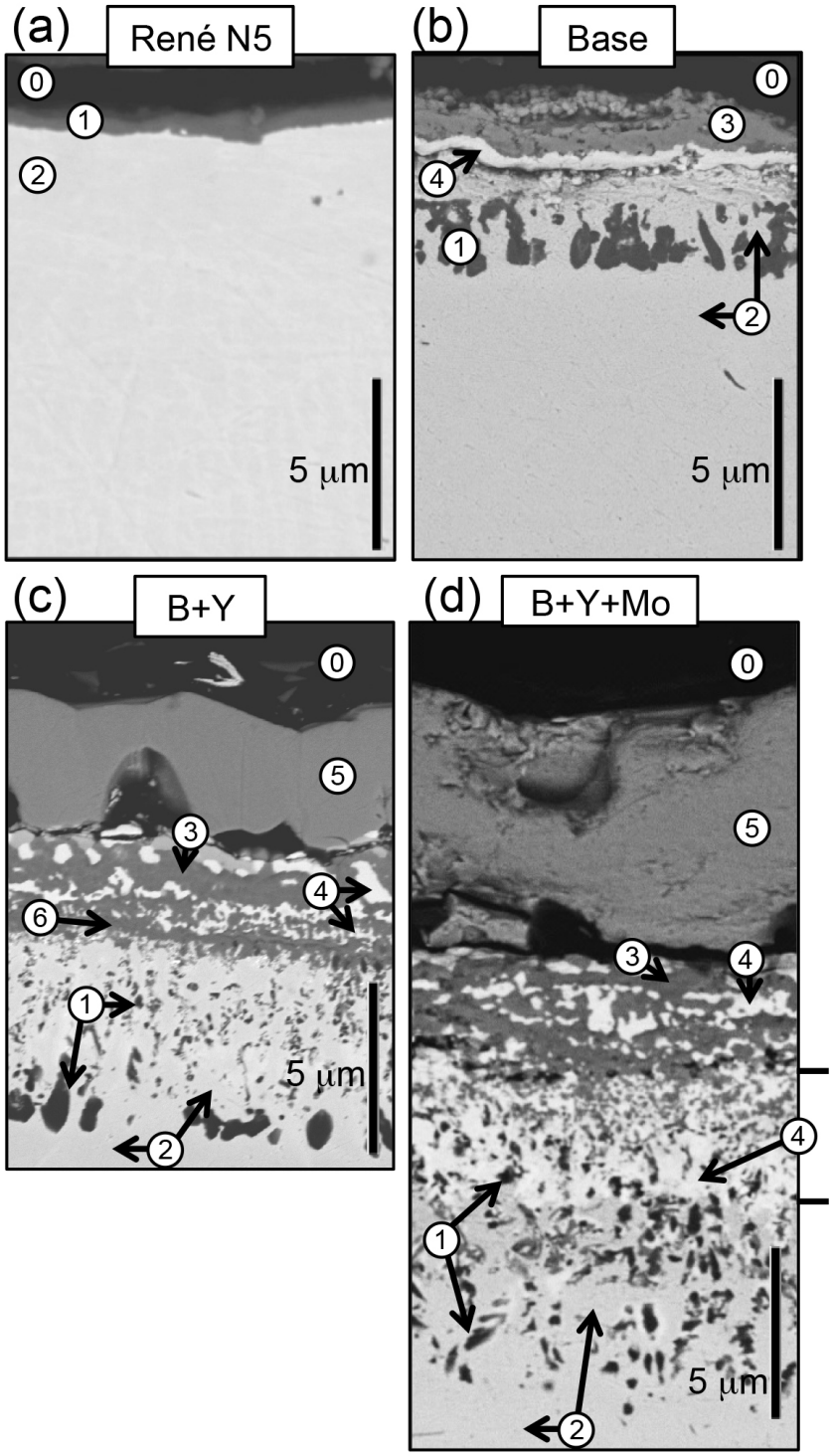

Figure 4.3: Backscattered electron images of cross-sections of the TGO on (a) Ni-base René N5 and (b-d) the three preliminary Co-base alloys after 1 h air 1100°C exposure [150]. Features are labeled according to EDS analysis: (0) mounting epoxy, (1) Al_2O_3, (2) alloy, (3) $(Co,Ni)(Cr,Al)_2O_4$ spinel, (4) W/Ta-rich oxide, (5) (Co,Ni)O, (6) Cr_2O_3. Copyright 2016 by The Minerals, Metals & Materials Society, used with permission.

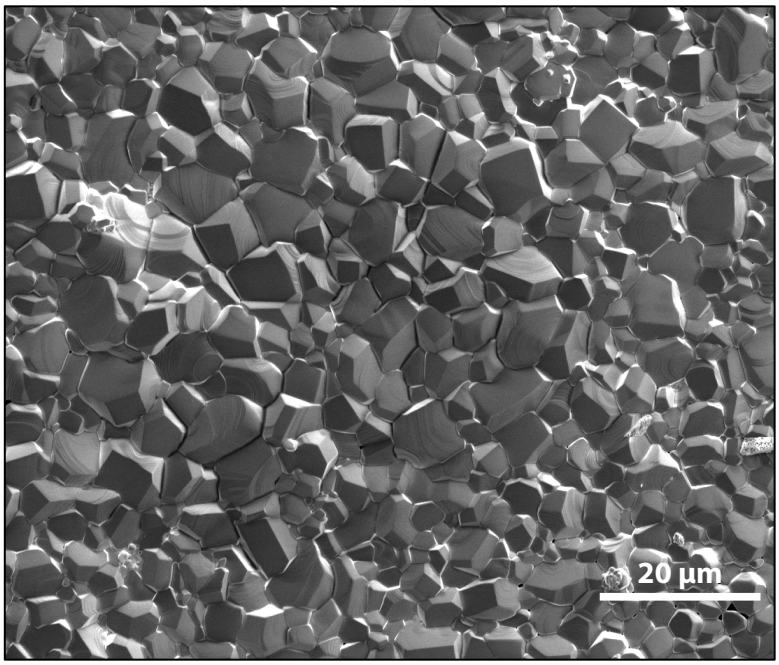

Figure 4.4: Secondary electron micrograph of the characteristic faceted morphology of outer (Co,Ni)O oxide frequently observed on the surface of oxidized Co-alloys. The monoxide in this figure is from the B+Y alloy after 1 h air 1100°C (Figure 4.3 feature 5).

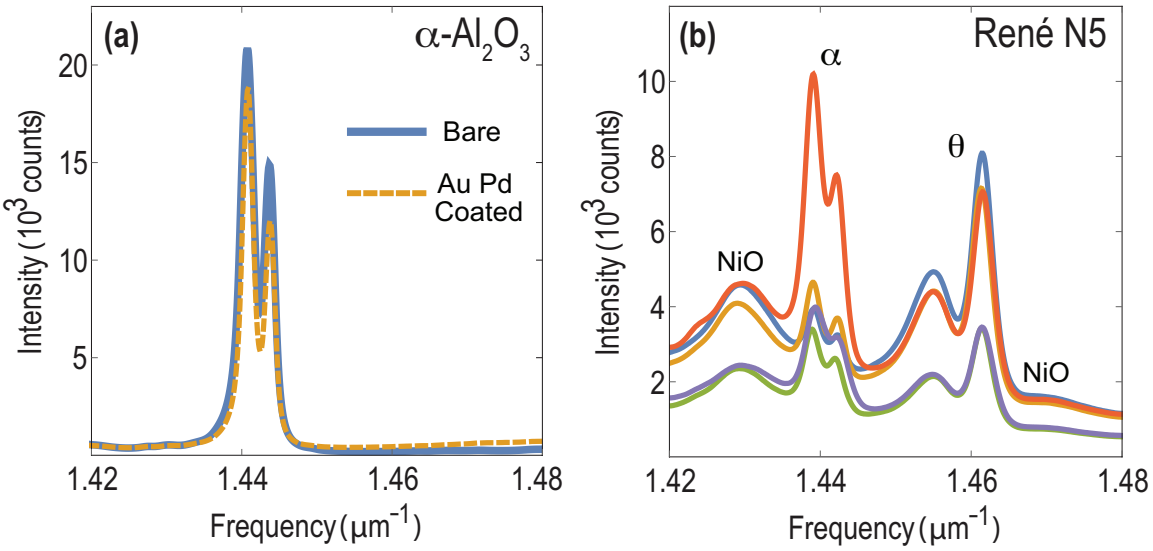

Figure 4.5: PSLS measurements of (a) a polycrystalline α-Al_2O_3 plate, and (b) Ni-base commercial alloy René N5 after 1 h air 1100°C [159].

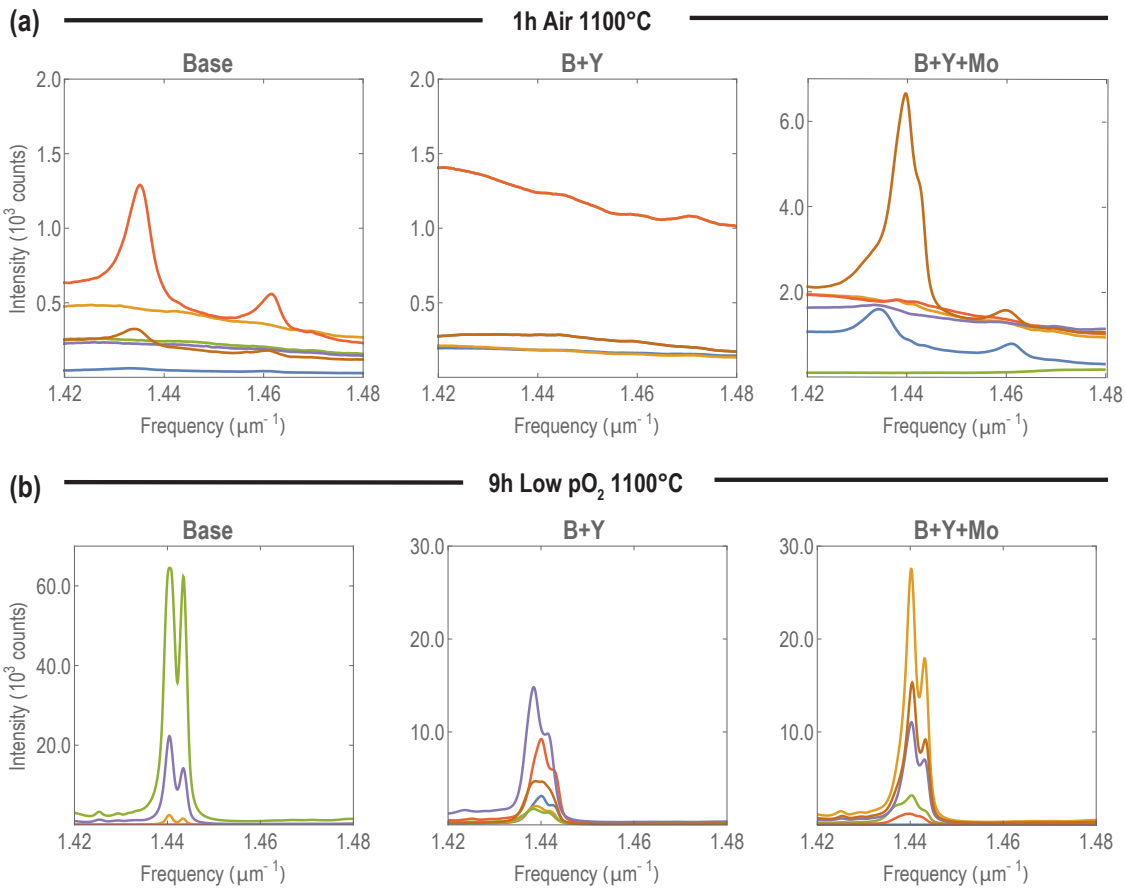

Figure 4.6: PSLS measurements of the preliminary Co alloys after (a) 1 h air 1100°C exposure and (b) low pO_2 exposure, often displaying the α-Al_2O_3 doublet at ~1.44 μm^{-1}.

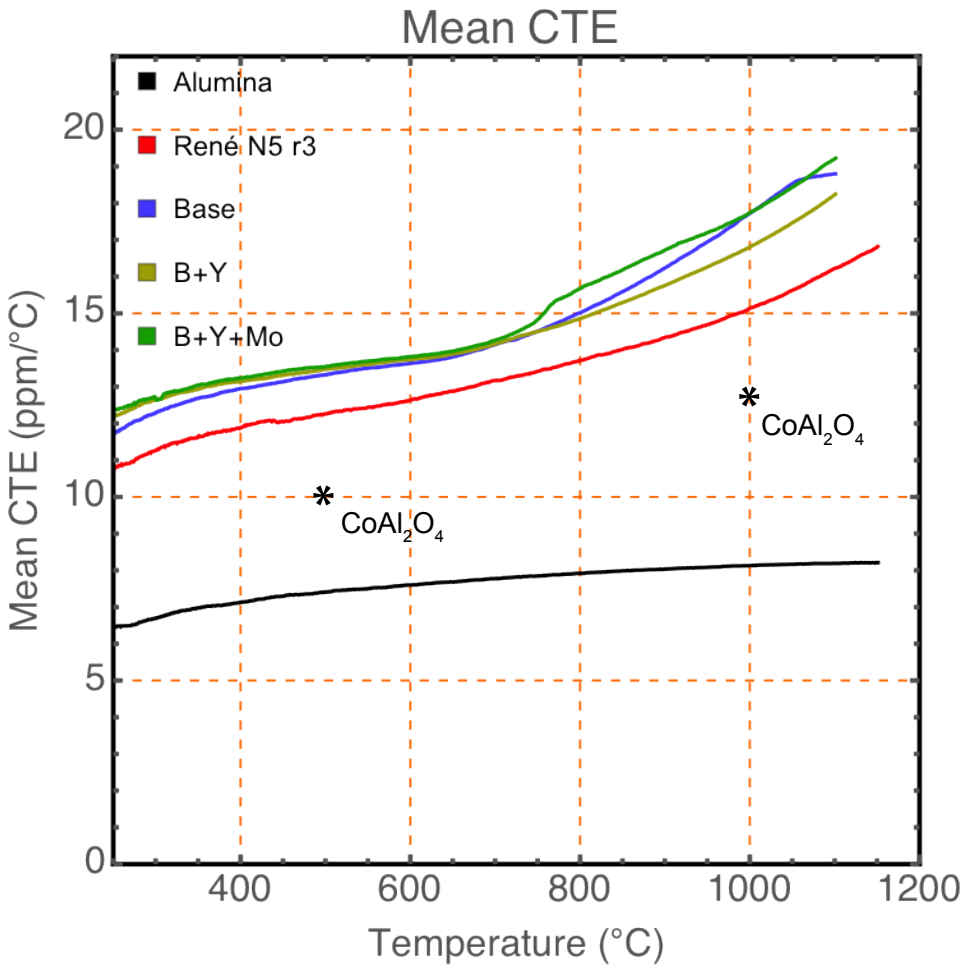

Figure 4.7: Mean CTE as measured by dilatometry of the three preliminary Co-base alloys in comparison with Ni-base René N5 and polycrystalline α-Al_2O_3. Alumina was used as the calibration material, and is also the desired TGO to be in contact with the underlying metal substrate. It is of note that the three Co-base alloys only generated α-Al_2O_3 under low P_{O2} conditions. The mean CTE of $CoAl_2O_4$ is also marked, as reported by [160].

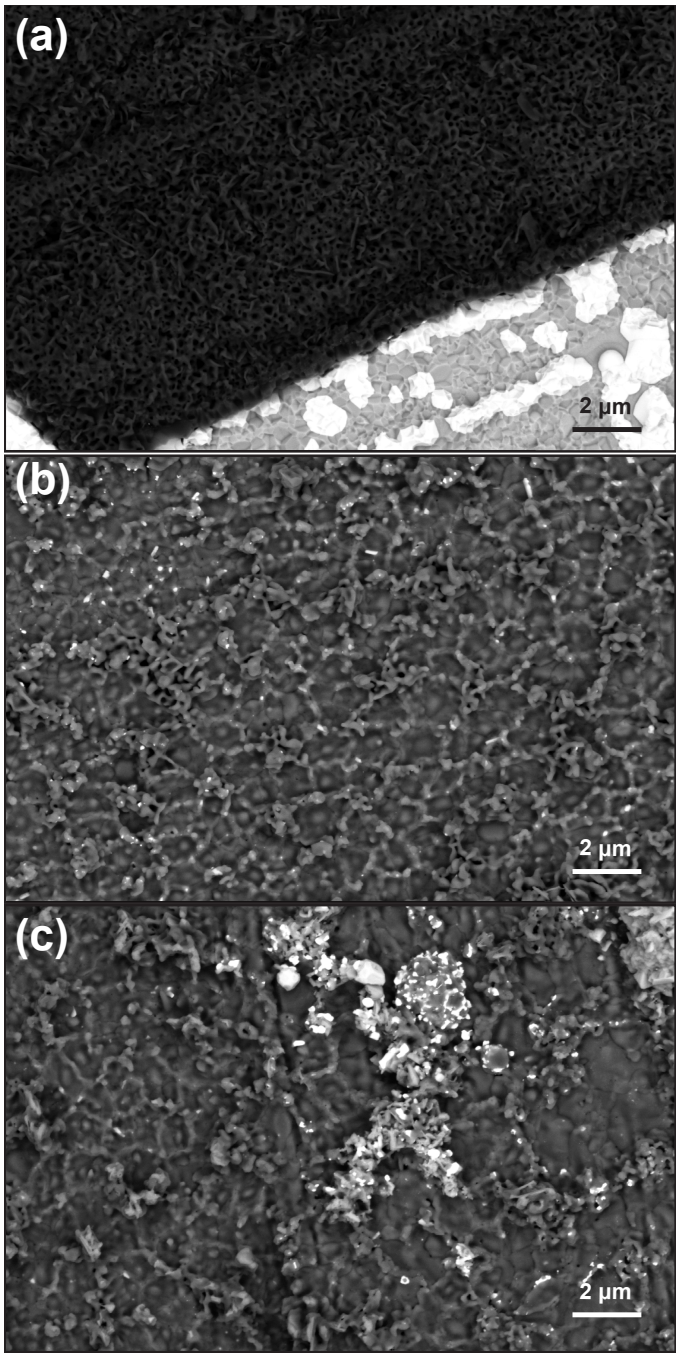

Figure 4.8: Backscatter SEM micrographs of the surfaces of the (a) Base, (b) B + Y, and (c) B + Y + Mo alloys after 1100°C low P_{O2} exposure. All samples consisted predominantly of Al_2O_3 (web-like dark grey), with the exception of the Base alloy which had little alumina scale left (dark grey/black) on top of the alloy surface exposed by spalls (white and lighter grey).

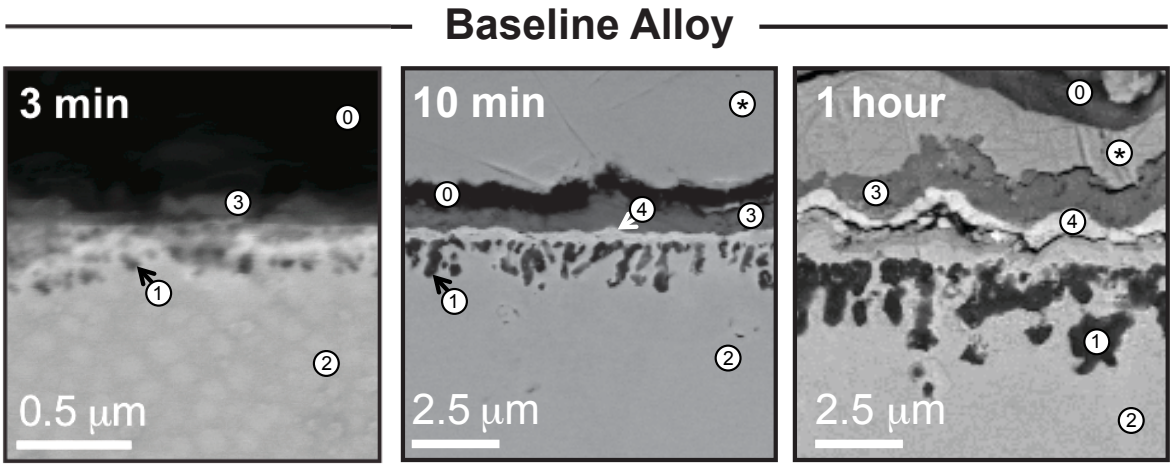

Figure 4.9: Backscattered electron images of the baseline alloy in cross-section after exposure to air at 1100°C for various times [150]. Features are labeled according to EDS analysis: (*) Ni plating, (0) mounting epoxy, (1) Al_2O_3 particles observed to initially nucleate internally within the alloy matrix by 3 minutes, (2) the alloy, (3) non-protective Co-containing oxide scale formed by 3 minutes, (4) W/Ta-rich oxide formed between 3 and 10 minutes.

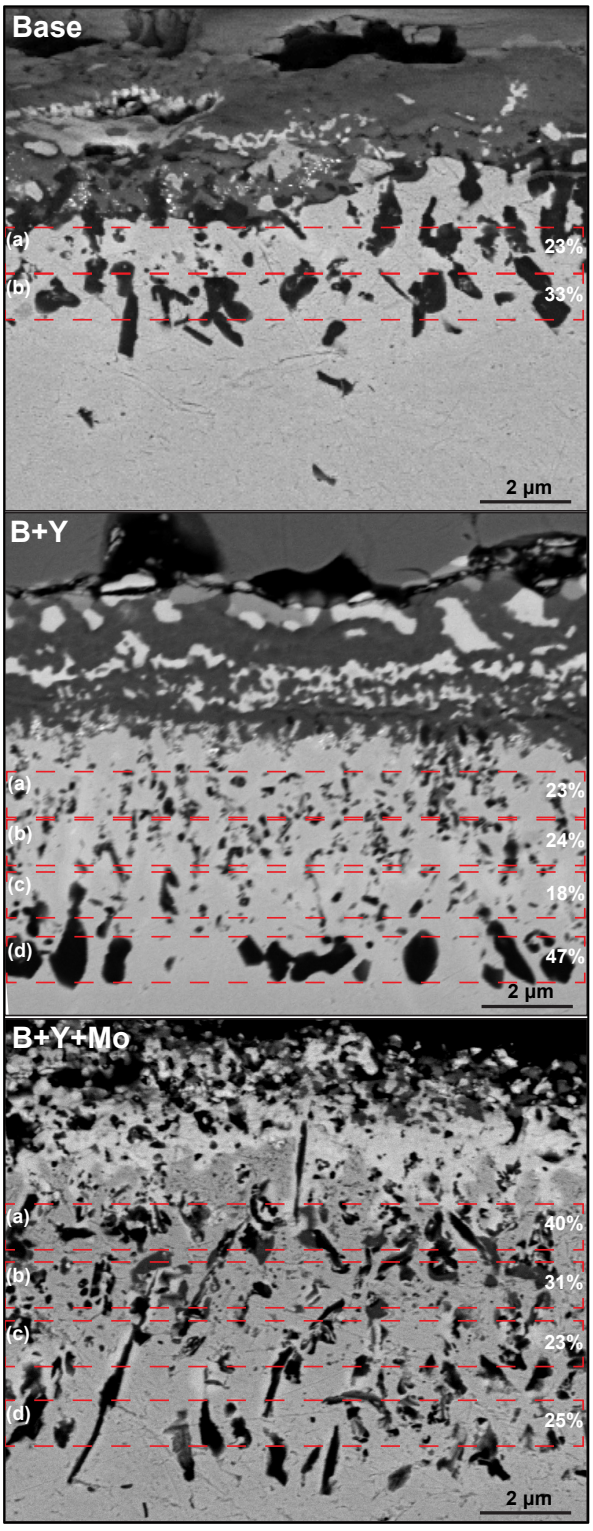

Figure 4.10: ImageJ analysis of the alumina (black) phase fractions at different depths within the IOZs of the three Co-base alloys after 1 h air 1100°C.

5 Validation of PSLS as Screening Methodology for Alumina Formation

The need for a combinatorial approach to explore systematically the oxidation behavior of senary Co-based γ/γ' alloys to identify promising areas in composition space for design of improved alloys was established in the previous chapter and will be elaborated in Chapter 6. An effective combinatorial high-throughput exercise, however, requires a rapid screening approach to identify those samples that exhibit promising behavior in the performance target, in this case the ability to form a continuous alumina layer during short term (1 h) oxidation at 1100°C. Preliminary work on the developmental alloys suggested photo-stimulated luminescence spectroscopy (PSLS) can detect α-Al_2O_3 at the surface through its characteristic doublet in the spectrum. However, it is not clear what its capabilities are when alumina is covered with other oxides, especially if they are much thicker, and whether the alumina detected is continuous or not. These issues are examined in the present chapter to ascertain the capabilities of the technique and its potential use on the combinatorial oxidation study in Chapter 6.

The current chapter describes the PSLS response of 50 different Co-base alloys, René N5, and a few model systems of oxide layers deposited on bulk α-Al_2O_3. The 50 Co-base alloys herein are a subset of 234 total samples produced using a combinatorial ion plasma deposition (IPD) technique discussed in the next chapter. For the purposes of the present discussion, it is asserted that these Co alloys cover a relevant range of different compositions and thermally grown oxide (TGO) layers, as well as of different PSLS responses. It will be demonstrated that the PSLS approach is not only valid for identifying alloy compositions with promising oxidation behavior, but that this capability depends on overlying oxide thickness and composition.

5.1 Characteristic PSLS signals for phases of interest

As noted earlier, the presence of α-Al_2O_3 in the PSLS spectrum is characterized in the presence of the R-line doublet at 1.442 μm^{-1} and 1.445 μm^{-1}. In addition, there are characteristic PSLS signals for the metastable polymorphs of alumina, notably θ-Al_2O_3 with doublet peaks at approximately 1.458 μm^{-1} and 1.465 μm^{-1} [82,116]. γ-Al_2O_3 also exhibits a PSLS signal with a broad, indistinct hump at approximately 1.45 μm^{-1}, with greater intensities at lower wavenumbers (Figure 5.1) [83]. Finally, other oxide phases also generate distinct PSLS signals, notably those arising from the rock salt NiO phase. These peaks are due to vibrational interactions, and are thus present at set shifts from the incident light. A two-phonon peak is present at a shift of ~0.11 μm^{-1}, and a two-magnon peak is located at a shift of ~0.15 μm^{-1} [151]. These peaks for the Al_2O_3 polymorphs and NiO tend to dominate the PSLS spectra in many of the samples examined in this chapter. Since the primary purpose of PSLS screening was the identification of oxide phases present, the stress-states of the alumina was not considered here.

5.2 Experimental Details

Three libraries comprising 234 alloy samples across Co-Ni-W-Al-Cr-Ta composition space were generated using a high-throughput combinatorial synthesis technique based on ion-plasma deposition (IPD) [137], as described in Chapter 3. The details of these libraries are not critical for the present discussion but will be explored in depth in Chapter 6. Briefly, the specimens consisted of ~110 μm alloy layers deposited on 2.5 mm thick by 12.5 mm diameter substrates of approximate composition 79Co-9Al-7W-3Cr-2Ta (at.%). The generated alloys spanned approximate composition ranges 0.1-1.1 atomic ratio Ni:Co, 7-15 at.% Al, 2-10 at.% W, 1-9 at.% Cr, and ~3 at.% Ta. The surfaces of these buttons were

prepared using a vibratory polisher (VibroMet™) with 0.05 μm alumina suspension, and subsequently oxidized for 1h in air at 1100°C yielding a variety of oxide phases and microstructures. The compositions of the alloys discussed in this chapter are summarized in Table 5.1, and the compositions of all combinatorial buttons measured experimentally are listed in the Appendix. A button of commercial Ni-base alloy René N5 was also oxidized under the same conditions for comparison.

Oxidized samples were screened for the presence of α-Al_2O_3 using PSLS conducted on a LabRam Aramis spectrometer (Horiba Ltd., Kyoto, Japan) with a 50x long-range objective lens and a 3.3 mW, 633 nm laser with approximately 5 μm incident spot diameter. Two perpendicular lines of 12 measurements each, 1 mm apart and 9 s in duration, were taken across the oxidized surface of each combinatorial button. Each button was then characterized by what fraction of the 24 PSLS measurements, ϕ, exhibited the presence of the α-Al_2O_3 doublet. The relative intensity of the α-Al_2O_3 doublet was not ascribed particular significance, as long as the doublet was detectable, owing to the multiple factors that may influence the signal (notably the thickness and optical properties of the overlying oxides, as well as light scattering on grain boundaries, reflecting off surface facets of the surface oxide, etc.). Measurements taken on a polycrystalline stress-free α-Al_2O_3 wafer were used as a baseline. Reference PSLS measurements were also collected from oxides grown at 1100°C in air on commercially pure (>99%) Co, Ni, W, Cr, and Ta, as well as commercial $CoWO_4$ and $NiWO_4$ powders (Alfa Aesar, Tewksbury, MA).

Based on the results from the PSLS screening, a group of 50 oxidized samples were cross-sectioned and analyzed to establish relationships between luminescence signal and scale thickness. ImageJ software [153] was used to segment the oxide scale from BSE

micrographs of the samples in cross-section, and automatically calculate the average scale thickness from over 4000 measurements along ~2 mm of exposed sample length. While manually determining the segmentation values for gray-scale pixels is somewhat subjective, two separate segmentations of the same micrographs yielded reproducible thickness values, with changes on the order ~0.5 μm between segmentations. Such changes due to segmentation differences are especially minimal considering the typical standard deviation of oxide thicknesses within a single micrograph were on the order of ~1.5 – 4.5 μm.

To assess the translucency of various oxides to the optical signal, thin oxide films were created by electron-beam deposition of layers of metallic Co and/or Ni on alumina substrates, followed by oxidation at 1000°C or 1100°C, respectively. (A thin Au-Pd film was first deposited on the substrate to improve adhesion of the metallic layers.) An initial PSLS evaluation was then conducted on the surface of the samples to determine if the underlying α-Al_2O_3 was observable through the entirety of the Ni/Co oxide scale. Following this surface evaluation, the samples were embedded in epoxy and either cross-sectioned with a diamond wafering blade to evaluate the oxide layer thickness and morphology, or polished at a small angle tilt such that PSLS spectra could be acquired at various oxide thicknesses.

5.3 Results

5.3.1 Reference Oxides

Reference luminescence spectra from α-Al_2O_3 were shown in Figure 4.5. These include the bulk alumina surface, pristine or coated with a thin sputtered Au-Pd film, and from the TGO on René N5 after 1h in air at 1100°C. (These can be compared with the standard

spectra in Figure 5.1). The metal film did not seem to hinder the intensity of the signal, and the α-Al_2O_3 doublet is clearly evident on René N5, together with θ-Al_2O_3 and NiO peaks. Spectra of thermally grown oxides from single elements and tungstate powders are shown in Figure 5.2 to help identify any peaks that might interfere with the detection of the α-Al_2O_3 doublet. Among the oxides characterized, only NiO exhibited distinct peaks within the frequency range of interest, in agreement with literature reports [151]. Notably, the measurements taken from CoO does not appear to have any pronounced signal- and the measured spectrum is fairly flat. Both $CoWO_4$ and $NiWO_4$ were found to have no outstanding peaks as well. However, a plethora of other mixed oxides have the potential to be present as TGO on these senary alloys, and may produce PSLS signals not accounted for in this initial reference screening.

5.3.2 Combinatorial Samples

Figure 5.3 and Figure 5.4 show high and low magnification images of oxidized samples illustrating the range of behaviors observed in PSLS, from samples wherein all 24 measurements showed the α-Al_2O_3 doublet (ϕ=1) (Figure 5.3a'), to those wherein none had detectable α-Al_2O_3 (Figure 5.3c', Figure 5.4d'). In all cases the PSLS measurements were taken with the excitation beam normal to the surface of the scale. Figure 5.3 shows that the scales are multi-layer and generally much thicker than those measured on the René N5 specimen, i.e. $\gtrsim 1\mu m$.

Samples in which the α-Al_2O_3 doublet was detected in the majority of the 24 individual PSLS spots for each alloy tended to have thinner scales, which were consistently underlain by a continuous layer of alumina as illustrated in Figure 5.3(a). PSLS peaks for NiO were

generally not detected, in spite of the overlaying (Co,Ni)O layer, although θ-Al_2O_3 was sometimes observed (labeled in Figure 5.3a'). Furthermore, samples with a visible θ-Al_2O_3 signal also had a greater intensity of the spectrum at 1.42 μm^{-1} compared with that at 1.48 μm^{-1}. This is ascribed to the likely presence of some γ-Al_2O_3, which exhibits a broad peak at the lower wavenumbers [83].

Conversely, samples wherein few or none of the measurements showed α-Al_2O_3 ($\phi \rightarrow 0$) exhibited much thicker scales, often above 20 μm. Some of these samples were found to contain a continuous alumina layer, albeit under large amounts of other oxides. This group also included cases where alumina formed as internal particles instead of a continuous scale at the lowest portion of the oxidized region, such as Figure 5.3(c). A slowly rising, low-intensity signal was occasionally observed in some samples at high wavenumbers ~1.48 μm^{-1} (Figure 5.3b', c', and Figure 5.4a'), which could not be ascribed to any of the investigated oxide phases in Figure 5.2.

Samples with an intermediate percentage of PSLS measurements showing α-Al_2O_3 typically had microstructures similar to those of Figure 5.3(b). Transitions in the luminescence response, from samples with all measurements showing α-Al_2O_3 to those with no detectable α-Al_2O_3, were found to occur within a relatively narrow range of scale thickness (approximately 10 μm to 14 μm). Figure 5.4 illustrates these behaviors; all four scales appear very similar microstructurally, yet display PSLS responses exhibiting α-Al_2O_3 ranging from 0 to 21 out of 24 measurements ($0 \leq \phi \leq 0.875$). The microstructural features and PSLS responses for these four samples are summarized in Table 5.2. It is noted that the overlying monoxide layer thickness is approximately the same for all samples, as is the bulk

alloy Cr content. However, the extent of α-Al_2O_3 detection and intensity appears to increase with the Ni:Co ratio of the monoxide layer, which approximately tracks the concomitant increase in the same ratio of the bulk alloy.

The microstructural features observed across the different types of samples are also described in detail in Figure 5.3, where different layers are labeled with numbers. These microstructural features will also be further discussed in Chapter 6. (Co,Ni)O (B1, rock-salt) is present in most samples, and when present it is always the outermost (1) and frequently the thickest layer in the scale. A much thinner spinel layer (2) is typically observed below the monoxide, in some cases forming a mixed layer with other oxides. The spinel lies over a layer of W-rich oxide (3) identified as $(Co,Ni)WO_4$ based on SEM/EDS analyses and frequently incorporating Al-rich oxide particles. As the most stable oxide, Al_2O_3, is found at the bottom of the scale, either as a continuous layer (4) or as an internally oxidized zone (IOZ) within metal depleted of Al (5) and above the remaining bulk alloy (6). Such discrete alumina particles have been shown to also generate the α-Al_2O_3 signal in PSLS measurements on a sample with no continuous alumina when the IOZ is exposed to the laser, e.g. in a polished cross section [150,161].

Occasionally, pockets of IOZ are found undercut by a continuous Al_2O_3 layer, directly below the W-rich oxide; the oxide particles may be dispersed within either a Ni-enriched alloy matrix, or else within (Co, Ni)-rich oxide. For the purposes of determining oxide scale thickness, regions of undercut IOZ were included in the overall scale thickness regardless of the degree of oxidation of the matrix. The rationale is that oxidation would continue to rapidly consume material around the discrete oxide particles until that reaction front reaches

the continuous Al_2O_3 scale. The implication is that an IOZ undercut by Al_2O_3 is arguably a more desirable morphology than one wherein only the metal substrate is present below.

Average thickness data taken from cross-sections were combined with the PSLS measurements from the button surfaces and plotted in Figure 5.5. The abscissa is defined on the basis of an integer number of spectra showing the α-Al_2O_3 doublet, so there is no scatter in their data. However, the thickness measurements can vary over a wide range and thus exhibit significant dispersion. Nevertheless, it is clear that there is a trend of increasing probability of detection of α-Al_2O_3 by PSLS with concomitant reduction in scale thickness, which could be quantified by linear regression. The relationship is given by:

$$\delta = 19.1\ \mu m - (14.9\ \mu m)\ \phi \qquad (5.1)$$

wherein δ is the total oxide scale thickness in μm and ϕ is the fraction of PSLS measurements clearly showing at least one α-Al_2O_3 doublet, regardless of intensity. (The fit for the negative slope has a 95% CI of −15.6 to −14.4.) This relationship is more reliable for the higher values of ϕ and becomes less valid for low values, e.g. fewer than 5 positive readings, since the thickening of the scale may make it more difficult to detect underlying alumina even if it were present.

5.3.3 Tilt-Polish of Monoxide-on-Alumina

The oxide generated by the Ni layer deposited on α-Al_2O_3 comprised 20 μm of NiO atop ~2 μm of $NiAl_2O_4$, whereas that produced by the Co deposition included 40 μm of CoO atop ~2.5 μm of $CoAl_2O_4$, and the mixed monoxide generated by co-deposition of Ni and Co on α-Al_2O_3 comprised ~14 μm of (Co,Ni)O at a Ni:Co ratio of ~1.51 on top of ~1.5 μm of $(Co,Ni)Al_2O_4$ (Figure 5.6). Comparative PSLS measurements normal to the surface of these

oxides revealed very different responses, with the α-Al_2O_3 doublet faintly detected in the Ni and NiCo samples, but not at all in the Co one. To gain further insight and resolve whether the difference was due simply to the greater thickness of the CoO, the single-deposition samples were polished at a shallow tilt relative to the substrate plane. The mixed NiCo sample was not tilt polished due to issues maintaining adherence of the oxide layer. Luminescence response was then measured at different distances from the alumina substrate along the tilt polish, representing different oxide thicknesses, as depicted in Figure 5.7. Measurements were taken starting from the exposed α-Al_2O_3 substrate Figure 5.7(a,f) and progressively up the polished surface to assess the effect of thickness (and layer composition) on the magnitude of the luminescence signal.

It is noted that during tilt polishing, a thin section of NiO near the $NiAl_2O_4$ layer in Figure 5.7 appears to have spalled off, exposing the underlying spinel. This portion of the tilt was not included in the analysis. The α-Al_2O_3 doublet was observed on the exposed alumina substrate and was not appreciably attenuated by the $NiAl_2O_4$ scale, Figure 5.7(b). At a combined thickness of 6.9 μm of NiO + spinel, the doublet intensity was reduced by two orders of magnitude, but still clearly visible in (c). Moving to even greater scale thicknesses, the doublet remained through ~15.5 μm of Ni-containing oxides (d), and was still faintly visible through 21.7 μm (e). Furthermore, the characteristic NiO peaks became more distinct at greater scale thicknesses, as evident in Figure 5.7(d, e). In contrast, the Co-oxides displayed much greater absorptivity to the PSLS signal. α-Al_2O_3 was detectable on the exposed alumina (f), but the $CoAl_2O$ layer appeared to attenuate the doublet intensity by a factor of 2, as shown in Figure 5.7(g). Moving into regions with both CoO and spinel, the

doublet was greatly reduced in intensity (h, i), and completely occluded by ~3.6 μm Co-oxides (j).

5.4 Discussion

The use of PSLS for identification of different Al_2O_3 polymorphs in thin oxidation scales [83,116], and for measuring their state of stress [119] is well established in the literature. It has also been shown that PSLS and Raman can be used to screen the oxidation behavior of combinatorial libraries of NiAl based bond coats [136]. Advanced Ni-base superalloys are arguably marginal alumina formers compared with bond coats, but yield continuous surface scales that can be probed readily by PSLS, as in Figure 4.5(b). These scales may contain other oxides covering the α-Al_2O_3 [162] but it is possible to detect the latter since in most practical cases the overlayers are thin and suitably translucent [163]. At issue here is whether PSLS can be a viable screening technique for the presence of α-Al_2O_3 in combinatorial libraries of Co alloys when the alumina is covered by multilayer scales with complex composition and thickness ranging from a few to tens of micrometers, as illustrated in Figure 5.3.

5.4.1 Detectability of α-Al_2O_3 PSLS Signal

The cumulative evidence reveals PSLS is a reliable indicator of the presence of a continuous α-Al_2O_3 layer directly over the Co γ/γ' alloys for scales of order $\lesssim 5\mu m$ thick. These are generally multi-layer and typically more complex than those evolving in established Ni-base superalloys. Nevertheless, doublet intensities of similar or higher magnitude than those measured in the Ni alloys can be detected in the Co alloys in spite of the overlayers, as inferred from the comparison of Figure 4.5(b) and Figure 5.3(a'). It is

self-evident that in the thinner scales, the overlayers on these Co alloys are sufficiently translucent to the excitation beam (633 nm) and the luminescent signal (690 nm) to enable detection of the continuous alumina under them or discrete internal oxides embedded in them (Figure 5.8, paths a-e). Yet with thicker scales the overlaying oxides have limited translucency that changes with thickness and composition, as clearly inferred from Figure 5.7. Therefore, for the scales on the thicker end of the distribution in Figure 5.5, i.e. >20 μm, the absence of positive PSLS results may not necessarily negate the presence of alumina at the bottom because the optical signal may be absorbed beyond the level of detection. Nevertheless, one may argue that even if continuous alumina were to actually be present in these thicker oxide scales, this oxidation behavior of the alloys in the combinatorial library would not be considered desirable for oxide scale adhesion, validating the utility of PSLS for screening favorable oxidation behavior.

A large fraction of the examined compositions contain both continuous alumina and internal particles, and exhibit a wide range of PSLS responses in spite of their overall similar thickness, as illustrated in Figure 5.4. In these cases the differences cannot be attributed to the overall thickness, nor to the presence or absence of additional oxide layers. Instead, the results in Figure 5.7 suggest the primary difference leading to variability in the PSLS response is likely to arise from the composition of the outer (Co,Ni)O layer (Table 5.2). There are other potential differences between the scales in Figure 5.4, e.g. the relative population of IOZ pockets above the continuous alumina scale wherein the alumina particles are dispersed in a metal matrix, versus those embedded in oxide, especially if the latter is NiO rich. The inference is that the opacity of a significant metal layer would prevent any response from oxide particles within it, or from any underlying continuous alumina (Figure

5.8, paths f, g). Furthermore it is unclear how translucent the tungstate layer is (e.g. layer 3 in Figure 5.3), although its presence in scales showing substantial PSLS responses suggests it is not a dominant optical barrier.

Figure 5.7 suggests that Co-rich monoxide, and perhaps the associated spinel, are much more absorbing to the PSLS signal generated by underlying alumina than the Ni-rich layers. Note that the signal becomes weaker with greater amounts of overlying oxide until it is completely obscured by a total of ~3.6 μm of combined CoO + $CoAl_2O_4$, Figure 5.7(j), yet still remaining slightly visible through more than 20 μm of combined NiO + $NiAl_2O_4$, Figure 5.7(e). Moreover, a (Co,Ni)O solid solution layer produced by oxidation of a Co-Ni film on bulk α-Al_2O_3 (Figure 5.6), yields a diminished intensity for the alumina doublet than the NiO layer of similar thickness. The hypothesis is consistent with the PSLS response of the scales in Figure 5.4, wherein the PSLS response varies consistently with the Ni:Co ratio of the monoxide layer, as shown in Table I. It is also known that the Cr content of the alloy can modify the luminescence response of α-Al_2O_3 [33], but the Cr content of the alloys in this library was very similar. Observations of the present dataset show that the occurrence of more Ni-rich oxides was generally associated with thinner scales, again supporting the suitability of PSLS as a screening technique for Co-based γ-γ' alloys.

The rationale for the differences in opacity of CoO over NiO to the relevant optical wavelengths is not clear. Experimental values of the absorption coefficients for NiO [34] at the 633 nm and 690 nm are ~500 cm^{-1} and ~700 cm^{-1}, respectively, while those for CoO [35] are ~2000 cm^{-1} and ~1000 cm^{-1}, respectively (Figure 5.9). These differences may qualitatively account for the effect of Co on attenuating the PSLS signal. Conversely, the oxide band gaps are reported as 3.5eV for NiO and 2.6eV for CoO [36], corresponding to

wavelengths of 354 nm and 476 nm. Since these are smaller wavelengths than those involved in the PSLS probing, i.e. 633-690 nm, the band gap alone does not account for the observed difference in opacity between the two oxides. The inference is that the oxide absorptivity is more relevant to its effects on the PSLS signal than the band gap energy.

Overall, the compositional regions forming α-Al_2O_3 scale with thinner amounts of overlying oxides in combinatorial libraries of Co alloys may be identified by the described PSLS screening technique.

5.4.2 PSLS Signals Beyond Al_2O_3

While not integral to the use of PSLS as a screening technique, some comments may be made regarding the observed PSLS peaks other than the α-Al_2O_3. In the current experiments using a 633 nm (~1.58 μm^{-1}) excitation laser, the NiO vibrational peaks will be expected at approximately 1.43 μm^{-1} and 1.47 μm^{-1}, and indeed these are seen on the NiO TGO grown on Ni metal (Figure 5.2), Ni-base René N5 (Figure 4.5), as well as the NiO deposited on bulk α-Al_2O_3 (Figure 5.7). However, this signal is not observed on the TGO grown on any of the combinatorial samples, which exhibit non-trivial amounts of mixed (Co,Ni)O (Figure 5.3, Figure 5.4). This demonstrates that these two NiO vibrational peaks are not merely weakened, but entirely degraded by the solution of Co in the rock-salt monoxide phase, at least down to a Ni:Co atomic ratio of ~0.3, as in Table 5.2(d). Interestingly, while TGO CoO grown on Co metal does not appear to display any definite peaks in this experimental setup (Figure 5.2), additional peaks do arise in systems with other elements. From the tilt polish of CoO and $CoAl_2O_4$ on top of bulk Al_2O_3 (Figure 5.7), a broad peak at higher frequencies (~1.48 μm^{-1}) around the spinel layer, that then disappears moving into thicker amounts of overlying CoO. In addition, the sample of mixed (Co,Ni)O deposited on bulk

Al_2O_3 displays a broad, yet somewhat more definite peak at ~1.475 μm^{-1} (Figure 5.6), apparently from the halite solid solution. These results may explain the source of similar peaks in the combinatorial samples (~1.47 to 1.48 μm^{-1} in Figure 5.3(b', c'), Figure 5.4 (a'), which tend to form mixed (Co,Ni)O as well as spinels.

5.4.3 Implications for Other Studies

While the present PSLS technique was useful for the purposes of rapid oxide screening, there are opportunities present to gain greater insight into material systems by making modifications to the experimental procedures. In the presented results, only the presence of α-Al_2O_3 doublets was utilized as a figure of merit, and signals from other oxides were largely ignored. Furthermore, the incident laser was not adjusted from the readily available HeNe 633 nm. As discussed, both the PSLS signals generated, as well as the translucency of any overlying oxides will depend on the material thickness, composition, and the wavelengths involved. The implications are that with further experimental refinement, these PSLS techniques may be made more sensitive to the current system, and also be useful for broader screening in other TGO systems. For example, with the experimental ability to cycle through a variety of incident wavelengths, the absorbency difference between NiO and CoO could be maximized (Figure 5.9). Perhaps by combining the ability to alter both wavelength and intensity of incident light, more insight could be rapidly gained on the thickness and composition of the outer monoxide layers by analyzing the minimum intensity needed to observe an α-Al_2O_3 doublet for different wavelengths at which the absorbency difference between NiO and CoO changes by varying amounts.

These considerations of how the opacity of intermediate layers changes with composition and light frequency also yields insight into efforts to measure the stress state of

alumina TGO underneath a deposited TBC layer. Christensen et al. [164] were able to conduct such measurements, however there was reportedly great difficulty in achieving sufficient signal through the overlying TBC, despite it being based on partially stabilized zirconia (PSZ), which should not have a high absorptivity to the incident wavelength. Notwithstanding the inherent translucency of the PSZ, the TBC layer as-deposited was fairly thick (~100 μm), and had a high density of free surfaces from the dense vertical cracks formed during synthesis. These free surfaces likely lead to extensive scattering of the PSLS signals. Knowing that Rayleigh scattering scales with λ^{-4}, and that α-Al_2O_3 may be excited by 633 nm light, a red HeNe laser like that used in the present work may provide less light scattering in the TBC than the cyan 488 nm argon-ion laser used by Christensen et al.

5.5 Conclusions

These experiments have shown that PSLS is a valid method for screening Co-based γ/γ' alloys for their ability to form alumina scales during oxidation. The characteristic fluorescence doublet of thermally grown α-Al_2O_3 can be detected through appreciable amounts of oxides overlying the Al_2O_3, scale, especially for samples where the thickness of these oxides is $\leq$ 5 μm. The absence of detectable α-Al_2O_3 via PSLS cannot distinguish between those samples that do not form continuous alumina scales and those with large amounts of opaque overlying oxides, but these behaviors are both arguably undesirable in practice. This study has also demonstrated that the opacity of overlying oxides is a function of both thickness and composition. Of particular importance is the outer layer of (Co,Ni)O, whose absorptivity of the relevant PSLS wavelengths increases with Co concentration. Overall, the PSLS screening technique is both rapid and non-destructive and can be combined with a high-throughput combinatorial synthesis technique to explore the oxidation

behavior over a wide range of composition space. PSLS screening will be applied in Chapter 6 to a large sample set generated by combinatorial synthesis in order to rapidly explore oxidation behavior across composition space.

5.6 Tables and Figures

Table 5.1: Compositions of the combinatorial alloys depicted in Figure 5.3 and Figure 5.4, as measured by SEM EDS.

Alloy in Figure	Co (at.%)	Ni (at.%)	W (at.%)	Al (at.%)	Cr (at.%)	Ta (at.%)	Ni:Co (at.)
5.3a	41	33	7	13	4	2	0.79
5.3b / 5.4a	38	35	10	11	1	4	0.92
5.3c	66	11	9	8	2	4	0.17
5.4b	46	28	9	12	2	4	0.61
5.4c	51	24	9	10	2	4	0.47
5.4d	54	20	9	10	2	4	0.37

Table 5.2: Comparison of compositions and scale thicknesses in Figure 5.4, with corresponding PSLS α-Al_2O_3 doublets

Sample	Fraction of PSLS spectra with α-Al_2O_3 Doublets, ϕ	PSLS Doublet Intensity	Approximate (Co,Ni)O Thickness (μm)	Oxide Ni:Co (at.)	Alloy Ni:Co (at.)	Alloy Cr (at.%)
(a)	0.83	10,000	7	0.64	0.92	1
(b)	0.88	200	6	0.55	0.61	2
(c)	0.25	100	7	0.49	0.47	2
(d)	0.0	0	7	0.31	0.37	2

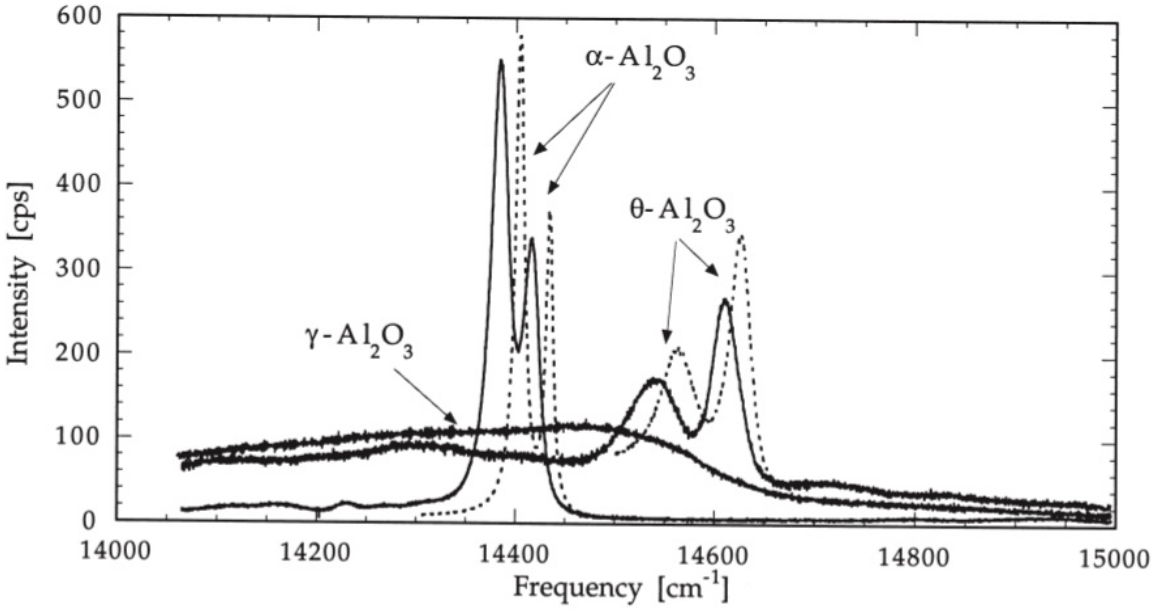

Figure 5.1: Characteristic PSLS signals from α- θ- and γ-Al_2O_3 polymorphs. Dashed lines refer to the stress-free frequencies [83]. N-line peaks are faintly observed around 14200 cm^{-1}.

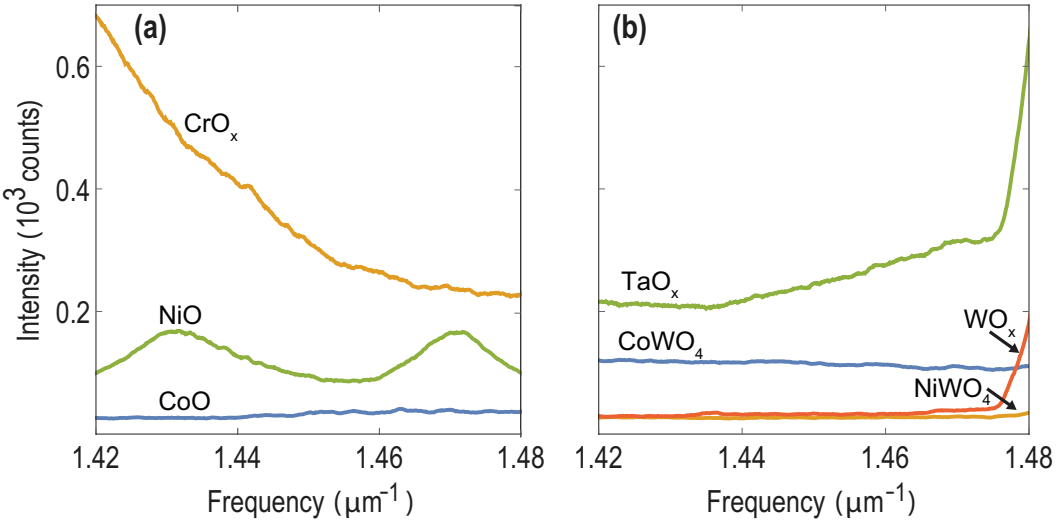

Figure 5.2: Measured PSLS spectra of thermally grown oxides (TGO) grown on commercially pure Ni, Co, Cr, W and Ta for 1 h in air at 1100°C, as well as $CoWO_4$ and $NiWO_4$ powders [159]. All plots are scaled to the same intensities. Characteristic NiO doublets were identified [151]. W, Ta, and Cr TGO exhibit signal towards the outer limits of the measured spectra (1.42 μm^{-1} and 1.48 μm^{-1}). No peaks that could potentially interfere with the PSLS signal for α-Al_2O_3 were observed.

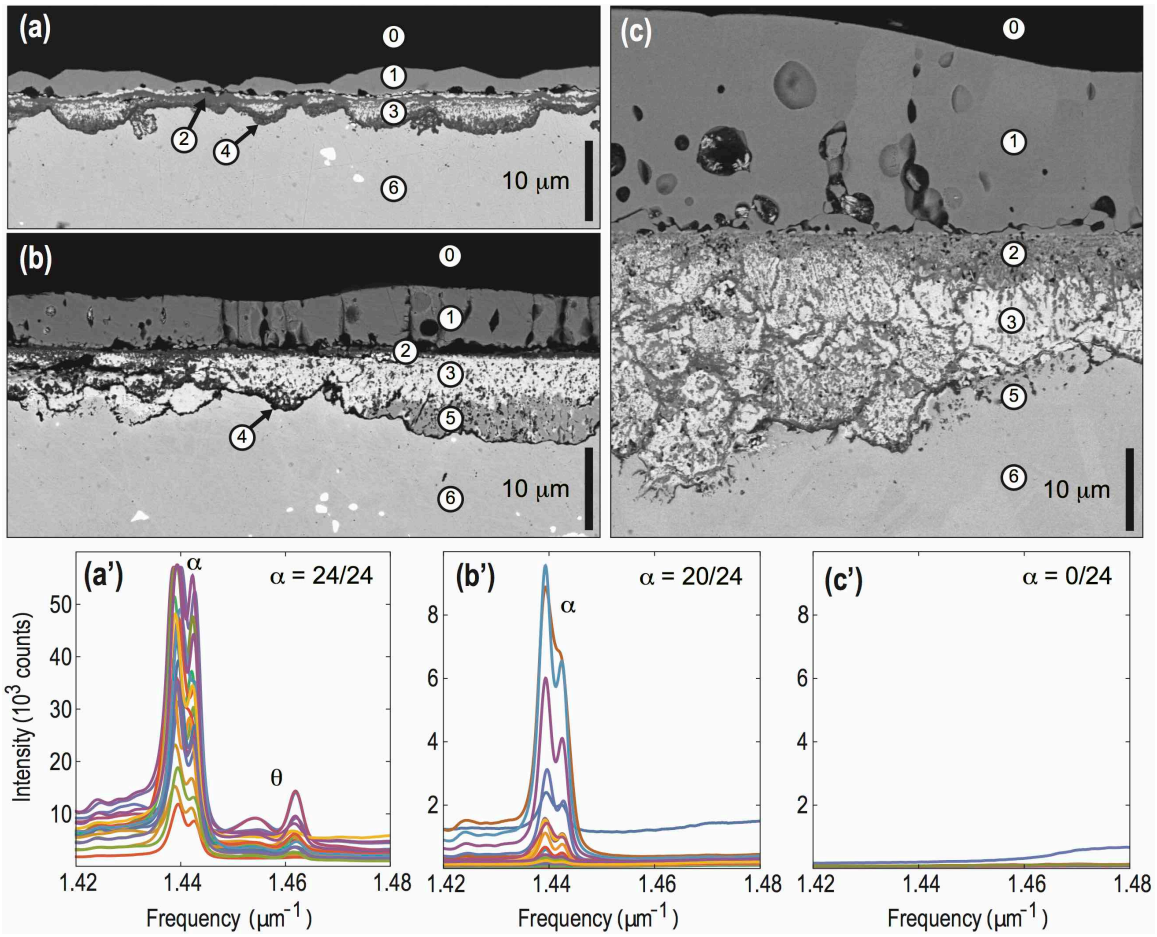

Figure 5.3: (a-c) Backscattered electron images of three oxidized combinatorial alloys representing the variety of scale microstructures in cross-section [159]. Oxides have been characterized based on SEM EDS: (1) (Co,Ni)O, (2) (Co,Ni)$(Al,Cr)_2O_4$, (3) (Co,Ni)WO_4, (4) Al_2O_3 scale, (5) IOZ particles in metal matrix, (6) IPD alloy. (0) denotes the mounting epoxy. (a'-c') PSLS spectra corresponding to the samples in (a-c), taken normal to the sample surfaces. Note the difference in the intensity scales. Alloy compositions are given in Table 5.1

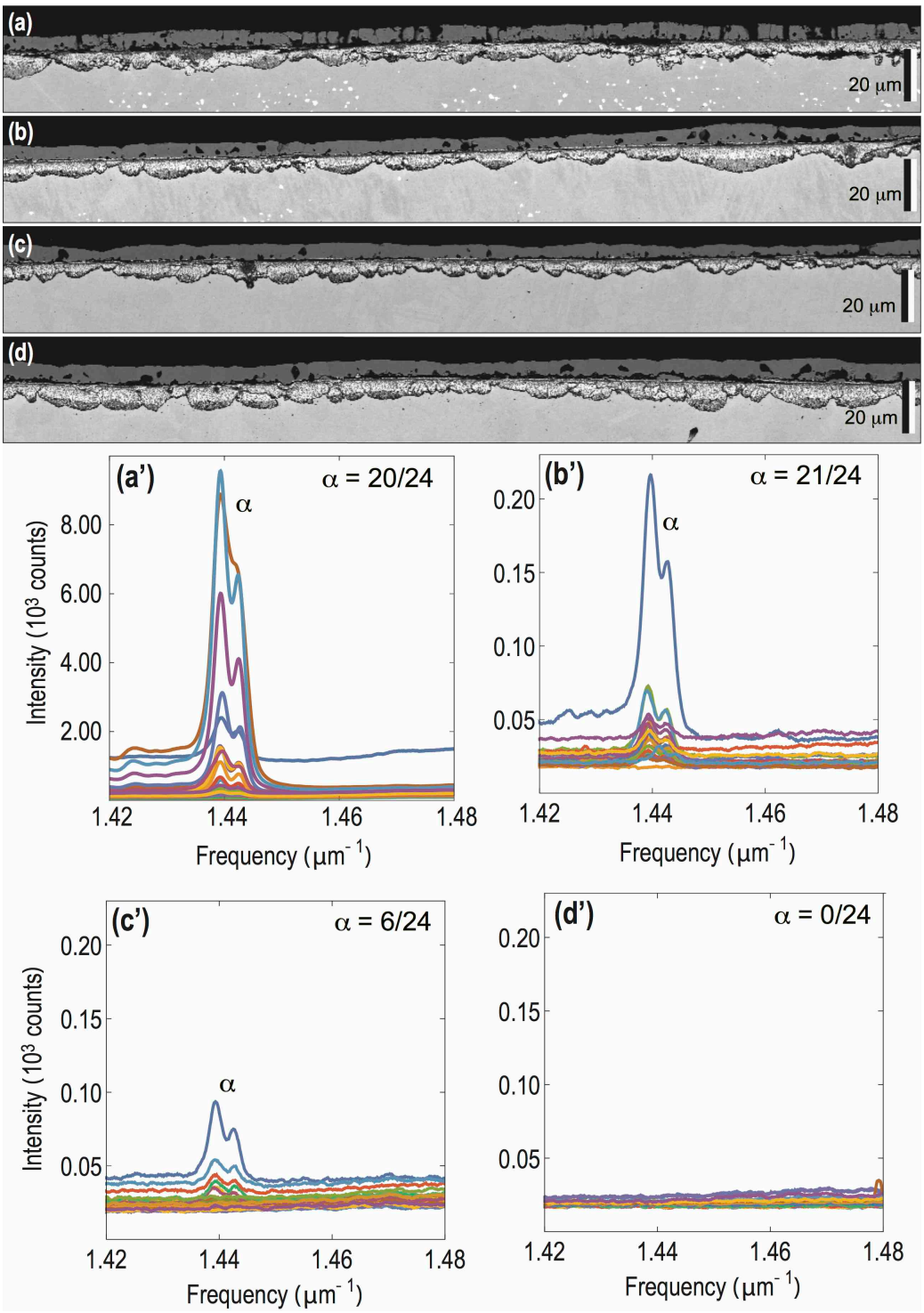

Figure 5.4: (a-d) Backscattered electron images of the cross-sections of scales grown on four combinatorial buttons [159]. (a'-d') Corresponding PSLS spectra measured from the sample surfaces. Note the difference in the intensity scale among (a') and (b'-d'). The compositions of the monoxide layer on top are given in Table 5.2, and the alloy compositions are given in Table 5.1.

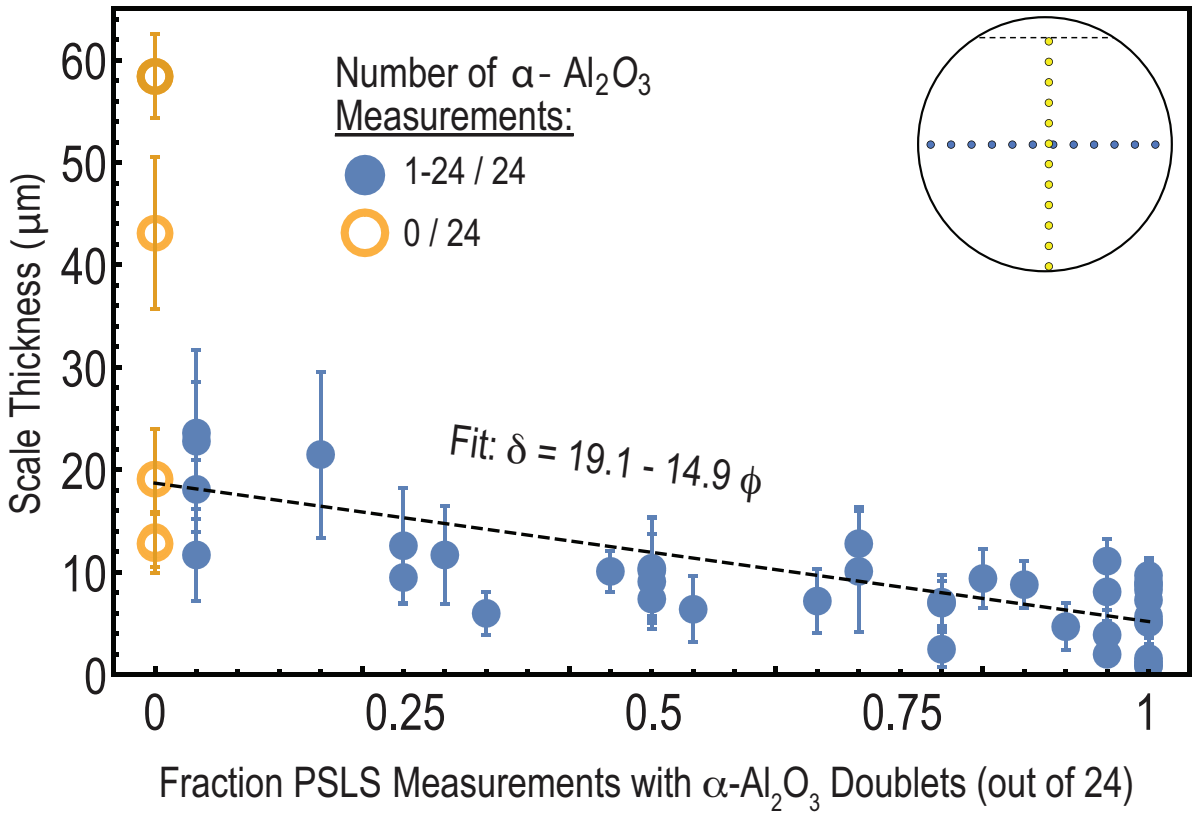

Figure 5.5: Average and standard deviation scale thicknesses as measured by SEM in cross-section vs. the fraction of corresponding PSLS measurements exhibiting the characteristic α-Al_2O_3 doublet from the surface (out of 24 spot measurements) [159]. Samples with α-Al_2O_3 doublets were fit to a linear trend to establish the relation between PSLS and scale thickness. Inset shows the approximate location of the 24 measurements for each combinatorial button across the oxidized surface with respect to a fiducial mark.

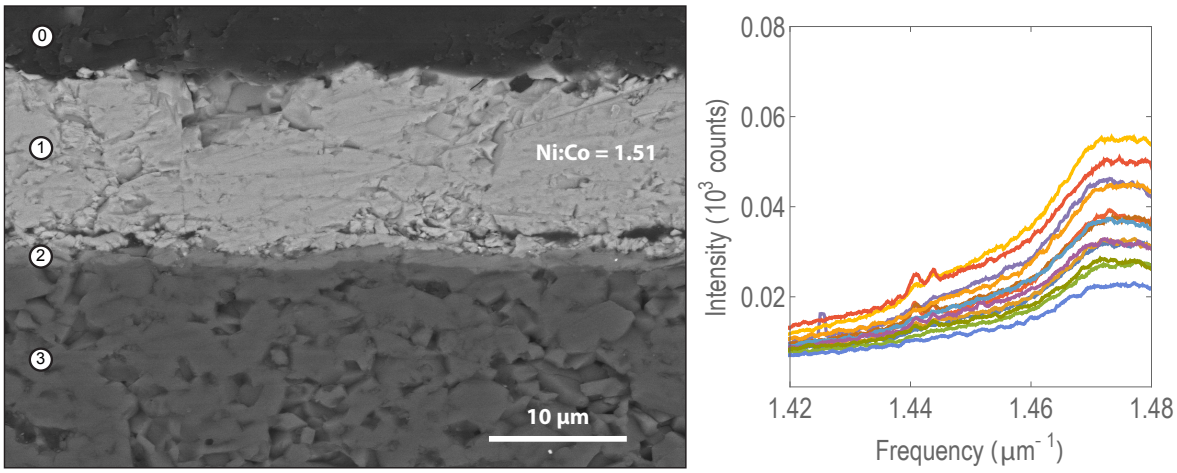

Figure 5.6: BSE SEM micrograph of the mixed (Co,Ni)O layer (1) on top of an α-Al_2O_3 substrate (3) with a thin reaction layer of (Co,Ni)Al_2O_4 spinel in between (2), as viewed in cross-section. The mounting epoxy (0) is also labeled. The PSLS spectra taken from the sample surface prior to cross-sectioning is given, and the α-Al_2O_3 doublet is slightly visible through the total ~15.5 µm overlying Ni-oxide layer. Additionally, a broad hump at ~1.48 μm^{-1} is ubiquitous, likely from the mixed (Ni,Co)Al_2O_4 spinel.

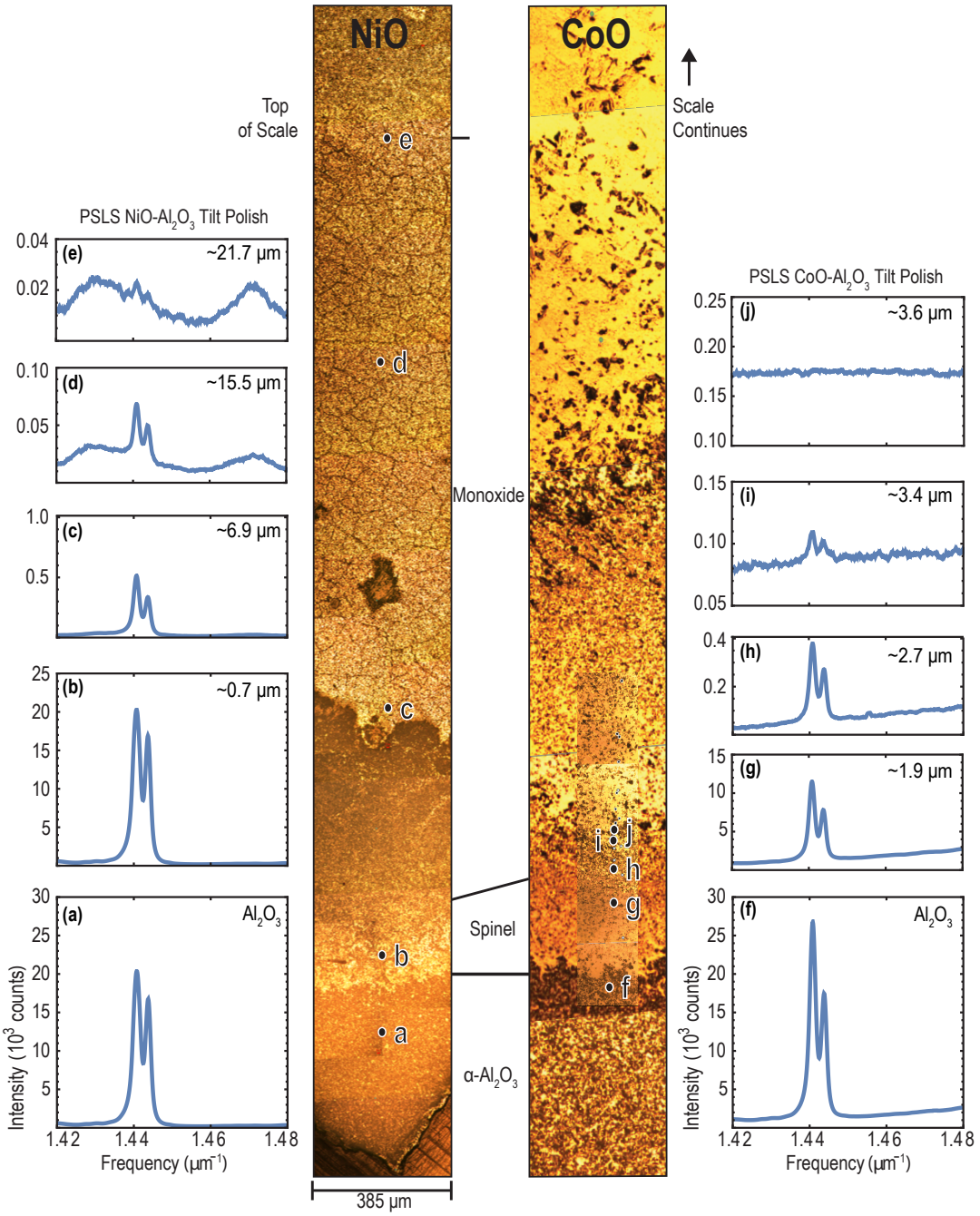

Figure 5.7: Stitched optical images of NiO (left) and CoO (right) scales on top of α-Al_2O_3 substrates polished at a slight angle relative to the alumina, as seen from above [159]. Corresponding PSLS surface measurements (a-j) are provided with the approximate thickness of oxide overlying the alumina substrate in the upper right corner of each spectrum. Lateral dimensions of the optical images are shown via the scale bar at the bottom of the NiO sample. α-Al_2O_3 doublets appear much more attenuated by the Co oxides. An intermediate (Co,Ni)O layer was also tested, as shown in Figure 5.6.

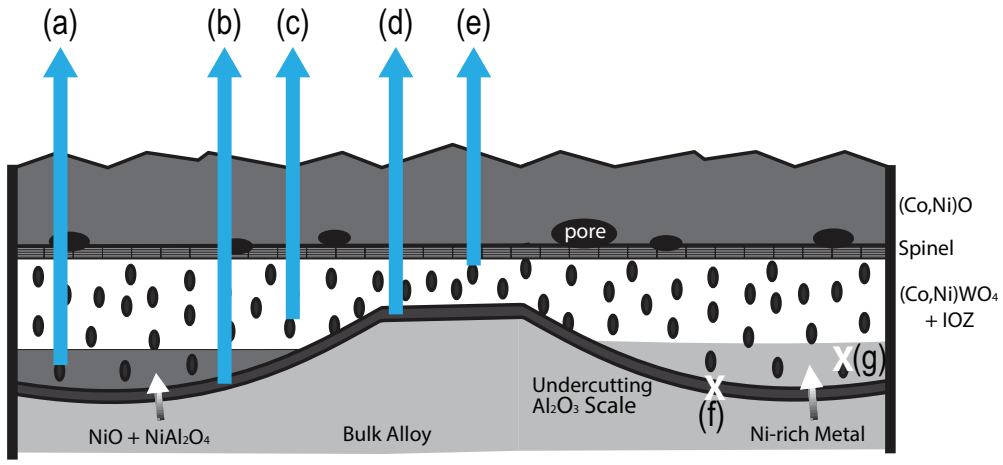

Figure 5.8: Schematic of multilayer scale with features that can generate the PSLS signal for α-Al_2O_3 [159]. The primary source is the continuous alumina scale formed right above the metal (b, d), but discrete particles in the IOZ may also contribute if embedded in an oxide matrix (a, c, e). However, when metal is present above the alumina scale it will arguably block not only the signal from the latter (f) but also from any internal oxide particles formed (g) until continuing oxidation will convert the metal to oxide(s).

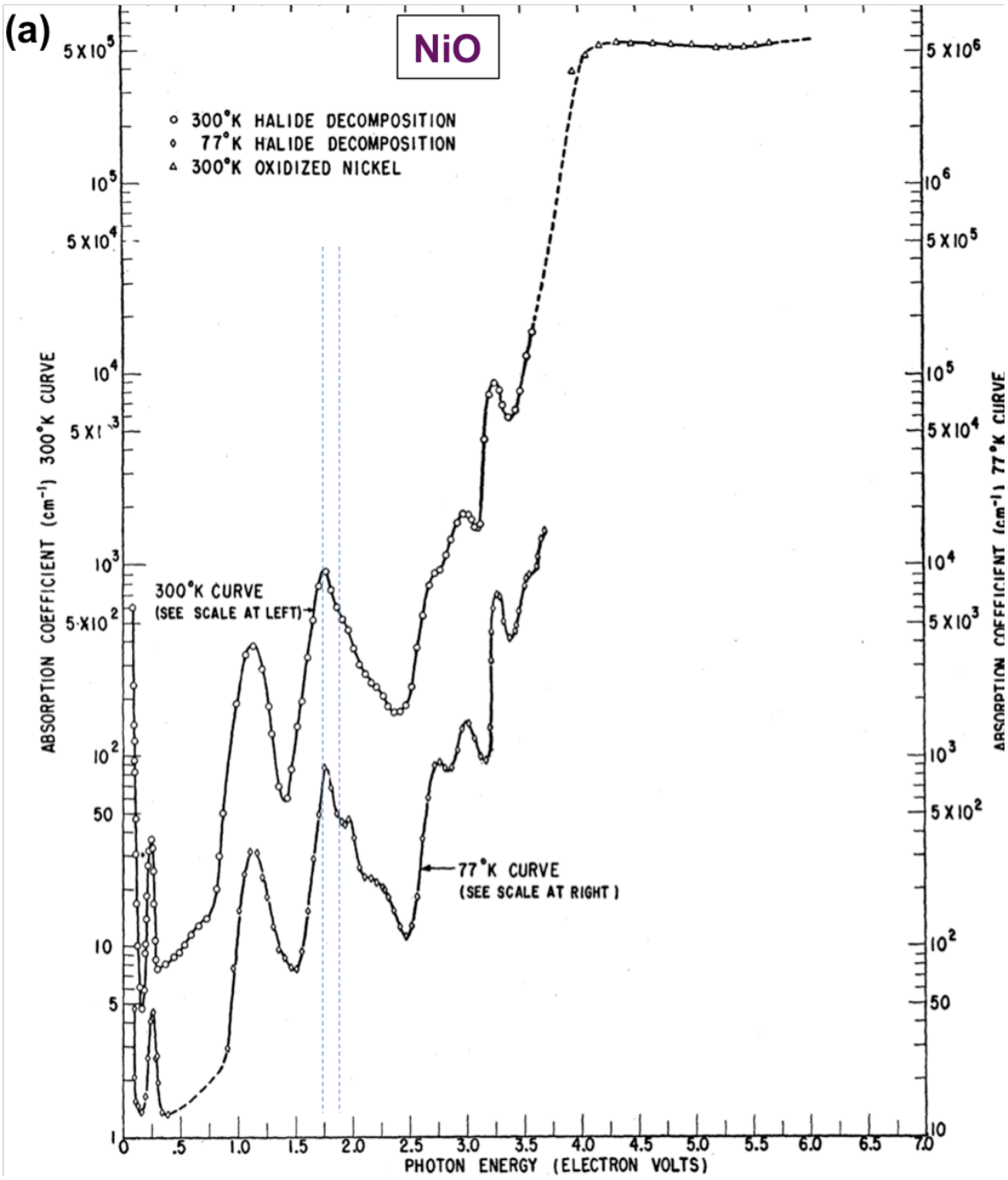

(figure continued on next page)

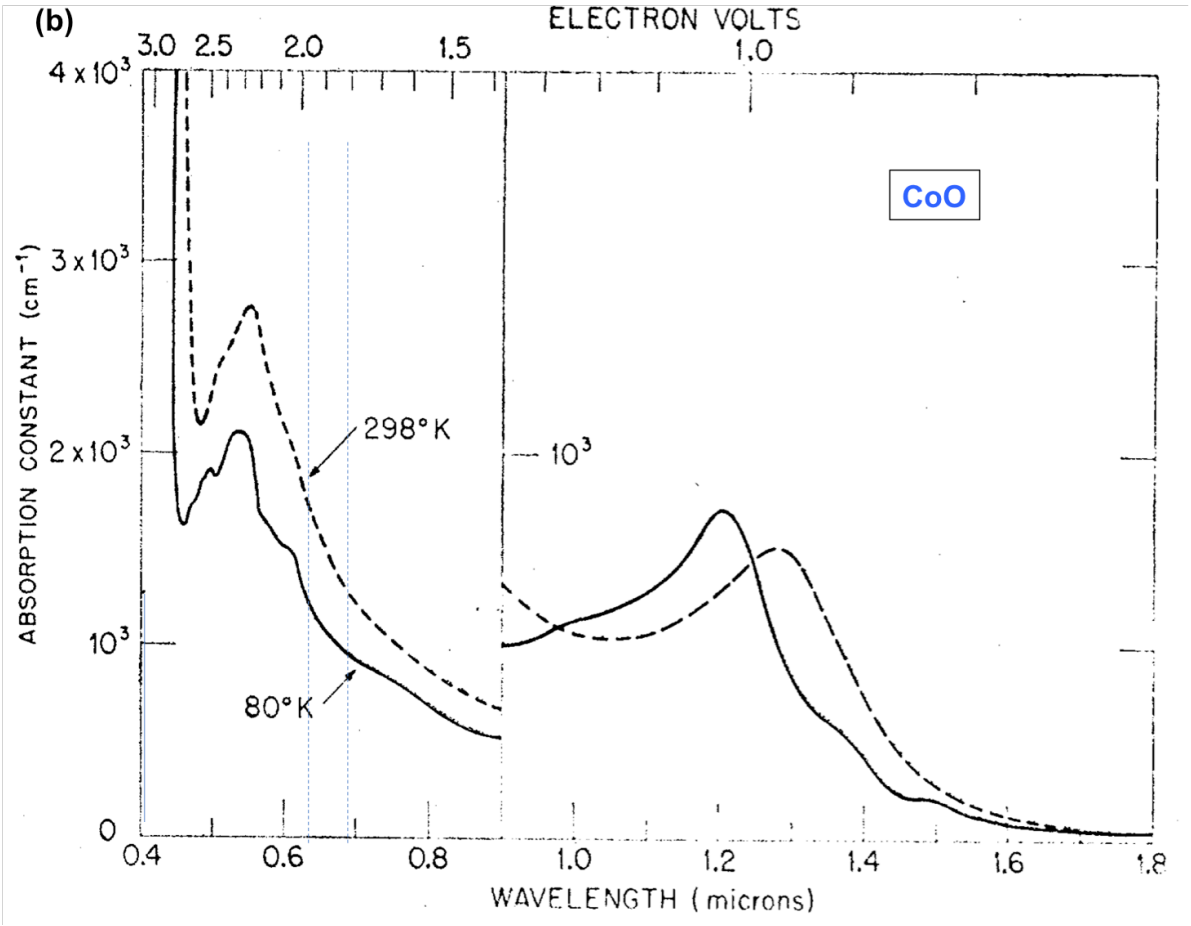

Figure 5.9: Experimentally measured optical absorptivity of (a) NiO [165,166] and (b) CoO [167] as a function of wavelength at room temperature. The incident and excited wavelengths used for PSLS screening in the present studies are marked by vertical dashed lines.

6 Combinatorial Exploration of Alloy Composition

This chapter presents a systematic investigation of oxidation behavior in the senary Co-Ni-Al-W-Cr-Ta alloy system using a combinatorial synthesis approach based on ion plasma deposition (IPD) with multiple alloy targets. The approach generated 234 unique alloys, allowing investigation of a wide swath of composition space. The oxidation response of these combinatorial samples was assessed by PSLS, as discussed in Chapter 5. Promising compositions that form α-Al_2O_3 scale and lesser amounts of less protective, undesirable oxides are highlighted. The focus is on developing an understanding of the relative role of individual elements on the short-term oxidation behavior of Co-base γ/γ'. The relevant design space outlined in this work allows identification of promising baseline compositions that can then be refined and additional elements added to create optimized alloys.

6.1. Experimental Details

6.1.1. Alloy Synthesis

Three combinatorial libraries on the system Co-Ni-Al-W-Cr-Ta were synthesized by IPD [137,150] using 5 different cathodes (Table 6.1) in groups of 3 at a time, as described in Chapter 3. Each library comprised a triangular array of 78 buttons, 12.7 mm diameter by 2.5 mm thick, each coated with a ~110 μm thick layer representing one of a spectrum of compositions of interest (Appendix A). Synthesis was designed to systematically alter two primary variables across each library, depending on the cathodes used for deposition. Cathodes 1 and 2 were common to all libraries and represented a range of Ni:Co ratios along one axis. The third cathode was selected to explore changing individually the Al (3), W (4), or Cr (5) contents across the libraries. Buttons of an alloy similar in composition to cathode

1 were used as substrates to minimize interdiffusion and CTE mismatch with the IPD alloys deposited on them.

After deposition, samples were solution heat treated and polished to a 0.05 μm finish using a vibratory polisher (VibroMet™, Buehler, Lake Bluff, IL) with alumina suspension, leaving ~100 μm of the test alloys with typical grain sizes of ~7 μm [10] (Figure 3.2). IPD alloy compositions were then measured by energy dispersive X-ray spectroscopy (EDS) on a 1 mm^2 area of the heat-treated button surfaces using a scanning electron microscope (SEM, FEI XL30 Sirion FEG, Houston, TX) at 15 kV. Select compositions were also quantified with electron probe microanalysis (EPMA) using an alloy reference sample that had itself been characterized via inductively coupled plasma (ICP) analysis. For the subset of homogenized alloys characterized by both techniques, EDS measurements for Al and Cr were on average within ±0.5% of EPMA values, which is within the scatter typical for both methods, but Ni, Ta and W were all higher in EDS, by 1-2% on average. The latter uncertainty relates to the overlap of the Ni/Co peaks, as well as the W/Ta peaks at the lower energies, a problem with these elements shared with analyses of Ni-base superalloys [168]. In consequence, the balance Co concentrations measured by EDS and EPMA could be different by ~4-5% on average, while the differences in the Ni:Co atomic percent ratios are within ~0.1. Nevertheless, these deviations are consistent in all measurements so the trends observed should be qualitatively correct.

6.1.2. Oxidation

Buttons were oxidized for a prescribed time in flowing dry air at 1100°C by inserting them into the hot zone of a furnace preheated to the target temperature under the same environment. All of the buttons labeled with colors in Figure 6.1(j-l), and plotted in Figure

6.3 were oxidized for 1 h. Additional combinatorial buttons were selected to study the effects of oxidation time. These buttons were cut in half with a diamond wafering-blade, and each half of the button was oxidized for 1 h, and either 15 min or 4 h. After dwelling in the furnace hot zone for the given time, samples were withdrawn over the course of 5 min. Spallation of oxide from the test surfaces was rarely observed.

6.1.3. Characterization

Oxidized samples were rapidly screened for the presence of continuous α-Al_2O_3 scale and extent of coverage using PSLS [119,137], as described in Chapter 5. Each button was then classified by determining what fraction of the PSLS measurements, 24 per sample, exhibited the characteristic α-Al_2O_3 fluorescence doublet at 1.44 μm^{-1}. As noted in Chapter 5, oxidized button surfaces with larger fractions of positive PSLS readings correspond to continuous α-Al_2O_3 scales with thinner amounts of overlying oxide [169]. Phase diagrams used to predict the potential alloy phases present were calculated using the PANDAT™ software with the PanCo-2018[**] database (CompuTherm LLC, Middleton, WI) containing all metal elements of interest: Co-Ni-Al-W-Cr-Ta.

Oxidized buttons were characterized in cross section using backscattered electron (BSE) imaging and SEM/EDS to characterize the oxide scale. A 10 kV accelerating voltage was used for EDS analysis of the oxides to reduce the electron interaction volume and sample drift, but was not sufficiently energetic to differentiate between W and Ta signals. A lamella was extracted for transmission electron microscopy (TEM) from a selected oxide cross

[**] ITIC calculations in this chapter were made using the 2018 version of the PanCobalt database, courtesy of Jun Zhou, Computherm LLC. This version is observed to more accurately model the μ-Co_7W_6 phase. In the rest of the dissertation, PANDAT calculations were conducted with the available PanCobalt-2011 version, which occasionally and unreasonably predicts a pure W BCC phase, (W) in many fields.

section using focused ion beam (FIB) in an FEI Helios Dualbeam Nanolab 650, finishing with an accelerating voltage of 5 kV. TEM high angle annular dark field (HAADF) imaging and EDS were conducted in an FEI Titan FEG TEM-STEM at 300 kV.

6.2. Results

6.2.1. Characteristics of the Pristine Alloys

Alloy compositions prior to oxidation across the three libraries are compared in Figure 6.1(a-f). As planned, all libraries display an increasing Ni:Co from left to right, with increasing Al, decreasing W, and increasing Cr contents from bottom to top for libraries 1, 2, and 3, respectively. The concentrations of the remaining components are generally constant for each library. Minor phases other than γ and γ' are often found in the unoxidized IPD alloys after the solution heat treatment, exemplified by the W-rich (brighter) and Al-rich (darker) segregates noted in Figure 6.2(a,b); their prevalence in the three libraries is shown in Figure 6.1(g-i). The compositions of the pristine alloys (prior to oxidation) corresponding to the micrographs shown in various figures (mostly after oxidation) are listed in Table 6.2.

6.2.2. Oxidized Alloy PSLS

Samples from the different libraries were screened for their oxidation behavior at 1100°C using PSLS. The broader results are summarized in Figure 6.1(j-l), with samples colored based on ϕ, defined as the fraction of the 24 PSLS spectra taken from each sample

exhibiting the characteristic α-Al_2O_3 doublet[††]. As demonstrated in Chapter 5, higher values of ϕ (brighter green) generally correspond to thinner layers of undesirable phases overlying the α-Al_2O_3 scale. Examination of Figure 6.1 reveals that α-Al_2O_3 formation is observed most frequently in Library 1 at the higher Al and Ni contents (top and right corners in j), in Library 2 at the higher Ni and W contents (right corner in k), and in Library 3 at the higher Cr and Ni contents (top and right corners in l).

6.2.3. Most Promising Al_2O_3 Formers

Notwithstanding the relatively large number of combinatorial samples that show a promising PSLS response in Figure 6.1(j-l), only a small fraction of them yield suitably thin α-Al_2O_3 scales combined with a minimum of extraneous overlaying oxides. Examples of these scales, both with the highest PSLS scores ($\phi = 1$), are shown in Figure 6.2(c,d). Oxide phases in these images were tentatively identified based on SEM EDS by comparing the measured ratios of different cations. The thinnest scales were observed at the high Al and high Cr corners of Libraries 1 and 3, corresponding to the samples in Figure 6.2(b) and (a), respectively, marked on Figure 6.1(j,l). The highest Cr sample in Figure 6.2(a, c, e) exhibits a desirable continuous Al_2O_3 layer across the surface (point 4 in e), with a thin layer of overlying spinel (point 2 in e). The average scale thickness in this case is on the order of 1 μm. The highest Al sample contains these layers as well, but also forms less desirable phases in many locations, e.g. Figure 6.2(d, f). In this case, the thin layers of Al_2O_3 and spinel are present at multiple locations with pockets of a W-rich oxide sandwiched between

[††] The compositions of alloys shown in the presented figures are labeled in Table 6.2, Figure 6.1, and Figure 6.3. For example, the alloys in Figures 2(a) and (b) are labeled "2a", and "2b" respectively.

them (point 3 in f), often overlaid by (Co,Ni)O (point 1 in f). These patches of additional oxide phases contribute to a greater average scale thickness, ~5-9 μm.

6.2.4. Oxidation Behavior Mapped onto Alloy Phase Fields

The oxidation behavior, as reflected in φ, may be conveniently compared with the calculated phase constitution corresponding to each alloy, as illustrated in Figure 6.3. These diagrams are isothermal-isoconcentrate (ITIC) sections in senary Co-Ni-Al-W-Cr-Ta space at 1100°C, calculated with the PanCo-2018 thermodynamic database [140]. Three components of the alloy vary within each Gibbs triangle, corresponding to a given library, with the remaining components having essentially constant concentrations throughout the range investigated. The measured compositions of the IPD alloys prior to oxidation are then plotted onto the ITIC sections, and assigned colors based on their ϕ value after oxidation—cf. Figure 6.1(j-l). In this manner one can, in principle, identify compositions with favorable alumina forming behavior and the desired γ/γ' microstructure. Because IPD alloys within each library do not have exactly the same concentrations of the elements kept nominally constant, only those alloys that are compositionally close (within approximately ±1 at.%) to the ITIC sections in Figure 6.3 are plotted. Therefore, the phase constitutions depicted should be reasonably representative of the plotted IPD alloys and may be compared with the experimental observations.[‡‡]

It is first noted in all the calculated ITIC sections in Figure 6.3 that considerable alloying is required to reach the boundary of any field containing γ + γ′ at 1100°C, i.e. fields (21),

[‡‡] Note that, while the components plotted in the ITIC sections in Figure 6.3 suggested correspondence with each of the libraries, there are compositions of different libraries that may fall within the composition range plotted, e.g. Figure 6.3(c) contains points of libraries 1 and 2.

(31), (33), (41), and (42). Importantly, only in Figure 6.3(b) is there a field (21) predicted to contain $\gamma + \gamma'$ with no other phase, consistent with the broader findings for the W library in Figure 6.1(h). However, most of the compositions in this field have low values of ϕ, whereas those compositions with larger values of ϕ fall into fields containing other phases, e.g. μ-Co_7W_6 ($D8_5$) in (31). This W-rich phase was indeed found in a significant fraction of the compositions with high ϕ values in the latter field. In the other two libraries $\gamma + \gamma'$ is predicted to co-exist with the μ phase (31) and in some instances also with β-(Co,Ni)Al (B2). The presence of γ' was not always evident in the SEM sections but was confirmed in samples within the fields marked (21) and (31) in all three libraries, e.g. Figure 6.4, as well as in some samples not falling directly within the ITIC sections of Figure 6.3, e.g. 3b. The β phases, which could act as Al reservoirs during oxidation, are also predicted in several fields but usually not concurrently with γ' except when μ or A2 are present, e.g. fields (41) and (43). Al-rich phases consistent with β are indeed observed in a significant fraction of the Al library buttons as mapped in Figure 6.1(g), sometimes with μ as in Figure 6.2(b), but not in any of the samples examined in the other libraries.

6.2.5. Oxide Phases and Microstructure

Examination of scales across all the libraries reveals that the least desirable ones occur closer to the Co-rich corner of the libraries and typically form Al_2O_3 primarily by internal oxidation. The scales can be in some cases as thick as 60 μm. A lamella taken from one of the samples with thicker oxides and a modest ϕ value, labeled 6 in Figure 6.1(j) and Figure 6.3(a), was analyzed by TEM/EDS, revealing a complex microstructure with multiple phases shown in Figure 6.5. The compositions of the labeled oxide constituents, which are representative of most thick scales, are listed in Table 6.3.

(Co,Ni)O (B1) was often present and always as the outermost oxide (points 1 and 2 in Figure 6.5). $CoWO_4$ ($E1_b$) tungstate particles (3) were usually found at the bottom of this layer, underlain by $(Ni,Co)(Al,Cr)_2O_4$ spinel ($H1_1$) present either as a thin single-phase layer (4), or occasionally as a thicker porous layer mixed with tungstate. Pores (0) were frequently observed at or near the (Co,Ni)O/spinel interface. Beneath the spinel layer there were frequently discrete Al-rich oxides (5, 7, 9) embedded in a $(Co,Ni)WO_4$ matrix (6, 8, 10). These Al-rich particles are seen to transition from spinel to alumina with increasing distance from the outermost surface (Table 6.3). Concomitantly, the Ni:Co ratio in the enveloping tungstate matrix increases in the same direction. The darker region under the layer of tungstate is found to contain monoxide (11), spinels (12, 13), as well as some pores (0). These oxides are much more Ni-rich than their counterparts closer to the surface (cf. 1, 2, 4 in Table 6.3). Finally, Al_2O_3 is present as a thin, continuous layer (14, 15) next to the bulk, unoxidized alloy.

To illustrate the broader effects of alloy composition on the scale constituents and morphology, cross-sections were taken from samples where nominally only one of the key components was changed (Figure 6.6, Table 6.2) [§§]. The individual samples are also labeled in Figure 6.3, which reveals that moving to directions of higher Ni, Al, W, and Cr will be accompanied by higher ϕ values (green), as noted earlier in Figure 6.1. Reflecting these trends, the cross-sections in Figure 6.6 show that increasing each component individually reduces the average scale thickness, albeit to different degrees. Only moderate reductions in

[§§] Increase in one component, e.g. Al, while keeping W and Cr constant can only be accomplished by reducing either Co or Ni, or both. Ideally a change in one element should be implemented keeping the relative proportions of the others constant, but that is not feasible in a combinatorial study. Therefore, the samples selected are those that most closely approximate the desired comparison.

thickness are observed when increasing the Ni:Co ratio, Figure 6.6(a→b), while the oxide phases present are fairly consistent. In most cases, there is only a slight reduction in the amount of tungstate and overlying monoxide. On the other hand, increasing Al content, Figure 6.6(c→d) has a much more pronounced beneficial effect on oxidation. The scale thickness is substantially decreased, and tungstate and monoxide phases are largely minimized across much of the sample surface. However, even in the sample with highest Al content some parts of the scale still contain these less desirable oxides, e.g. Figure 6.2(d). (Note the similarity in composition between samples 2b and 6d in Figure 6.1 and Table 6.2). Increasing the W content in the alloys, Figure 6.6(e→f) has a mildly beneficial effect in that the average oxide thickness is clearly reduced, though undesirable phases are still plentiful in the thinner scales, even if no tertiary phases were present in the alloy for either sample. The thick layer of mixed oxide phases under the monoxide in (e) transitions to a thinner layer comprising primarily tungstate, with continuous overlying spinel and diminished outer monoxide. These effects are in contrast with Cr additions, Figure 6.6(g→h), which are found to substantially reduce the scale thickness, but also have a marked effect in precluding many of the less desirable oxides. This is epitomized in the sample at the tip of the library, Figure 6.2(a,c), which has a similar composition to the alloy in 6h as shown in Table 6.2. The tungstate phases are substantially reduced at higher Cr contents (brighter regions in Figure 6.6h), and outer monoxides are seldom observed. What remains is a thin layer of primarily Al_2O_3 and outer spinel.

6.2.6. Computational Results

The first principles calculations of Al chemical potential in γ/γ′ for both ternary Co-W-Al and Ni-W-Al systems are shown in Table 6.4. For each solvent metal W content is

increased, as Al content is held approximately constant in order to examine the second order effects of alloy composition on the thermodynamic driving force to form Al_2O_3. It is seen that the type of solvent metal has a large effect on the μ(Al) dependence on W content. Increasing W content lowers μ(Al) in the Co-base system, and conversely raises μ(Al) in the Ni-base system

6.2.7. IOZ Pocket Investigation

The presence of IOZ pockets undercut by a continuous Al_2O_3 scale, e.g. Figure 6.2(d,f) and Figure 6.6(a-c, e-g) was sufficiently pervasive to deserve further investigation. The IOZ particles are most often observed within the tungstate layer below the spinel, but they can also be found within a matrix of Ni-rich monoxide or Ni-rich metal, usually below the tungstate. The structure of these pockets poses interesting questions regarding their morphology, the sequence of evolution of the various oxides and the mechanism for the formation of the continuous alumina layer at the bottom. Shorter-time oxidation experiments were undertaken to elucidate the evolution of these features. The sample oxidized for 15 min in Figure 6.7(a) exhibits multiple regions where the continuous Al_2O_3 scale had not completely undercut the bottom of the IOZ pocket, as illustrated in Figure 6.7(a), whereas all IOZ pockets are underlain by continuous Al_2O_3 after 1 h, e.g. Figure 6.7(b). Furthermore, the lower portions of IOZ matrix after 15 min were primarily metallic, whereas the equivalent IOZ matrix in the 1 h sample was fully oxidized. A sample from the same coupon as Figure 6.5 was polished parallel to the scale plane at a small angle relative to the surface, as shown in Figure 6.8. The IOZ pockets are shown surrounded by a thin, continuous alumina at their boundaries, Figure 6.8(a). The corresponding surface polish of the unoxidized alloy in Figure 6.8(b) reveals an average grain size comparable to the in-

plane dimension of the IOZ pockets. Insight provided from these observations is discussed later.

6.3. Discussion

Salient findings of this investigation are (i) the demonstration that thin, continuous alumina scales with minimal overlying oxides are feasible within phase fields where γ′ is stable, albeit only within a relatively small domain of the composition space explored; (ii) insight into the effect of different alloying elements on the alloy constituents and oxidation behavior, particularly regarding the production of extraneous oxides; (iii) an understanding of the processes of internal oxidation; and (iv) an identification of alloying strategies for achieving desirable oxidation behavior in a γ/γ′ alloy with minimal presence of deleterious intermetallic phases. These issues are further discussed in this section.

6.3.1. Desirable Al_2O_3 Scale

It is evident from the combinatorial results in Figure 6.1(j-l) that a substantial fraction of the three libraries exhibit desirable formation of alumina with a high fraction of positive PSLS results ($\phi \rightarrow 1$) in well-defined composition domains, validating the approach. Regions defined by this criterion in Figure 3 correspond approximately to $X_{Al} \gtrsim 11$, $7 \lesssim X_W \lesssim 10$, $X_{Cr} \gtrsim 4$, and $X_{Ni} \gtrsim 26$, all in atomic percent (Table 6.5). It is also noted that within these regions a significant fraction of the samples with high ϕ values fall into fields predicted to contain γ′ at 1100°C; this prediction was confirmed (Figure 6.4) for enough samples to provide confidence that it is feasible to form an α-Al_2O_3 scale in a Co-based γ/γ′ alloy. Nevertheless, these scales can range over a wide range of thickness and morphology, which in principle narrows the composition space of interest.

A conceptually optimum scale is based on a slow-growing continuous thin layer of α-Al_2O_3 with no extraneous, non-protective oxides, analogous to that on second-generation Ni-base superalloys. The closest scale produced in this study is illustrated in Figure 6.2(c,e), comprising a thin continuous α-Al_2O_3 scale (~0.5 μm thick) with a thin over-layer of spinel, giving a total thickness on par with that formed on CMSX-4 and René N5 under the same conditions [150,162]. However, of all the samples investigated only that in Figure 6.2(a), and perhaps Figure 6.6(h), exhibited those desirable scales. These two samples were at the high-Cr corner of library 3 ($X_{Cr} \approx 9$ at.%), with 6h falling at the boundary of the γ+γ′+μ and γ+μ+β in Figure 6.3(c). This suggests the fraction of γ′, if present, is probably small as expected from the effects of Cr in reducing γ′ stability. Indeed, the sample in 2a, which has the highest Cr content, did not have a detectable amount of γ′.

Most samples investigated exhibited significant amounts of extraneous oxides, usually in the form of IOZ pockets with discrete Al_2O_3 particles embedded in tungstate and spinel matrices, often undercut by thin, continuous alumina and overlaid by spinel and (Co,Ni)O. Even samples 2a, 6h and 2b exhibit noticeable populations of these features interspersed in an otherwise thin alumina scale. The origin of these IOZ pockets is discussed later, but the implication is that they are generally undesirable because they result in thick scales that are more susceptible to spallation under thermal cycling. It is worth considering that these alloys are likely to be protected by thermal barrier coatings (TBCs) with oxidation-resistant bond coats. Oxidation resistance is thus required only in the event of coating loss or fatigue-related cracking [170], and the oxide scale should be sufficiently robust to protect the alloy and ensure the survivability of the component. Previous multilayer mechanics calculations for the superalloy – bond coating – TBC system demonstrate similar magnitudes of driving

forces for coating failure in nickel-base compared to cobalt-base superalloy systems for alloys in the two systems that have comparable coefficients of thermal expansion [41].

6.3.2. Effects of Alloying Additions

While alloys with desirable oxidation behavior can be identified in fields where γ′ is stable at 1100°C, it is also noted that many of these alloys may contain additional intermetallic phases, notably β-(Ni,Co)Al and μ-Co_7W_6.[***] In general, β and μ are considered detrimental in superalloy applications because of their effect on stress-rupture and toughness, respectively [171,172]. The β phase is predicted at low Ni contents with increasing Al content, fields (23) and (32) in Figure 6.3(a-c), and at higher Ni contents with increasing W and Cr contents, fields (34), (41) and (43) in the same figures. However, it was only observed experimentally in the higher Al contents in Library 1, e.g. 2b, 6c and 6d, cf. Figure 6.1(g,j). In general, β appears to supersede γ′ as the Al content increases, often in combination with μ following the trend established early in the ternary Co-Al-W [7]. Therefore, suppressing β is desirable not only because of its likely detrimental effect on mechanical properties, but also because it appears to concomitantly reduce the fraction of strengthening γ′ phase.

The μ phase is generally predicted in combination with β, fields (32), (34), (41) and (43) in Figure 6.3, but also without it, as in fields (22) and (31). Within the limitations of the samples examined, μ was predominantly observed in field (31) and at near its boundary with (32). Given the Al and W contents where μ is present, one may trace the origin of the γ+μ field (22) to the Co-Al-W ternary, where it bounds the γ+β+μ field [7]. As Ni is added the γ′

[***] These phases also incorporate other elements in solid solution, e.g. Cr in β and Ta in μ.

field expands, presumably at the expense of β, increasing the Al:W ratio in the $L1_2$ phase [2,11]. Concomitantly the partitioning of W shifts toward the γ phase [13], stabilizing μ into field (31). Note that μ is also prevalent in the Cr library, presumably due to the de-stabilization of the γ′ phase [22,23], but not present in the W library, Figure 6.1(h), wherein most of the samples have lower W content than those in Libraries 1 and 3. It is evident from the discussion above that, while the general trends are qualitatively reasonable, additional refinement of the existing database would further the understanding of the extent of alloying additions that can be tolerated before precipitating out the undesirable β and μ phases.

Consider now the role of alloying additions on the oxidation behavior. Most of the scales examined are deemed inadequate because of the presence of thick IOZ pockets with tungstate/spinel matrices, often undercut by a thin alumina scale, and covered by a thick monoxide layer with a thinner, underlying spinel, e.g. Figure 6.5-Figure 6.7. While the mechanism of evolution of these features, discussed in the next section, is seemingly complex, one may hypothesize that the fundamental variables that control internal oxidation [155,173] are still at play. The role of Al is self-evident as increasing its activity would accelerate the diffusion to the putative oxidation front and promote the transition to continuous alumina formation. The concentration, however, must satisfy the requirements for γ′ stability and is limited by the onset of β formation. The role of Cr is often ascribed to the "third element effect" on the promotion of alumina, which is well documented for M-Cr-Al alloys (M=Ni, Fe, Co) [174]. While there is still debate on the mechanism, a common explanation is the formation of chromia at the surface, limiting oxygen ingress and enabling Al diffusion to become competitive in forming a scale rather than internal oxides [42,174]. One might argue that the formation of thin alumina scales in the alloys with the highest

Cr:Al ratios (Table 6.2) is consistent with this view, especially since these alloys are overlaid by a thin layer of spinel, e.g. Figure 6.2(c). However, when Cr was detectable in the spinel layers analyzed in other samples, e.g. Figure 6.5, it was present in a much lower concentration than Al (spot 4 in Table 6.3).

The role of W in promoting alumina is somewhat counterintuitive and must be viewed in the context of its interplay with Ni. First principles calculations summarized in Table 6.4 reveal that the chemical potential of Al in the γ/γ' equilibrium increases concomitantly with W additions in Ni-Al-W alloys, whereas the opposite is true in Co-Al-W, wherein μ_{Al} decreases as W is added. Moreover, it is known that as the γ' field expands with the addition of Ni its Al:W ratio increases and the W partitioning shifts toward the γ phase [19]. While the quaternary calculation has not been performed, one can hypothesize based on Table 6.4 that the chemical potential of Al would still increase with W additions with the partial substitution of Ni for Co. Moreover, increasing the Ni:Co ratio has been shown to enhance aluminum diffusivity in the bulk alloy [175]. Both effects are expected to favor the transition from internal oxidation to continuous alumina [155].

6.3.3. Formation of IOZ Pockets

The formation of IOZ pockets underlain by a continuous oxide layer has been reported for Ni-Cr [7] and Ni-Al [176] alloys, along with mechanisms proposed to explain their evolution. The general features are found in the present alloys, e.g. Figure 6.2, Figure 6.6, and Figure 6.7, but the microstructure is arguably more complex because of the larger number of cations involved. However, the major steps resemble those proposed in [174], as depicted schematically in Figure 6.9. Upon initial exposure to high-temperature, the first event is the formation of oxides of the major components that spread to form a layer of

(Ni,Co)O with variable thickness and porosity, depending on the alloy composition. The presence of spinel immediately under the top layer suggests Al oxidation starts concomitantly or soon thereafter. In one scenario Al could be concurrently oxidized with Ni and Co to form spinel. Alternatively, alumina could form in discrete particles at the onset of internal oxidation, and then react with the surrounding monoxide to form spinel. The absence of any alumina particles embedded into the top spinel layer but their presence within the bottom spinel layer in a typical IOZ pocket suggest that the scenario of direct oxidation may be more likely. Further experiments at shorter times, however, are needed to elucidate this issue.

Because oxygen permeation is evidently allowed by the top layers, as shown by the subsequent evolution of the scale, the next step is the internal oxidation of the Al within the alloy, wherein the Al concentration and diffusion rates are not sufficiently competitive to form initially a continuous alumina scale. Concomitantly, there is continued outward migration of Ni and Co to feed the growth of the monoxide layer. Presumably W is less mobile, so as Al gets depleted from the upper layer of the alloy the oxygen ingress leads to the formation of the tungstate layer, which embeds the alumina particles. (Tungstate is also observed above the spinel layer, as represented by point (3) in Figure 6.5. It is hypothesized that this tungstate was the product of the initial rapid oxidation stage and arguably marks the approximate surface of the alloy when oxidation started.) In the upper portions of the IOZ, the alumina particles are partially converted to spinel by the continued oxygen ingress after Al is locally depleted. Internal oxidation, however, continues ahead of the tungstate regions so the bottom of the IOZ zone comprises alumina particles embedded into alloy, as noted in Figure 6.7(a).

Ideally the above processes would continue until oxygen diffusion becomes less competitive owing to the increasing diffusion distances and the decreasing chemical potential at the metal/outer oxide interface. If concentrations were uniform and bulk diffusion predominated, the different oxidation fronts would be expected to advance parallel to the original surface. There are, however, places where Al diffusion is competitive at much earlier times, leading to the local formation of continuous alpha alumina closer to the surface. This view is supported by the observation that the boundaries of the IOZ pockets are on the scale of the alloy grain size, as shown in the tapered section of Figure 6.8, suggesting that the faster diffusion of Al in these regions facilitates the formation of the continuous alumina layer. (The mechanism by which this occurs is not yet clear, but it does not seem to exhibit the features of the particle coalescence proposed in [174]). Once these patches of continuous alumina form there is a competition between the advancement of the IOZ front and the lateral spreading of the alumina layer. The latter is favored by the divergence of the diffusion fluxes for oxygen and aluminum along the interfaces of the alumina layer, which progressively encroaches on the IOZ front. This view is supported by the shape of the IOZ pockets, which are progressively constrained from growing as the lateral growth of the alumina proceeds, as shown in Figure 6.7. Moreover, upward cation diffusion continues through the opening in the alumina layer until the latter fully bridges the gap, as inferred from the thicker monoxide layer over the center of the pocket in Figure 6.2(d,f), Figure 6.6(b) and Figure 6.7(b). Because the IOZ front is always ahead of the growth fronts for the tungstate and spinel, when the gap closes there is a region of IOZ where the alumina particles are embedded into the unoxidized alloy. Downward diffusion of oxygen, clearly evident by the continued, albeit slow growth of the alumina scale,

gradually converts these pockets of metal matrix into spinel, consuming some of the internally formed alumina particles. The reduction in the population of IOZ pockets with increasing Cr and Al contents suggests that the lateral growth of the continuous alumina is accelerated by increasing the activity of Al in the bulk. The alloy grain size in the present samples is also fairly small, ~7 μm. In the next chapter, TGO morphology will be investigated on samples with larger ~1 mm grains and single crystalline samples as well.

6.3.4. Prospective Alloying Strategies

The results from this combinatorial study outline the challenges presented for designing Co-γ/γ′ alloys with desirable oxidation resistance, an adequate content of γ′ and minimal contents of W or Al-rich tertiary phases. The trends indicate that increasing Al and Cr contents, and to a lesser extent Ni and W, all benefit oxidation behavior. However, higher concentrations of these elements also lead to the precipitation of undesirable alloy phases. The thermodynamic calculations suggest that a field containing only γ and γ′ exists only in the ITIC for the W library, i.e. (21) in Figure 6.3(b). However, none of the alloys in that field exhibit a high fraction of positive PSLS results ($\phi \leq 0.6$). Conversely, substantial numbers of samples showing more favorable oxidation behavior ($\phi \geq 0.8$) contain the μ phase in addition to γ and γ′, as seen on fields (31) in Figure 6.3(a,b,c). In order to balance out these effects, it is useful to plot the oxidation behavior across composition space on top of the corresponding alloy phase diagram, as has been done in Figure 6.3 using PANDAT alloy phase calculations. In this view, many of the samples with more desirable oxidation behavior (plotted in green) fall within phase fields containing the desired γ′ phase. While a W-rich phase is also predicted to occur in many of these samples, the second ITIC of Figure 6.3 (Co-W-Ni) shows some samples lying within the two-phase γ/γ′ field with more

promising oxidation behavior. A starting point to define the design space for Co - γ/γ′ alloys in the six-component space can then be defined by compositions in the range (30-40) Ni, (5-8) W, ~11 Al, ~2 Cr and ~4 Ta (all in at.%) Note, however, that a high ϕ value is not a sufficient condition for a desirable scale, as small thickness is also a desirable attribute. The thinner scales in this investigation arise from samples 2a and 6h in Figure 6.1(l), shown in cross section in Figure 6.2(c) and Figure 6.6(h). These correspond to Cr contents of ~9 at.% but the 6h sample is at the border between fields (31) and (32) in Figure 6.3(c), where γ′ is replaced by β and μ is preserved. In essence, increasing Cr favors thinner scales but also reduces the γ′ solvus, as noted earlier. A strategy to modify the composition to improve the combination of oxidation behavior and mechanical properties will be pursued in the following chapter.

6.4. Synopsis

This combinatorial study has identified alloy composition regions of promising oxidation behavior in the Co-Ni-Al-W-Cr-Ta system. Alloys with: ≥11 at.% Al, ≥4 at.% Cr, between 7 – 10 at.% W, and ≥26 at.% Ni exhibit relatively thin layers of continuous α-Al_2O_3 after 1 h isothermal exposure in air at 1100°C. Decreasing W alloy content was observed to be deleterious to Al_2O_3 scale forming behavior, and DFT calculations suggest this may be due to the effect of W additions raising μ_{Al}. In contrast to beneficial effects on oxidation behavior, Al, W, and Cr additions were also observed to favor the precipitation of undesirable alloy phases, notably β-(Co,Ni)Al and μ-Co_7W_6. Thus, selection of the optimal concentrations of alloying additions may be achieved by combining the experimental oxidation results of this study with calculations of the phase constitution using the PANDAT database. The following chapter will take these identified trends between composition,

oxidation behavior and alloy phases, and combine them to outline the design space for improved Co-base γ/γ’ alloys, arriving at a series of alloys designated ”DMREF”.

6.5. Tables and Figures

Table 6.1**:** Compositions of the substrates and the IPD cathodes.†

	Co	Ni	Al	W	Cr	Ta	S	Ni:Co
Substrate	79.7	0.0	8.9	6.7	3.3	1.5	0.5	0:1
Cathode 1	77.1	0.0	12.2	5.9	3.4	1.4	3	0:1
Cathode 2	33.5	35.4	14.4	11.8	3.4	1.5	2	1:1
Cathode 3	33.4	34.6	**20.7**	6.5	3.4	1.4	1	1:1
Cathode 4	40.9	40.4	13.8	**0.0**	3.5	1.4	1	1:1
Cathode 5	30.0	29.3	11.8	6.0	**21.5**	1.4	4	1:1

† Compositions measured by ICP in atomic percent, except for S, which is in parts per million by weight (ppmw).

Table 6.2**:** Compositions of selected IPD alloys prior to oxidation (SEM-EDS, at. %).

Figure	Co	Ni	Al	W	Cr	Ta	Ni:Co	Al:W	Cr:Al
2a	38	32	11	8	9	3	0.83	1.5	0.78
2b	38	35	16	7	2	3	0.91	2.2	0.12
4	41	36	11	7	2	4	0.88	1.6	0.17
5	51	24	10	9	2	4	0.47	1.2	0.16
6a	51	23	10	8	4	3	0.45	1.2	0.38
6b	41	33	10	9	4	3	0.81	1.2	0.37
6c	42	32	12	9	2	3	0.76	1.3	0.16
6d	38	34	15	8	2	4	0.88	1.9	0.14
6e	42	40	12	2	2	3	0.95	5.9	0.20
6f	37	38	12	9	2	4	1.02	1.3	0.16
6g	46	28	10	9	4	3	0.62	1.1	0.38
6h	41	29	10	8	9	3	0.71	1.2	0.90
7	39	35	12	10	2	3	0.89	1.2	0.17

Table 6.3**:** Spot measurements of constituents in Figure 6.5 (TEM EDS).

Spot	Composition (at.%)						$\frac{Ni}{Co}$	$\frac{(Al+Cr)}{(Ni+Co)}$	$\frac{W}{(Ni+Co)}$	Nominal Oxide
	O	Co	Ni	Al	Cr	W				
1	53	36	12	-	-	-	0.3	-	-	(Co,Ni)O
2	63	29	8	-	-	-	0.3	-	-	(Co,Ni)O
3	60	17	-	-	-	23	0.0	-	1.4	$CoWO_4$
4	59	8	4	27	1	-	0.4	2.4	-	$(Co,Ni)Al_2O_4$
5	64	8	5	17	6	-	0.7	1.7	-	$(Co,Ni)(Al,Cr)_2O_4$
6	59	11	8	-	-	22	0.7	-	1.2	$(Co,Ni)WO_4$
7*	62	3	8	27	1	-	2.7	2.6	-	$(Co,Ni)Al_2O_4$
8	64	6	12	-	-	19	2.1	-	1.1	$(Co,Ni)WO_4$
9*	67	-	-	32	1	-	-	N/A	-	Al_2O_3
10	66	4	12	-	-	18	2.8	-	1.1	$(Co,Ni)WO_4$
11*	64	5	31	-	-	-	6.3	-	-	(Co,Ni)O
12*	66	3	6	26	-	-	2.2	3.0	-	$(Co,Ni)Al_2O_4$
13*	65	-	9	26	-	-	N/A	2.9	-	$NiAl_2O_4$
14	63	-	-	37	-	-	-	N/A	-	Al_2O_3
15*	66	-	-	34	-	-	-	N/A	-	Al_2O_3

* Measurements taken with an FEI Tecnai G2 Sphera at 200 kV.

Table 6.4**:** DFT calculations of the Al chemical potential in γ-γ′ phases at 900°C

Solvent Metal	Al (at.%)	W (at.%)	μ(Al) (eV/atom)	Δμ(Al) (eV/atom)
Co	9.0	4.0	-0.740	-0.098
Co	10.0	10.0	-0.838	
Ni	14.0	0.0	-2.810	0.920
Ni	14.5	15.3	-1.890	

Table 6.5**:** Candidate compositions with promising oxidation behavior (at.%).

Library	Co	Ni	W	Al	Cr	Ta
1	Bal.	≥ 22	9	≥ 11	2	3.5
2	Bal.	≥ 22	7-10	11	2	3.5
3	Bal.	≥ 26	9	10	≥ 4	3.5

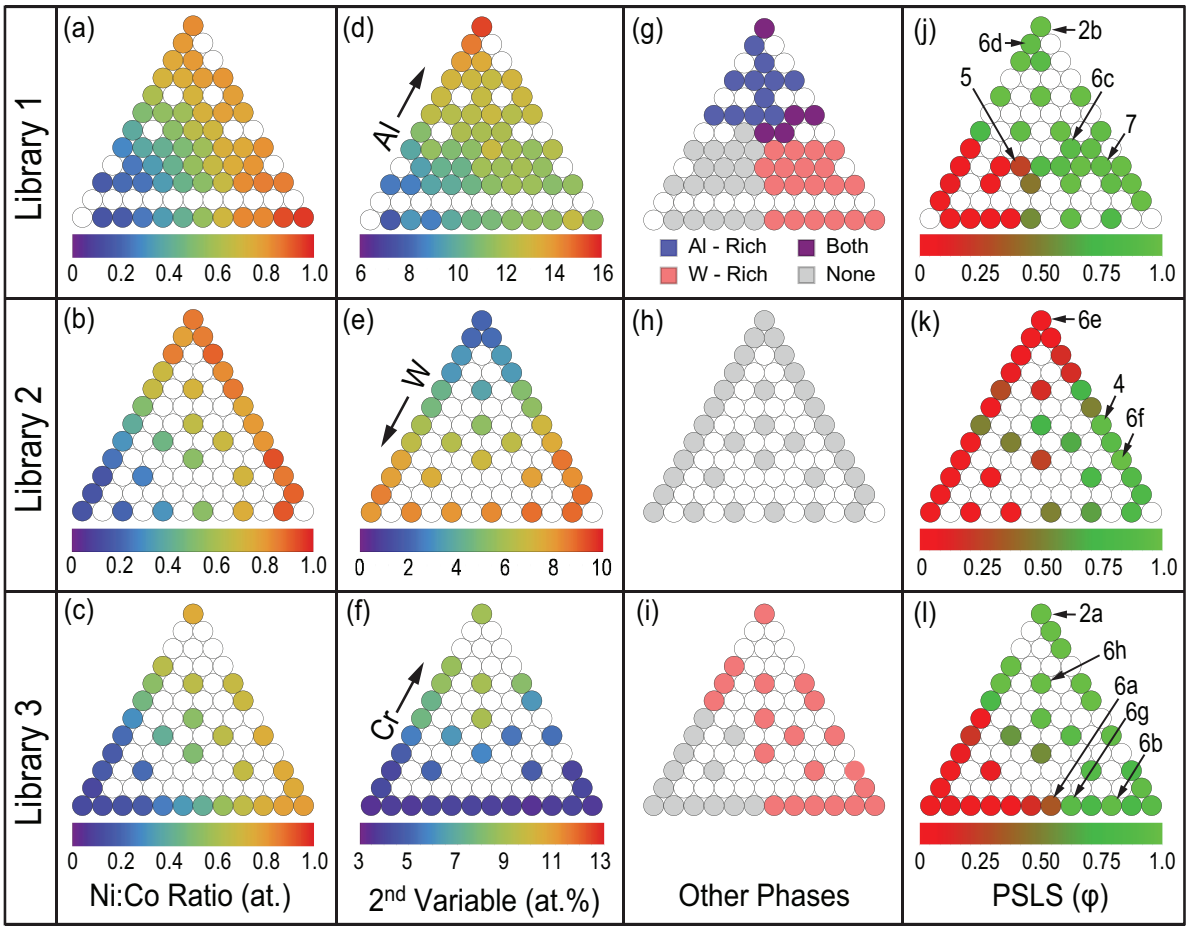

Figure 6.1**:** Overview of the relevant features for the combinatorial libraries. (a-f) depict the compositions of the IPD generated alloys prior to oxidation, The Ni:Co ratio increases from left to right in (a-c), whereas the key alloying elements investigated, namely Al, W and Cr, vary along the height in the direction of the arrows. The remaining elements remain fairly constant across each individual library. (g-i) depict the presence or absence of secondary minor phases beyond the γ/γ' matrix, while (j-l) illustrate the oxidation behavior based on the detection of α-Al_2O_3 by PSLS. ϕ represents the fraction of PSLS spectra showing the characteristic α-Al_2O_3 doublet out of 24 measurements for each sample, as described in Chapter 5. The labels on the different samples in (j-l) correspond to micrographs in the different figures that follow.

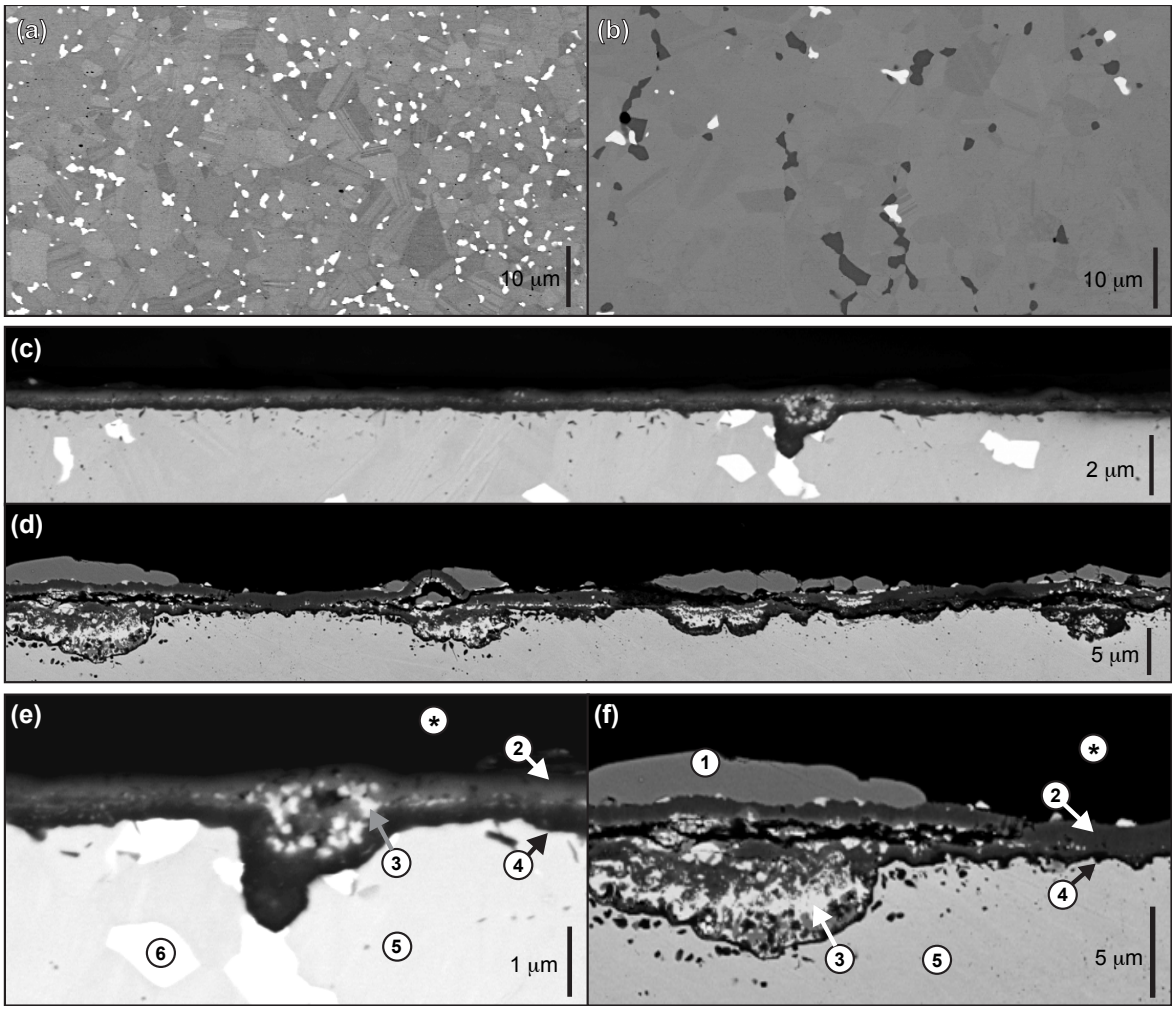

Figure 6.2: Backscattered electron micrographs of (a,b) IPD alloy surfaces corresponding to the Al-rich and Cr-rich tips of libraries 1 and 3, respectively (Table 2), prior to oxidation, and (c-f) these same alloys in cross-section after oxidation. Figures (a,c,e) correspond to the same high-Cr alloy, and (b,d,f) to a different high-Al sample. The scales shown are among the thinnest observed after the oxidation at 1100°C for 1h in air. Phases are identified based on SEM EDS information: (1) (Co,Ni)O, (2) (Co,Ni)Al_2O_4, (3) (Co,Ni)WO_4, (4) Al_2O_3 scale, (5) remaining bulk alloy. The brighter phases in (a) and (b), labeled (6) in (e), are μ-Co_7W_6 intermetallics, and the darker phases in (b) are Al-rich B1 phases (β). (*) denotes the epoxy mount in (e) and (f). The positions of these two alloys are labeled on Figure 6.1 and Figure 6.3 as "2a" and "2b" respectively.

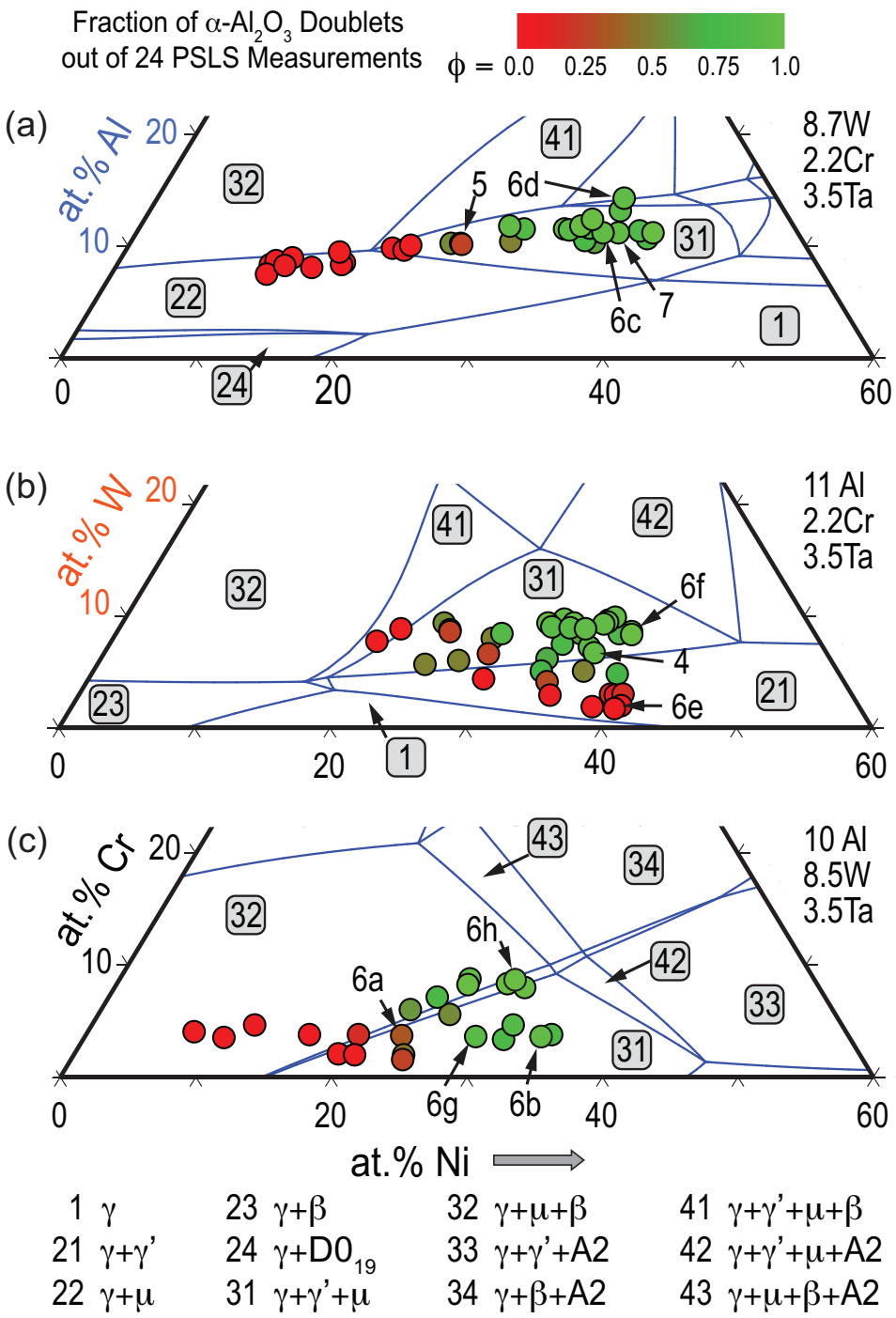

Figure 6.3: ITIC sections of the composition space relevant to the combinatorial libraries, calculated using the PanCo-2018 database. All sections are at constant 1100°C, with the rest of the elements listed on the right. Thus, the corners of these plots are not 100% one element, but rather primarily one element plus the three remaining elements at their respective constant concentrations. The key to the phase field labels is at the bottom. Please note that any of these sections may contain alloys that are part of more than one library. Alloys presented in other figures are labeled on the ITIC diagram where present, e.g. the alloy in Figure 6.5 is labeled "5".

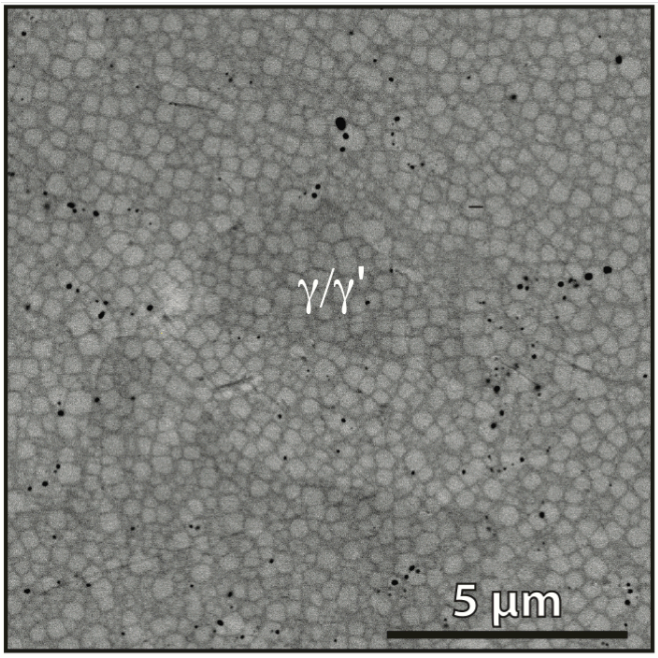

Figure 6.4: Two-phase γ/γ′ microstructure in one of the combinatorial alloys after oxidation, labeled "4" in Table 6.2, Figure 6.1, and Figure 6.3. This alloy composition is predicted to lie just outside the two-phase field, in the γ+γ′+μ field (Figure 6.3 field (31)), but it is found not to exhibit any μ phase experimentally. The very fine nature of the γ′ particles is likely due to the very short 1 h effective alloy aging time during the oxidation exposure.

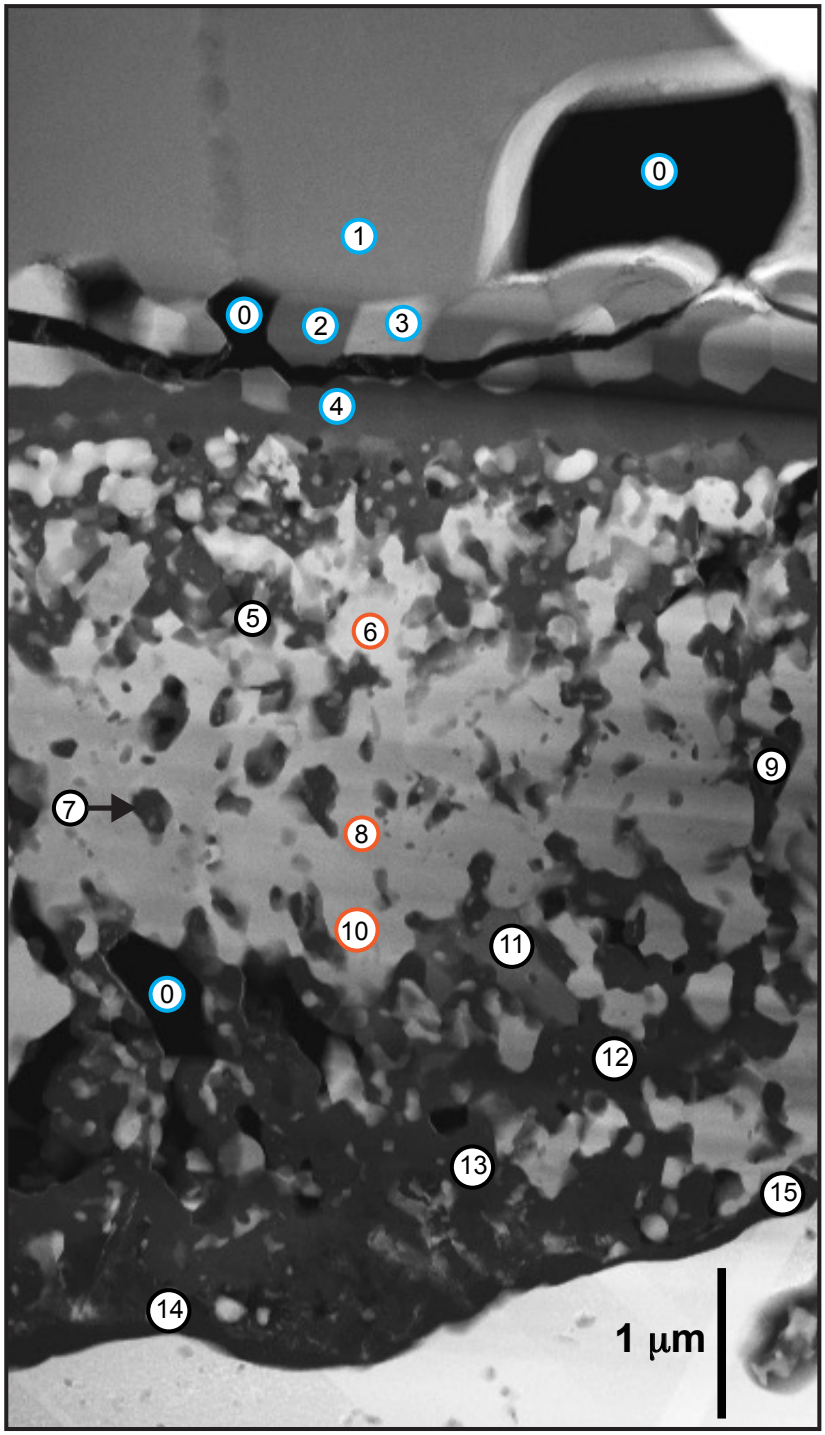

Figure 6.5: Bright field TEM image of a FIB lamella of the oxide scale grown on a combinatorial sample (Co - 24Ni - 10Al - 9W - 2Cr - 4Ta at.%, labeled "5" in Figure 6.1 and Figure 6.3) after 1 h in air at 1100°C. Spot measurements were taken by TEM EDS as labeled, and are given in Table 6.3. There are three general categories of oxides: outer oxides closer to the gas interface (blue circles), tungstates (orange circles), and internal particles or scale of spinel / alumina, as well as an embedded particle of monoxide (black circles).

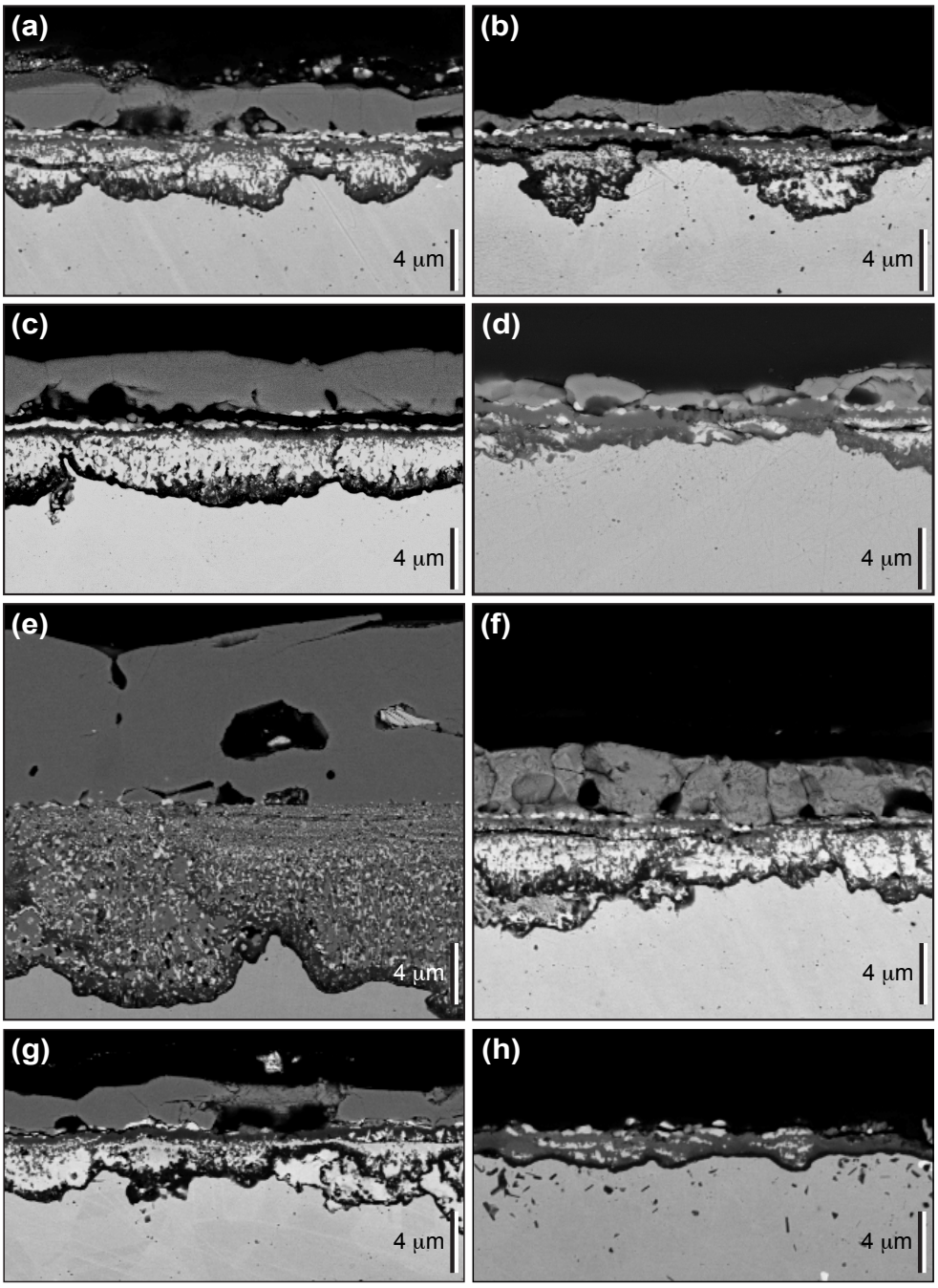

Figure 6.6: Backscattered electron micrographs of oxidized combinatorial samples shown in cross-section. Alloys selected primarily vary in only one component left to right. The 7b alloy in (b) has increased Ni:Co ratio over (a), with the other solute metals fairly constant. Likewise, (d) has increased Al compared with (c), (f) has increased W content over (e), and (h) has increased Cr content over (g). All increases lead to thinner scales. Compositions of the unoxidized alloys as measured by SEM EDS are given in Table 6.2, and labeled in Figure 6.1 and Figure 6.3 as "6a" – "6h" respectively.

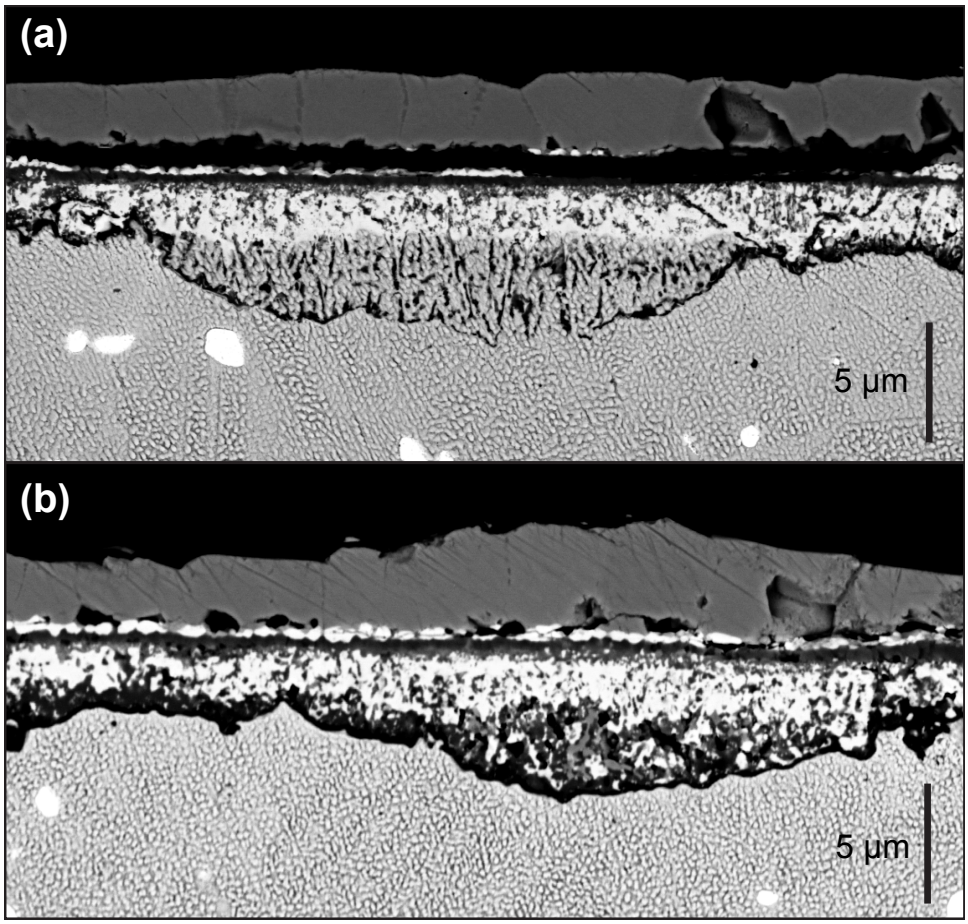

Figure 6.7: Backscattered electron micrographs showing the same alloy composition in both (a) and (b) (labeled in Figure 6.1, Figure 6.3, and Table 6.2 as "7") in cross-section after oxidation in air at 1100°C for (a) 15 minutes, and (b) 1 hour. Black particles are internal Al_2O_3, and the lowest lying oxide, shown in black is Al_2O_3 scale. As time progresses, the underlying Al_2O_3 grows laterally to form a complete layer.

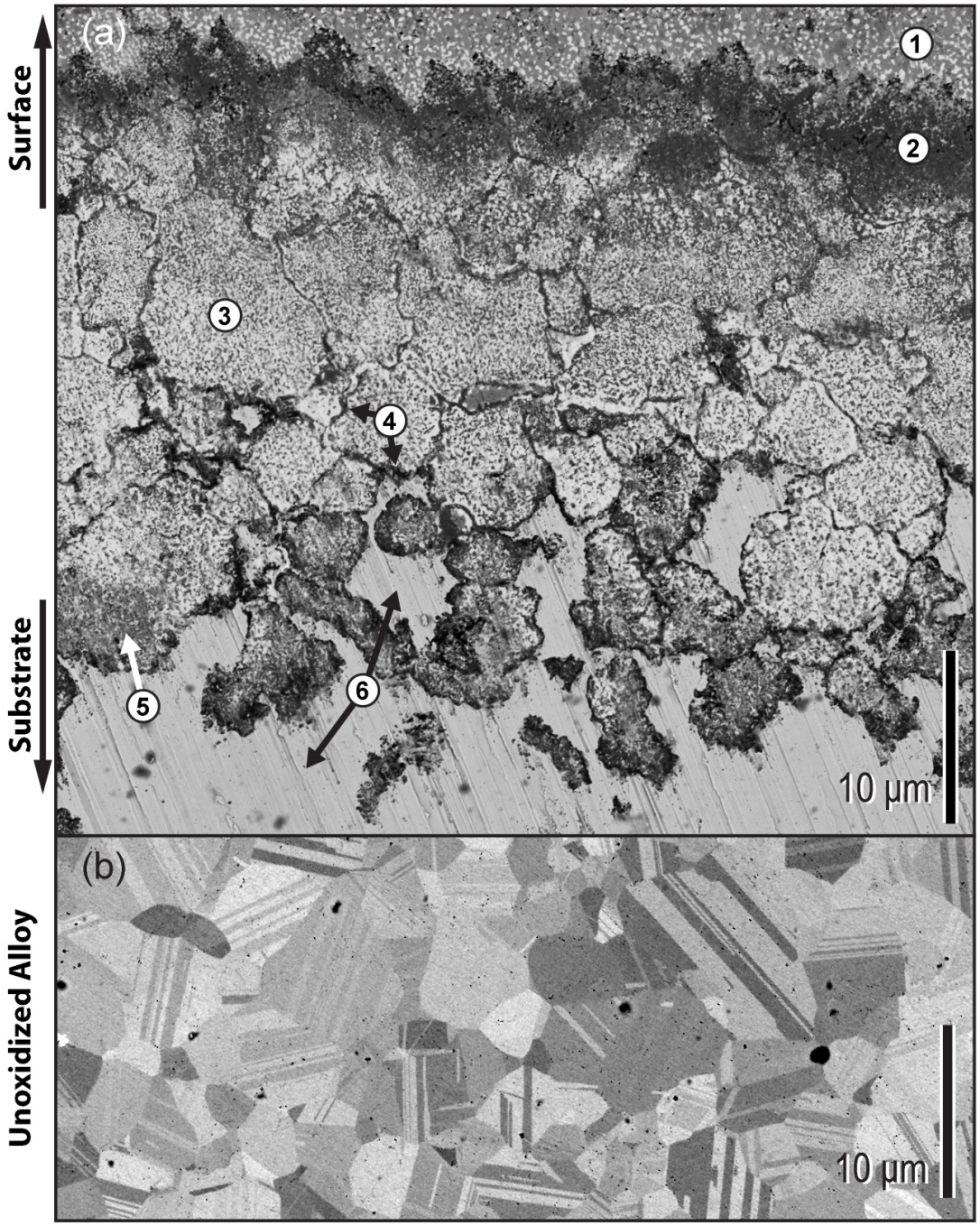

Figure 6.8: In plane views of (a) the scale/substrate interfacial region polished at a slight angle relative to the button surface, and (b) the alloy microstructure prior to oxidation. The specimen is the same as in Figure 6.5, and is labeled in Table 6.2, Figure 6.1, and Figure 6.3 as "5". In reference to Figure 6.5, the numbers in (a) correspond to the (1) the layer of tungstate and monoxide directly under the thicker monoxide layer, (2) the layer of spinel underneath, (3) the IOZ region with a tungstate matrix, (4) the traces of the continuous alumina layer surrounding each IOZ pocket, (5) the IOZ region with a Ni-rich oxide matrix, and (6) the remaining alloy near the oxide scale. Note the similarity in grain sizes between the unoxidized alloy and the lateral dimension of the IOZ regions near the top, e.g. (3).

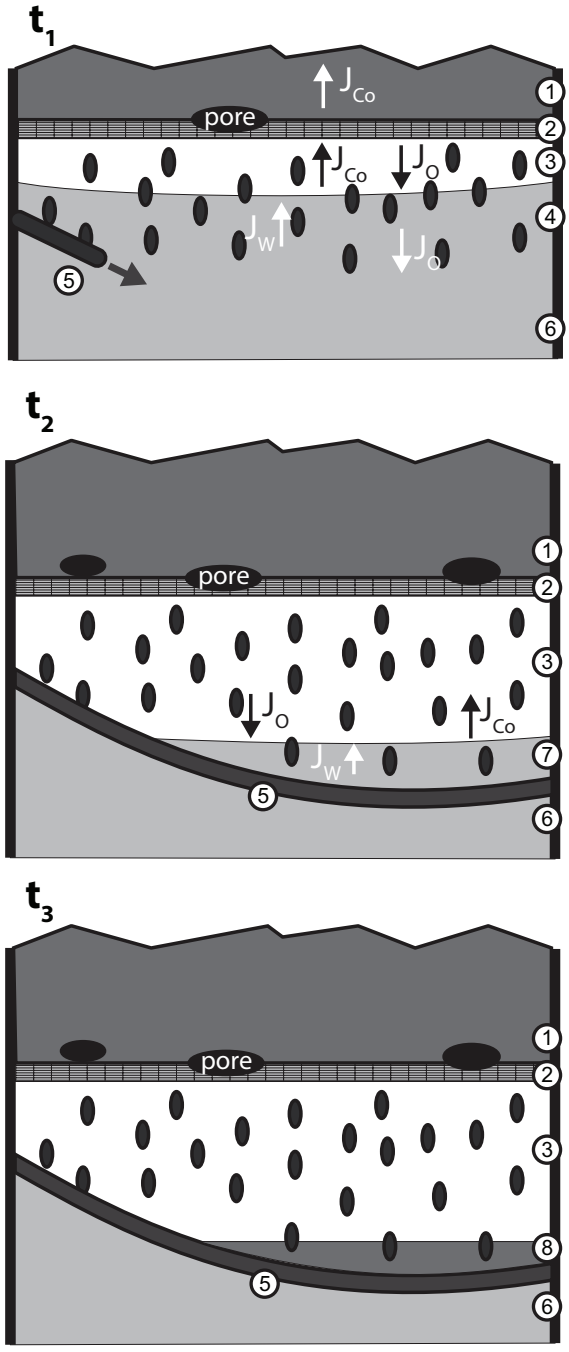

Figure 6.9: Schematic of the proposed chronology behind the formation of IOZ pockets above continuous Al_2O_3 scale, with features labeled: (1) (Co,Ni)O, (2) mixed oxides, (3) $(Co,Ni)WO_4$, (4) Al_2O_3 IOZ, (5) undercutting Al_2O_3 scale, (6) bulk alloy, (7) Ni-rich metal, (8) Ni-rich oxides. An IOZ of Al_2O_3 particles forms within the bulk metal, until a patch of semi-continuous Al_2O_3 forms at some point along the reaction front (t_1). This patch grows laterally across the reaction front, until the entire IOZ is closed off from the bulk alloy (t_2). Growth of the oxide scales continues quickly above the Al_2O_3 layer, depleting W and Co from the metallic IOZ matric, and eventually oxidizing it into Ni-rich monoxide and/or spinel (t_3).

7 Design of a Multicomponent Oxidation Resistant Alloy

Previous chapters have outlined compositional domains within the Co-Ni-Al-W-Cr-Ta system that have promising oxidation behavior. They also established the underlying trends for the dependence of phase equilibria and oxide scale formation on alloy composition. This chapter will demonstrate how the knowledge base established previously can guide the identification and development of improved Co-base γ/γ' alloys, while also advancing the scientific understanding of this materials system. Though the resultant alloy does possess a remarkable combination of properties, the purpose of this investigation was not to develop a commercially viable material. Instead, the activity was undertaken as a proof of concept, to demonstrate the effectiveness of the discovery and design strategy.

Additionally, the conditions used for the oxidation experiments have thus far consisted of isothermal exposures in air for 1 h at 1100°C. This was to identify alloy compositions that can form a continuous α-Al_2O_3 scale at this shorter time period. Such behavior was assumed to be a prerequisite for oxidation resistance under more realistic conditions for an engine environment: thermal cycling and much longer exposure times. This chapter will examine these more severe exposures on alloys identified as improvements on the baseline.

The ultimate goal of the development strategy was to create a base alloy that achieves both a high-γ' solvus temperature and adequate oxidation resistance based on the formation of a continuous α-Al_2O_3 layer in air at 1100°C. The senary composition space was anticipated to have sufficient alloying additions to achieve these goals but following the history of Ni-base superalloys it is anticipated other alloying additions may be desirable.

However, the senary system has been adequate to develop the fundamental understanding of the effects of the key elements on alloy behavior. In general, increased concentrations of Ni, Al, W, and Cr all reduce the total scale thickness as described in Chapter 6. Specifically, Al and Cr were found to be the most effective in forming continuous α-Al_2O_3 scale with minimal amounts of other undesirable oxide phases. This chapter will build on these findings to arrive at an alloy that meets the targets specified above. A base senary composition can then be alloyed further for enhanced behavior; e.g., reactive elements (RE) could be explored to improve scale adhesion [53]. As longer oxidation times are explored, the use of PSLS can be extended from detecting the presence of α-Al_2O_3 to evaluate the stress state in the alumina by piezospectroscopy [119].

7.1. Design Approach

A series of Co-based γ/γ' compositions, termed DMREF alloys after the NSF program sponsoring this work, were designed based on the critical outcomes of Chapter 6, namely

- The composition regions of more promising oxidation behavior, namely those alloys that are able to form continuous α-Al_2O_3 scale with smaller amounts of overlying oxides after 1 h in air at 1100°C.
- The elucidated dependence of the thermally grown oxide (TGO) on the content of individual alloying additions.
- The role of alloy composition on the formation of phases beyond γ/γ', especially those that might be deleterious to mechanical behavior.

These insights were combined with phase equilibria calculations using the PANDAT PanCobalt-2011 thermodynamic database (CompuTherm LLC, Middleton, WI) [140].

Isothermal isoconcentrate (ITIC) sections similar to those in Figure 6.3 were calculated at 1100°C for the composition regions of more promising oxidation behavior. The calculated γ/γ' alloy two-phase field of interest was then overlaid with the rapid PSLS screening of oxidation results. From this, compositions predicted to have both more promising oxidation behavior and a γ/γ' microstructure were identified. The predicted absence of tertiary phases was confirmed experimentally from observations in Chapter 6.

Building on this initially identified region, a potential design space was outlined by moving compositionally along directions known to benefit oxidation, and towards the corners of the calculated γ/γ' field (Figure 7.1). The edges of this design space were selected as initial DMREF alloys. After synthesis and experimental characterization of these alloys, further refinements were made to the composition to select for improved oxidation and γ' stability, while staying within the two-phase field.

Following the design approach, isothermal-isoconcentrate (ITIC) sections were calculated for compositions shown in Chapter 6 to yield more promising oxidation behavior. No γ/γ' two-phase field was expected at 1100°C with constant 25.0 at.% Ni, 2.0 at.% Cr, 3.5 at.% Ta, so a section was instead calculated at an increased Ni content of 35 at.% to stabilize the γ' phase [19]. The desired γ/γ' field was present in this higher-Ni ITIC section, and the results from PSLS screening of oxidized samples were overlaid on this plot (Figure 7.2). By comparing the samples with more promising oxidation behavior (green) with those in the γ/γ' field(s), an alloy composition with balanced properties was identified and designated as 2-6G, marked by an asterisk in Figure 7.1 and Figure 7.2 (and previously marked "4" in Figure 6.3b). This alloy would serve as a starting point for the design of the DMREF alloy

series. The composition of this baseline alloy measured by EPMA was Co–32.4Ni–4.4W–11.7Al–3.3Cr–1.5Ta at.% (Table 7.1).

From the starting alloy 2-6G as measured by EPMA, the Ta content was increased slightly to 3.5 at.% to increase stability of the γ' phase. Subsequently, the design space of the DMREF alloys was outlined by moving towards the corners of the calculated γ/γ' phase field in directions favorable for oxidation behavior, schematically indicated in Figure 7.1. In this manner, the compositions of alloys DMREF-8 and DMREF-9 were defined. DMREF-8 has increased Al content from the starting composition 2-6G, which is known to benefit Al_2O_3 formation. DMREF-9 has both increased Al and Cr contents over 2-6G, and decreased W content to stay within the calculated γ/γ' phase field. While reduced W content is expected to undesirably increase oxide thickness based on previous experiments in this senary alloy space [177], Al and Cr additions were observed to strongly benefit alumina formation, and might be expected to outweigh the effect of less of W on oxidation behavior. Minor compositional alterations to DMREF-9 were subsequently made to ensure its location within a two-phase γ/γ' field, resulting in DMREF-10, namely lowered Al and raised Ni (Table 7.1). While future alloy designs may desire the presence of tertiary alloy phases, or at least tolerate them, the goal of the present approach was to demonstrate the development of a two-phase alloy.

7.2. Experimental Details

Alloy compositions formulated by the above approach were synthesized via arc melting under gettered Ar ($<10^{-10}$ O_2). Oblate ellipsoidal buttons 11 mm tall by 28 mm diameter and ~ 40 g were melted, inverted and remelted three times during synthesis to minimize macrosegregation, and then solution treated at 1245°C for 12 h, quenched and aged at

1000°C for 50 h under vacuum. For the third stage of development, 8 kg of alloy DMREF-10+ was cast by commercial supplier Sophisticated Alloys (Butler, PA) with specifically controlled low S content. This ingot was then tested in polycrystalline form, as well as cast into single crystals via the process described in Chapter 3.

Samples for oxidation were prepared as described in previous chapters. Isothermally oxidized samples were injected rapidly into the hot zone of a controlled-atmosphere furnace preheated to 1100°C. Samples were held for the prescribed dwell time, and then extracted from the hot zone over the course of 5 minutes. Cyclic oxidation was performed in laboratory air and a tube furnace preheated to 1100°C, with the samples injected and ejected automatically using a computer controlled mechanism. Samples were held at the maximum temperature for 1 h and at room temperature for 20 min between cycles. The effective ramp rate was approximately 200°C/min, as shown in Figure 3.3. PSLS [178] was used for initial screening of the thermally grown oxide [169]. For piezospectroscopy mapping, a more advanced setup with faster acquisition times was used, utilizing a 488 nm incident laser (Ar/Kr) of ~140 mW. The cyan incident laser also shifted the location of the NiO Raman peaks away from the α-Al_2O_3 fluorescence doublet [151], allowing the frequency shift of the doublet to be evaluated more easily. PSLS mapping of the alumina stress state was conducted after 1, 9, 25, 64, 100, and every subsequent hundred thermal cycles.

After the desired oxidation, samples were prepared for sectioning by sealing the surface with adhesive M-bond 610 and curing for 1 h at 175°C. Sealed samples were embedded in epoxy and cross-sectioned, followed by mounting again in epoxy to infiltrate any exposed fractures or pores. The exposed cross-section surface was then finished to 0.05 μm using a vibratory polisher with diamond suspension. The latter was used for the exposed cross-

sections, instead of alumina suspension, to prevent any embedded grit particles from interfering with chemical analysis of the oxide microstructure.

7.3. Results

The compositions and critical temperatures of the alloys investigated in this chapter are summarized in Table 7.1. The findings are described in the following sections.

7.3.1. First Stage of Development: DMREF 8 and 9

7.3.1.1. Alloy Microstructure and Physical Properties

No γ' phase was detectable in BSE imaging after solution treating for 12 h at 1245°C and aging for 50 h at 1000°C) for DMREF-8, as shown in Figure 7.3. However, evidence for the γ' phase was observed in both DTA (Figure 7.4) and X-ray diffraction (Figure 7.5) of the alloy prior to oxidation. The small endotherms labeled as the γ' solvi (* in Figure 7.4) in the DTA measurements were attributed as such based on prior literature investigations of γ/γ' calorimetry [179]. Furthermore, small amounts of an Al-rich phase, likely β-(Ni,Co)Al, appear in addition to the γ/γ' phases as evident in Figure 7.3(b,d). DMREF-9 was also found to contain small amounts of the Al-rich β phase, but in that case a high fraction of γ' was clearly visible by BSE imaging, e.g. Figure 7.3(d). The γ' solvi of DMREF-8 and 9 were 1226°C and 1195°C respectively (Table 7.1). The β-phase would not be reasonably attributed to the endotherms labeled γ' in the DTA results due to the small phase fraction.

7.3.1.2. Short Term Oxidation Behavior

After isothermal oxidation in air at 1100°C for 1 h, both DMREF-8 and -9 exhibited significant α-Al_2O_3 signal by PSLS. Microstructural images in Figure 7.6 (c-f) reveal that both alloys indeed contained continuous Al_2O_3 scale, with DMREF-8 having some portions

of oxide ~4.5 μm in thickness, and other regions of ~2 μm, for an average oxide thickness of 3.2 μm. DMREF-9 had a more consistent average thickness of ~1.9 μm. The ~2 μm thick oxide scale regions in both samples appeared to be primarily Al_2O_3 overlaid by a layer of spinel, while those portions of DMREF-8 that were thicker additionally consisted of outer (Co,Ni)O, and an inner region of Al_2O_3 IOZ embedded within tungstate above the continuous Al_2O_3. (The microstructure of these IOZ pockets has been discussed at length in Chapter 6.) Based on these alloys outlining the general design space for oxidation resistant γ/γ' Co-Ni-W-Al-Cr-Ta compositions, DMREF-9 was chosen for further refinement based on its superior oxidation resistance, and it's minimally depressed γ' solvus over DMREF-8, despite the higher Cr content.

7.3.2. Second Stage of Development: DMREF-10

7.3.2.1. Alloy Composition and Constitution

While a limited amount of β phase may not necessarily give rise to unacceptable mechanical properties, the present exercise was to generate a two-phase γ/γ' alloy. As such, the arguably undesirable β phase observed in DMREF-9 was removed by slightly lowering the Al content, and raising the Ni content to increase the Al solubility, i.e. to expand the size of the γ/γ' two-phase field. The result was DMREF-10, which had a high γ' phase fraction cuboidal γ' morphology with no additional alloy phases after heat treatment, (Figure 7.7a).

7.3.2.2. Short term Isothermal Oxidation

Oxidation for 1 h in air at 1100°C revealed alumina formation, with a total oxide scale thickness ~2 μm, e.g. Figure 7.7(b,c). More in-depth analysis by TEM, shown in Figure 7.8 identified the phase and compositions summarized in Table 7.2. The scale after 1 h

consisted of occasional outer (Co,Ni)O monoxides, layers of spinel $Co(Al,Cr)_2O_4$, particles of tantalate $(Co,Ni)(Ta,W)_2O_6$, mixed oxides, and finally continuous Al_2O_3 scale. The presence of such tantalates is a notable difference from the prior DMREF-8 and 2-6G samples, which were instead observed to have tungstate (not observed in DMREF-10). Underneath these oxides was an alloy depleted in Al, followed by high aspect-ratio particles that appeared to be aluminum nitrides as opposed to oxides (cf. Table 3.2). Finally, the density of the pristine DMREF-10 alloy was measured to be 8.65 g/cm^3, comparable to the 2nd generation Ni-base superalloys used in aero engines (Figure 7.9).

7.3.2.3. Longer Isothermal Exposure and Cyclic Oxidation

Though a thin, adherent alumina scale was observed on the DMREF-10 alloy after 1 h in air at 1100°C, the oxidation behavior was less ideal at longer 50 h exposures of hot time, both isothermal and cycling (Figure 7.10). The oxide scale formed was found to be still relatively thin, ~4 μm in both the isothermal and cyclic exposures, with a correspondingly small underlying γ' denuded region of ~7 μm in the isothermally oxidized sample and ~5 μm in the cyclic sample. Yet almost the entire oxide had spalled, delaminating between the alumina layer and underlying metal as shown clearly in Figure 7.10(a). Measuring the weight gain over time during 1100°C cyclic oxidation (Figure 7.11), the DMREF-10 alloy exhibited an initial rapid gain of 0.5 mg/cm^2 by 1 h, which remains fairly constant until 5 h, where the sample rapidly loses mass for a zero mass-gain (ZMG) between 15-25 h. In comparison, a piece of single crystal René N5 had a much lower mass gain of 0.1 mg/cm^2 by 1 h, which continued to increase parabolically with a rate constant of ~0.001 mg^2/cm^{4}h for the first 350 h (total weight gain of 0.64 mg/cm^2 after 350 h) and did not experience significant mass loss through 1000 h.

7.3.3. Third Stage of Development: DMREF-10+

The DMREF-10 composition was then modified with small RE additions of Hf and Y, as well as grain boundary strengtheners C and B, to yield an alloy designated as DMREF-10+. After commercial casting and analysis by ICP, the alloy was measured to have a low-sulfur content of 0.7 ppmw (Table 7.1). The ingot was then used in both polycrystalline form, denoted "DMREF-10+PX", and cast into single crystals using a Bridgman furnace. The latter was designated as "DMREF-10+SX". Aside from these changes to the grain structure, there were no observed differences in alloy microstructure. Prior to solution heat treatment, EPMA was conducted (courtesy of Gareth Seward and Sean Murray at UCSB) on a single crystalline piece to conduct Scheil analysis of solidification segregation (Figure 7.12), with estimated average partition coefficients given in Table 7.3. Furthermore, EPMA of the alloy after solutionizing verified that the compositions had been appropriately homogenized between the dendritic and interdendritic regions.

BSE microscopy of the unoxidized alloy after heat treatment revealed a very similar microstructure to that of DMREF-10, cf. Figure 7.7(a,d). Upon cyclic oxidation, however, DMREF-10+ excelled over its unmodified counterpart (Figure 7.11). A polycrystalline sample experienced 0.32 mg/cm^2 weight gain after 1 h, while single crystalline samples experienced gains of 0.38 mg/cm^2 after 1 h. The zero net-mass gain point (ZMG) for DMREF-10+PX was not observed until between 450 and 500 one-hour cycles, while single crystalline samples reached the ZMG between 250-350 h, and Ni-base René N5 did not experience significant mass loss through over 1000 cycles. Analysis of the DMREF-10+PX sample after 500 h of cyclic exposure at 1100°C shows large oxide nodules forming along the edges and corners of the sample (Figure 7.13). In cross-section, it was observed that

while the majority of the sample surface consists of a continuous alumina layer overlain by spinels and tantalates (Figure 7.13c), significant oxide growth is experienced along the geometrically sharp features of the sample (b). These large nodules are observed to be somewhat friable, and to consist of repeated layers of refractory oxide and spinel, as well as a thick outer layer of monoxide. However, it should be noted that a continuous layer of alumina was still present under these thick nodule regions. Closer analysis of the oxides present along the flat faces of this sample via TEM of a FIB lamella is shown in Figure 7.14. The oxide features were nominally identified based on TEM EDS, and were fairly similar to the features observed on DMREF-10 after 1 h exposure. There is an inner continuous layer of Al_2O_3 (5), above which lay tantalate particles with some solubility for Ni and W, $(Co,Ni)(W,Ta)_2O_6$ (3) sandwiched between two layers of spinel, the inner (4) $(Co,Ni)Al_2O_4$, and the outer containing some Cr, (2) $(Co,Ni)(Al,Cr)_2O_4$. Finally, there is a layer of large-grained spinel (1), of the same composition as the underlying small-grained spinel layer. This differs from the 1 h exposure of DMREF-10, which only had occasional small grains of monoxide above a fine-grained spinel layer (Figure 7.8, point 1).

One factor influencing spallation behavior of TGO scale is the coefficient of thermal expansion (CTE) mismatch between the oxides and metal substrate. Dilatometry measurements of the alloys and polycrystalline Al_2O_3 are presented in Figure 7.15, showing that the mean CTE was not drastically different between René N5 and DMREF-10+, especially at the oxidation temperature 1100°C. Finally, PSLS measurements of the α-Al_2O_3 stress state at various stages of the cyclic oxidation are shown in Figure 7.16, comparing DMREF-10+SX with single crystalline René N5. After the first oxidation cycle, both samples have a residual stress of ~4.5 GPa. However as exposure progresses, the stress in

the Ni-base René N5 sample remains fairly constant, while that in DMREF-10+ continuously increases through 300 h to ~7.5 GPa.

7.4. Discussion

7.4.1. Alloy Phase Stability

With the current set of experimental results obtained in the course of these investigations it is possible to provide some assessment of the accuracy of the PanCobalt-2011 database. Although the DMREF-8 and -9 compositions are predicted to lie within a two-phase γ/γ' field, both have some amount of the Al-rich β phase. This is not unexpected, as the compositions lie close to the three-phase γ/γ'/β field, and the phase fraction of β observed experimentally is fairly small. Moreover, the combinatorial buttons often contained additional phases beyond those predicted by the calculated ITIC sections. The inference is that the phase fields and boundary locations are reasonably accurate, as discussed previously in Chapter 6. While it is more difficult to validate the presence of the γ' phase via microscopy (as noted for DMREF-8, cf. Figure 7.3 and Figure 7.5), measured γ' solvi and solidi temperatures from DTA can then be compared with PANDAT predictions, as shown in Table 7.1. The fact that the γ' precipitate size in DMREF-8 is too small to be observed in the micrographs may be attributed to its higher content of Ta and W, delaying coarsening behavior. Overall, there is good agreement between the database and experiments, with the predicted temperatures typically within 50°C of measurements. With these results in mind, one implication for alloy design is that there may be more design space available for DMREF alloys in the direction of increasing W content. Since the phase boundaries calculated are not exact, and no μ phase was detected in any of the experimental DMREF

alloys so far, there may be flexibility to move in this direction before precipitating undesirable μ particles.

7.4.2. Oxide Features

First, there are interesting comparisons between the DRMEF-8, DMREF-9, and the starting alloy 2-6G derived from the combinatorial exercise (Figure 7.6). While both DMREF alloys have thinner average scales, DMREF-8 does exhibit a similar scale morphology to 2-6G, notably in the IOZ pockets of alumina particles embedded in tungstate and underlain by a continuous alumina scale. However, these IOZ pockets are fairly uniform laterally, unlike the combinatorial alloy displaying noticeably hemi-ellipsoidal regions of moderate aspect ratio above a more convoluted alumina layer. As discussed in Chapter 6, it was found that the IOZ pockets in the combinatorial samples were of the same size range as the grain size, ~7 μm. Since the DMREF alloys were arc-melted, they exhibit grain sizes orders of magnitude larger, ~1 mm. Thus, alloy grain boundaries are much less likely to impact the representative oxidation behavior.

The presence of IOZ is avoided entirely in the case of DRMEF-9 and -10, instead consisting of continuous alumina overlain by thin amounts of other oxides. Interestingly, discrete particles of refractory oxides towards the top of the scale stack, next to a continuous spinel layer, are another common feature across many of the investigated alloys. In the combinatorial alloys previously (Chapter 6, Figure 6.6, point 3), discrete tungstate particles $CoWO_4$ were observed in-between outer monoxide (Co,Ni)O and underlying aluminum spinel $(Co,Ni)Al_2O_4$. The oxides on DMREF-10 and -10+ samples are morphologically similar but the refractory oxide in this case is the tantalate $(Co,Ni)(Ta,W)_2O_6$. Since monoxides were rarely observed, these particles are sandwiched between two aluminum

spinel layers $(Co,Ni)Al_2O_4$, with the upper layer having some Cr solubility. The change in refractory oxide phase is logical in that DMREF-9 and -10 both have significantly reduced W content and increased Ta content compared with DMREF-8 and the aforementioned combinatorial alloys. The lack of a monoxide layer in the case of DMREF-9 and -10 occurs concomitantly with lesser overall amount of oxide scale, and is likely attributed to the higher Al content favoring formation of aluminum spinel and a more rapid onset of alumina formation prior to any monoxide layers. As mentioned in the last chapter, tungstates were postulated to be forming as discrete particles higher up in the scale stack, and separate from the large amount of tungstate embedding the IOZ alumina, because they are the result of rapid initial oxidation at the original alloy surface. If that were the case, a similar process may be occurring in DMREF-9 and -10 whereby rapid initial oxidation at the alloy surface forms tantalate particles due to the lack of Ta solubility in the other surrounding oxides. Underlying layers of spinel and alumina could then form by continued oxidation, in an undercutting manner similar to that proposed by Stott et al. [174].

One unexpected observation is the presence of high aspect ratio AlN particles within the depleted alloy region under the oxide scales. These nitrides are undesirable, as they absorb Al necessary to maintain alumina scale growth, but they were only observed in the arc-melted samples, DMREF-8, -9, and -10. DMREF-10+ has approximately the same baseline composition as DMREF-10, however it was made by a commercial supplier, and does not exhibit nitride formation. Nor do any of the combinatorial alloys produced by IPD. One might hypothesize that N might have been introduced during arc melting, perhaps due to a small leak. However, nitrides were not observed in the as-heat treated alloys and are only observed after oxidation, suggesting N is unlikely to have introduced during melting or the

solutionizing treatment., Furthermore, the presence of nitrides underneath the alumina layer despite the lower affinity of nitrogen for Al relative to that of oxygen ($\Delta G°_{AlN}$ = -346 kJ/mol vs. $\Delta G°_{Alumina}$ = -1746 kJ/mol at 1100°C [180]), suggests that the nitrides form upon cooling, after TGO formation has occurred. Regardless of the N source, the lack of nitrides in non-arc melted samples suggests this behavior is not representative of the alloy compositions at large.

7.4.3. Cyclic Oxidation Behavior

It is evident that the modified alloy DMREF-10+ successfully improved the cyclic life relative to DMREF-10, as measured by the ZMG time, by over 200 hours (Figure 7.11). Yet, while the initial mass gain within the first few cycles was reduced, it was still greater on DMREF-10+ than on René N5. Furthermore, the ZMG time of DMREF-10+ was significantly below that for René N5, which does not exhibit a net mass loss by 1000 h. Thus, it should be discussed what causes these differences in behavior.

The coefficients of thermal expansion between DMREF-10 and -10+ should not change significantly with the small alloying additions, and DMREF-10+ itself is found to have a CTE very similar to René N5 (Figure 7.15). Therefore, the stress evolved due to CTE mismatch between alloy and TGO alumina should be approximately the same in both these Co-base and Ni-base alloys. This conclusion is supported by PSLS mapping of the α-Al_2O_3 stress state after 1 h exposure (Figure 7.16), where DMREF-10+ and René N5 both exhibited approximately 4.5 GPa of presumably biaxial stress [119]. The driving force for scale spallation, energy release rate (ERR), is also a function of scale thickness [41]. The two DMREF alloys had total scale thicknesses of ~2.5 μm, compared with ~0.7 μm on René N5, and thus the ERR will be greater for the DMREF-10 and -10+ systems than for René

N5, despite the similar stress states. (It is acknowledged that the scale is not comprised solely of alumina, and the effective CTE of the TGO may be different for the Co alloys than for N5, but it is assumed for simplicity that the thickness effect is probably dominant.) As exposure continues, it is also notable that the stress state in DMREF-10+ evolves significantly to ~7.5 GPa, while the stress state on René N5 remains relatively constant (Figure 7.16). The cause of this evolution is not obvious, and will likely require more in-depth TEM and EDS observation of the alumina TGO and overlying oxide layers. One likely explanation is that as high temperature exposure continues, counter-diffusion of Al and O along alumina grain boundaries forms additional oxide within the pre-existing layer, leading to an in-plane compressive strain. Similar results have been observed by Tolpygo et al. in alumina-forming FeCrAl alloys investigated by PSLS [71,181]. The evolution of residual stress in TGO over time is a competitive process between CTE mismatch, growth stresses within the scale, and relaxation of stress due to oxide and metal substrate creep. Thus, a proper evaluation of why DMREF-10+ exhibits evolution of a much greater residual α-Al_2O_3 stress than in René N5 will require comparing the high temperature creep between the alloys. Reactive element additions have also been shown to alter counterdiffusion of Al along α-Al_2O_3 grain boundaries due to segregation phenomena [182]. One may anticipate that TEM EDS of TGO grain boundaries may shed light on the differences between the oxides that can give rise to changes in growth stress.

Beyond the driving forces for spallation, there is also the interfacial toughness between the alloys and TGOs, which must be overcome for delamination to occur. Unfortunately, interfacial toughness is very difficult to directly measure experimentally [183]. However, it is known that interfacial adhesion is deleteriously affected by the presence of sulfur, and

benefitted by the presence of RE additions [10]. TEM EDS investigations should also be conducted on the alloy-TGO interface to assess differences in elemental partitioning at that location as well. Based on the low ICP measurements of sulfur content in both the arc-melted DMREF-10 and commercially cast DMREF-10+, it seems more likely that RE additions would be affecting this interface more so than sulfur content. The observed higher stress state on DMREF-10+ also informs the observed failure mechanism of DMREF-10+ at higher cycle numbers, where the majority of the sample surface has a thin, adherent alumina scale, but many large nodules of oxide have occurred at the edges and corners (Figure 7.13). This is likely the result of periodic spallation of the oxide at corners and edges due to the geometric stress-concentrations as the oxide tends to expand laterally at these locations. This leads to increased and repeated TGO fracture and reformation, giving rise to the repeated layers of oxide observed to pile up within these corner 'nubs' (Figure 7.13b). Such an oxidation process would likely dominate the overall sample weight gain measured, and account for the observed non-parabolic behavior (Figure 7.11). Aspects of sample geometry acting as stress-concentrators would also explain the greater mass gain of the DMREF-10+ samples cut as discs vs. that cut as a parallelepiped, and the fact that these discs exhibit a reduced ZMG time (Figure 7.11). Indeed, greater amounts of oxide nodules were observed along the rounded circumference of the buttons relative to the flat side faces on the parallelepiped.

7.4.4. Effects of Grain Structure

In general, it is expected that enhanced diffusion along alloy grain boundaries would aid in the establishment of continuous alumina scale. Indeed, the formation of a convoluted alumina layer undercutting discrete IOZ "pockets" observed in combinatorial samples was

attributed to grain boundary effects in the IPD alloys in Chapter 6. In that case, the alloy synthesis technique led to a very small ~7 μm grain size, and correspondingly IOZ pockets of a similar scale (Figure 6.8). It is to be expected that in the present arc-melted samples, with ~1 mm grains orders of magnitude larger than the IPD alloys, the TGO would correspondingly be less influenced by grain boundary diffusion. Indeed, the alumina scale in the case of the DMREF alloys is much more uniform. While continuous Al_2O_3 still undercuts a layer of IOZ particles in the case of DMREF-8 (Figure 7.6), the scale is essentially flat. If the DMREF alloys were less prone to alumina formation, the lack of alloy grain boundaries to act as continuous scale initiation sites might lead to more problematic, thicker oxide scales overlying extensive IOZ regions. As is, the DMREF alloys all have sufficient alloying additions to form continuous Al_2O_3 via predominantly bulk diffusion. One can further compare the behavior of DMREF-10+PX vs. SX in Figure 7.13(a), Figure 7.16(b).

Differences in weight gain during cyclic oxidation between these samples (Figure 7.11) were attributed to the differences in geometry, with disc-shaped SX pieces and the parallelepiped PX sample. Primary mass gain and loss was observed to occur from large nodules forming along sample edges and corners, and in the case of the disc samples, along the curved circumferential face. Visibly, the primary difference between the PX and SX oxides was the outlining of the grain structure in the PX sample by gray oxide patches overlying the blue spinel layer (Figure 7.13a). In the SX sample, such coloration was more uniform across the entire surface (Figure 7.16b). These differences likely arise from minor changes in oxide layers overlying the continuous Al_2O_3 and spinel layers (e.g. the formation of refractory-rich particles on the surface, seen in Figure 7.13c as white particles), and may

be attributed to the different grain-orientations exposed air in the PX sample, vs. the uniform (001) surface of the SX sample. These small changes can be verified by cross-sectioning an SX sample, and by conducting EBSD on the cross-sectioned PX sample to compare grain orientation with overlying TGO structure.

7.5. Synopsis

The design process and experiments discussed herein have demonstrated not only a new Co-base γ/γ' alloy with an unprecedented combination of oxidation resistance and high γ' solvus, but also the efficacy of combining high throughput experimental techniques with computational modeling for the alloy design process. The resultant DMREF-10+ alloy exhibits a γ' solvus of 1204°C, forms a ~2.5 μm oxide scale containing continuous alumina after 1 h at 1100°C, and is able to withstand cyclic oxidation for over 200 h before reaching the onset of net mass loss. The PSLS technique used to aid in the initial DMREF series design process also demonstrates that stress evolution in the TGO α-Al_2O_3 is of great importance to cyclic behavior, as continued stress generation is a major factor in DMREF-10+ not occurring in Ni-base René N5. The combined ITIC diagrams used to develop the DMREF-10+ alloy also suggest there may be additional room within the design space with increasing W content. Finally, further refinement of the DMREF-10+ composition will likely involve analysis of how low-concentration elements such as the RE additions partition to and affect interfacial toughness at the alloy-TGO interface, and diffusion along alumina grain boundaries. Overall, the design approach has yielded a very promising Co-base alloy for commercial development, and has provided insight into how Co-base γ/γ' alloys may be optimized in the future.

7.6. Figures and Tables

Table 7.1: Alloy compositions and corresponding solidi and solvi.
Composition changes for each alloy involved in the development are shown in bold.

Alloy	2-6G	DMREF-8	DMREF-9	DMREF-10‡	DMREF-10+‡
Ni:Co (at.%)	0.7	**0.87**	0.87	**0.93**	0.94
Co (at.%)	46.6	40.0	40.5	39.8	39.4
Ni (at.%)	32.4	34.9	35.2	37.1	36.8
Al (at.%)	11.7	**14.0**	14.3	**13.1**	13.3
W (at.%)	4.4	4.4	**1.0**	1.0	1.0
Cr (at.%)	3.3	3.3	**5.9**	5.5	5.8
Ta (at.%)	1.5	**3.5**	3.2	3.5	3.5
C (at.%)	-	-	-	-	**0.06**
B (at.%)	-	-	-	-	**0.08**
Y (at.%)	-	-	-	-	**0.004**
Hf (at.%)	-	-	-	-	**0.026**
S* (ppmw)	-	-	-	1.8	0.7
T_{solvus},°C (PANDAT)	1112	1216	1244	1229	1240
$T_{solidus,}$ °C (PANDAT)	1370	1277	1262	1300	1275
T_{solvus}, °C (DTA)	-	1226	1195	1200	1204
$T_{solidus}$ °C (DTA)	-	1324	1328	1343	1329

‡ Composition measured by ICP, all others by EPMA

Table 7.2: TEM EDS measurements of the features observed in DMREF-10 after 1h air 1100°C exposure (at.%).

Point	Nominal Phase	Ni:Co	Co	Ni	Al	W	Cr	Ta	O	N
1	(Co,Ni)O	0.9	27	24	-	-	-	-	50	-
2	$CoAl_2O_4$	0.4	13	5	42	-	1	-	38	-
3	$Co(Al,Cr)_2O_4$	0.3	14	4	26	-	13	-	43	-
4	$(Co,Ni)(Ta,W)_2O_6$	0.5	9	4	4	2	2	25	54	-
5	Mixed	0.7	6	4	34	-	3	1	53	-
6	Al_2O_4	-	-	-	39	-	-	-	61	-
7	Depleted Alloy	0.9	44	39	5	1	6	4	-	-
8	AlN	0.9	3	3	54	-	-	-	1	38

Table 7.3: Fit segregation parameters for DMREF-10+SX, compared with literature values of Co- and Ni-base alloys, with values greater than 1 reflecting partitioning to dendrite cores

Alloy	Co	Ni	Al	W	Cr	Ta	Re	Mo
DMREF-10+	1.04	0.99	0.96	1.19	1.04	0.68	-	-
Co-base “CrTa” [40]	1.01	-	0.96	1.01	0.99	0.61	-	-
CMSX-4 [184]	1.09	0.89	0.91	1.18	1.00	0.89	1.40	1.12

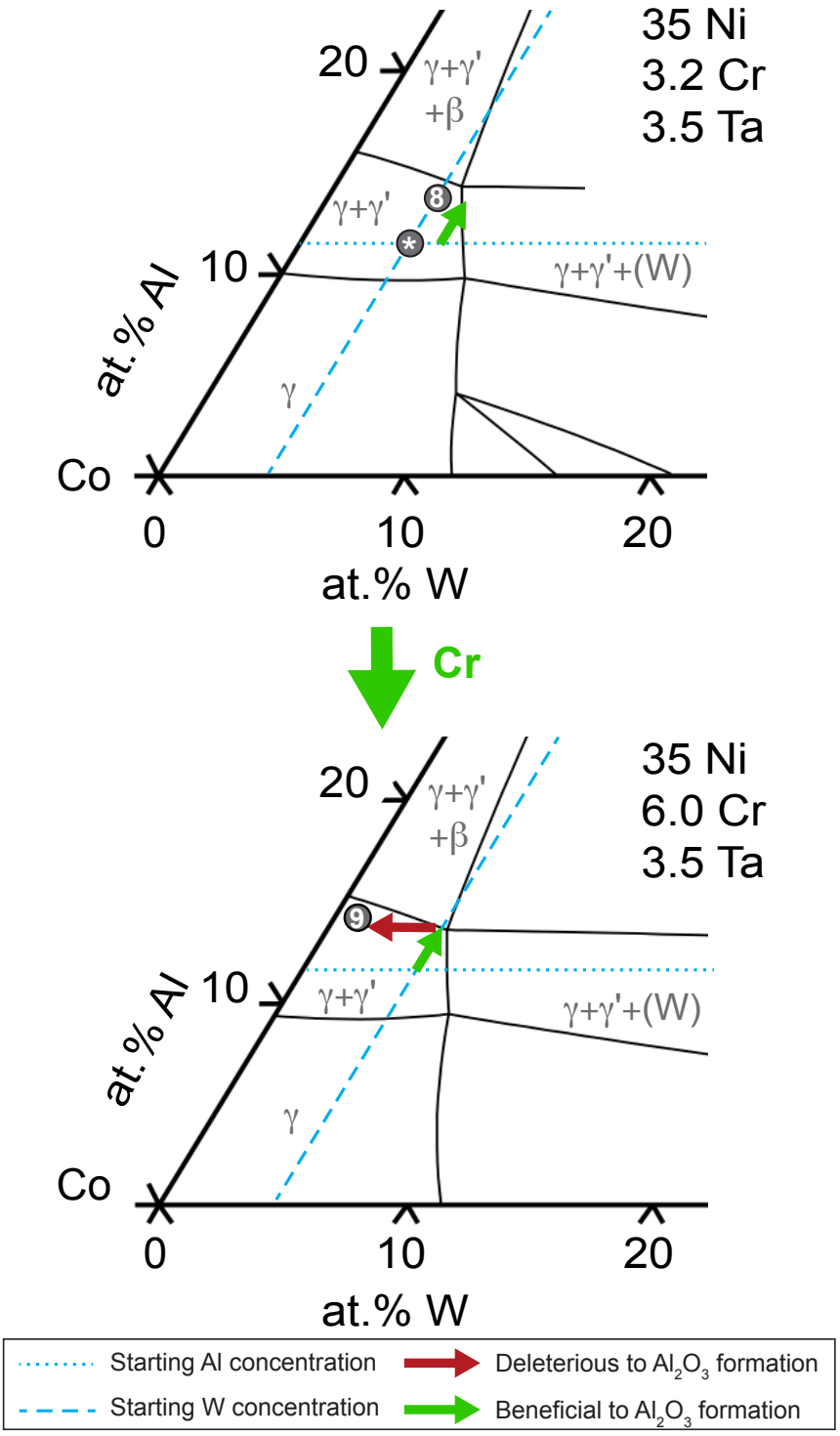

Figure 7.1: ITIC sections at 1100°C through Co-Al-W at constant 3.2 (top) or 6.0 (bottom) Cr – 3.5 Ta – 35.0 Ni at.%, with the compositions of button 2-6G (*), DMREF-8, and DMREF-9 plotted, as measured by EPMA. Compositional effects on oxidation behavior are marked with red arrows if deleterious, and green if beneficial, based on prior studies in this composition space [177].

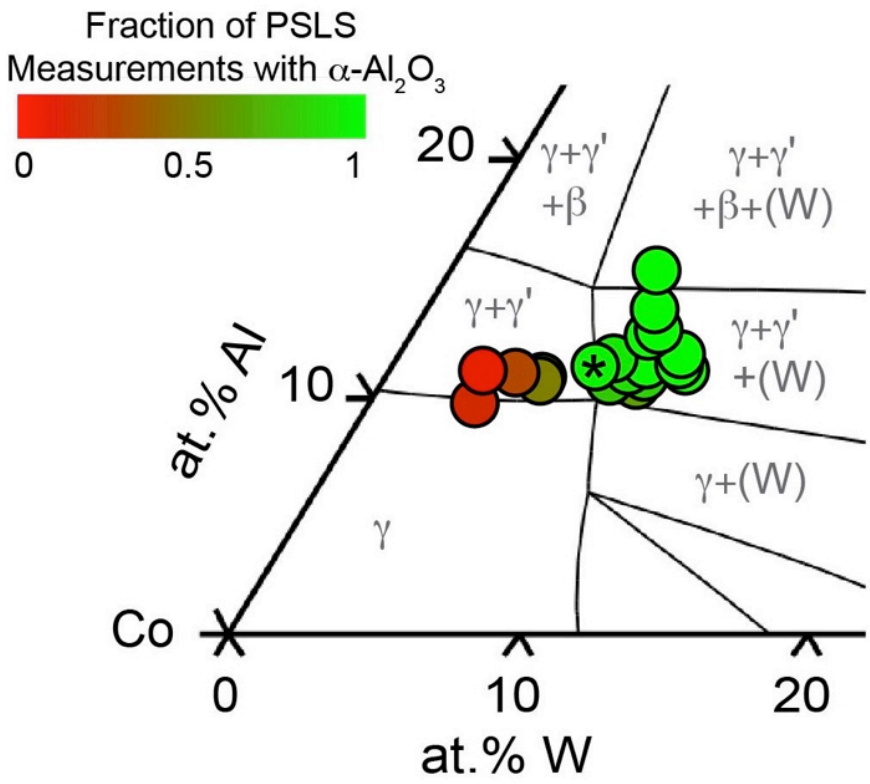

Figure 7.2: ITIC section at 1100°C through Co-Al-W at a constant 2.0Cr, 3.5Ta, and 35.0 Ni at.%, with overlaid PSLS assessment of oxidation behavior. The composition of button 2-6G as measured by SEM EDS is marked (*), and lies within regions of both more desirable oxidation behavior (green) and the calculated γ/γ' two-phase field. It is noted that subsequent compositional analysis by EPMA found that this composition (*) was actually slightly lower in Ta content than observed by SEM EDS (c.f. Table 7.1). This composition is also labeled on Figure 6.4(b) as '5'. The ITIC section in this figure would appear approximately as a vertical slice (W isoconcentrate line) through that of Figure 6.4(b).

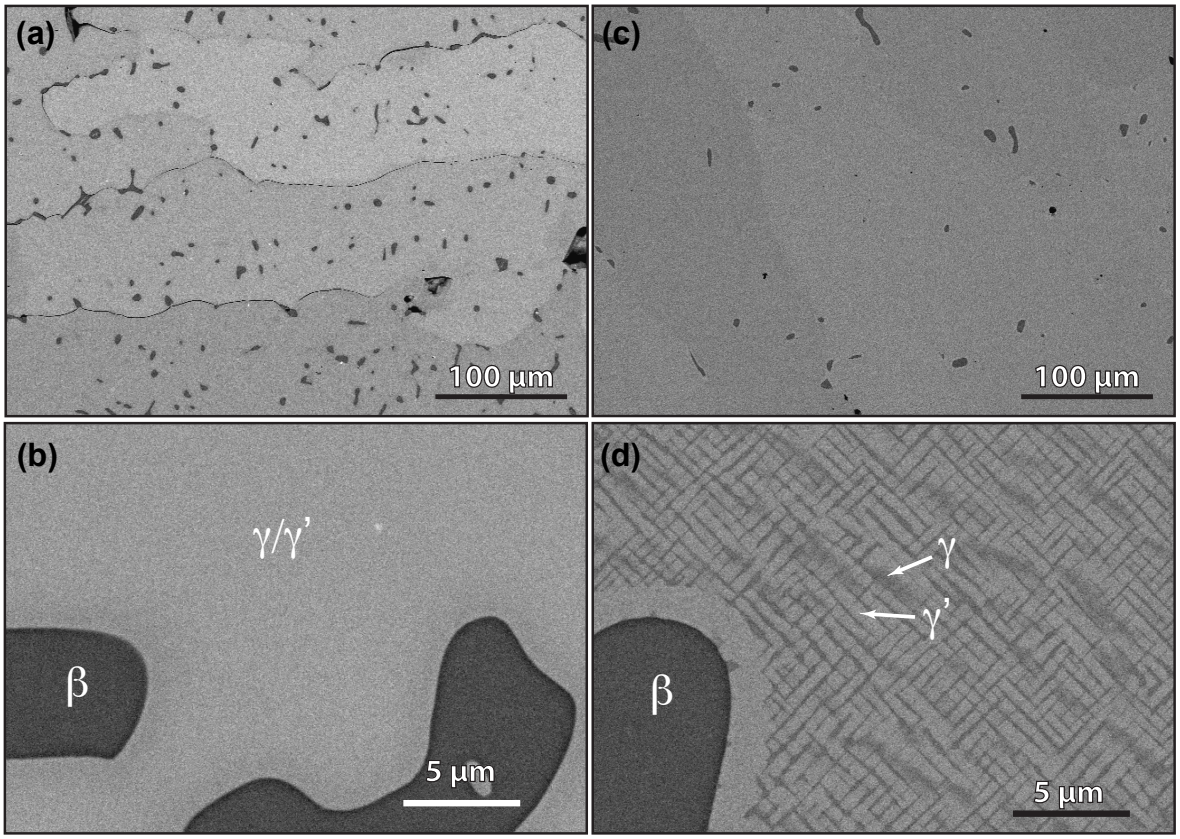

Figure 7.3: Alloy microstructure after heat treatment of DMREF-8 (a,b) and DMREF-9 (c,d). An Al-rich β tertiary phase is frequently observed (dark grey) in both alloys. Cuboidal γ/γ' is seen in DMREF-9 at high magnification (d) where γ' is the brighter particles and γ appears as darker channels. Individual γ' precipitates are not distinguishable from the γ matrix in DMREF-8 (b), however DTA and XRD verify their presence (Figure 7.4 and Figure 7.5)

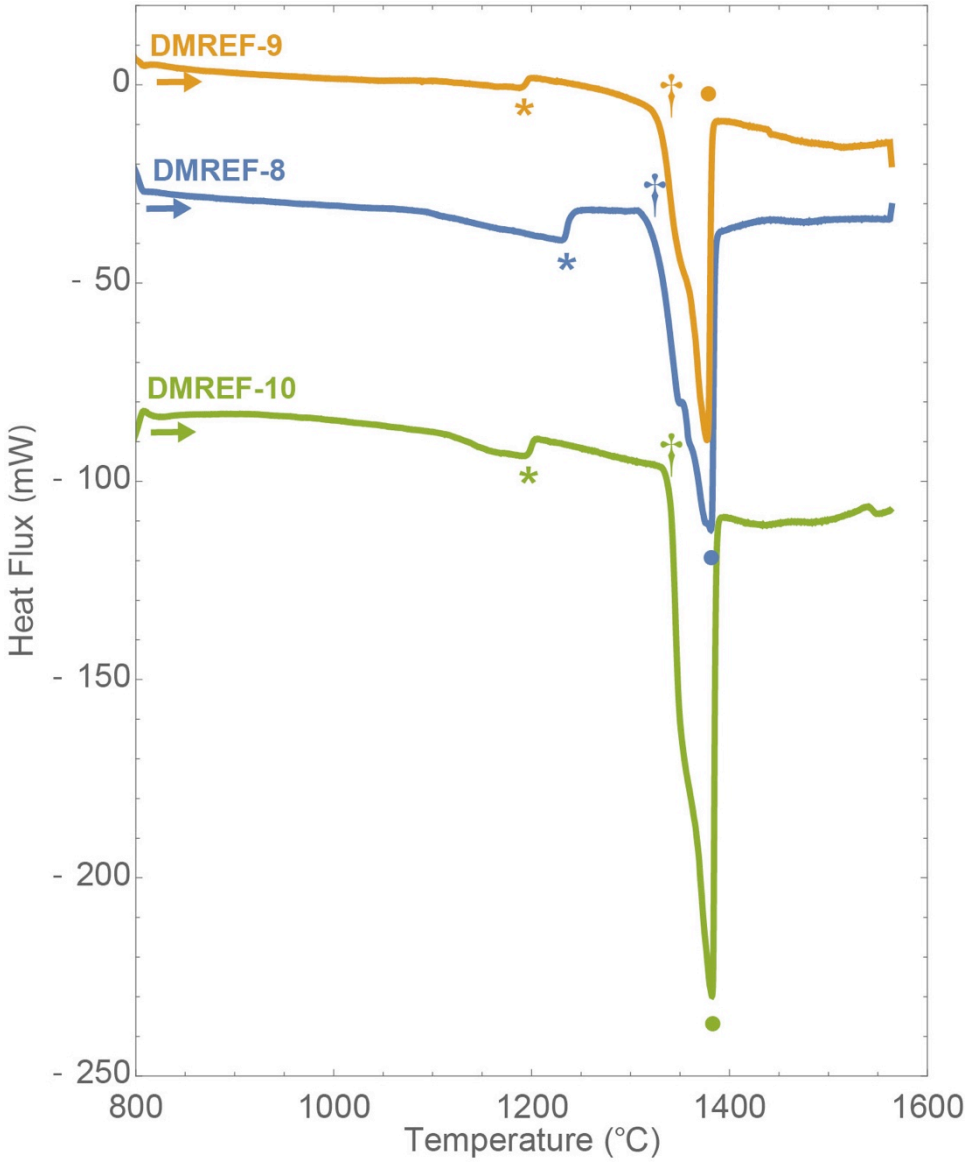

Figure 7.4: DTA heating curves of DMREF-8, 9, and 10 (vertically offset for clarity). Features marked are the γ' solvus (*) [179], solidus (†), and liquidus (•).

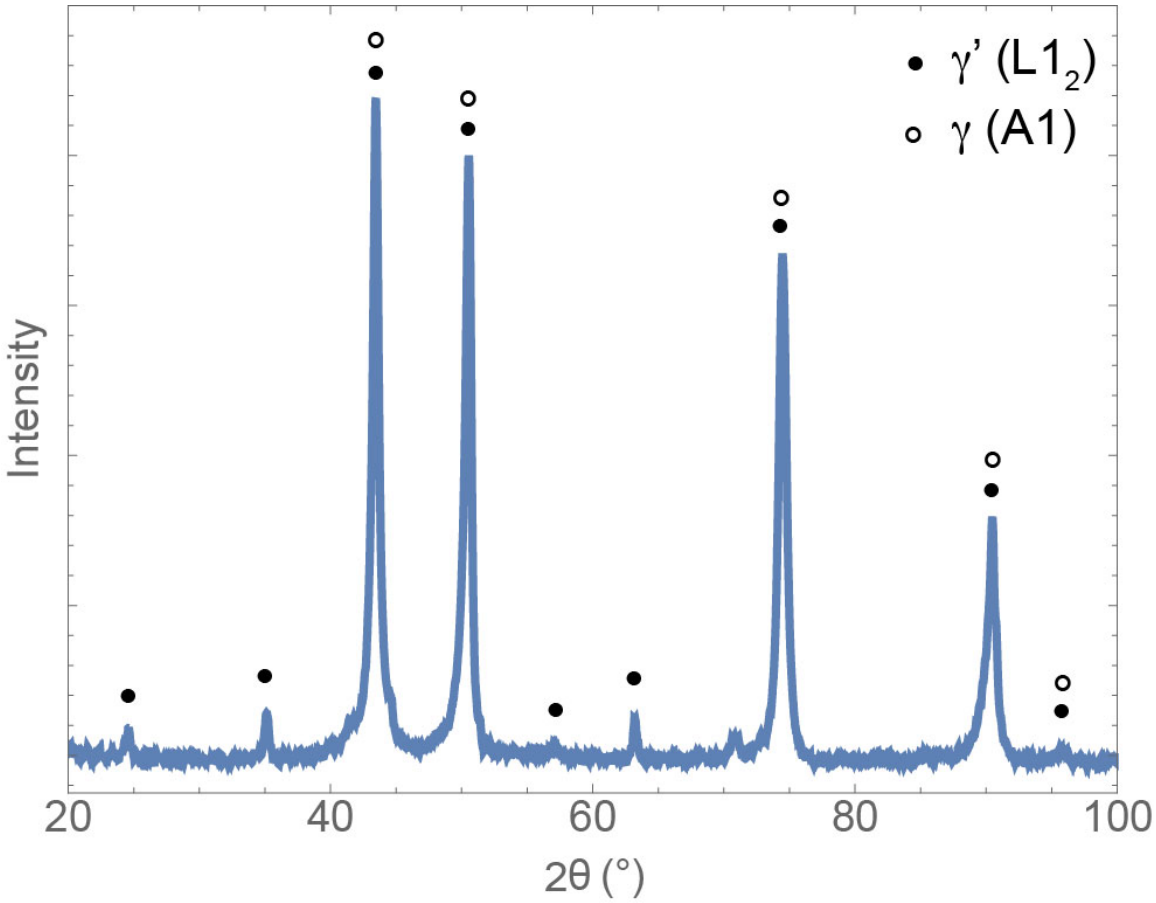

Figure 7.5: XRD scan of DMREF-8, exhibiting reflections from both the γ and γ' phases [19].

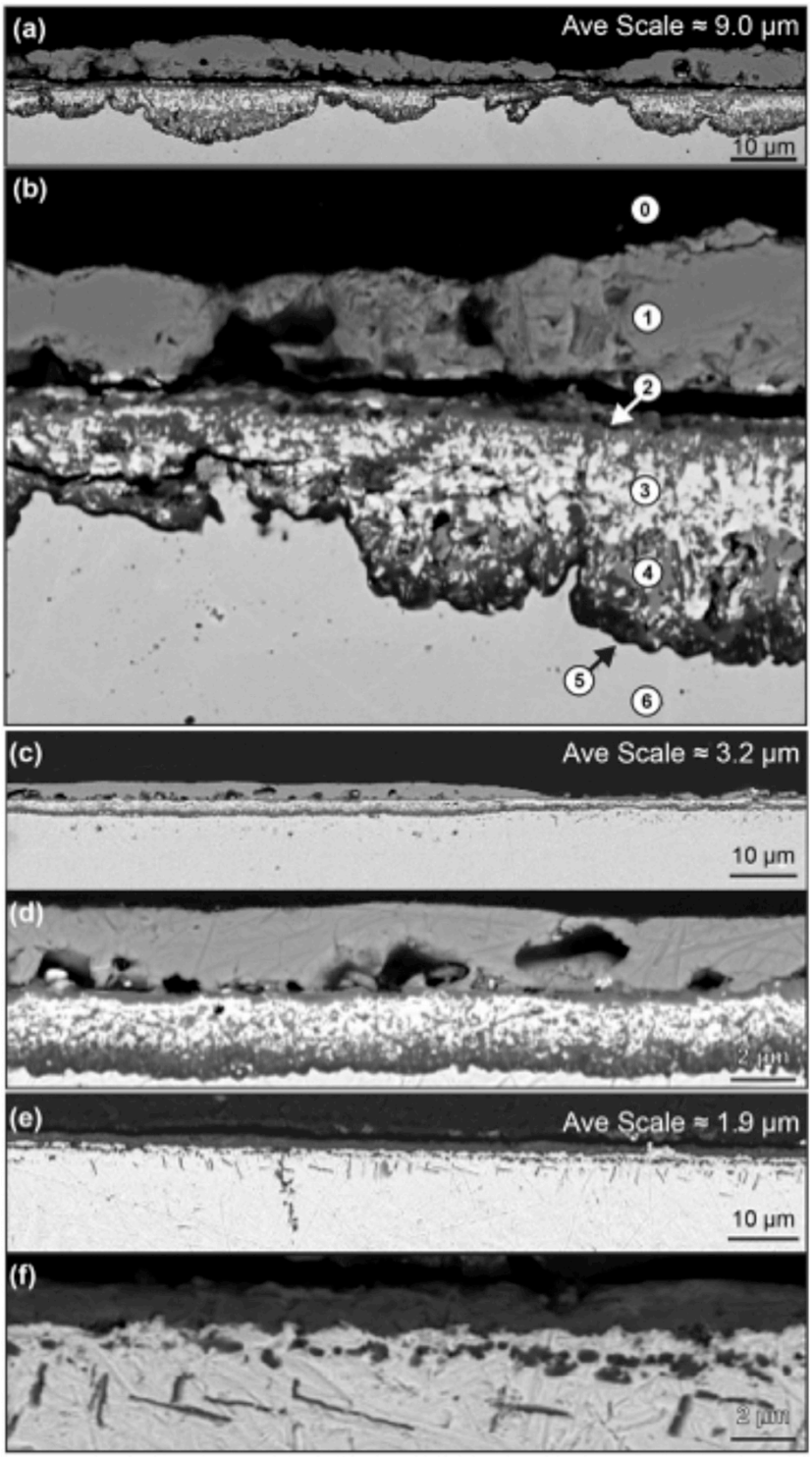

Figure 7.6: (a,b) 2-6G, (c,d) DMREF-8, and (e,f) DMREF-9 in cross-section after 1 h air 1100°C. Oxide features on the combinatorial button are labeled: (0) mounting epoxy, (1) outer (Co,Ni)O, (2) spinel (Co,Ni)Al_2O_4 layer, (3) tungstate (Co,Ni)WO_4 embedding Al-rich IOZ particles, (4) Ni-rich oxides embedding Al-rich IOZ particles, (5) continuous Al_2O_3 scale, and (6) the underlying alloy.

Figure 7.7: DMREF-10 (a,b,c), DMREF-10+PX (d,e,f), and René N5 (g,h,i) showing the unoxidized microstructure (a,d,g), and oxide scale in cross section after 1 h in air at 1100°C (b,c,e,f,h,i). Alloy morphology and oxidation behavior is almost identical between DMREF-10 and -10+. René N5, however, exhibits brighter γ channels than γ' precipitates (g) due to changes in W partitioning behavior over the Co-systems. The TGO on René N5 is also almost entirely Al_2O_3 scale.

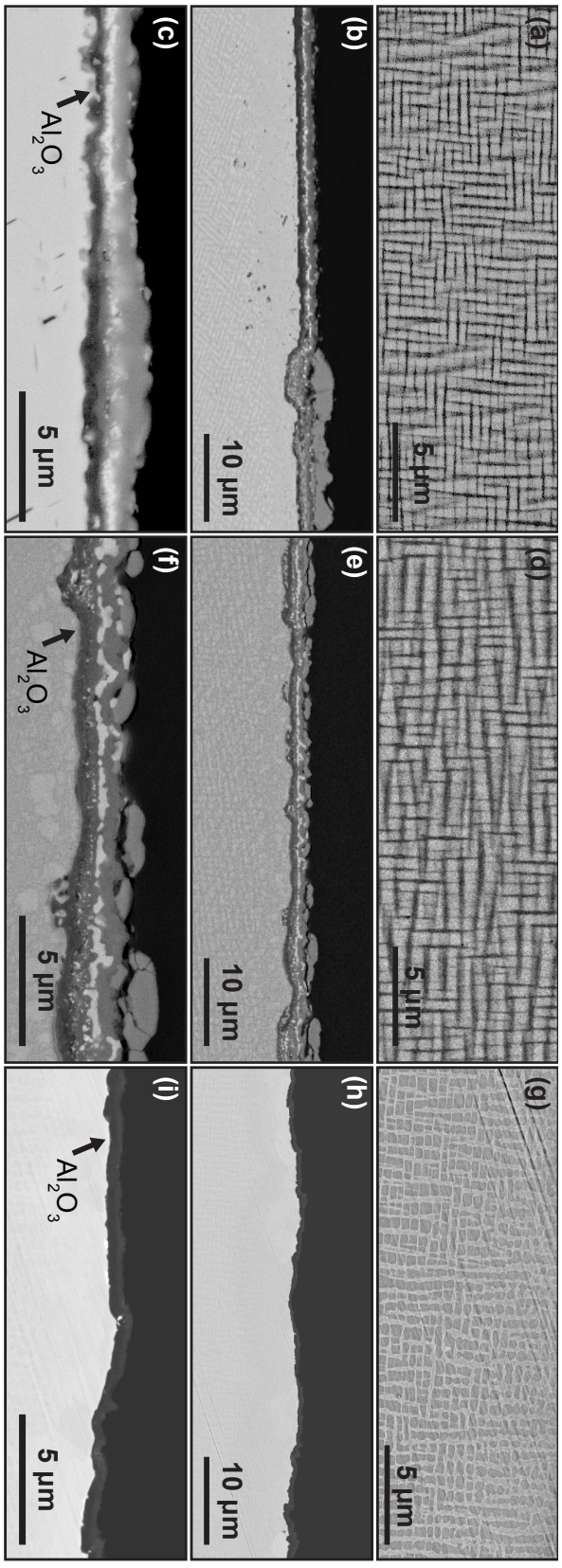

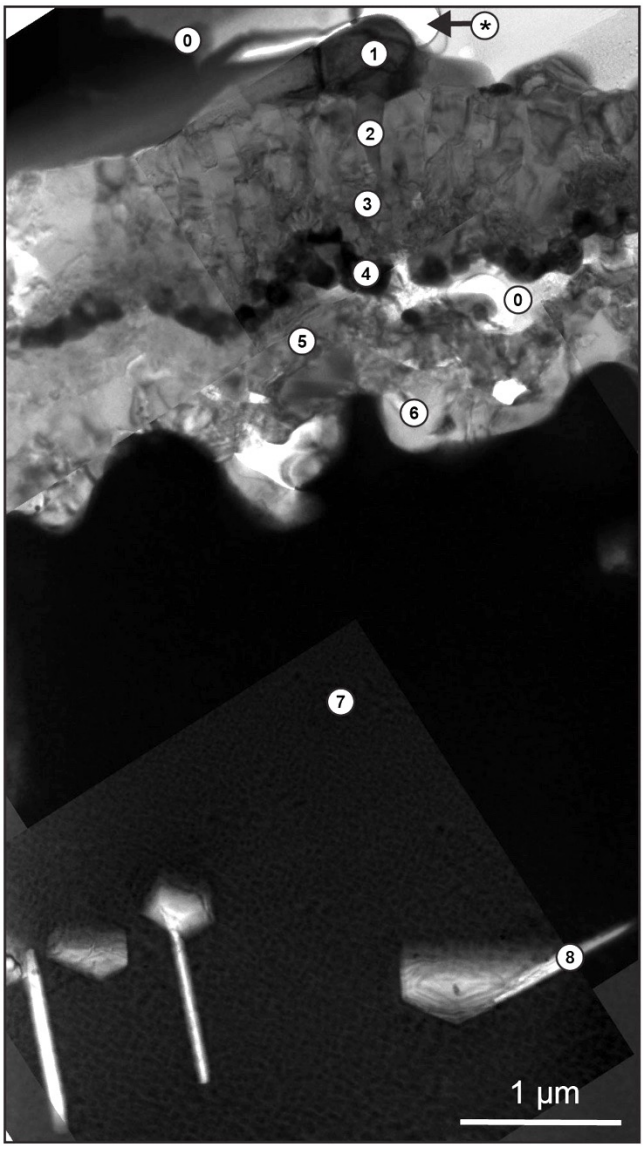

Figure 7.8: Bright-field TEM micrographs (stitched) of DMREF-10 oxidized for 1h in air at 1100°C (cf. SEM BSE micrograph, Figure 7.7b,c). Labeled points correspond to TEM EDS measurements (Table 2), and are nominally identified as (*) voids, (0) epoxy, (1) (Co,Ni)O, (2) $CoAl_2O_4$, (3) $Co(Al,Cr)_2O_4$, (4) $(Co,Ni)(Ta,W)_2O_6$, (5) mixed oxides, (6) Al_2O_3, (7) metal within the alloy depletion region, and (8) AlN.

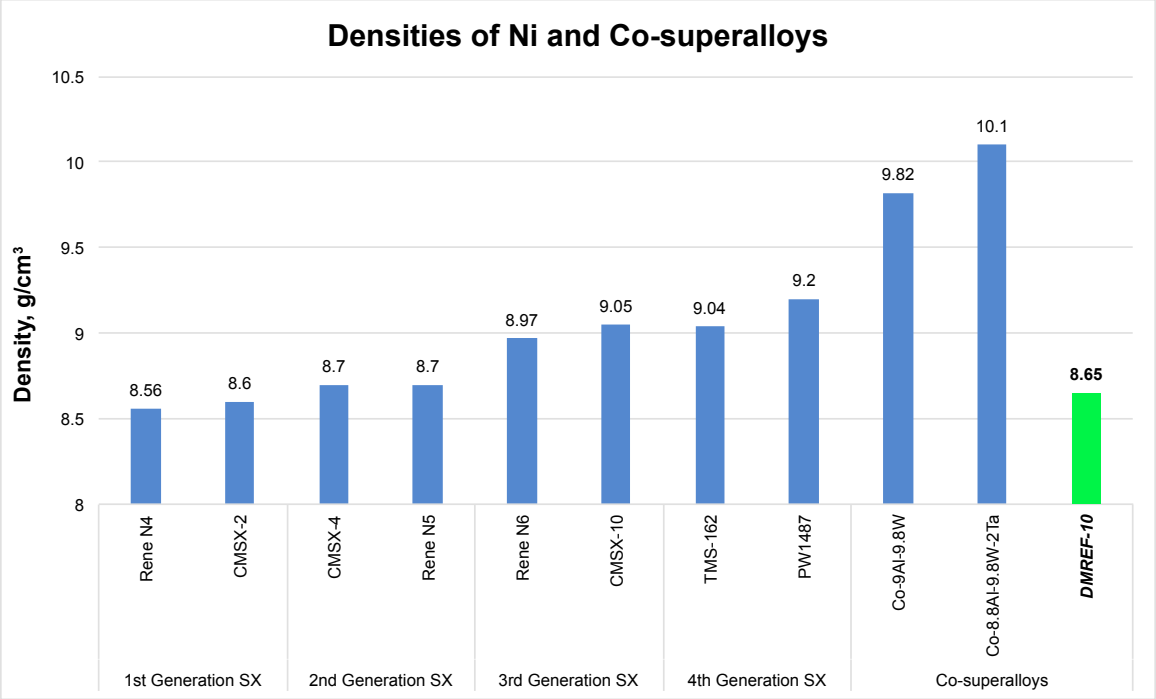

Figure 7.9: Experimental Co alloy density as measured by Archimedes method, compared with commercial superalloys (g/cm^3) [6].

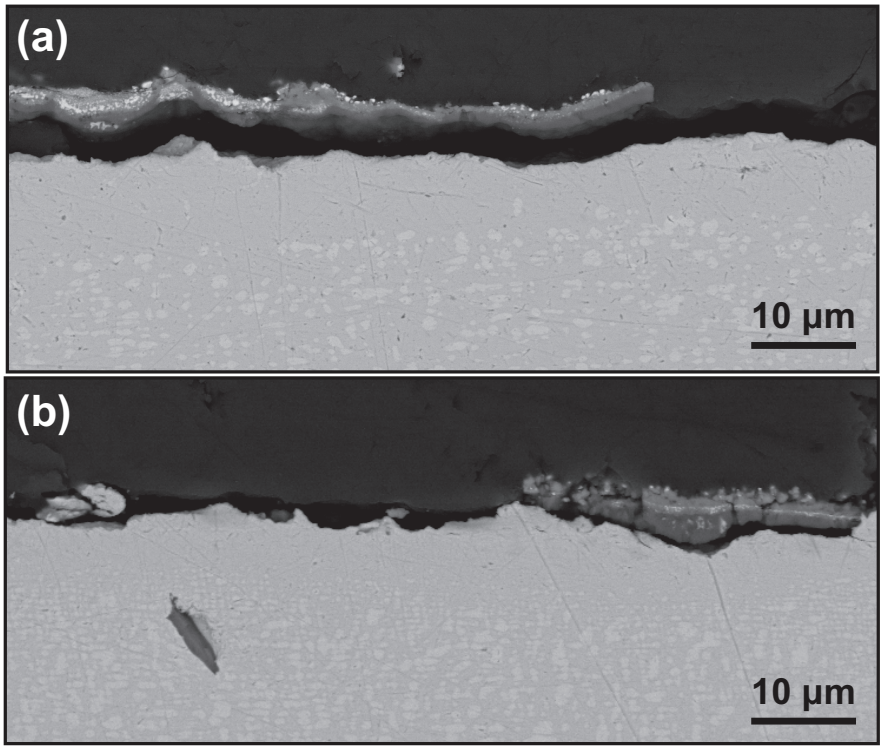

Figure 7.10: Alloy DMREF-10 after (a) 50 h isothermal exposure, and (b) 50 h of cyclic oxidation, 1 h per cycle, at 1100°C in air. While both the oxide scale itself and the underlying alloy depletion region are both relatively thin, significant spallation is observed at the alumina – alloy interface in both exposure conditions.

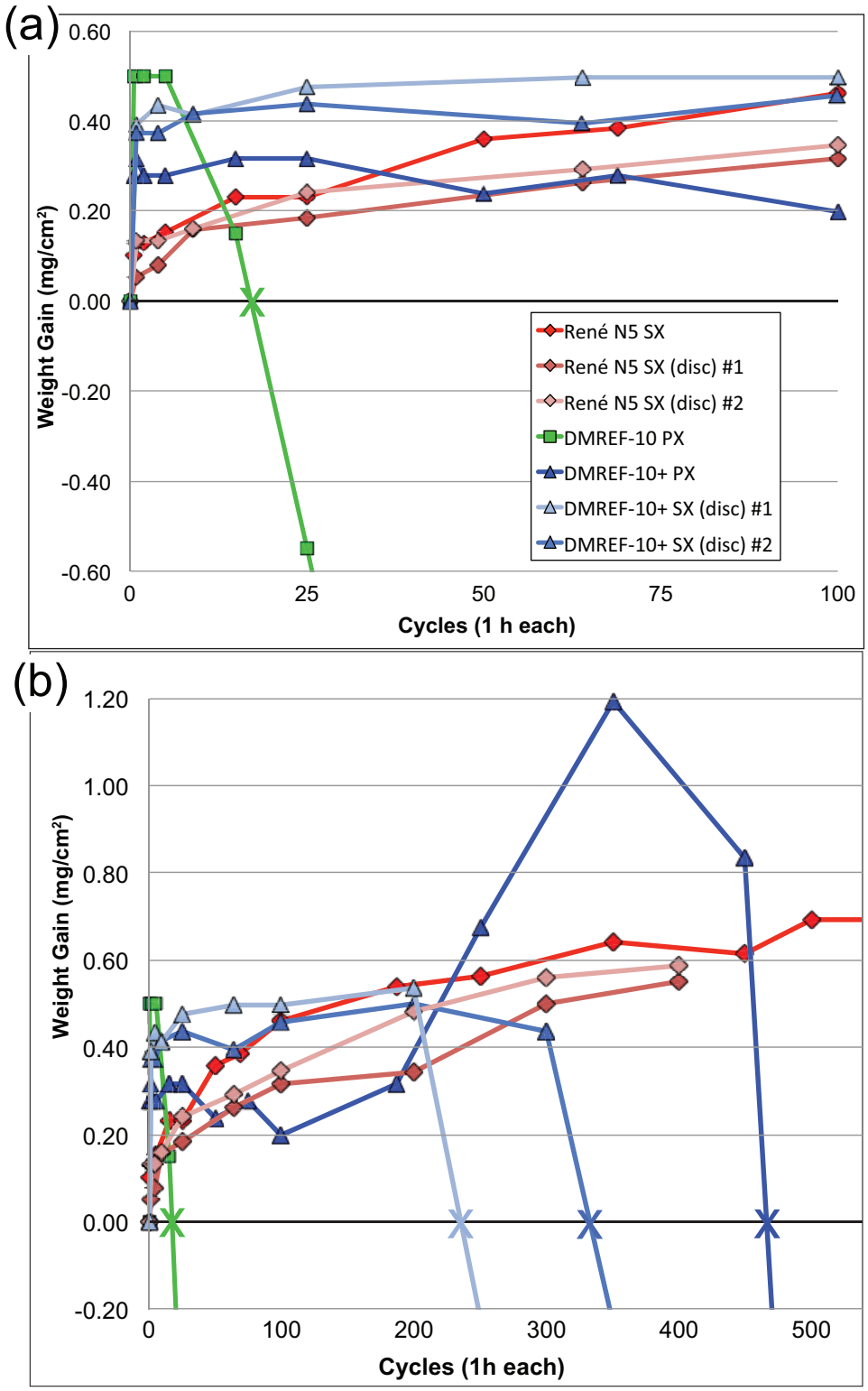

Figure 7.11: Weight gain per area of Ni-base alloy René N5 vs. Co-base alloys DMREF-10 and DMREF-10+ (with RE additions Table 7.1), during 1 h cycles in air at 1100°C. ZMG points are labeled 'X'. Samples were polished on all sides to 1200 grit finish, and were parallelepiped-shaped unless otherwise marked. Part (a) is a zoomed-in section of part (b).

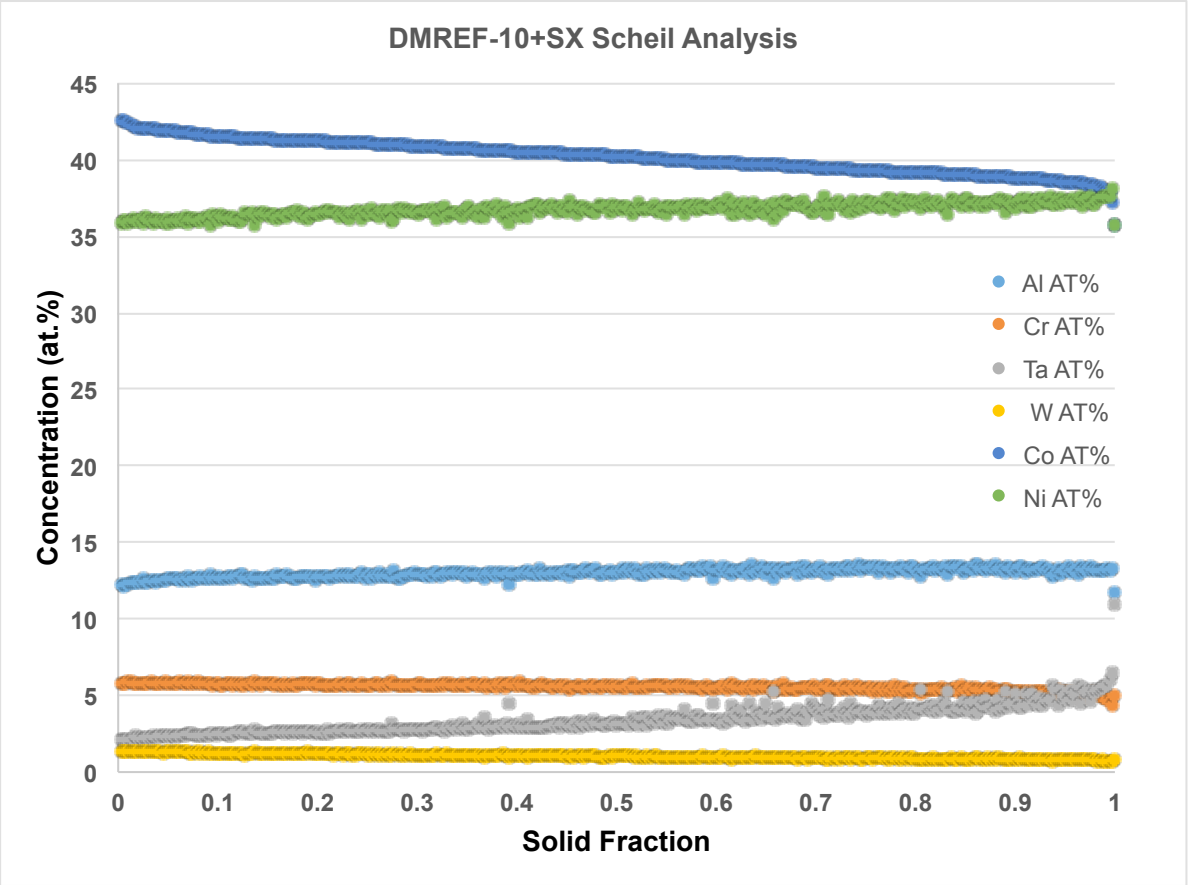

Figure 7.12: Scheil analysis of EPMA composition data from as-cast single-crystalline DMREF-10+. Data is arranged from high to low Co content, to match measurements of dendrite cores vs. interdendritic regions. Fit partition coefficients are listed in Table 7.3.

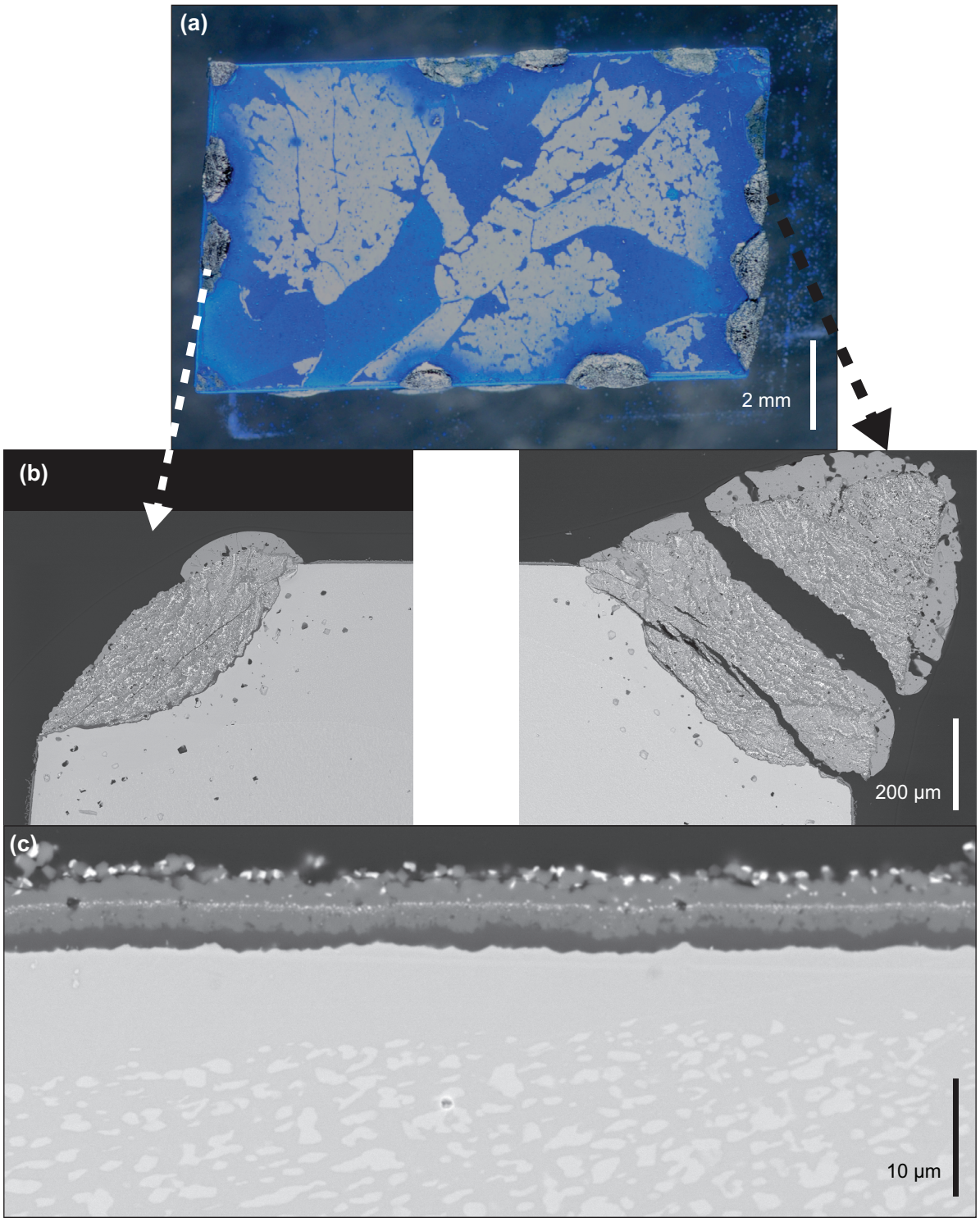

Figure 7.13: Alloy DMREF-10+PX after 500 h cyclic exposure at 1100°C in air. (a) Macroscopic optical image of the sample surface, showing large nodules of oxide forming along the sample edges, (b) those edges in backscattered electron microscopy, and (c) the thin, intermediate scale along the flat sample faces.

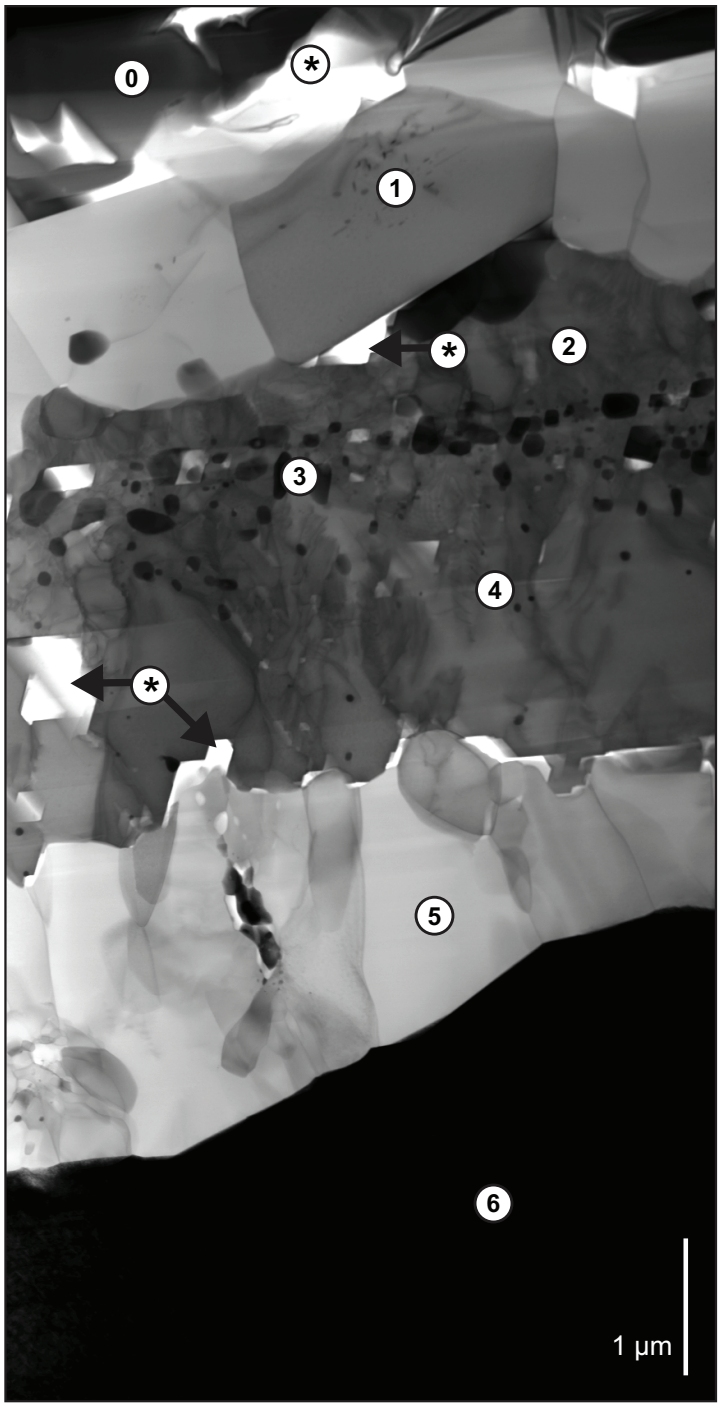

Figure 7.14: Bright field TEM micrograph of alloy DMREF-10+PX after 500 h cyclic oxidation at 1100°C. Features are nominally identified based on TEM EDS measurements: (*) voids, (0) Pt deposited during FIB, (1) large grained $(Co,Ni)(Al,Cr)_2O_4$ spinel, (2) small grained spinel of similar composition to feature one, (3) $(Co,Ni)(Ta,W)_2O_6$, (4) $(Co,Ni)Al_2O_4$, (5) Al_2O_3, and (6) the underlying alloy.

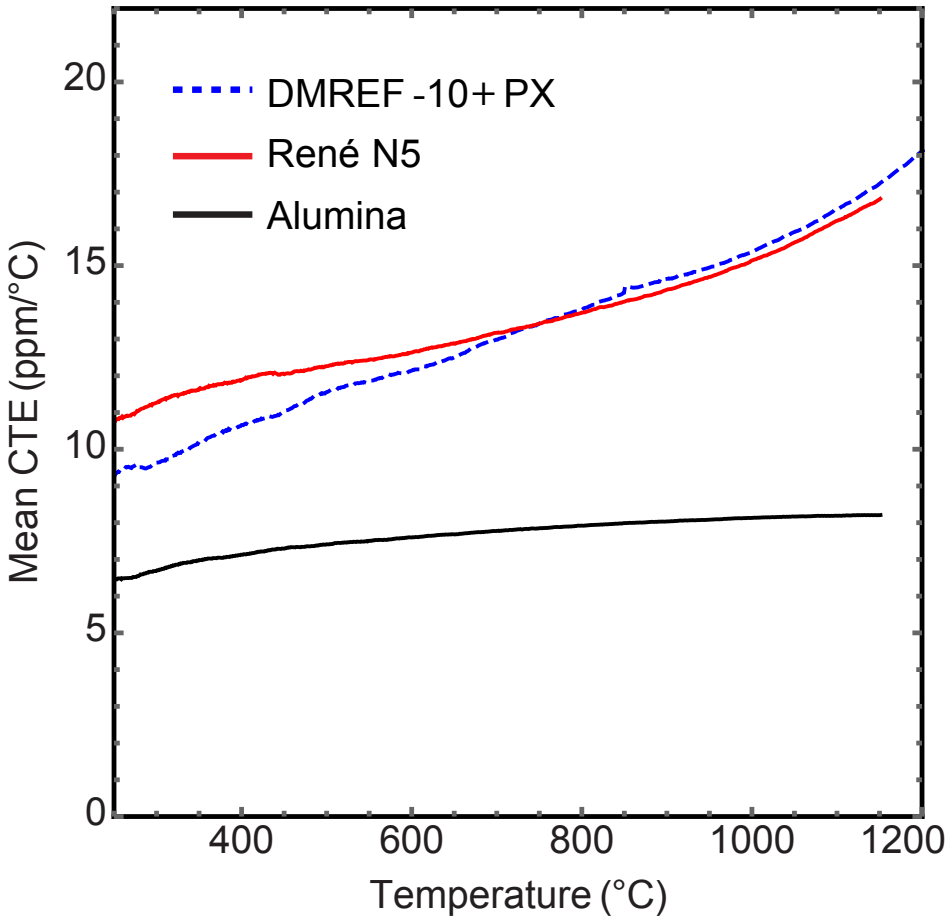

Figure 7.15: Mean coefficients of thermal expansion of Ni-base alloy René N5 and Co-base alloy DMREF-10+ from room temperature to 1200°C, in comparison with polycrystalline α-Al_2O_3. The thermal expansion at 1100°C is observed to be very similar between the two alloys.

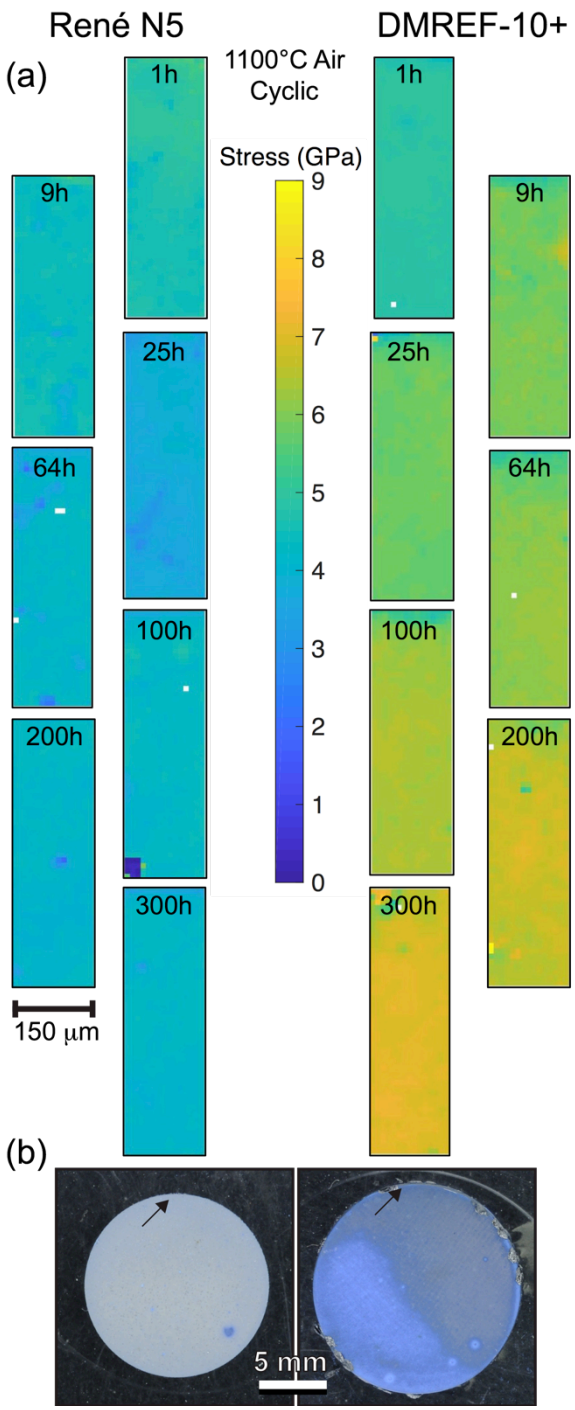

Figure 7.16: (a) PSLS maps of the stress states within α-Al_2O_3 TGO scale on single-crystalline Ni-base René N5 (left) and Co-base DMREF-10+SX measured after various thermal cycles at 1100°C in air. Maps were taken from the edge of cylindrical buttons, as shown in (b) optical images after 300 cycles (samples #1 in Figure 7.11). Residual stress at room temperature is observed to remain fairly constant at ~4.5 GPa between 1 to 300 h in René N5, while increasing dramatically from ~4.5 to ~7.5 GPa in DMREF-10+SX between 1 to 300 h.

8. Conclusions and Recommendations

The primary goal of these investigations was to systematically explore Co-alloy composition space, developing an experimental basis for how composition affects oxidation behavior and phase stability. This goal is part of a larger effort to broaden scientific understanding of the Co-base γ/γ' alloy system and its potential as an alternative to Ni-base γ/γ' superalloys. To this end, high-throughput experimental methods and computational techniques were combined to assess the Co-Ni-W-Al-Cr-Ta senary system, and subsequently higher-order systems once desirable properties were achieved.

It was found that forming the desired TGO comprising continuous α-Al_2O_3 scale with minimal amounts of overlying oxide is non-trivial in Co-base γ/γ' alloys. Instead, a non-protective alumina IOZ is often observed, leading to substantial oxide formation and substrate metal degradation. In these scenarios, the external oxides formed over alumina are typically (Co,Ni)O, spinel $(Co,Ni)(Al,Cr)_2O_4$, and tungstates $(Co,Ni)WO_4$. With reduced W content and increased Ta concentration, the tungstate oxides may be superseded by equivalent tantalates $(Co,Ni)Ta_2O_6$. Closer investigation of oxide compositions across the scale stack show the Ni:Co ratio in the monoxide is lower (more Co-rich) than in the substrate alloy, and the Ni:Co increases within the tungstate layer with increased distance from the oxide-gas interface. Such behavior has the potential of leaving lower portions of the scale stack significantly Ni-rich. A continuous alumina layer underneath thick internal oxidation zones (IOZ) has frequently been observed, and is shown to grow via lateral propagation of initial Al_2O_3 patches. The IOZ pockets are in the size range of the alloy grain structure, suggesting enhanced diffusion along alloy grain boundaries is playing a role

in initiating continuous scale growth. Indeed, samples with larger-sized grains display a less-convoluted alumina scale.

Experiments using PSLS have demonstrated that α-Al_2O_3 is generally detectable underneath these outer oxides, and can thus be used as a screening technique for more desirable alumina-forming compositions. PSLS sensitivity to the α-Al_2O_3 has been shown to be a function of both oxide thickness and composition. CoO is more attenuating to the PSLS signal than NiO, and this behavior is attributed to the differences in oxide absorptivity. No significant characteristic spectra were observed on TGO of the other constituent oxides (Co, W, Cr, Ta) within the frequency range of interest (1.42 – 1.48 μm^{-1}), with the exception of the NiO peaks. Yet these peaks at ~1.43 and 1.47 μm^{-1} were seen to be attenuated by Co solubility in the monoxide. Instead, a low-intensity, broad peak at ~1.48 μm^{-1} arose from the mixed (Co,Ni)O, as well as $CoAl_2O_4$ oxides.

PSLS was used to screen the oxidation behavior of a large set of different Co-base alloys created from combinatorial synthesis. After 1 h in air at 1100°C, the following region was identified to offer more promising oxidation behavior: ≥11 at.% Al, ≥4 at.% Cr, between 7 – 10 at.% W, and ≥26 at.% Ni, exhibiting relatively thin oxides overlying a continuous alumina scale. Increasing Al and Cr concentrations were most beneficial for reducing total scale thickness, followed to a lesser extent by increasing W and Ni contents. DFT calculations show that the influence of tungsten on alumina formation may be due to its effects on the chemical potentials in the alloy system. In essence, W additions increase μ_{Al} in the Ni-base system and decrease it in the Co-base system. Many of the alloys exhibiting desirable alumina formation also precipitate out less-desirable alloy phases, β-NiAl and μ-Co_7W_6. Alloys are more prone to form these phases at higher Ni, W, Al, and Cr

concentrations. Yet it has been confirmed that a Co-base alloy in this senary space can achieve two-phase γ/γ' morphology while exhibiting alumina-forming behavior. The approximate composition designated as 2-6G, namely Co - 32Ni - 4W - 12 Al - 3Cr – 2Ta at.% was identified as a starting point for further alloy development.

Applying a CalPhaD database (PanCo-2011/-2018), a series of alloys designated "DMREF" were explored by moving from the initial 2-6G composition in directions demonstrated to favor oxidation behavior, while still remaining within the calculated γ/γ' phase field. The resultant alloy, DRMEF-10 (Co - 27Ni - 1W - 13Al - 6Cr - 4Ta at.%) achieved a combination of properties exceeding those demonstrated in the literature for cobalt alloys to date. These include i) continuous α-Al_2O_3 formation after 1 h in air at 1100°C, ii) γ' solvus temperature ~1200°C, iii) a precipitate phase fraction exceeding 50% at 1000°C, and iv) a density comparable to 2nd generation Ni-base superalloys. Upon cyclic oxidation, the DMREF-10 composition experienced net mass loss after ~15 h at 1100°C, but this was successfully extended via micro-alloying additions of C, B, Y, and Hf, ("DMREF-10+") to over 300 h. This zero mass gain (ZMG) point is still far below that of René N5, which does not experience net mass loss in air at 1100°C even after 1000 h. Based on oxide microstructure, this inferior behavior is seen to arise from significant oxide formation and spallation at the sample edges and corners. Such behavior is attributed to greatly increased α-Al_2O_3 compressive stress over time, causing spallation at sharp features acting as stress concentrators. While the causes of increased stress in the DMREF-10+ sample remain to be elucidated, PSLS piezospectroscopic measurements have confirmed differences in residual stress. Both alloys exhibit ~4.5 GPa in the alumina scale after 1 h, but DMREF-10+ is seen to increase to ~7.5 GPa by 300 h, while the stress in René N5 remains relatively constant.

Lastly, CalPhaD calculations and experimental castings demonstrate that DMREF-10+ exhibits resistance to freckle formation from melt density inversion during solidification, and this alloy has been successfully cast as single crystal pieces.

In summary, Co-base alloys with high γ' solvi and continuous α-Al_2O_3 forming behavior are possible, and design space exists for further refinement. The investigations presented herein provide a foundation for the effects of compositional changes on alloy behavior around this space. An important limiting alloy design has been that compositional increases that benefit oxidation behavior (increased Ni, W, Al, Cr) are limited by the eventual precipitation of nominally undesirable β and μ phases, as well as reduction in γ' solvus in the case of Cr additions. Arriving at a desirable balance of alloy properties is greatly aided by application of a thermodynamic database, allowing estimation of the solvi and solidi, as well as predictions of the phase field boundaries.

It is recommended that further work on such Co-base γ/γ' alloys is fed back into refinement of CalPhaD database to aid in further alloy design. Oxidation behavior under cyclic exposure conditions should be investigated in further detail to identify and mitigate the causes of increased stress in α-Al_2O_3 TGO in the cobalt system. This likely involves high resolution TEM and EDS of boundaries and interfaces within the TGO. Comparisons should be made between DMREF-10+ and René N5 with respect to any differences in elemental segregation, and RE alterations to the DMREF-10+ composition could also be explored to investigate their potential ability to inhibit stress generation in alumina via oxide formation along TGO grain boundaries. While the present studies on exposure to a filtered air atmosphere at 1100°C have established baseline oxidation behavior, wider ranges of exposure conditions should be investigated as well. These include intermediate

temperatures in the range of 800-1000°C. Furthermore, exposure to atmospheres containing water vapor will also be important, to establish whether the DMREF-10+ composition can maintain alumina-forming behavior in a more realistic environment for gas turbine engine operation. Thermo-mechanical cycling should also be considered, such as sustained-peak low-cycle fatigue (SPLCF) similar to that experienced in turbine engines. The DMREF alloys outlined may be more resistant to failure under these conditions due to the alumina-forming oxidation behavior reducing oxide-assisted crack growth. In general, other mechanical properties of these alloys, such as creep life, should also be investigated.

Although the γ' solvi demonstrated in this research are high relative to other Co-base solvi in literature, they are still below those of 2nd generation Ni-base superalloys. Efforts must continue to be made in increasing the stability of this phase, likely via higher-order alloying additions. In their current state, the current DMREF alloys may still be useful for additive manufacturing purposes, and further studies in this field may yield insights into how their reduced solidification segregation and improved oxidation resistance benefit 3D printing applications. Lastly, the high-throughput experimental techniques used herein for Co-base superalloys could prove useful for nascent investigations of multiple principle element alloys (MPEAs). Combinatorial synthesis would allow rapid generation of large amounts of alloys across the wide swaths of space available to MPEAs. Although the mechanism of protection to be employed is still unclear, oxidation resistance will still be important for these alloys, and PSLS screening may prove useful as well.

References

[1] U.S. Energy Information Administration (EIA), What is U.S. electricity generation by energy source?, Freq. Asked Quest. (n.d.). https://www.eia.gov/tools/faqs/faq.php?id=427&t=3.

[2] U.S. Energy Information Administration (EIA), Electric Power Monthly with data for January 2018, U.S. Energy Information Administration (EIA), 2018. https://www.eia.gov/electricity/monthly/current_month/epm.pdf.

[3] U.S. Federal Aviation Administration (FAA), FAA Aerospace Forecast Fiscal Years 2018-2038, U.S. Federal Aviation Administration (FAA), 2018. https://www.faa.gov/data_research/aviation/.

[4] U.S. Environmental Protection Agency (EPA), Inventory of U.S. greenhouse gas emissions and sinks, 1990-2015, U.S. Environmental Protection Agency (EPA), 2017. http://www3.epa.gov/climatechange/emissions/usinventoryreport.html.

[5] R. Eldrid, L. Kaufman, P. Marks, The 7FB: The next evolution of the F gas turbine, GER-4194 April. (2001).

[6] R.C. Reed, The Superalloys, Cambridge University Press, New York, 2006.

[7] J. Sato, T. Omori, K. Oikawa, I. Ohnuma, R. Kainuma, K. Ishida, Cobalt-base high-temperature alloys, Science. 312 (2006) 90–91. doi:10.1126/science.1121738.

[8] J. Dahl, Turbojet Engine Diagram, Wikimedia- Jet Engine. (2007). https://commons.wikimedia.org/wiki/File:Jet_engine.svg.

[9] M. Cervenka, Jet Engine Materials, Coat. Turbine Bl. (n.d.). http://www.phase-trans.msm.cam.ac.uk/2003/Superalloys/coatings/index.html.

[10] A.G. Evans, D.R. Clarke, C.G. Levi, The influence of oxides on the performance of advanced gas turbines, J. Eur. Ceram. Soc. 28 (2008) 1405–1419. doi:10.1016/j.jeurceramsoc.2007.12.023.

[11] D.L. Klarstrom, Wrought cobalt-base superalloys, J. Mater. Eng. Perform. 2 (1993) 523–530.

[12] T. Nishizawa, K. Ishida, The Co−Ni (Cobalt-Nickel) system, Bull. Alloy Phase Diagr. 4 (1983) 390–395. doi:10.1007/BF02868090.

[13] F.S. Pettit, Oxidation mechanisms for nickel-aluminum alloys at temperatures between 900°C and 1300°C, Trans. Metall. Soc. AIME. 239 (1967) 1296–1305.

[14] I. Ansara, N. Dupin, H.L. Lukas, B. Sundman, Thermodynamic assessment of the Al-Ni system, J. Alloys Compd. 247 (1997) 20–30.

[15] A.J. McAlister, The Al-Co (Aluminum-Cobalt) System, J. Phase Equilibria. 10 (1989) 646–650.

[16] K. Oikawa, T. Ota, F. Gejima, T. Ohmori, R. Kainuma, K. Ishida, Phase equilibria and phase transformations in new B2-type ferromagnetic shape memory alloys of Co-Ni-Ga and Co-Ni-Al systems, Mater. Trans. 42 (2001) 2472–2475.

[17] A. Markström, B. Sundman, K. Frisk, A Revised Thermodynamic Description of the Co-W-C System, J. Phase Equilibria Diffus. 26 (2005) 152–160. doi:10.1361/15477030522473.

[18] T.M. Pollock, J. Dibbern, M. Tsunekane, J. Zhu, A. Suzuki, New Co-based γ-γ' high temperature alloys, JoM. 62 (2010) 58–63.

[19] K. Shinagawa, T. Omori, J. Sato, K. Oikawa, I. Ohnuma, R. Kainuma, K. Ishida, Phase Equilibria and Microstructure on γ' Phase in Co-Ni-Al-W System, Mater. Trans. 49 (2008) 1474.
[20] H.-Y. Yan, V.A. Vorontsov, D. Dye, Effect of alloying on the oxidation behaviour of Co–Al–W superalloys, Corros. Sci. 83 (2014) 382–395. doi:10.1016/j.corsci.2014.03.002.
[21] G.R. Wallwork, A.Z. Hed, Mapping of the oxidation products in the ternary Co-Cr-Al system, Oxid. Met. 3 (1971) 213–227.
[22] M.S. Titus, A. Suzuki, T.M. Pollock, High temperature creep of new L12-containing cobalt-base superalloys, Superalloys 2012. (2012) 823–832.
[23] A. Mottura, A. Janotti, T.M. Pollock, Alloying Effects in the γ' Phase of Co-based Superalloys, Superalloys 2012. (2012) 685–693.
[24] K. Ishida, T. Nishizawa, The Co-Cr (Cobalt-Chromium) system, Bull. Alloy Phase Diagr. 11 (1990) 357–370. doi:10.1007/BF02843315.
[25] T. Omori, J. Sato, K. Shinagawa, I. Ohnuma, K. Oikawa, R. Kainuma, K. Ishida, Experimental Determination of Phase Equilibria in the Co-Cr-Ni System, J. Phase Equilibria Diffus. 35 (2014) 178–185. doi:10.1007/s11669-014-0292-z.
[26] K.P. Gupta, The Co-Cr-W (Cobalt-Chromium-Tungsten) System, J. Phase Equilibria Diffus. 27 (2006) 178–183. doi:10.1361/154770305X97597.
[27] R.K. Rhein, P.C. Dodge, M.-H. Chen, M.S. Titus, T.M. Pollock, A. Van der Ven, Role of vibrational and configurational excitations in stabilizing the L 1 2 structure in Co-rich Co-Al-W alloys, Phys. Rev. B. 92 (2015). doi:10.1103/PhysRevB.92.174117.
[28] J.G. Goiri, A. Van der Ven, Phase and structural stability in Ni-Al systems from first principles, Phys. Rev. B. 94 (2016). doi:10.1103/PhysRevB.94.094111.
[29] A.K. Sinha, Topologically close-packed structures of transition metal alloys, Prog. Mater. Sci. 15 (1972) 81–185. doi:10.1016/0079-6425(72)90002-3.
[30] F.C. Frank, J.S. Kasper, Complex alloy structures regarded as sphere packings. I. Definitions and basic principles, Acta Crystallogr. 11 (1958) 184–190. doi:10.1107/S0365110X58000487.
[31] T. Omori, K. Oikawa, J. Sato, I. Ohnuma, U.R. Kattner, R. Kainuma, K. Ishida, Partition behavior of alloying elements and phase transformation temperatures in Co–Al–W-base quaternary systems, Intermetallics. 32 (2013) 274–283. doi:10.1016/j.intermet.2012.07.033.
[32] S. Kobayashi, Y. Tsukamoto, T. Takasugi, H. Chinen, T. Omori, K. Ishida, S. Zaefferer, Determination of phase equilibria in the Co-rich Co–Al–W ternary system with a diffusion-couple technique, Intermetallics. 17 (2009) 1085–1089. doi:10.1016/j.intermet.2009.05.009.
[33] E.A. Lass, M.E. Williams, C.E. Campbell, K.-W. Moon, U.R. Kattner, γ′ Phase Stability and Phase Equilibrium in Ternary Co-Al-W at 900 °C, J. Phase Equilibria Diffus. (2014). doi:10.1007/s11669-014-0346-2.
[34] I. Povstugar, C.H. Zenk, R. Li, P.-P. Choi, S. Neumeier, O. Dolotko, M. Hoelzel, M. Göken, D. Raabe, Elemental partitioning, lattice misfit and creep behaviour of Cr containing γ′ strengthened Co base superalloys, Mater. Sci. Technol. 32 (2016) 220–225. doi:10.1179/1743284715Y.0000000112.
[35] A. Suzuki, H. Inui, T.M. Pollock, L1 $_2$ -Strengthened Cobalt-Base Superalloys, Annu. Rev. Mater. Res. 45 (2015) 345–368. doi:10.1146/annurev-matsci-070214-021043.

[36] A. Suzuki, High-temperature strength and deformation of γ/γ′ two-phase Co–Al–W-base alloys, Acta Mater. 56 (2008) 1288–1297. doi:10.1016/j.actamat.2007.11.014.
[37] D.A. Porter, K.E. Easterling, Phase transitions in metals and alloys, Chapman & Hall, London, UK, 1992.
[38] S. Tin, T.M. Pollock, Stabilization of thermosolutal convective instabilities in Ni-based single-crystal superalloys: Carbide precipitation and rayleigh numbers, Metall. Mater. Trans. A. 34 (2003) 1953–1967. doi:10.1007/s11661-003-0160-7.
[39] J. Koßmann, C.H. Zenk, I. Lopez-Galilea, S. Neumeier, A. Kostka, S. Huth, W. Theisen, M. Göken, R. Drautz, T. Hammerschmidt, Microsegregation and precipitates of an as-cast Co-based superalloy—microstructural characterization and phase stability modelling, J. Mater. Sci. 50 (2015) 6329–6338. doi:10.1007/s10853-015-9177-8.
[40] M. Tsunekane, A. Suzuki, T.M. Pollock, Single-crystal solidification of new Co–Al–W-base alloys, Intermetallics. 19 (2011) 636–643. doi:10.1016/j.intermet.2010.12.018.
[41] R.W. Jackson, M.S. Titus, M.R. Begley, T.M. Pollock, Thermal expansion behavior of new Co-based alloys and implications for coatings, Surf. Coat. Technol. 289 (2016) 61–68. doi:10.1016/j.surfcoat.2015.12.083.
[42] N. Birks, G.H. Meier, F.S. Pettit, Introduction to the High-Temperature Oxidation of Metals, 2nd ed., Cambridge University Press, 2006.
[43] H.J.T. Ellingham, Reducibility of oxides and sulphides in metallurgical processes, J. Soc. Chem. Ind. 63 (1944) 125–160. doi:10.1002/jctb.5000630501.
[44] C.S. Tedmon, The Effect of Oxide Volatilization on the Oxidation Kinetics of Cr and Fe-Cr Alloys, J. Electrochem. Soc. 113 (1966) 766. doi:10.1149/1.2424115.
[45] H.J. Grabke, Oxidation of NiAl and FeAl, Intermetallics. (1999) 1153–1158.
[46] V.K. Tolpygo, D.R. Clarke, Alumina scale failure resulting from stress relaxation, Surf. Coat. Technol. 120–121 (1999) 1–7. doi:10.1016/S0257-8972(99)00331-X.
[47] M.Y. He, A.G. Evans, J.W. Hutchinson, Effects of morphology on the decohesion of compressed thin films, Mater. Sci. Eng. A. (1998) 14.
[48] D.R. Mumm, A.G. Evans, I.T. Spitsberg, Characterization of a cyclic displacement instability for a thermally grown oxide in a thermal barrier system, Acta Mater. 49 (2001) 2329–2340. doi:10.1016/S1359-6454(01)00071-4.
[49] D.R. Clarke, Stress generation during high-temperature oxidation of metallic alloys, Curr. Opin. Solid State Mater. Sci. 6 (2002) 237–244. doi:10.1016/S1359-0286(02)00074-8.
[50] A.H. Heuer, A. Reddy, D.B. Hovis, B. Veal, A. Paulikas, A. Vlad, M. Rühle, The effect of surface orientation on oxidation-induced growth strains in single crystal NiAl: An in situ synchrotron study, Scr. Mater. 54 (2006) 1907–1912. doi:10.1016/j.scriptamat.2006.02.021.
[51] R.E. Bedworth, N.B. Pilling, The oxidation of metals at high temperatures, J. Inst. Met. 29 (1923) 529–582.
[52] I. Levin, D. Brandon, Metastable alumina polymorphs: crystal structures and transition sequences, J. Am. Ceram. Soc. 81 (1998) 1995–2012.
[53] P.Y. Hou, Segregation Phenomena at Thermally Grown Al_2O_3 Alloy Interfaces, Annu. Rev. Mater. Res. 38 (2008) 275–298. doi:10.1146/annurev.matsci.38.060407.130323.

[54] J.S. Wang, A.G. Evans, Effects of strain cycling on buckling, cracking and spalling of a thermally grown alumina on a nickel-based bond coat, Acta Mater. 47 (1999) 699–710. doi:10.1016/S1359-6454(98)00328-0.
[55] V.K. Tolpygo, D.R. Clarke, Spalling failure of a-alumina films grown by oxidation: I. Dependence on cooling rate and metal thickness, Mater. Sci. Eng. A. (2000) 9.
[56] A.G. Evans, M.Y. He, J.W. Hutchinson, Effect of interface undulations on the thermal fatigue of thin films and scales on metal substrates, Acta Mater. 45 (1997) 3543–3554.
[57] A.M. Karlsson, C.G. Levi, A.G. Evans, A model study of displacement instabilities during cyclic oxidation, Acta Mater. 50 (2002) 1263–1273. doi:10.1016/S1359-6454(01)00403-7.
[58] V.K. Tolpygo, D.R. Clarke, Spalling failure of a-alumina films grown by oxidation. II. Decohesion nucleation and growth, Mater. Sci. Eng. A. (2000) 11.
[59] M.R. Begley, J.W. Hutchinson, The Mechanics and Reliability of Films, Multilayers and Coatings, Cambridge University Press, Cambridge, 2017. doi:10.1017/9781316443606.
[60] A.G. Evang, B.J. Dalgleish, The fracture resistance of metal-ceramic interfaces, Acta Metall. Mater. 40 (1992) S295–S306.
[61] A.G. Evans, D.R. Mumm, J.W. Hutchinson, G.H. Meier, F.S. Pettit, Mechanisms controlling the durability of thermal barrier coatings, Prog. Mater. Sci. 46 (2001) 505–553.
[62] M.P. Brady, I.G. Wright, B. Gleeson, Alloy design strategies for promoting protective oxide-scale formation, JOM. 52 (2000) 16–21.
[63] D.L. Douglass, A critique of internal oxidation in alloys during the post-Wagner era, Oxid. Met. 44 (1995) 81–111.
[64] R.A. Rapp, Kinetics, microstructures and mechanism of internal oxidation - Its effect and prevention in high temperature alloy oxidation, Corrosion. 21 (1965) 382–401.
[65] W. Zhao, Y. Kang, J.M.A. Orozco, B. Gleeson, Quantitative Approach for Determining the Critical Volume Fraction for the Transition from Internal to External Oxidation, Oxid. Met. 83 (2015) 187–201. doi:10.1007/s11085-014-9516-1.
[66] Cambridge University, The Interactive Ellingham Diagram, DoITPoMS TLP Libr. Ellingham Diagr. (2004). https://www.doitpoms.ac.uk/tlplib/ellingham_diagrams/interactive.php.
[67] Centre d'information du cobalt & Battelle Memorial Institute, Cobalt Monograph, The Centre, Brussels, 1960.
[68] M. Kinoshita, W.D. Kingery, H.K. Bowen, Phase Separation in NiO-CoO Solid Solution Single Crystals, J. Am. Ceram. Soc. 56 (1973) 398–399.
[69] F. Bondioli, A.M. Ferrari, C. Leonelli, T. Manfredini, L. Linati, P. Mustarelli, Reaction Mechanism in Alumina/Chromia (Al_2O_3-Cr_2O_3) Solid Solutions Obtained by Coprecipitation, J. Am. Ceram. Soc. 83 (2004) 2036–2040. doi:10.1111/j.1151-2916.2000.tb01508.x.
[70] S.S. Kim, T.H. Sanders, Thermodynamic Modeling of the Isomorphous Phase Diagrams in the Al_2O_3-Cr_2O_3 and V_2O_3-Cr_2O_3 Systems, J. Am. Ceram. Soc. 84 (2004) 1881–1884. doi:10.1111/j.1151-2916.2001.tb00930.x.

[71] V.K. Tolpygo, D.R. Clarke, Microstructural evidence for counter-diffusion of aluminum and oxygen during the growth of alumina scales, Mater. High Temp. 20 (2003) 261–271. doi:10.3184/096034003782748892.
[72] E.J. Opila, Volatility of Common Protective Oxides in High-Temperature Water Vapor: Current Understanding and Unanswered Questions, Mater. Sci. Forum. 461–464 (2004) 765–774. doi:10.4028/www.scientific.net/MSF.461-464.765.
[73] D.J. Young, B.A. Pint, Chromium Volatilization Rates from Cr_2O_3 Scales into Flowing Gases Containing Water Vapor, Oxid. Met. 66 (2006) 137–153. doi:10.1007/s11085-006-9030-1.
[74] A.M. Beltran, The oxidation and hot-corrosion resistance of cobalt-base superalloys, Tech. Briefs. (1970) 51–53.
[75] L.M. Pike, 100+ Years of Wrought Alloy Development at Haynes International, in: E. Ott, A. Banik, J. Andersson, I. Dempster, T. Gabb, J. Groh, K. Heck, R. Helmink, X. Liu, A. Wusatowska-Sarnek (Eds.), 8th Int. Symp. Superalloy 718 Deriv., John Wiley & Sons, Inc., Hoboken, NJ, USA, 2014: pp. 15–30. doi:10.1002/9781119016854.ch2.
[76] C. Wagner, Passivity and inhibition during the oxidation of metals at elevated temperatures, Corros. Sci. 5 (1965) 751–764. doi:10.1016/S0010-938X(65)80003-8.
[77] Y. Kang, In-situ and ex-situ studies on early-stage scale establishment, Doctoral, University of Pittsburgh, 2016.
[78] P.R.S. Jackson, G.R. Wallwork, High temperature oxidation of iron-manganese-aluminum based alloys, Oxid. Met. 21 (1984) 135–170. doi:10.1007/BF00741468.
[79] P. Tomaszewicz, G.R. Wallwork, The oxidation of Fe-Al alloys containing chromium, nickel, or manganese, Corrosion. 40 (1984) 152–157.
[80] H. Götlind, F. Liu, J.-E. Svensson, M. Halvarsson, L.-G. Johansson, The Effect of Water Vapor on the Initial Stages of Oxidation of the FeCrAl Alloy Kanthal AF at 900 °C, Oxid. Met. 67 (2007) 251–266. doi:10.1007/s11085-007-9055-0.
[81] Y. Kitajima, S. Hayashi, T. Nishimoto, T. Narita, S. Ukai, Acceleration of Metastable to Alpha Transformation of Al_2O_3 Scale on Fe–Al Alloy by Pure-Metal Coatings at 900 °C, Oxid. Met. 75 (2011) 41–56. doi:10.1007/s11085-010-9219-1.
[82] X. Peng, D.R. Clarke, F. Wang, Transient-alumina transformations during the oxidation of magnetron-sputtered CoCrAl nanocrystalline coatings, Oxid. Met. 60 (2003) 225–240.
[83] V.K. Tolpygo, D.R. Clarke, Microstructural study of the theta-alpha transformation in alumina scales formed on nickel-aluminides, Mater. High Temp. 17 (2000) 59–70. doi:10.1179/mht.2000.011.
[84] E. Airiskallio, E. Nurmi, M.H. Heinonen, I.J. Väyrynen, K. Kokko, M. Ropo, M.P.J. Punkkinen, H. Pitkänen, M. Alatalo, J. Kollár, B. Johansson, L. Vitos, High temperature oxidation of Fe–Al and Fe–Cr–Al alloys: The role of Cr as a chemically active element, Corros. Sci. 52 (2010) 3394–3404. doi:10.1016/j.corsci.2010.06.019.
[85] E. Airiskallio, E. Nurmi, M.H. Heinonen, I.J. Väyrynen, K. Kokko, M. Ropo, M.P.J. Punkkinen, H. Pitkänen, M. Alatalo, J. Kollár, B. Johansson, L. Vitos, Third element effect in the surface zone of Fe-Cr-Al alloys, Phys. Rev. B. 81 (2010). doi:10.1103/PhysRevB.81.033105.
[86] H.A. Wriedt, The O-W (oxygen-tungsten) system, Bull. Alloy Phase Diagr. 10 (1989) 368–384. doi:10.1007/BF02877593.

[87] V.K. Sikka, C.J. Rosa, The oxidation kinetics of tungsten and the determination of oxygen diffusion coefficient in tungsten trioxide, Corros. Sci. 20 (1980) 1201–1219.
[88] T. Millner, J. Neugebauer, Volatility of the oxides of tungsten and molybdenum in the presence of water vapor, Nature. 163 (1949) 601–602.
[89] A.E. Newkirk, E.L. Simons, Thermogravimetry of Tungsten Trioxide., Anal. Chem. 37 (1965) 146–147. doi:10.1021/ac60220a038.
[90] M.E. El-Dahshan, D.P. Whittle, J. Stringer, The oxidation of cobalt—tungsten alloys, Corros. Sci. 16 (1976) 77–82.
[91] S. Espevik, R.A. Rapp, P.L. Daniel, J.P. Hirth, Oxidation of ternary Co-Cr-W alloys, Oxid. Met. 20 (1983) 37–65.
[92] S. Espevik, R.A. Rapp, P.L. Daniel, J.P. Hirth, Oxidation of Ni-Cr-W ternary alloys, Oxid. Met. 14 (1980) 85–108.
[93] A.-C. Yeh, S.-C. Wang, C.-F. Cheng, Y.-J. Chang, S.-C. Chang, Oxidation Behaviour of Si-Bearing Co-Based Alloys, Oxid. Met. (2016). doi:10.1007/s11085-016-9623-2.
[94] D.W. Yun, S.M. Seo, H.W. Jeong, Y.S. Yoo, Effect of refractory elements and Al on the high temperature oxidation of Ni-base superalloys and modelling of their oxidation resistance, J. Alloys Compd. (2017). doi:10.1016/j.jallcom.2017.03.179.
[95] K. Kitayama, Thermogravimetric Study of the M-Co-O System: I, M = Ta and Nb at 1200°C, J. Am. Ceram. Soc. 75 (1992) 1447–1451. doi:10.1111/j.1151-2916.1992.tb04208.x.
[96] K. Kitayama, Thermogravimetric study of the M-Ni-O system. I. M = Ta and Nb, J. Solid State Chem. 83 (1989) 37–44.
[97] R.S. Roth, J.L. Waring, Effect of oxide additions on the polymorphism of tantalum pentoxide. III. "Stabilization" of the low temperature structure type, J. Res. Natl. Bur. Stand. Sect. Phys. Chem. 74A (1970) 485. doi:10.6028/jres.074A.038.
[98] L. Klein, A. Bauer, S. Neumeier, M. Göken, S. Virtanen, High temperature oxidation of γ/γ′-strengthened Co-base superalloys, Corros. Sci. 53 (2011) 2027–2034. doi:10.1016/j.corsci.2011.02.033.
[99] S.-I. Baik, X. Yin, D.N. Seidman, Correlative atom-probe tomography and transmission electron microscope study of a chemical transition in a spinel on an oxidized nickel-based superalloy, Scr. Mater. 68 (2013) 909–912. doi:10.1016/j.scriptamat.2013.02.025.
[100] K. Kawagishi, H. Harada, A. Sato, A. Sato, T. Kobayashi, The oxidation properties of fourth generation single-crystal nickel-based superalloys, Jom. 58 (2006) 43–46.
[101] L.B. Pfeil, Improvements relating to heat-resisting alloys containing chromium, 574088, n.d.
[102] D. Naumenko, B.A. Pint, W.J. Quadakkers, Current Thoughts on Reactive Element Effects in Alumina-Forming Systems: In Memory of John Stringer, Oxid. Met. (2016). doi:10.1007/s11085-016-9625-0.
[103] B.A. Pint, Progress in Understanding the Reactive Element Effect Since the Whittle and Stringer Literature Review, in: Proc. John Stringer Symp. High Temp. Corros., ASM International, Indianapolis, IN, 2003: pp. 9–19.
[104] D.P. Whittle, J. Stringer, Improvements in high temperature oxidation resistance by additions of reactive elements or oxide dispersions, Philos. Trans. R. Soc. Lond. A. 295 (1980) 309–329.

[105] B.A. Pint, Optimization of reactive-element additions to improve oxidation performance of alumina-forming alloys, J. Am. Ceram. Soc. 86 (2003) 686–695.
[106] H. Hindam, D.P. Whittle, Peg Formation by Short-Circuit Diffusion in Al_2O_3 Scales Containing Oxide Dispersions, J. Electrochem. Soc. Accel. Brief Commun. 129 (1982) 1147–1149.
[107] J.L. Smialek, Effect of Sulfur Removal on Al_2O_3 Scale Adhesion, Metall. Trans. A. 22 (1991) 739–752.
[108] J.L. Smialek, D.T. Jayne, J.C. Schaeffer, W.H. Murphy, Effects of hydrogen annealing, sulfur segregation and diffusion on the cyclic oxidation resistance of superalloys: a review, Thin Solid Films. 253 (1994) 285–292. doi:10.1016/0040-6090(94)90335-2.
[109] G.H. Meier, F.S. Pettit, J.L. Smialek, The effects of reactive element additions and sulfur removal on the adherence of alumina to Ni- and Fe-base alloys, Mater. Corros. Korros. 46 (1995) 232–240. doi:10.1002/maco.19950460407.
[110] W. Cao, S.-L. Chen, F. Zhang, K. Wu, Y. Yang, Y.A. Chang, R. Schmid-Fetzer, W.A. Oates, PANDAT software with PanEngine, PanOptimizer and PanPrecipitation for multi-component phase diagram calculation and materials property simulation, Calphad. 33 (2009) 328–342. doi:10.1016/j.calphad.2008.08.004.
[111] A. Borgenstam, L. Höglund, J. Agren, A. Engström, DICTRA, a tool for simulation of diffusional transformations in alloys, J. Phase Equilibria. 21 (2000) 269–280.
[112] H. Chen, T. Barman, Thermo-Calc and DICTRA modelling of the β-phase depletion behaviour in CoNiCrAlY coating alloys at different Al contents, Comput. Mater. Sci. 147 (2018) 103–114. doi:10.1016/j.commatsci.2018.02.013.
[113] D.C. Harris, M.D. Bertolucci, Symmetry and Spectroscopy: An Introduction to Vibrational and Electronic Spectroscopy, Oxford University Press, New York, NY, 1978.
[114] P.J. Larkin, Infrared and Raman Spectroscopy: Principles and Spectral Interpretation, 2nd ed., Elsevier, 2018.
[115] D. Tuschel, Photoluminesscence Spectroscopy using a Raman spectrometer, Spectroscopy. 31 (2016) 14–21.
[116] Q. Wen, D.M. Lipkin, D.R. Clarke, Luminescence characterization of chromium-containing theta-alumina, J. Am. Ceram. Soc. 81 (1998) 3345–3348.
[117] H. Yu, D.R. Clarke, Effect of codoping on the R-line luminescence of Cr^{3+}-doped alumina, J. Am. Ceram. Soc. 85 (2002) 1966–1970.
[118] J. He, D.R. Clarke, Determination of the piezospectroscopic coefficients for Chromium-doped sapphire, J. Am. Ceram. Soc. 78 (1995) 1347–1353.
[119] D.M. Lipkin, D.R. Clarke, Measurement of the stress in oxide scales formed by oxidation of alumina-forming alloys, Oxid. Met. 45 (1996) 267–280.
[120] F. Pyczak, B. Devirent, H. Mughrabi, The Effects of Different Alloying Elements on the Thermal Expansion Coefficients, Lattice Constants and Misfit of Nickel-Based Superalloys Investigated by X-Ray Diffraction, in: TMS, 2004: pp. 827–836. doi:10.7449/2004/Superalloys_2004_827_836.
[121] C.C. Jia, K. Ishida, T. Nishizawa, Partition of alloying elements between γ (A1), γ′(L12), and β (B2) phases in Ni-Al base systems, Metall. Mater. Trans. A. 25 (1994) 473–485.

[122] M. Pröbstle, S. Neumeier, P.S. Feldner, R. Rettig, H.E. Helmer, R.F. Singer, M. Göken, Improved creep strength of nickel-base superalloys by optimized γ/γ'partitioning behavior of solid solution strengthening elements, Mater. Sci. Eng. A. (2016). http://www.sciencedirect.com/science/article/pii/S0921509316310565 (accessed September 6, 2016).
[123] S.H. Liu, C.P. Liu, W.Q. Liu, X.N. Zhang, P. Yan, C.Y. Wang, Investigation of the elemental partitioning behaviour and site preference in ternary model nickel-based superalloys by atom probe tomography and first-principles calculations, Philos. Mag. 96 (2016) 2204–2218. doi:10.1080/14786435.2016.1192298.
[124] M. Kolb, C.H. Zenk, A. Kirzinger, I. Povstugar, D. Raabe, S. Neumeier, M. Göken, Influence of rhenium on γ′-strengthened cobalt-base superalloys, J. Mater. Res. 32 (2017) 2551–2559. doi:10.1557/jmr.2017.242.
[125] G.N. Irving, J. Stringer, D.P. Whittle, The high-temperature oxidation resistance of Co-Al alloys, Oxid. Met. 9 (1975) 427–440.
[126] C.A. Phalnikar, E.B. Evans, W.M. Baldwin, High Temperature Scaling of Cobalt-Chromium Alloys, J. Electrochem. Soc. 103 (1956) 429–438.
[127] G.N. Irving, J. Stringer, D.P. Whittle, The oxidation behavior of Co-Cr-Al alloys at 1000°C, Corrosion. 33 (1977) 56–60.
[128] W.S. Walston, K.S. O'Hara, E.W. Ross, T.M. Pollock, W.H. Murphy, Rene' N6: Third Generation Single Crystal Superalloy, in: Superalloys 1996 Eighth Int. Symp., TMS, 1996: pp. 27–34. doi:10.7449/1996/Superalloys_1996_27_34.
[129] G.A. López, S. Sommadossi, W. Gust, E.J. Mittemeijer, P. Zieba, Phase Characterization of Diffusion Soldered Ni/Al/Ni Interconnections, Interface Sci. 10 (2002) 13–19.
[130] L. Zhu, C. Wei, L. Jiang, Z. Jin, J.-C. Zhao, Experimental determination of the phase diagrams of the Co-Ni-X (X = W, Mo, Nb, Ta) ternary systems using diffusion multiples, Intermetallics. 93 (2018) 20–29. doi:10.1016/j.intermet.2017.11.005.
[131] H. Choi, B. Yoon, H. Kim, C. Lee, Isothermal oxidation of air plasma spray NiCrAlY bond coatings, Surf. Coat. Technol. 150 (2002) 297–308.
[132] J.Q. Stewart, S.A. Korff, Distinction between scattering and absorption, Astrophys. J. 71 (1930) 62–66.
[133] M.A. Payne, J.B. Miller, A.J. Gellman, High-throughput characterization of early oxidation across AlxFeyNi1−x−y composition space, Corros. Sci. 91 (2015) 46–57. doi:10.1016/j.corsci.2014.10.034.
[134] T. Gebhardt, D. Music, T. Takahashi, J.M. Schneider, Combinatorial thin film materials science: From alloy discovery and optimization to alloy design, Thin Solid Films. 520 (2012) 5491–5499. doi:10.1016/j.tsf.2012.04.062.
[135] D. Naujoks, J. Richert, P. Decker, M. Weiser, S. Virtanen, A. Ludwig, Phase formation and oxidation behavior at 500°C in a Ni-Co-Al thin-film materials library, ACS Comb. Sci. (2016). doi:10.1021/acscombsci.6b00052.
[136] C.J. Metting, J.K. Bunn, E. Underwood, S. Smoak, J. Hattrick-Simpers, Combinatorial approach to turbine bond coat discovery, ACS Comb. Sci. 15 (2013) 419–424. doi:10.1021/co3000902.
[137] R.R. Adharapurapu, J. Zhu, V.S. Dheeradhada, D.M. Lipkin, T.M. Pollock, A combinatorial investigation of palladium and platinum additions to β-NiAl overlay coatings, Acta Mater. 77 (2014) 379–393. doi:10.1016/j.actamat.2014.02.030.

[138] A.J. Elliott, T.M. Pollock, S. Tin, W.T. King, S.-C. Huang, M.F.X. Gigliotti, Directional solidification of large superalloy castings with radiation and liquid-metal cooling: A comparative assessment, Metall. Mater. Trans. A. 35 (2004) 3221–3231. doi:10.1007/s11661-004-0066-z.
[139] U.R. Kattner, The thermodynamic modeling of multicomponent phase equilibria, JOM. 49 (1997) 14–19. doi:10.1007/s11837-997-0024-5.
[140] J. Zhu, M.S. Titus, T.M. Pollock, Experimental Investigation and Thermodynamic Modeling of the Co-Rich Region in the Co-Al-Ni-W Quaternary System, J. Phase Equilibria Diffus. 35 (2014) 595–611. doi:10.1007/s11669-014-0327-5.
[141] G. Kresse, J. Furthmüller, Efficiency of ab-initio total energy calculations for metals and semiconductors using a plane-wave basis set, Comput. Mater. Sci. 6 (1996) 15–50.
[142] G. Kresse, D. Joubert, From ultrasoft pseudopotentials to the projector augmented-wave method, Phys. Rev. B. 59 (1999) 1758.
[143] J.P. Perdew, K. Burke, M. Ernzerhof, Generalized gradient approximation made simple, Phys. Rev. Lett. 77 (1996) 3865.
[144] CASM v0.2.1, 2017. doi:10.5281/zenodo.546148.
[145] J.C. Thomas, A.V. der Ven, Finite-temperature properties of strongly anharmonic and mechanically unstable crystal phases from first principles, Phys. Rev. B. 88 (2013). doi:10.1103/PhysRevB.88.214111.
[146] B. Puchala, A. Van der Ven, Thermodynamics of the Zr-O system from first-principles calculations, Phys. Rev. B. 88 (2013). doi:10.1103/PhysRevB.88.094108.
[147] A. Van der Ven, J.C. Thomas, Q. Xu, J. Bhattacharya, Linking the electronic structure of solids to their thermodynamic and kinetic properties, Math. Comput. Simul. 80 (2010) 1393–1410. doi:10.1016/j.matcom.2009.08.008.
[148] A. Jain, S.P. Ong, G. Hautier, W. Chen, W.D. Richards, S. Dacek, S. Cholia, D. Gunter, D. Skinner, G. Ceder, K.A. Persson, The Materials Project: A materials genome approach to accelerating materials innovation, APL Mater. 1 (2013) 011002. doi:10.1063/1.4812323.
[149] EDAX Interactive Periodic Table, EDAX. (n.d.). https://www.edax.com/resources/interactive-periodic-table (accessed September 27, 2018).
[150] C.A. Stewart, R.K. Rhein, A. Suzuki, T.M. Pollock, C.G. Levi, Oxide scale formation in novel γ-γ' cobalt-based alloys, in: M. Hardy, E. Huron, U. Glatzel, B. Griffin, B. Lewis, C. Rae, V. Seetharaman, B. Lewis (Eds.), Proc. 13th Int. Symp. Superalloys, TMS (The Minerals, Metals & Materials Society), 2016: pp. 991–999.
[151] N. Mironova-Ulmane, A. Kuzmin, I. Steins, J. Grabis, I. Sildos, M. Pärs, Raman scattering in nanosized nickel oxide NiO, J. Phys. Conf. Ser. 93 (2007) 012039. doi:10.1088/1742-6596/93/1/012039.
[152] C. Wagner, Theoretical analysis of the diffusion processes determining the oxidation rate of alloys, J. Electrochem. Soc. 99 (1952) 369–380.
[153] C.A. Schneider, W.S. Rasband, K.W. Eliceiri, NIH Image to ImageJ: 25 years of image analysis, Nat. Methods. 9 (2012) 671–675. doi:10.1038/nmeth.2089.
[154] R.. Rapp, The transition from internal to external oxidation and the formation of interruption bands in silver-indium alloys, Acta Metall. 9 (1961) 730–741. doi:10.1016/0001-6160(61)90103-1.

[155] J.L. Meijering, Internal Oxidation in Alloys, in: H. Herman (Ed.), Adv. Mater. Res., Wiley-Interscience, New York, NY, 1971: pp. 1–81.
[156] A. Martınez-Villafane, F.H. Stott, J.G. Chacon-Nava, G.C. Wood, Enhanced Oxygen Diffusion Along Internal Oxide– Metal Matrix Interfaces in Ni–Al Alloys During Internal Oxidation, Oxid. Met. 57 (2002) 267–279.
[157] C. Xu, W. Gao, Pilling-Bedworth ratio for oxidation of alloys, Mater. Res. Innov. 3 (2000) 231–235.
[158] J.L. Meijering, Some aspects of internal oxidation in Ag-, Cu-, Ni- and Fe-alloys, in: Pittsburgh Int. Conf. Surf. React., Corrosion Publishing Company, Pittsburgh, PA, 1948: pp. 101–104. https://babel.hathitrust.org/cgi/pt?id=mdp.39015018419286;view=1up;seq=9.
[159] C.A. Stewart, A. Suzuki, T.M. Pollock, C.G. Levi, Rapid Assessment of Oxidation Behavior in Co-Based γ/γ′ Alloys, Oxid. Met. (2018). doi:10.1007/s11085-018-9849-2.
[160] I. Zaplatynsky, Thermal expansion of some nickel and cobalt spinels and their solid solutions, Contract. 129 (1971) 03.
[161] E.A.G. Shillington, D.R. Clarke, Spalling failure of a thermal barrier coating associated with aluminum depletion in the bond-coat, Acta Mater. 47 (1999) 1297–1305.
[162] K. Kawagishi, A.-C. Yeh, T. Yokokawa, T. Kobayashi, Y. Koizumi, H. Harada, Development of an oxidation-resistant high-strength sixth-generation single-crystal superalloy TMS-238, Pap. Present Superalloys Seven Springs Mt. Resort Champion Pa. USA. (2012) 9–13.
[163] L. Qiu, F. Yang, W. Zhang, X. Zhao, P. Xiao, Effect of Al content on the lifetime of thermally grown oxide formed on Ni–Al alloys after isothermal oxidation, Corros. Sci. 89 (2014) 13–20. doi:10.1016/j.corsci.2014.07.023.
[164] R.J. Christensen, D.M. Lipkin, D.R. Clarke, K. Murphy, Nondestructive evaluation of the oxidation stresses through thermal barrier coatings using Cr^{3+} piezospectroscopy, Appl. Phys. Lett. 69 (1996) 3754–3756.
[165] R. Newman, R.M. Chrenko, Optical properties of nickel oxide, Phys. Rev. 114 (1959) 1507–1513.
[166] R. Newman, R.M. Chrenko, Effects of MnO and CoO on the 0.24-ev NiO Absorption Line, Phys. Rev. 115 (1959) 882.
[167] G.W. Pratt Jr, R. Coelho, Optical Absorption of CoO and MnO above and below the Néel Temperature, Phys. Rev. 116 (1959) 281–286.
[168] L.J. Carroll, Q. Feng, J.F. Mansfield, T.M. Pollock, Elemental partitioning in Ru-containing nickel-base single crystal superalloys, Mater. Sci. Eng. A. 457 (2007) 292–299. doi:10.1016/j.msea.2006.12.036.
[169] C.A. Stewart, A. Suzuki, T.M. Pollock, C.G. Levi, Rapid assessment of oxidation behavior in Co-based γ/γ' alloys, Oxid. Met. (2018).
[170] M.A. Lafata, L.H. Rettberg, M.Y. He, T.M. Pollock, Oxidation-Assisted Crack Growth in Single-Crystal Superalloys during Fatigue with Compressive Holds, Metall. Mater. Trans. A. 49 (2018) 105–116. doi:10.1007/s11661-017-4392-3.
[171] Y. Xu, L. Zhang, J. Li, X. Xiao, X. Cao, G. Jia, Z. Shen, Relationship between Ti/Al ratio and stress-rupture properties in nickel-based superalloy, Mater. Sci. Eng. A. 544 (2012) 48–53. doi:10.1016/j.msea.2012.03.006.

[172] M. Simonetti, P. Caron, Role and behaviour of μ phase during deformation of a nickel-based single crystal superalloy, Mater. Sci. Eng. A. (1998) 12.
[173] C. Wagner, Reaktionstypen bei der Oxydation von Legierungen, Z. Für Elektrochem. 63 (1959) 772–790.
[174] F.H. Stott, G.C. Wood, J. Stringer, The influence of alloying elements on the development and maintenance of protective scales, Oxid. Met. 44 (1995) 113–145.
[175] Y. Minamino, Y. Koizumi, N. Tsuji, T. Yamada, T. Takahashi, Interdiffusion in Co Solid Solutions of Co-Al-Cr-Ni System at 1423 K., Mater. Trans. 44 (2003) 63–71.
[176] H.M. Hindam, W.W. Smeltzer, Growth and Microstructure of α-Al_2O_3 on Ni-Al Alloys: Internal Precipitation and Transition to External Scale, J. Electrochem. Soc. 127 (1980) 1622–1630.
[177] C.A. Stewart, R.K. Rhein, A. Suzuki, T.M. Pollock, C.G. Levi, Oxidation behavior across composition space relevant to Co-based γ/γ' alloys., (2018).
[178] D.R. Clarke, V.K. Tolpygo, M. Gentleman, Luminescence-Based Characterization of Protective Oxides: from Failure Mechanisms to Non-Destructive Evaluation, Mater. Sci. Forum. 461–464 (2004) 621–630. doi:10.4028/www.scientific.net/MSF.461-464.621.
[179] E.A. Lass, Application of Computational Thermodynamics to the Design of a Co-Ni-Based γ′-Strengthened Superalloy, Metall. Mater. Trans. A. 48 (2017) 2443–2459. doi:10.1007/s11661-017-4040-y.
[180] National Institute of Standards and Technology, NIST Chemistry WebBook, NIST Standard Reference Database Number 69, Gaithersburg MD, 20899, n.d.
[181] V.K. Tolpygo, D.R. Clarke, Competition between stress generation and relaxation during oxidation of an Fe-Cr-Al-Y alloy, Oxid. Met. 49 (1998) 187–212.
[182] M. Le Gall, A.M. Huntz, B. Lesage, C. Monty, J. Bernardini, Self-diffusion in α-Al_2O_3 and growth rate of alumina scales formed by oxidation: effect of Y_2O_3 doping, J. Mater. Sci. 30 (1995) 201–211.
[183] D. Jorgensen, Design and Characterization of High-Strength Bond Coats for Improved Thermal Barrier Coating Durability, Doctoral, University of California Santa Barbara, 2016.
[184] G. Matache, A. Paraschiv, C. Puşcaşu, R. Condruz, Solidification Segregation in CMSX-4 Superalloy: Experiments and Simulation Predictions, (n.d.) 4.

9 Appendix: Data of Combinatorial Samples

Sample buttons in the three combinatorial libraries each have a different alloy composition from IPD synthesis. Individual buttons are labeled, for example, 1-1A, where the first number is the library (1 = +Al library in Figure 6.1(a,d,g,j), 2 = +W library in Figure 6.1(b,e,h,k), and 3 = +Cr library in Figure 6.1(c,f,i,l)). The second number is the horizontal row of the button, with 1 being the largest bottom row of each library, and 12 being the top row, consisting of a single button. The letter is the position of the button from the left edge of the library, starting with 'A'. An example diagram is given below:

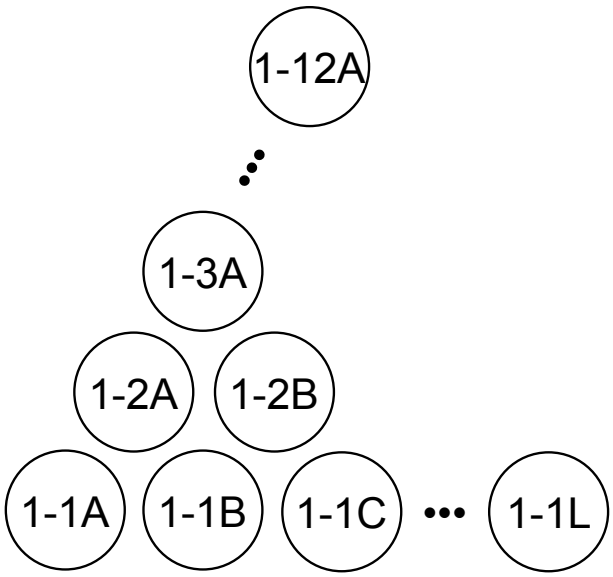

Figure 9.1: Naming scheme for combinatorial buttons, showing the first library, Figure 6.1a

Table 9.1: Experimental data for combinatorial libraries. Compositions measured by 15 keV SEM EDS on unoxidized surfaces, "Alloy Phases" codes correspond to: 1) no other phases observed beyond γ and potentially γ', 2) μ-Co_7W_6, 3) β-NiAl, 6) both μ and β. Oxide thickness and standard deviation (SD) are as measured by ImageJ in cross-section after 1 h 1100°C exposure to air. Data which have not been measured are marked "-".

Button	Co (at%)	Ni (at%)	W (at%)	Al (at%)	Cr (at%)	Ta (at%)	Ni:Co (at)	Alloy Phases	PSLS α-Al_2O_3 (out of 24)	Ave Oxide (um)	SD Oxide (um)
1-1A	-	-	-	-	-	-	-	-	-	-	-
1-1B	65.8	11.2	9.4	7.7	2.3	3.6	0.17	1	0	47	7.5
1-1C	63.7	12.3	8.8	9.2	2.6	3.4	0.19	1	0	-	-
1-1D	60	16.2	9.7	8.6	1.7	3.9	0.27	1	1	19	3
1-1E	55	20.1	9.6	9.9	1.8	3.6	0.37	1	1	14	3.5
1-1F	51.1	23.3	9.7	10.5	1.7	3.7	0.46	1	13	17	4.6
1-1G	46.5	28.5	9.6	10.8	1.8	2.8	0.61	2	-	-	-
1-1H	41.7	31.9	10.1	11.3	1.6	3.5	0.77	2	23	12	2.4
1-1I	38.2	35	9.8	11.5	2.3	3.3	0.92	2	-	-	-
1-1J	38.3	35.2	10	11.4	1.4	3.8	0.92	2	20	13	1.7
1-1K	35.3	36.2	10.3	12.7	1.9	3.7	1.03	2	-	-	-
1-1L	35.5	37.6	10.1	11.3	2.3	3.3	1.06	2	-	-	-
1-2A	-	-	-	-	-	-	-	-	0	60	3.9
1-2B	-	-	-	-	-	-	-	-	-	-	-
1-2C	-	-	-	-	-	-	-	-	-	-	-
1-2D	-	-	-	-	-	-	-	-	-	-	-
1-2E	-	-	-	-	-	-	-	-	-	-	-
1-2F	-	-	-	-	-	-	-	-	-	-	-
1-2G	-	-	-	-	-	-	-	-	-	-	-
1-2H	-	-	-	-	-	-	-	-	-	-	-
1-2I	-	-	-	-	-	-	-	-	-	-	-
1-2J	-	-	-	-	-	-	-	-	-	-	-
1-2K	-	-	-	-	-	-	-	-	24	-	-
1-3A	64.2	12.1	9.4	8.5	2	3.7	0.19	1	2	-	-
1-3B	61.2	14.6	9.2	8.6	2.5	3.9	0.24	1	-	-	-
1-3C	59.1	15.5	9.5	9.7	2.3	3.8	0.26	1	0	18.6	4.5
1-3D	54.3	20	9.3	10	2.6	3.7	0.37	1	-	-	-
1-3E	50.5	24	9.1	10.5	2.1	3.8	0.48	1	11	11.3	2
1-3F	46.8	27.2	9.4	11.3	1.9	3.4	0.58	2	-	-	-
1-3G	41.6	30.9	9.7	11.8	2.3	3.7	0.74	2	24	10	1.8
1-3H	38.2	34.9	9.3	11.7	2	3.8	0.91	2	-	-	-
1-3I	38	35.6	10.2	11.2	1.9	3.3	0.94	2	23	-	-
1-3J	37.6	35.2	9.8	11.5	2.6	3.3	0.94	2	24	10.1	2.1
1-4A	-	-	-	-	-	-	-	-	1	-	-
1-4B	59.1	16	9.1	9.5	2.5	3.9	0.27	1	-	-	-
1-4C	54.4	20.4	9.2	10.3	2.1	3.5	0.37	1	0	14	2.6
1-4D	51.2	24.1	8.9	10.4	1.7	3.6	0.47	1	6	11	2.5
1-4E	45.8	28	8.8	11.8	2	3.6	0.61	2	21	10	2.6
1-4F	42.4	31.3	9.4	11.7	1.6	3.6	0.74	2	22	-	-
1-4G	39.7	32.8	9.7	11.9	2.1	3.8	0.82	2	24	1.8	1.6
1-4H	39.1	35	9.6	11.5	2	2.8	0.89	2	23	-	-
1-4I	-	-	-	-	-	-	-	-	24	-	-

Table 9.1 continued

Button	Co (at%)	Ni (at%)	W (at%)	Al (at%)	Cr (at%)	Ta (at%)	Ni:Co (at)	Alloy Phases	PSLS α-Al_2O_3 (out of 24)	Ave Oxide (um)	SD Oxide (um)
1-5A	57.7	18	9.5	9.8	1.2	3.8	.31	1	0	14	3.1
1-5B	51.8	21.8	9	11.5	2.2	3.8	0.42	1	-	-	-
1-5C	50.9	23.3	8.7	11	2.6	3.6	0.46	1	-	-	-
1-5D	48.1	25.8	8.7	11.3	2.2	3.9	0.54	1	-	-	-
1-5E	44.5	28.2	9.5	12.8	1.9	3.1	0.63	2	-	-	-
1-5F	40.5	32.7	9.3	11.9	2.1	3.5	0.81	2	22	8.5	2
1-5G	40.7	33.9	9.2	11.5	1.9	2.9	0.83	2	23	8.3	2.1
1-5H	38.4	34.5	9.2	12.3	2.1	3.5	0.9	2	-	-	-
1-6A	-	-	-	-	-	-	-	-	19	8	2.4
1-6B	-	-	-	-	-	-	-	-	-	-	-
1-6C	46.3	26.8	8.7	12.1	2	4.1	0.58	1	23	-	-
1-6D	42.8	30.3	8.8	12	2.3	3.8	0.71	6	-	-	-
1-6E	41.6	32	9.1	12.1	1.9	3.5	0.77	6	24	9.5	2.2
1-6F	-	-	-	-	-	-	-	-	-	-	-
1-6G	-	-	-	-	-	-	-	-	23	-	-
1-7A	46.8	25.8	8.4	12.5	2.8	3.8	0.55	3	-	-	-
1-7B	45.7	27.4	8.8	12.3	2.2	3.6	0.6	3	-	-	-
1-7C	44.9	28.4	8.4	12.4	2.3	3.6	0.63	3	-	-	-
1-7D	40.4	32.5	8	12.8	1.9	4.4	0.8	3	-	-	-
1-7E	39.6	34	8.5	12.3	1.8	3.7	0.86	6	-	-	-
1-7F	39.9	33.3	8.7	12.7	1.9	3.5	0.84	6	-	-	-
1-8A	-	-	-	-	-	-	-	-	24	7.1	2.5
1-8B	-	-	-	-	-	-	-	-	-	-	-
1-8C	40.8	32.5	8.2	12.7	2.2	3.6	0.79	3	24	-	-
1-8D	-	-	-	-	-	-	-	-	-	-	-
1-8E	-	-	-	-	-	-	-	-	24	6	2.3
1-9A	40.8	32.2	8	13.1	2.1	3.7	0.79	3	-	-	-
1-9B	40.5	33.1	8.1	12.9	1.8	3.6	0.82	3	-	-	-
1-9C	39.4	34.2	8.4	12.7	2	3.5	0.87	3	-	-	-
1-9D	39.2	35	8.2	13.1	1.4	3.1	0.89	3	-	-	-
1-10A	-	-	-	-	-	-	-	-	24	6	2.3
1-10B	38.7	34.2	8	13.5	1.9	3.7	0.88	3	22	-	-
1-10C	-	-	-	-	-	-	-	-	-	-	-
1-11A	38.4	33.9	7.7	14.6	2	3.5	0.88	3	23	6.7	2
1-11B	-	-	-	-	-	-	-	-	-	-	-
1-12A	37.9	34.5	7.1	15.5	1.9	3	0.91	6	24	7	2.4

Table 9.1 continued

Button	Co (at%)	Ni (at%)	W (at%)	Al (at%)	Cr (at%)	Ta (at%)	Ni:Co (at)	Alloy Phases	PSLS α-Al_2O_3 (out of 24)	Ave Oxide (um)	SD Oxide (um)
2-1A	66.3	11	8	8.6	2.5	3.5	0.17	1	0	-	-
2-1B	-	-	-	-	-	-	-	-	-	-	-
2-1C	63	14.2	8.3	8.3	2.5	3.7	0.22	1	1	-	-
2-1D	-	-	-	-	-	-	-	-	-	-	-
2-1E	56.7	19.2	8.1	10.1	2.2	3.7	0.34	1	0	-	-
2-1F	-	-	-	-	-	-	-	-	-	-	-
2-1G	47.5	27.5	8.3	10.7	2.2	3.8	0.58	1	12	9	1.8
2-1H	-	-	-	-	-	-	-	-	-	-	-
2-1I	41.2	33.7	8.8	10.6	2.3	3.4	0.82	1	15	-	-
2-1J	-	-	-	-	-	-	-	-	-	-	-
2-1K	37.1	37.4	8.9	10.9	2.2	3.4	1.01	1	20	-	-
2-1L	-	-	-	-	-	-	-	-	-	-	-
2-2A	66	11.4	8.5	8.7	2	3.5	0.17	1	0	-	-
2-2B	-	-	-	-	-	-	-	-	-	-	-
2-2C	-	-	-	-	-	-	-	-	-	-	-
2-2D	-	-	-	-	-	-	-	-	-	-	-
2-2E	-	-	-	-	-	-	-	-	-	-	-
2-2F	-	-	-	-	-	-	-	-	-	-	-
2-2G	-	-	-	-	-	-	-	-	-	-	-
2-2H	-	-	-	-	-	-	-	-	-	-	-
2-2I	-	-	-	-	-	-	-	-	-	-	-
2-2J	-	-	-	-	-	-	-	-	-	-	-
2-2K	37	36.5	8.8	11.6	2.2	3.9	0.99	1	20	11	2.7
2-3A	66.1	11.3	7.8	8.9	2.5	3.5	0.17	1	0	-	-
2-3B	-	-	-	-	-	-	-	-	-	-	-
2-3C	60	17.3	7.4	9.3	2.3	3.7	0.29	1	0	-	-
2-3D	-	-	-	-	-	-	-	-	-	-	-
2-3E	-	-	-	-	-	-	-	-	-	-	-
2-3F	-	-	-	-	-	-	-	-	-	-	-
2-3G	-	-	-	-	-	-	-	-	-	-	-
2-3H	42.4	32.9	7.8	10.8	2.6	3.5	0.78	1	19	8.3	2.8
2-3I	-	-	-	-	-	-	-	-	-	-	-
2-3J	38.3	36.5	8.2	11.2	2.9	3	0.95	1	21	-	-
2-4A	61.6	16.3	7.7	8.8	2.1	3.4	0.26	1	0	-	-
2-4B	-	-	-	-	-	-	-	-	-	-	-
2-4C	-	-	-	-	-	-	-	-	-	-	-
2-4D	-	-	-	-	-	-	-	-	-	-	-
2-4E	47.7	27.9	6.9	11	2.7	3.9	0.58	1	6	14	4.2
2-4F	-	-	-	-	-	-	-	-	-	-	-
2-4G	-	-	-	-	-	-	-	-	-	-	-
2-4H	-	-	-	-	-	-	-	-	-	-	-
2-4I	36.9	37.5	8.7	11.5	1.8	3.7	1.02	1	24	8.5	2.3

Table 9.1 continued

Button	Co (at%)	Ni (at%)	W (at%)	Al (at%)	Cr (at%)	Ta (at%)	Ni:Co (at)	Alloy Phases	PSLS α-Al_2O_3 (out of 24)	Ave Oxide (um)	SD Oxide (um)
2-5A	58.3	19.8	6.5	9.4	2.4	3.5	0.34	1	0	-	-
2-5B	-	-	-	-	-	-	-	-	-	-	-
2-5C	51.5	26	6.3	10.2	2.6	3.4	0.5	1	12	10.4	4.7
2-5D	-	-	-	-	-	-	-	-	-	-	-
2-5E	-	-	-	-	-	-	-	-	-	-	-
2-5F	43.4	32.4	6.5	11.5	2.6	3.6	0.75	1	16	8.4	3
2-5G	-	-	-	-	-	-	-	-	-	-	-
2-5H	39.3	35	7.5	11.7	2.7	3.7	0.89	1	22	-	-
2-6A	54.2	23.7	6	10.2	2.2	3.7	0.44	1	12	11	4.9
2-6B	-	-	-	-	-	-	-	-	-	-	-
2-6C	-	-	-	-	-	-	-	-	-	-	-
2-6D	45.4	32.5	5.4	10.9	2.2	3.6	0.72	1	17	12	5.3
2-6E	-	-	-	-	-	-	-	-	-	-	-
2-6F	-	-	-	-	-	-	-	-	-	-	-
2-6G	40.6	35.6	7	11.4	1.9	3.5	0.88	1	23	9	2
2-7A	50.8	28.6	4.7	10.1	2.5	3.3	0.56	1	1	24	7
2-7B	-	-	-	-	-	-	-	-	-	-	-
2-7C	-	-	-	-	-	-	-	-	-	-	-
2-7D	-	-	-	-	-	-	-	-	-	-	-
2-7E	-	-	-	-	-	-	-	-	-	-	-
2-7F	42.6	35.6	5.4	10.8	2.4	3.2	0.84	1	12	12	3.9
2-8A	45.5	33.4	4.4	11.1	2	3.6	0.74	1	7	13	4.7
2-8B	-	-	-	-	-	-	-	-	-	-	-
2-8C	45.4	36.1	3.6	9.8	2.4	2.6	0.79	1	4	2	7.2
2-8D	-	-	-	-	-	-	-	-	-	-	-
2-8E	40.3	38.2	5.1	11.7	1.7	3	0.95	1	17	14	3
2-9A	45.7	34.2	3.2	11.2	2.7	3.1	0.75	1	2	-	-
2-9B	-	-	-	-	-	-	-	-	-	-	-
2-9C	-	-	-	-	-	-	-	-	-	-	-
2-9D	42.5	38.6	3.3	10.7	2.2	2.8	0.91	1	4	23	6
2-10A	41.5	39	3.2	11.6	1.8	3	0.94	1	1	-	-
2-10B	-	-	-	-	-	-	-	-	-	-	-
2-10C	39.9	39.5	3.3	12	1.6	3.6	0.99	1	4	-	-
2-11A	44.1	37.8	2.1	10.8	2.7	2.4	0.86	1	0	-	-
2-11B	42.7	39.9	2.2	10.1	2.4	2.7	0.94	1	1	-	-
2-12A	41.5	39.5	2	11.8	2.4	2.8	0.95	1	1	25	4.7

Table 9.1 continued

Button	Co (at%)	Ni (at%)	W (at%)	Al (at%)	Cr (at%)	Ta (at%)	Ni:Co (at)	Alloy Phases	PSLS α-Al_2O_3 (out of 24)	Ave Oxide (um)	SD Oxide (um)
3-1A	68	8.8	8.3	8.1	3.5	3.3	0.13	1	0	-	-
3-1B	68.6	9.4	8.1	7.4	3.8	2.7	0.14	1	2	-	-
3-1C	64.4	10.1	8.3	10	3.7	3.6	0.16	1	0	9.7	2.3
3-1D	63.8	11.9	8.6	8.9	4	2.8	0.19	1	0	-	-
3-1E	57.5	16.2	8.8	9.7	4	3.7	0.28	1	1	10.2	2.3
3-1F	54.6	19.8	9	9.7	4	2.8	0.36	1	4	8.8	3
3-1G	50.9	23	8.4	10.3	3.9	3.4	0.45	2	8	7.1	2.3
3-1H	46.1	28.4	9	9.9	3.8	2.9	0.62	2	22	6	2.5
3-1I	42.6	30.6	9	10.5	3.5	3.7	0.72	2	19	-	-
3-1J	41.1	33.2	8.9	10.3	3.8	2.6	0.81	2	23	5	2.7
3-1K	39.7	33.9	8.7	10.3	4	3.4	0.86	2	19	-	-
3-1L	39.2	34	9.1	11	3.7	3	0.87	2	22	-	-
3-2A	65.5	7.7	9.3	9.9	4.2	3.5	0.12	1	0	38.2	10.4
3-2B	-	-	-	-	-	-	-	-	-	-	-
3-2C	-	-	-	-	-	-	-	-	-	-	-
3-2D	-	-	-	-	-	-	-	-	-	-	-
3-2E	-	-	-	-	-	-	-	-	-	-	-
3-2F	-	-	-	-	-	-	-	-	-	-	-
3-2G	-	-	-	-	-	-	-	-	-	-	-
3-2H	-	-	-	-	-	-	-	-	-	-	-
3-2I	-	-	-	-	-	-	-	-	-	-	-
3-2J	-	-	-	-	-	-	-	-	-	-	-
3-2K	40.2	33.4	8.7	10.6	4.1	3.1	0.83	2	23	-	-
3-3A	63.5	11.8	8.6	8.6	4.1	3.3	0.19	1	0	-	-
3-3B	-	-	-	-	-	-	-	-	-	-	-
3-3C	60	14.7	8.3	8.5	5	3.5	0.24	1	2	-	-
3-3D	-	-	-	-	-	-	-	-	-	-	-
3-3E	-	-	-	-	-	-	-	-	-	-	-
3-3F	-	-	-	-	-	-	-	-	-	-	-
3-3G	-	-	-	-	-	-	-	-	-	-	-
3-3H	42.2	30.7	8.7	10.4	4.8	3.3	0.73	2	21	-	-
3-3I	-	-	-	-	-	-	-	-	-	-	-
3-3J	39.9	33	8.6	10.8	4	3.7	0.83	2	19	-	-
3-4A	60.7	11.8	9.3	9.8	4.8	3.5	0.19	1	2	19.6	4.6
3-4B	-	-	-	-	-	-	-	-	-	-	-
3-4C	-	-	-	-	-	-	-	-	-	-	-
3-4D	-	-	-	-	-	-	-	-	-	-	-
3-4E	46.6	25.6	8.8	10.2	5.8	3	0.55	2	13	7.6	3.2
3-4F	-	-	-	-	-	-	-	-	-	-	-
3-4G	-	-	-	-	-	-	-	-	-	-	-
3-4H	-	-	-	-	-	-	-	-	-	-	-
3-4I	-	-	-	-	-	-	-	-	-	-	-

Table 9.1 continued

Button	Co (at%)	Ni (at%)	W (at%)	Al (at%)	Cr (at%)	Ta (at%)	Ni:Co (at)	Alloy Phases	PSLS α-Al_2O_3 (out of 24)	Ave Oxide (um)	SD Oxide (um)
3-5A	58.8	14.2	8.6	9.4	5.6	3.5	0.24	1	5	-	-
3-5B	-	-	-	-	-	-	-	-	-	-	-
3-5C	50.2	22.5	8.3	9.5	6.2	3.3	0.45	1	14	-	-
3-5D	-	-	-	-	-	-	-	-	-	-	-
3-5E	-	-	-	-	-	-	-	-	-	-	-
3-5F	42	29.9	8.7	10.6	5.4	3.3	0.71	2	22	-	-
3-5G	-	-	-	-	-	-	-	-	-	-	-
3-5H	39.1	32.1	8.7	11.2	5.3	3.6	0.82	2	23	-	-
3-6A	53.5	17.8	9	9.3	7.6	2.8	0.33	1	1	12.9	4.6
3-6B	-	-	-	-	-	-	-	-	-	-	-
3-6C	-	-	-	-	-	-	-	-	-	-	-
3-6D	43.9	25.5	8.4	10.3	9	3	0.58	2	23	2.7	1.2
3-6E	-	-	-	-	-	-	-	-	-	-	-
3-6F	-	-	-	-	-	-	-	-	-	-	-
3-6G	-	-	-	-	-	-	-	-	-	-	-
3-7A	46.6	23.9	8.2	10.4	7.4	3.6	0.51	2	19	3.4	2.1
3-7B	-	-	-	-	-	-	-	-	-	-	-
3-7C	-	-	-	-	-	-	-	-	-	-	-
3-7D	-	-	-	-	-	-	-	-	-	-	-
3-7E	-	-	-	-	-	-	-	-	-	-	-
3-7F	40.2	30.2	8.3	11.3	6.2	3.7	0.75	2	24	1.3	0.7
3-8A	44.4	25.6	8.2	10.1	8.5	3.2	0.58	2	24	1.6	0.5
3-8B	-	-	-	-	-	-	-	-	-	-	-
3-8C	40.8	28.8	8.2	9.9	8.9	3.3	0.71	2	24	2.3	1
3-8D	-	-	-	-	-	-	-	-	-	-	-
3-8E	40.3	29.9	8.5	10.1	8.2	3.1	0.74	2	24	-	-
3-9A	40.5	28.4	8.2	10.2	8.6	4	0.7	2	24	-	-
3-9B	-	-	-	-	-	-	-	-	-	-	-
3-9C	-	-	-	-	-	-	-	-	-	-	-
3-9D	-	-	-	-	-	-	-	-	-	-	-
3-10A	-	-	-	-	-	-	-	-	-	-	-
3-10B	-	-	-	-	-	-	-	-	-	-	-
3-10C	-	-	-	-	-	-	-	-	24	-	-
3-11A	-	-	-	-	-	-	-	-	-	-	-
3-11B	-	-	-	-	-	-	-	-	24	-	-
3-12A	37.9	31.5	7.7	11.3	8.8	2.8	0.83	2	24	1.1	0.3